# Spatial Coherence and Entanglement in Optical Fields: Generation, Measurement, and Application

*A Thesis Submitted*

In Partial Fulfilment of the Requirements
for the Degree of

**Doctor of Philosophy**

by

**Abhinandan Bhattacharjee**

**DEPARTMENT OF PHYSICS**
**INDIAN INSTITUTE OF TECHNOLOGY KANPUR**

**October, 2021**

# CERTIFICATE

It is certified that the work contained in the thesis entitled "**Spatial Coherence and Entanglement in Optical Fields: Generation, Measurement, and Application**", by "**Abhinandan Bhattacharjee**", has been carried out under my supervision and that this work has not been submitted elsewhere for a degree.

Anand Kumar Jha

**Prof. Anand Kumar Jha**
(Thesis Supervisor)
**Department of Physics**
**Indian Institute of Technology Kanpur**

**October, 2021**

# Declaration

This is to certify that the thesis titled **"Spatial Coherence and Entanglement in Optical Fields: Generation, Measurement, and Application"** has been authored by me. It presents the research conducted by me under the supervision of **Prof. Anand Kumar Jha**. To the best of my knowledge, it is an original work, both in terms of research content and narrative, and has not been submitted elsewhere, in part or in full, for a degree. Further, due credit has been attributed to the relevant state-of-the-art and collaborations (if any) with appropriate citations and acknowledgements, in line with established norms and practices.

Abhinandan Bhattacharjee

Name: **Abhinandan Bhattacharjee**

Programme: PhD
Roll No: 15209261
Department: Physics
Indian Institute of Technology Kanpur
Kanpur 208016

# SYNOPSIS

---

Name of Student : **Abhinandan Bhattacherjee**
Roll Number : **15209261**
Degree for which submitted : **Doctor of Philosophy**
Department : **Physics**
Thesis title : **Spatial Coherence and Entanglement in Optical Fields: Generation, Measurement, and Application**
Name of thesis supervisor : **Prof. Anand Kumar Jha**
Month and year of thesis submission : **October, 2021**

---

Coherence is the only requirement in an optical field for producing interference, and it has been used as a tool for characterizing statistical randomness in optical fields. Recently, engineering coherence in the spatial degree of freedom has found several applications such as imaging, microscopy, optical communication, sensing, etc. However, the existing experimental methods for generating and measuring spatial coherence lack control, accuracy and efficiency. Therefore, improved experimental methods are required for practical applications.

In the past few decades, numerous experiments have verified that a two-photon optical field possesses a mysterious nonlocal correlation named quantum entanglement and it causes strong measurement correlations between spatially separated photons in multiple bases that has no classical counterpart. Moreover, entanglement enables unique tasks– teleportation and dense coding, especially spatial entanglement has found several quantum information applications. However, spatial entanglement has not been extensively explored in practical long-distance experiments due to the difficulties in the existing detection and manipulation techniques. This thesis develops experimental tools and techniques for studying spatial coherence and entanglement in optical fields from three aspects: generation, measurement, and application.

We begin with the study of spatial coherence in a spatially partially coherent field. The spatial coherence in an optical field is quantified through either spatial cross-spectral density function or spatial coherence function. All existing techniques use a spatially completely coherent field and external randomness for generating spatially partially coherent fields. As a result, the generation accuracy depends on the details of external randomness. In contrast, our method uses the coherent mode representation of a spatially partially coherent field and demonstrates the generation of propagation-invariant spatially stationary field and Gaussian Schell Model (GSM) field. To demonstrate the effectiveness of this technique, we generate spatially partially coherent fields with custom-designed spatial coherence functions with very good accuracy. Moreover, our technique does not require any additional randomness.

Next, we develop a controllable and accurate method for measuring spatial coherence in an optical field. The existing measurement schemes are unsuitable for measuring two-dimensional spatial cross-spectral density function. We propose and demonstrate an image inversion-based interferometric method for measuring two-dimensional cross-spectral density function in a two-shot manner. Our method comprises a Michelson interferometer with an additional converging lens in one of the arms, and the cross-spectral density function of the input field gets encoded in the intensity distribution of the output interferograms. Using this method, we report measurements of several lab-synthesized structured two-dimensional cross-spectral density functions with very good agreement with theory.

We then present an experimental technique for measuring position-momentum Einstein Podolsky Rosen (EPR) correlation. The EPR correlation measurement is a widely used experimental tool for certifying position-momentum entanglement. The accurate measurement of EPR correlation enhances the performance of many applications. However, all existing techniques for measuring the EPR correlation involve coincidence detection and thus suffer from issues that result in less accurate measurements. We propose and demonstrate a measurement scheme that does not require coincidence detection. We show that if a pure two-photon state satisfies a certain set of conditions, then the EPR correlation can be obtained by doing intensity measurements on one of the photons. We experimentally demonstrate this technique for the pure two-photon field produced by type-I spontaneous parametric down-conversion (SPDC) and report the most accurate measurement of position-momentum EPR correlation so far.

We next demonstrate the utility of spatial coherence in imaging and free-space communication through random media. It is known that a spatially partially coherent light field performs better imaging than a spatially coherent field. The image quality increases as the spatial coherence length of the field becomes smaller. The spatial coherence length of most spatially partially coherent fields increases upon propagation. As a result, the field produces progressively decreasing image quality at subsequent transverse planes. We address this issue by engineering the propagation of spatial coherence of the illuminating field. Using a spatially partially coherent field with propagation-invariant spatial coherence function, we report imaging of different transverse planes with equal quality over 40 cm. Furthermore, we generate a spatially partially coherent field that can be tailored to have the minimum possible spatial coherence length at the plane of the object to be imaged. Using this source, we demonstrate imaging of spatially separated transverse planes with the maximum possible image quality. Next, we demonstrate the implication of spatially partially coherent fields with structured cross-spectral density functions in free-space communication. Recently, structured transverse intensity profiles of spatially coherent fields have been used for encoding information in free-space communication. However, in the presence of turbulence, the intensity structures of such fields start to degrade due to the perfect spatial coherence of the field, which makes retrieval of information very challenging. We address this issue by demonstrating the structural robustness of spatially partially coherent fields in the presence of turbulence. We show that for a given turbulence strength, the structural robustness of cross-spectral density functions increases as we decrease the spatial coherence length of the field.

Lastly, we present the revival of spatial entanglement in the two-photon SPDC field through propagation. Spatial entanglement has been extensively studied in position-momentum bases due to its applicability in quantum information science; however, it is not suitable for applications involving long-distance propagation. This is because the entanglement starts decaying when the photons propagate away from their source and the effect becomes even more pronounced in turbulence. Here we explore the propagation of spatial entanglement in angle-orbital angular momentum (OAM) bases and show that the angle-OAM entanglement exhibits remarkably different behaviour. As with the position-momentum case, initially, the angle-OAM entanglement decays with propagation, but as the photons continue to travel further from the source, the photons regain their strongly correlated behaviour, and the entanglement returns. We theoretically and experimentally demonstrate this behaviour and show that entanglement returns even in the presence of strong turbulence. The only effect of turbulence is to increase the propagation distance for revival, but once revived, the two photons remain entangled up to an arbitrary propagation distance.

**To My Family and All My Teachers.**

# Acknowledgments

First and foremost I would like to extend my sincere gratitude towards my supervisor Prof. Anand Kumar Jha for his unfathomable support and wonderful guidance throughout my Ph.D. journey. It is because of his continuous affirmations and encouragement that kept me inspired in the arduous journey of my experimental research. I am deeply indebted to his immense assistance and sharp insights that helped me do my research with dedication, honesty, and detached bent of mind.

Besides my advisor, I am thankful to Prof. Harshawardhan Wanare and Prof. Saikat Ghosh for bestowing their helpful feedback during peer review meetings. I sincerely thank all the collaborators including Prof. Jonathan Leach, Prof. Harshwardhan Wanare, Dr. Nilakantha Meher, Shaurya Aarav, Suman Karan, Mritunjay Joshi, and Rishabh Sahu, for their contribution to various research projects. I also thank Girish, Vatshal, Samarth, Shreshtha, Radhika, Sanjana, Ruchi, and other present and past QOE lab members for productive discussions. I applaud their efforts to create a positive lab environment. My deepest gratitude to all the members of the physics administration, technical and non-technical staff for aiding me with different formalities. A special thanks to Om Prakash Ji and the physics workshop team for providing customized mechanical equipment.

I would also like to thank my friends and seniors including Pritam, Suvankar, Bikash, Barun, Swadesh Da, Avijit, Arif, Pratik, Debojyoti, Mir, Moumita, Songshaptak, Sandip Da, Arif Da, Rajan Da, Tamal Da, and others for their valuable suggestions, and support throughout this journey. I submit my deepest regards to my parents and sister for their unwavering love and support, without which I would not have been able to complete my Ph.D.

Finally, I submit my humble gratitude to our institution IITK , all the concerned governmental funding agencies for providing the financial assistance.

October, 2021 *A*bhinandan Bhattacharjee

# Publications

## Publications included in this thesis:

1. **Abhinandan Bhattacharjee**, Mritunjay Kumar Joshi, Suman Karan, Jonathan Leach, and Anand Kumar Jha,
   *"Propagation-induced entanglement revival"*,
   `arXiv:2111.04420 [quant-ph]`,

2. **Abhinandan Bhattacharjee**, Nilakantha Meher, and Anand Kumar Jha,
   *"Measurement of two-photon position-momentum EPR correlations through single-photon intensity measurements"*,
   `arXiv:2102.04356 [quant-ph]`,

3. **Abhinandan Bhattacharjee** and Anand Kumar Jha,
   *"Experimental demonstration of structural robustness of spatially partially coherent fields in turbulence"*,
   `Optics Letters 45 (2020) 4068`,
   `arXiv:2006.11724 [physics.optics]`,

4. **Abhinandan Bhattacharjee**, Shaurya Aarav, Harshawardhan Wanare and Anand Kumar Jha,
   *"Controlling propagation of spatial coherence for enhanced imaging through scattering media"*,
   `Physical Review A 101 (2020) 043839`,
   `arXiv:1810.00686 [physics.optics]`,

5. **Abhinandan Bhattacharjee**, Rishabh Sahu, and Anand Kumar Jha,
   *"Generation of a Gaussian Schell-model field as a mixture of its coherent modes"*,
   `Journal of Optics 21 (2019) 105601`,
   `arXiv:1808.08774 [physics.optics]`,

6. **Abhinandan Bhattacharjee**, Shaurya Aarav, and Anand Kumar Jha,
   *"Two-shot measurement of spatial coherence"*,
   `Applied Physics Letters 113 (2018) 051102`,

arXiv:1712.04517 [physics.ins-det],

7. Shaurya Aarav, **Abhinandan Bhattacharjee**, Harshawardhan Wanare, and Anand Kumar Jha,
*"Efficient generation of propagation-invariant spatially-stationary partially coherent fields"*,
Physical Review A 96 (2017) 033815,
arXiv:1707.06850 [physics.optics].

# Contents

# List of Figures

# Chapter 1

# Background

## 1.1 Introduction

Correlation in optical fields exhibits many interesting physical phenomena, and the interference effect is one of its natural manifestations. In classical optics, if the interfering electric field vibrations are coherent, then it causes interference [1–3]. On the other hand, in quantum optical fields, the indistinguishability of the interfering alternatives leads to interference [4–12]. It has been shown that the degree of indistinguishability of the interfering alternatives is equal to the degree of coherence between them [13]. In other words, one observes interference as long as the interfering alternatives remain coherent. Thus, coherence is the intrinsic correlation in classical and quantum optical fields that enables the interference effect. Coherence has been extensively studied through various interference experiments for understanding statistical fluctuations in optical fields. A rigorous statistical theory has been formulated by Zernike [3], Wolf [2,14–16], Glauber [17,18], and other researchers [19, 20] for studying the quantification and propagation of coherence with both classical and quantum mechanical treatments. In recent times, spatial coherence in an optical field has offered advantages in many real-world applications such as imaging through random media [21–23], microscopy [24,25], optical coherence tomography (OCT) [26], sensing [27], particle trapping [28], etc. Therefore, it is important to have efficient techniques for generating and measuring spatial coherence that can be implemented in practical applications.

In the past few decades, interference experiments with two-photon fields [9, 29–32] have become an important research area for understanding the mysterious correlation in such optical fields called entanglement [33–35]. It refers to the inseparability in the global state, which implies that the global state is not equal to the tensor product of the states of individual photon fields. Moreover, this mysterious nonlocal correlation enables new quantum information protocols– teleportation [36] and superdense coding [37], which are impossible to perform without entanglement. Spontaneous parametric down-conversion (SPDC) is the most widely used source for generating entangled two-photon fields in polarization [38], position-momentum [39], angle-orbital angular momentum (OAM) [40], and time-energy [41] degrees of freedom. The spatial entanglement in SPDC two-photon field has shown promising utility in many applications such as quantum imaging [42–46], quantum holography [47–49], quantum metrology [50], quantum information processing [51, 52], quantum secure communication [51, 53, 54], etc. However, limitations in the existing detection and manipulation techniques restrict the experimental implications of spatial entanglement in realistic situations including long-distance propagation in the presence of turbulence and noise. Thus, efficient and controllable experimental tools are required for manipulating and detecting spatial entanglement from the prospect of many quantum information processing applications. This thesis focuses on developing experimental tools for studying spatial coherence and entanglement in optical fields. We divide this thesis into three research themes: generation of spatial coherence, measurement of spatial coherence and entanglement, and application of spatial coherence and entanglement.

The contents are organized in the following manner. In sections 1.2 and 1.3, we introduce the concept of spatial coherence in an optical field and describe the free-space propagation of spatial coherence, respectively. The section 1.4 reviews the coherent mode representation of an optical field. In section 1.5, we discuss Wigner distribution function for an optical field. In section 1.6, we introduce the concept of spatial entanglement. In sections 1.7 and 1.8, we introduce the basics of nonlinear optics and describe the SPDC process respectively. In section 1.9, we summarize and outline the contents of this thesis.

## 1.2 Spatial coherence in optical fields

In this section, we introduce the concept of spatial coherence with both classical and single-photon fields. We formulate the theory of spatial coherence in space-frequency domain [15].

### 1.2.1 Classical field

In the context of classical optical fields, we consider light as a classical wave. We describe the concept of spatial coherence through Young's double slit interference experiment. Figure 1.1 shows the schematic of a Young's double slit interferometer. Consider $E(\boldsymbol{r}_1, \omega)$ and $E(\boldsymbol{r}_2, \omega)$ denote electric field amplitudes at spatial points $\boldsymbol{r}_1 \equiv (\boldsymbol{\rho}_1, z)$ and $\boldsymbol{r}_1 \equiv (\boldsymbol{\rho}_2, z)$ at frequency $\omega$ respectively. Figure 1.1 shows that the light fields coming from $\boldsymbol{r}_1$ and $\boldsymbol{r}_2$ overlap at the detection point $\boldsymbol{r}_d$ at frequency $\omega$, where $\boldsymbol{r}_d \equiv (\boldsymbol{\rho}_d, z_d)$. We note that the fields at the detection plane and at the slit plane have the same frequency $\omega$ and we are interested in the spatial correlation between the two interfering fields. For the sake of simplicity, we drop the frequency argument from the electric field representation in our further analysis. We now write the electric field $E(\boldsymbol{\rho}_d; z_d)$ at the detection point $(\boldsymbol{\rho}_d; z_d)$ is given by

$$E(\boldsymbol{\rho}_d; z_d; \omega) = k_1 E(\boldsymbol{\rho}_1; z) e^{-ik_0 d_1} + k_2 E(\boldsymbol{\rho}_2; z) e^{-ik_0 d_2}, \tag{1.1}$$

where $k_1$ and $k_2$ are complex constants, depend on the size and geometry of the slits, $k_0$ is the central wave-vector magnitude, $d_{1,2} = |\boldsymbol{\rho}_d - \boldsymbol{\rho}_{1,2}|$. The corresponding intensity distribution $I(\boldsymbol{\rho}_d; z_d)$ is given by

$$I(\boldsymbol{\rho}_d; z_d) = \langle E^*(\boldsymbol{\rho}_d; z_d)E(\boldsymbol{\rho}_d; z_d)\rangle_e = |k_1|^2\langle E^*(\boldsymbol{\rho}_1; z)E(\boldsymbol{\rho}_1; z)\rangle_e + |k_2|^2\langle E^*(\boldsymbol{\rho}_2; z)E(\boldsymbol{\rho}_2; z)\rangle_e + k_1^* k_2 \langle E^*(\boldsymbol{\rho}_1; z)E(\boldsymbol{\rho}_2; z)\rangle_e e^{ik_0(d_2-d_1)} + c.c, \tag{1.2}$$

where $\langle ....\rangle_e$ represents ensemble average over large number of realizations of the field. The terms $I(\boldsymbol{\rho}_1; z) = \langle E^*(\boldsymbol{\rho}_1; z)E(\boldsymbol{\rho}_1; z)\rangle_e$ and $I(\boldsymbol{\rho}_2; z) = \langle E^*(\boldsymbol{\rho}_2; z)E(\boldsymbol{\rho}_2; z)\rangle_e$ are the intensities at first and second slits respectively. The term $W(\boldsymbol{\rho}_1, \boldsymbol{\rho}_2; z) = \langle E^*(\boldsymbol{\rho}_1; z)E(\boldsymbol{\rho}_2; z)\rangle_e$ represents the first order spatial correlation function or spatial cross-spectral density function [15] of the input field at $z = z$ plane. The above Eq. (1.2) takes the form

$$I(\boldsymbol{\rho}_d; z_d) = |k_1|^2 I(\boldsymbol{\rho}_1; z) + |k_2|^2 I(\boldsymbol{\rho}_2; z) + 2|k_1||k_2||W(\boldsymbol{\rho}_1, \boldsymbol{\rho}_2; z)| \cos(\phi_d + \phi). \tag{1.3}$$

Here $\phi_d = k_0 d$, $d = d_2 - d_1$, $\phi = \phi_W + \phi_k$, $\phi_W = arg[W(\boldsymbol{\rho}_1, \boldsymbol{\rho}_2; z)]$, $\phi_k = arg[k_1^* k_2]$. This is the general intensity expression for Young's double slit interferogram. The last term in $I(\boldsymbol{\rho}_d; z_d)$ is responsible for producing the interfernce fringes and it depends on the the cross-spectral density function $W(\boldsymbol{\rho}_1, \boldsymbol{\rho}_2; z)$ of the input field at the double slit plane. We now normalize the cross-spectral density function and define a new quantity: spatial degree of coherence function or spatial coherence function and it is given by [15]

$$\mu(\boldsymbol{\rho}_1, \boldsymbol{\rho}_2; z) = \frac{|W(\boldsymbol{\rho}_1, \boldsymbol{\rho}_2; z)|}{\sqrt{I(\boldsymbol{\rho}_1; z)I(\boldsymbol{\rho}_2; z)}}. \tag{1.4}$$

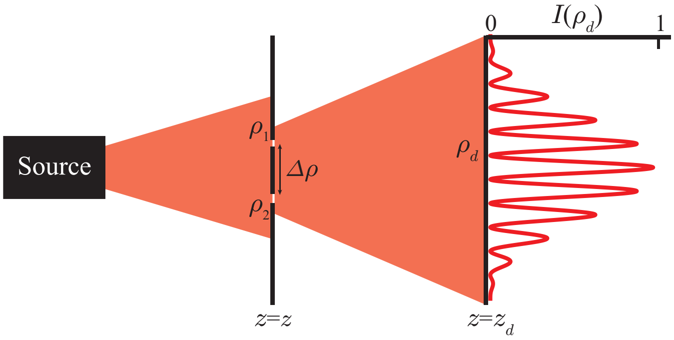

FIGURE 1.1: Schematic of a Young double-slit interferometer for illustrating spatial coherence between $\boldsymbol{\rho}_1$ and $\boldsymbol{\rho}_2$.

The above Eq. (1.4) implies that $0 \leqslant \mu(\boldsymbol{\rho}_1, \boldsymbol{\rho}_2; z) \leqslant 1$. We rewrite the Eq. (1.3) as

$$I(\boldsymbol{\rho}_d; z_d) = |k_1|^2 I(\boldsymbol{\rho}_1; z) + |k_2|^2 I(\boldsymbol{\rho}_2; z) + 2|k_1||k_2|\sqrt{I(\boldsymbol{\rho}_1; z) I(\boldsymbol{\rho}_2; z)}\mu(\boldsymbol{\rho}_1, \boldsymbol{\rho}_2; z)\cos(\phi_d + \phi). \tag{1.5}$$

The degree of interference effect is quantified through the fringe visibility. The visibility $V$ is given by

$$V = \frac{I_{max} - I_{min}}{I_{max} + I_{min}} = \frac{2|k_1||k_2|\sqrt{I(\boldsymbol{\rho}_1; z) I(\boldsymbol{\rho}_2; z)}}{|k_1|^2 I(\boldsymbol{\rho}_1; z) + |k_2|^2 I(\boldsymbol{\rho}_2; z)}\mu(\boldsymbol{\rho}_1, \boldsymbol{\rho}_2; z). \tag{1.6}$$

This shows that the fringe visibility relies on the degree of coherence between the spatial points $(\boldsymbol{\rho}_1; z)$ and $(\boldsymbol{\rho}_2; z)$. We assume $|k_1| = |k_2|$ and $I(\boldsymbol{\rho}_1; z) = I(\boldsymbol{\rho}_2; z)$. Most of the experiments follow this assumption. In this thesis, we work under the above assumption. The above visibility expression becomes

$$V = \mu(\boldsymbol{\rho}_1, \boldsymbol{\rho}_2; z) = \mu(\Delta\rho; z). \tag{1.7}$$

The ability of interference for light fields coming from $\boldsymbol{\rho}_1$ and $\boldsymbol{\rho}_2$ is solely decided by the degree of coherence between them. The visibility depends on the separation $\Delta\rho = |\boldsymbol{\rho}_1 - \boldsymbol{\rho}_2|$. By analyzing the visibility for different $\Delta\rho$ we get the profile of the spatial coherence function $\mu(\Delta\rho; z)$ and the width of that is defined as the spatial coherence length $\sigma_c$. Now, we catagorize different light sources by looking at the functional profile of $\mu(\Delta\rho; z)$.

Figures 1.2(a),(b), and (c) depict Young's double-slit fringes at different slit separation for spatially perfectly coherent source, spatially partially coherent source, and spatially incoherent source, respectively. Figure 1.2(d) illustrates $\mu(\Delta\rho; z)$ as a function of $\Delta\rho$ for a spatially perfectly coherent source and it shows that the $\mu(\Delta\rho; z)$ remains one at different slit separations. On the other hand, for a spatially partially coherent source, the visibility decreases with the increase in the slit separation $\Delta\rho$, and it is illustrated in Fig. 1.2(e), where $\mu(\Delta\rho; z)$ monotonically decays as a function of $\Delta\rho$. For a spatially incoherent source, no interference fringe is observed. Figures 1.2(d),(e) and (f) show that the spatial coherence length $\sigma_c$ is infinite, finite, and almost zero for spatially perfectly coherent

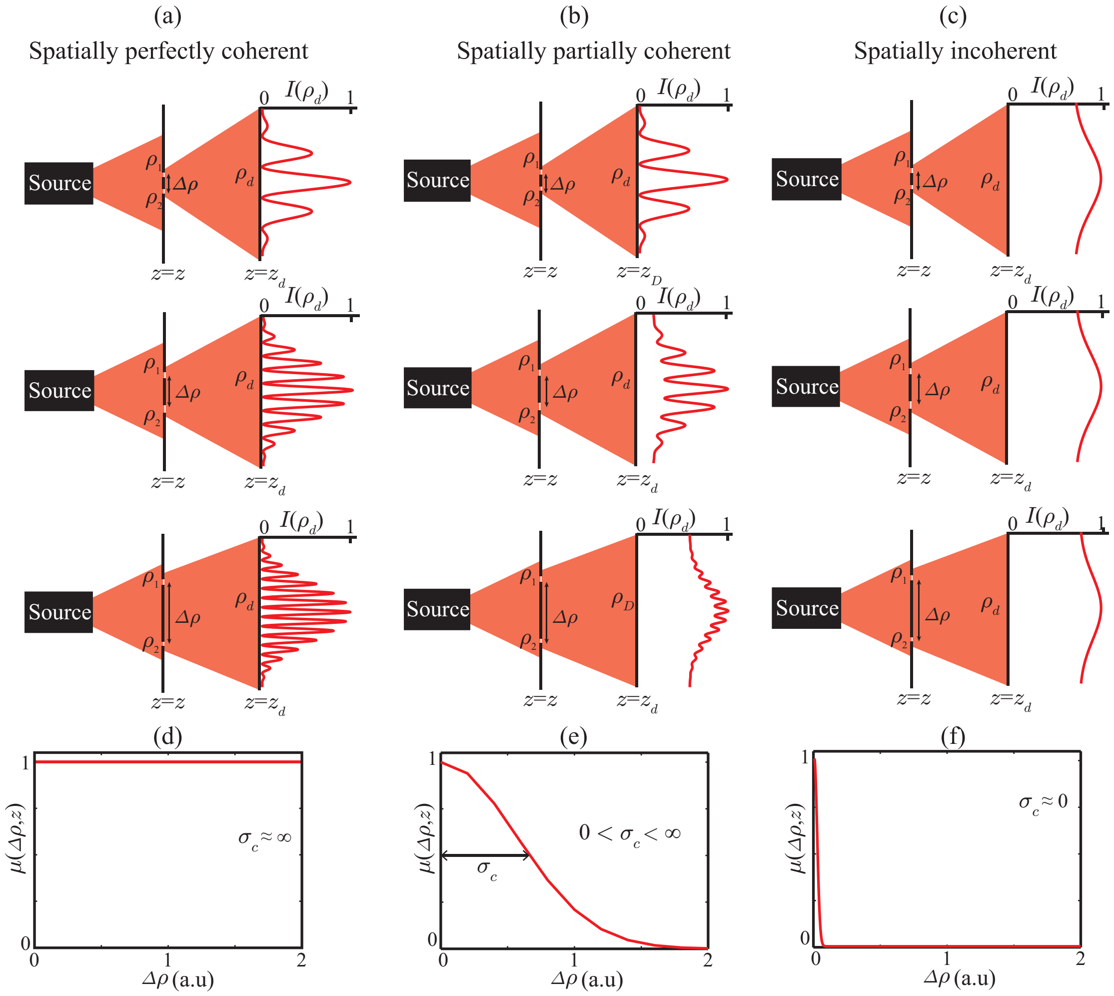

FIGURE 1.2: (a), (b), and (c) Depict the Young double-slit fringes for spatially perfectly coherent source, spatially partially coherent source and spatially incoherent source respectively. (d), (e), and (f) Depict $\mu(\Delta\rho)$ as a function of $\Delta\rho$ for spatially perfectly coherent source, spatially partially coherent source and spatially incoherent source respectively.

source, spatially partially coherent source, and spatially incoherent source, respectively. This analysis clearly shows that the interference signature gets washed out when the separation between the interfering fields $\Delta\rho$ exceeds the spatial coherence length $\sigma_c$.

### 1.2.2 Single-photon field

In this section, we revisit the Young's double slit interference experiment with quantum mechanical treatment for understanding spatial coherence in single-photon field. We first briefly review the concept of field operators. In the quantum theory of optical coherence [17], we quantize the electromagnetic field and represent the electric field amplitude $V(\boldsymbol{r}, t)$ by a Hermitian operator $\hat{V}(\boldsymbol{r}, t)$, the state of electromagnetic field is described by photon number. The field operator is written as [17]

$$\hat{V}(\boldsymbol{r}, t) = \hat{V}^{(+)}(\boldsymbol{r}, t) + \hat{V}^{(-)}(\boldsymbol{r}, t), \tag{1.8}$$

where, $\hat{V}^{(+)}(\boldsymbol{r}, t)$ and $\hat{V}^{(}-)(\boldsymbol{r}, t)$ are the positive and negative field operators, respectively. The operator $\hat{V}^{(}+)(\boldsymbol{r}, t)$ absorbs a photon at $(\boldsymbol{r}, t)$, whereas the operator $\hat{V}^{(-)}(\boldsymbol{r}, t)$ emits a photon at $(\boldsymbol{r}, t)$. The quantized electric field is expressed in the plane-wave basis in the form [17]

$$\hat{V}(\boldsymbol{r}, t) = \sum_{\boldsymbol{k}} i \left[\frac{\hbar\omega_{\boldsymbol{k}}}{2\epsilon_0 L}\right]^{\frac{1}{2}} \hat{a}_{\boldsymbol{k}}(t) e^{i(\omega_{\boldsymbol{k}} t - \boldsymbol{k}\cdot\boldsymbol{r})} - \sum_{\boldsymbol{k}} i \left[\frac{\hbar\omega_{\boldsymbol{k}}}{2\epsilon_0 L}\right]^{\frac{1}{2}} \hat{a}^{\dagger}_{\boldsymbol{k}}(t) e^{i(\omega_{\boldsymbol{k}} t - \boldsymbol{k}\cdot\boldsymbol{r})}. \tag{1.9}$$

Here $\hat{a}_{\boldsymbol{k}}(t)$ and $\hat{a}^{\dagger}_{\boldsymbol{k}}(t)$ are the annihilation and creation field operators respectively, for the plane-wave mode $\boldsymbol{k}$ and frequency mode $\omega_{\boldsymbol{k}}$, $L^3$ represents the quantization volume.

We now use the Fourier relation between time and frequency basis to write the field operator in the frequency basis

$$\hat{E}(\boldsymbol{r}, \omega) = \frac{1}{2\pi}\int_{-\infty}^{\infty} \hat{V}(\boldsymbol{r}, t) e^{i\omega t} dt = \hat{E}^{(+)}(\boldsymbol{r}, \omega) + \hat{E}^{(-)}(\boldsymbol{r}, \omega), \tag{1.10}$$

where

$$\hat{E}^{(+)}(\boldsymbol{r}, \omega) = \frac{1}{2\pi}\int_{-\infty}^{\infty} \hat{V}^{(+)}(\boldsymbol{r}, t) e^{i\omega t} dt, \qquad \hat{E}^{(-)}(\boldsymbol{r}, \omega) = \frac{1}{2\pi}\int_{-\infty}^{\infty} \hat{V}^{(-)}(\boldsymbol{r}, t) e^{i\omega t} dt. \tag{1.11}$$

The operators $\hat{E}^{(+)}(\boldsymbol{r}, \omega)$ and $\hat{E}^{(-)}(\boldsymbol{r}, \omega)$ absorbs and emits a photon respectively, at spatial point $\boldsymbol{r} \equiv (\boldsymbol{\rho}; z)$ and frequency $\omega$.

Consider $|\psi\rangle$ describes the normalized state of a single-photon field. We note that for quantum fields, position and momentum are parameters or variables, not operators. We have discussed above in this case, one detects the photon at a position or momentum mode through the annihilation and creation field operators. For example, the state $|\psi\rangle$

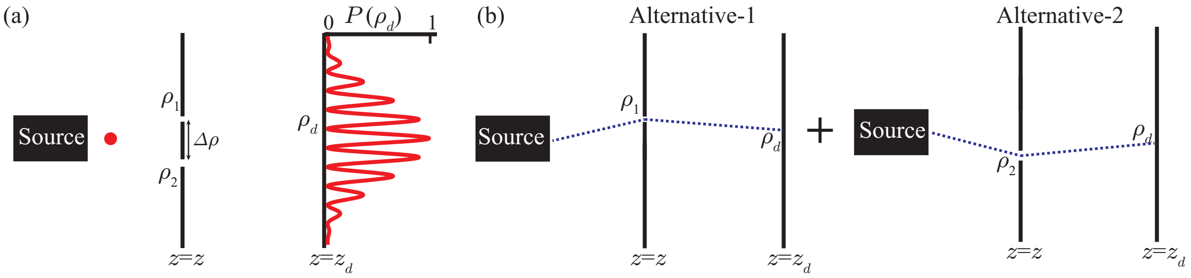

FIGURE 1.3: (a) Depicts the Young's double slit interference for a single photon source. (b) Illustrates the two interfering alternatives. The photon reaches the detector either through the slit at $\boldsymbol{\rho}_1$ in alternative-1 or through the slit at $\boldsymbol{\rho}_2$ in alternative-2.

gets detected at the transverse point $x$ through field operators $\hat{E}^{(+)}(x)$ and $\hat{E}^{(-)}(x)$. We express $|\psi\rangle$ in the position basis as

$$|\psi\rangle = A \int \psi(x) \hat{E}^{(-)}(x) |vac\rangle dx \tag{1.12}$$

where $A$ is a constant. The probability distribution of detecting the photon at $x$ is shown to be proportional to $|\psi(x)|^2$. In the recent literature on quantum optics [45, 55–58], the function $\psi(x)$ in termed as position wavefunction and we have adopted this terminology throughout this thesis.

Figure 1.3(a) shows Young's double-slit interferometer with a single-photon source; the emitted photon goes through one of the slits to reach the detector kept at the spatial point $\boldsymbol{r}_d \equiv (\boldsymbol{\rho}_d; z_d)$ and at frequency $\omega$. Figure 1.3(b) illustrates the two spatial alternatives through which the photon can reach the detector. We now show that the coherence between these two spatial alternatives causes interference.

Like section 1.2.1, here also we focus on the spatial correlation between interfering alternatives at the detection frequency $\omega$. For the sake of consistency, we drop the frequency argument in the field operators. The field operator $\hat{E}^{(+)}(\boldsymbol{\rho}_d; z_d)$ at the detection point $(\boldsymbol{\rho}_d; z_d)$ is given by

$$\hat{E}^{(+)}(\boldsymbol{\rho}_d; z_d) = k_1 \hat{E}^{(+)}(\boldsymbol{\rho}_1; z) e^{ik_0 d_1} + k_2 \hat{E}^{(+)}(\boldsymbol{\rho}_2; z) e^{ik_0 d_2}, \tag{1.13}$$

where $\hat{E}^{(+)}(\boldsymbol{\rho}_1;z)$ and $\hat{E}^{(+)}(\boldsymbol{\rho}_2;z)$ are the positive field operators for the slits at $(\rho_1;z)$ and $(\rho_2;z)$ respectively, $d_{1,2} = |\rho_d - \rho_{1,2}|$, $k_0$ represents the magnitude of the wave-vector, $k_1$ and $k_2$ are the complex constants. The single-photon counting rate at the spatial point $(\boldsymbol{\rho}_d;z_d)$ is given by [17]

$$\begin{aligned} P(\boldsymbol{\rho}_d;z_d) &= \langle\langle\psi|\hat{E}^{(-)}(\boldsymbol{\rho}_d;z_d)\hat{E}^{(+)}(\boldsymbol{\rho}_d;z_d)|\psi\rangle\rangle_e \\ &= |k_1|^2\langle\langle\psi|\hat{E}^{(-)}(\boldsymbol{\rho}_1;z)\hat{E}^{(+)}(\boldsymbol{\rho}_1;z)|\psi\rangle\rangle_e + |k_2|^2\langle\langle\psi|\hat{E}^{(-)}(\boldsymbol{\rho}_2;z)\hat{E}^{(+)}(\boldsymbol{\rho}_2;z)|\psi\rangle\rangle_e \\ &\quad + k_1^*k_2\langle\langle\psi|\hat{E}^{(-)}(\boldsymbol{\rho}_1;z)\hat{E}^{(+)}(\boldsymbol{\rho}_2;z)|\psi\rangle\rangle_e e^{ik_0(d_2-d_1)} + c.c, \end{aligned} \tag{1.14}$$

where $\langle ...\rangle_e$ respresents the ensemble average over many realizations of single-photon state. From Glauber's quantum theory of coherence [17], $P(\boldsymbol{\rho}_1;z) = \langle\langle\psi|\hat{E}^{(-)}(\boldsymbol{\rho}_1;z)\hat{E}^{(+)}(\boldsymbol{\rho}_1, z)|\psi\rangle\rangle_e$ and $P(\boldsymbol{\rho}_2;z) = \langle\langle\psi|\hat{E}^{(-)}(\boldsymbol{\rho}_2;z)\hat{E}^{(+)}(\boldsymbol{\rho}_2;z)|\psi\rangle\rangle_e$ are the counting rate associated with the alternative-1 and alternative-2 respectively. $W(\boldsymbol{\rho}_1,\boldsymbol{\rho}_2;z) = \langle\langle\psi|\hat{E}^{(-)}(\boldsymbol{\rho}_1;z)\hat{E}^{(+)}(\boldsymbol{\rho}_2;z)|\psi\rangle\rangle_e$ represents the first order correlation function at the double slit plane and we refer it as the spatial cross-spectral density function of the single-photon field. We define the spatial coherence function as $\mu(\boldsymbol{\rho}_1,\boldsymbol{\rho}_2;z) = |W(\boldsymbol{\rho}_1,\boldsymbol{\rho}_2;z)|/\sqrt{P(\boldsymbol{\rho}_1;z)P(\boldsymbol{\rho}_2;z)}$ and it quantifies the coherence between two spatial alternatives. The Eq. (1.14) takes the form

$$\begin{aligned} P(\boldsymbol{\rho}_d;z_d) = |k_1|^2P(\boldsymbol{\rho}_1;z) + |k_2|^2P(\boldsymbol{\rho}_2;z) + 2|k_1||k_2|\sqrt{P(\boldsymbol{\rho}_1;z)P(\boldsymbol{\rho}_2;z)}\mu(\boldsymbol{\rho}_1,\boldsymbol{\rho}_2;z) \\ \times\cos(\phi_d+\phi). \end{aligned} \tag{1.15}$$

Here $\phi_d = k_0d$, $d = d_2 - d_1$, $\phi = \phi_W + \phi_k$, $\phi_W = arg[W]$, and $\phi_k = arg[k_1^*k_2]$. The third term in the above expression causes interference, which relies on coherence between two spatial interfering alternatives. The interference effect for a single-photon field is interpreted as the interference of two spatial alternatives associated with the photon, in contrast to the interpretation of classical interference. However, we note that the expression of counting rate $P(\boldsymbol{\rho}_d;z_d)$ in the above Eq. (1.15) is analogous to the transverse intensity distribution $I(\boldsymbol{\rho}_d;z_d)$ in Eq. (1.5) for a classical field. Furthermore, under the assumption $P(\boldsymbol{\rho}_1;z) = P(\boldsymbol{\rho}_2;z)$ and $|k_1| = |k_2|$, the visibility $V$ of interference fringes becomes equal to the degree of coherence $\mu(\boldsymbol{\rho}_1,\boldsymbol{\rho}_2;z)$ between two spatial alternatives.

This implies that the characteristics of spatial cross-spectral density function $W(\boldsymbol{\rho}_1, \boldsymbol{\rho}_2; z)$ or coherence function $\mu(\boldsymbol{\rho}_1, \boldsymbol{\rho}_2; z)$ remain equivalent in both classical field and quantum single-photon field [19,59–61] and one can define spatially completely coherent, partially coherent and incoherent single-photon field parallel to that of classical field. From now on, we will consider spatial coherence in the classical field and spatial coherence in the single-photon field as a single concept. We will refer to this concept as spatial coherence in an optical field. So far our analysis has shown that the classical treatment reproduces the result of an interference experiment with a single-photon field. However, the classical treatment has failed to reproduce the results of two-photon or multiphoton quantum interference effects that involve coincidence detection or multi-fold detection respectively, such as Hong-Ou-Mandel [8], Franson [9, 30], etc [62, 63]. We note that the above mentioned coincidence based interference experiments are beyond the scope of this thesis.

In chapter 2 and 3, we present our experimental techniques for generating and measuring spatial coherence in a spatially partially coherent optical field respectively. Chapter 5 demonstrates the applications of spatial coherence in imaging and free-space communication.

## 1.3 Propagation of spatial coherence

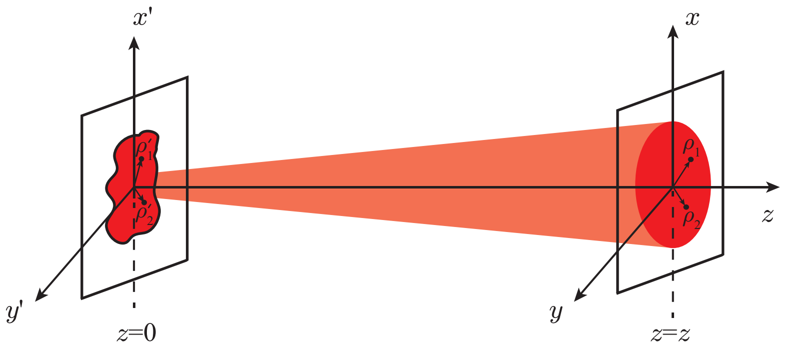

FIGURE 1.4: Illustrating the propagation of a planar spatially partially coherent source kept at $z = 0$.

Here we explore propagation of spatial cross-spectral density function in an optical field produced by a planar monochromatic spatially partially coherent source kept at $z = 0$ and how the cross-spectral density function $W(\boldsymbol{\rho}_1, \boldsymbol{\rho}_2; z)$ at any propagation distance $z$ is connected to the cross-spectral density function $W(\boldsymbol{\rho}'_1, \boldsymbol{\rho}'_2; z = 0)$ at the source plane. Consider $E(\boldsymbol{\rho}; z)$ represents the electric field at the location $(\boldsymbol{\rho}; z)$ and it satisfies the Helmholtz equation

$$\nabla^2 E(\boldsymbol{\rho}; z) + k^2 E(\boldsymbol{\rho}; z) = 0, \tag{1.16}$$

where $\nabla^2 = \frac{\partial^2}{\partial^2 x} + \frac{\partial^2}{\partial^2 y} + \frac{\partial^2}{\partial^2 z}$, $\boldsymbol{\rho} \equiv (x, y)$. We express the solution $E(\boldsymbol{\rho}; z)$ of the above Eq. (1.16) for a propagating wave in $+z-$direction in the transverse wave-vector basis in the following manner (see section 5.6.2 in Ref. [2])

$$E(\boldsymbol{\rho}; z) = C \int \mathrm{U}(\boldsymbol{q}) e^{i\boldsymbol{q}\cdot\boldsymbol{\rho} + ik_z z} d\boldsymbol{q}, \tag{1.17}$$

where $\boldsymbol{q} \equiv (q_x, q_y)$ is a transverse wave-vector or plane wave mode, $\mathrm{U}(\boldsymbol{q})$ denotes the electric field in the transverse wave-vector basis, and $C$ is a constant. We assume $q_x^2 + q_y^2 << k_z^2$ and it is known as paraxial approximation (see section 7.4 in Ref. [64]). Under this assumption, $k_z = k_0 - \frac{q^2}{2k_0}$, $k_0 = |\boldsymbol{k}| = \sqrt{q^2 + k_z^2}$. The Eq. (1.17) modified as

$$E(\boldsymbol{\rho}; z) = C e^{ik_0 z} \int \mathrm{U}(\boldsymbol{q}) e^{i\boldsymbol{q}\cdot\boldsymbol{\rho}} e^{-i\frac{q^2 z}{2k_0}} d\boldsymbol{q}. \tag{1.18}$$

We next find the propagation of spatial cross-spectral density function of a partially coherent source, by taking a ensemble average over many realization of $E(\boldsymbol{\rho}; z)$ and it is expressed as (see section 5.6.3 in Ref. [2])

$$W(\boldsymbol{\rho}_1, \boldsymbol{\rho}_2; z) = \langle E^*(\boldsymbol{\rho}_1; z) E(\boldsymbol{\rho}_2; z)\rangle_e = C^2 \iint \mathcal{A}(\boldsymbol{q}_1, \boldsymbol{q}_2) e^{i(\boldsymbol{q}_2\cdot\boldsymbol{\rho}_2 - \boldsymbol{q}_1\cdot\boldsymbol{\rho}_1)} e^{-i\frac{z}{2k_0}(q_2^2 - q_1^2)} d\boldsymbol{q}_1 d\boldsymbol{q}_2, \tag{1.19}$$

where $\mathcal{A}(\boldsymbol{q}_1, \boldsymbol{q}_2) = \langle \mathrm{U}^*(\boldsymbol{q}_1) \mathrm{U}(\boldsymbol{q}_2)\rangle_e$ is the angular cross-spectral density of the source. The Eq. (1.19) connects the cross-spectral density function $W(\boldsymbol{\rho}_1, \boldsymbol{\rho}_2; z)$ at $z = z$ with the source angular cross-spectral density function $\mathcal{A}(\boldsymbol{q}_1, \boldsymbol{q}_2)$. From the Eq. (1.19), the cross-spectral density function $W(\boldsymbol{\rho}_1', \boldsymbol{\rho}_2')$ at $z = 0$ is given by

$$W(\boldsymbol{\rho}_1', \boldsymbol{\rho}_2') = C^2 \iint \mathcal{A}(\boldsymbol{q}_1, \boldsymbol{q}_2) e^{i(\boldsymbol{q}_2 \cdot \boldsymbol{\rho}_2' - \boldsymbol{q}_1 \cdot \boldsymbol{\rho}_1')} d\boldsymbol{q}_1 d\boldsymbol{q}_2. \tag{1.20}$$

This shows that $W(\boldsymbol{\rho}_1', \boldsymbol{\rho}_2')$ and $\mathcal{A}(\boldsymbol{q}_1, \boldsymbol{q}_2)$ are connected by Fourier transformation. We use this relation and rewrite the Eq. (1.19) in the following form

$$W(\boldsymbol{\rho}_1, \boldsymbol{\rho}_2; z) = \frac{1}{(\lambda_0 z)^2} e^{i\frac{k_0}{2z}(\boldsymbol{\rho}_2^2 - \boldsymbol{\rho}_1^2)} \iint W(\boldsymbol{\rho}_1', \boldsymbol{\rho}_2') e^{i\frac{k_0}{2z}(\boldsymbol{\rho}_2'^2 - \boldsymbol{\rho}_1'^2)} e^{-i\frac{k_0}{z}(\boldsymbol{\rho}_2 \cdot \boldsymbol{\rho}_2' - \boldsymbol{\rho}_1 \cdot \boldsymbol{\rho}_1')} d\boldsymbol{\rho}_1' d\boldsymbol{\rho}_2'. \tag{1.21}$$

This is the general expression for the spatial cross-spectral density function $W(\boldsymbol{\rho}_1, \boldsymbol{\rho}_2; z)$ of a spatially partially coherent source at any $z = z$ plane. It expresses the cross-spectral density function $W(\boldsymbol{\rho}_1, \boldsymbol{\rho}_2; z)$ at propagation distance $z$ in terms of cross-spectral density function $W(\boldsymbol{\rho}_1', \boldsymbol{\rho}_2')$ at $z = 0$. Using Eq. (1.21), we analyse how the spatial coherence $\sigma_c$ changes with propagation distance $z$ for the following realistic sources.

### 1.3.1 Primary spatially incoherent source

Consider a planar spatially incoherent source is kept at $z = 0$. The cross-spectral density function at $z = 0$ is given by $W(\boldsymbol{\rho}_1', \boldsymbol{\rho}_2') = \frac{\lambda_0^2}{\pi} I(\boldsymbol{\rho}_1') \delta(\boldsymbol{\rho}_1' - \boldsymbol{\rho}_2')$ (see Ref [20], section 5.5.4), where $\lambda_0$ is the central wavelength and $I(\boldsymbol{\rho}_1')$ represents the transverse intensity distribution of the source at $z = 0$. We now propagate $W(\boldsymbol{\rho}_1', \boldsymbol{\rho}_2')$ from $z = 0$ to $z = z$ plane using the Eq. (1.21) and the cross-spectral density function $W(\boldsymbol{\rho}_1, \boldsymbol{\rho}_2; z)$ at $z = z$ is given by

$$W(\boldsymbol{\rho}_1, \boldsymbol{\rho}_2; z) = \frac{K}{z^2} e^{i\frac{k_0}{2z}(\boldsymbol{\rho}_2^2 - \boldsymbol{\rho}_1^2)} \int I(\boldsymbol{\rho}_1') e^{i\frac{k_0}{z}\boldsymbol{\rho}_1' \cdot (\boldsymbol{\rho}_2 - \boldsymbol{\rho}_1)} d\boldsymbol{\rho}_1'. \tag{1.22}$$

All constants are absorbed in $K$. We next write the spatial coherence function $\mu(\boldsymbol{\rho}_1, \boldsymbol{\rho}_2; z)$ as

$$\mu(\boldsymbol{\rho}_1, \boldsymbol{\rho}_2; z) = \int I(\boldsymbol{\rho}_1') e^{-i\frac{k_0}{z}\boldsymbol{\rho}_1' \cdot (\boldsymbol{\rho}_2 - \boldsymbol{\rho}_1)} d\boldsymbol{\rho}_1'. \tag{1.23}$$

The spatial coherence function $\mu(\boldsymbol{\rho}_1, \boldsymbol{\rho}_2; z)$ is the Fourier transform of the source transverse intensity distribution $I(\boldsymbol{\rho}_1')$. It is commonly known as van Cittert-Zernike theorem [2, 65]. We consider the intensity distrbition to be $I(\boldsymbol{\rho}_1') = \exp\left(-\frac{\rho_1'^2}{2a^2}\right)$, $a$ denotes the dimension of the source. The corresponding spatial coherence function is given by

$$\mu(\Delta\rho; z) = A \exp\left[-\frac{\Delta\rho^2}{2\sigma_c(z)^2}\right], \tag{1.24}$$

where $\sigma_c(z) = z/k_0 a = z\lambda_0/2\pi a$ is the spatial coherence length at propagation distance $z$. We now plot $\sigma_c(z)$ as a function of $z$ in Fig. 1.5 (solid curve) and it shows that $\sigma_c$ monotonically increases upon the propagation. This implies that even an incoherent source produces finite spatial coherence length upon propagation. The example of such sources are sunlight, light emitting diode (LED), etc.

### 1.3.2 Gaussian Schell model source

Gaussian schell model (GSM) source is one of the most widely used model of spatially partially coherence source in the literature [2, 66–69]. A GSM source is characterized by a Gaussian transverse intensity profile and a Gaussian spatial coherence function. The cross-spectral density function of GSM source at $z = 0$ plane is given by $W(\boldsymbol{\rho}_1', \boldsymbol{\rho}_2') = \sqrt{I(\boldsymbol{\rho}_1')I(\boldsymbol{\rho}_2')}\mu(\boldsymbol{\rho}_2' - \boldsymbol{\rho}_1')$ (Sec.5.6.2 in Ref. [2]), where $I(\boldsymbol{\rho}') = \exp\left(-\frac{\rho'^2}{2w_0^2}\right)$, and $\mu(\boldsymbol{\rho}_2' - \boldsymbol{\rho}_1') = \mu(\Delta\boldsymbol{\rho}') = \exp\left(-\frac{\Delta\rho'^2}{2\sigma_c^2}\right)$. $w_0$ and $\sigma_c$ are the beam size and spatial coherence length respectively at $z = 0$. Now, by substituting $W(\boldsymbol{\rho}_1', \boldsymbol{\rho}_2')$ in Eq. (1.21), one can show that (see

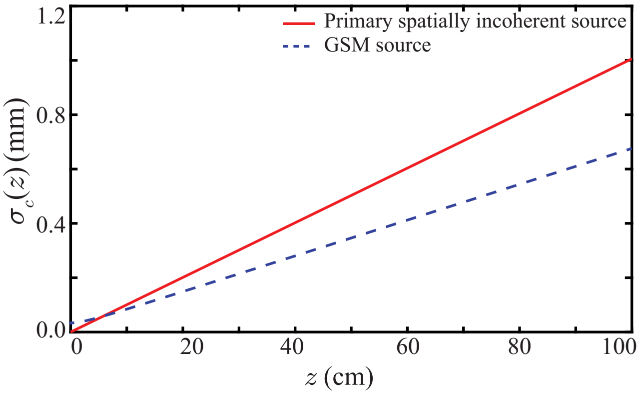

FIGURE 1.5: Spatial coherence length $\sigma_c(z)$ as a function of $z$ for spatially incoherent source (red solid curve) and GSM source (blue solid curve). Here, $a = 150$ $\mu$m, $\lambda_0 = 632$ nm, $w_0 = 150$ $\mu$m, and $\sigma_c = 0.02$ $\mu$m

Sec.5.6.4 in Ref. [2])

$$W(\boldsymbol{\rho}_1,\boldsymbol{\rho}_2;z) = N\exp\left[-i\frac{k_0}{2R(z)}(\rho_2^2-\rho_1^2)\right]\exp\left[-\frac{\rho_1^2+\rho_2^2}{4w(z)^2}\right]\exp\left[-\frac{\Delta\rho^2}{2\sigma_c(z)^2}\right], \quad (1.25)$$

where $w(z) = w_0\sqrt{1+\left(\frac{z}{k_0 w_0 \delta}\right)^2}$ and $\sigma_c(z) = \sigma_c\sqrt{1+\left(\frac{z}{k_0 w_0 \delta}\right)^2}$ are the beam size and spatial coherence length respectively, at $z = z$ plane. We plot $\sigma_c(z)$ as a function of $z$ in Fig. 1.5 (dashed curve) and it shows that $\sigma_c(z)$ monotonically increases upon propagation. These two examples show that the spatial coherence length of a spatially partially coherent field increases upon propagation. In chapters 2 and 5, we will propose and demonstrate the generation of spatially partially coherent fields having spatial coherence length that remains constant and decreases upon propagation.

## 1.4 Coherent mode representation

A spatially perfectly coherent field is represented at a transverse point $\boldsymbol{\rho}$ by the electric field $E(\boldsymbol{\rho})$, whereas a spatially partially coherent field is represented by cross-spectral density function $W(\boldsymbol{\rho_1},\boldsymbol{\rho}_2) = \langle E^*(\boldsymbol{\rho}_1)E(\boldsymbol{\rho}_2)\rangle_e$. The coherent mode representation is a method introduced by Wolf [15] for expressing the cross-spectral density function $W(\boldsymbol{\rho_1},\boldsymbol{\rho}_2)$ as an incoherent mixture of coherent modes and a coherent mode represents a spatially perfectly coherent field. A cross-spectral density function must satisfy the following conditions in order to have its coherent mode representation [15,70].

- $W(\boldsymbol{\rho_1},\boldsymbol{\rho_2})$ must be square integrable over the domain $D$, that is, $\iint_D |W(\boldsymbol{\rho_1},\boldsymbol{\rho_2})|^2 d\boldsymbol{\rho}_1$ $d\boldsymbol{\rho}_2$.

- $W(\boldsymbol{\rho_1},\boldsymbol{\rho_2})$ must be Hermitian, that is, $W^*(\boldsymbol{\rho_1},\boldsymbol{\rho_2}) = W(\boldsymbol{\rho_2},\boldsymbol{\rho_1})$.

- $W(\boldsymbol{\rho_1},\boldsymbol{\rho_2})$ must be a definite non-zero function, that is, $\iint_D f^*(\boldsymbol{\rho}_1)f^*(\boldsymbol{\rho}_1)W(\boldsymbol{\rho_1},\boldsymbol{\rho_2})d\boldsymbol{\rho}_1$ $d\boldsymbol{\rho}_2$, where $f(\boldsymbol{\rho})$ is a square integrable function.

Under the above conditions $W(\boldsymbol{\rho_1}, \boldsymbol{\rho_2})$ becomes a Hilbert-Schmidt kernel. According to Mercer theorem (see section 2.5.1 in Ref. [70]), we write the cross-spectral density function $W(\boldsymbol{\rho_1}, \boldsymbol{\rho_2})$ in the following form [15,70]

$$W(\boldsymbol{\rho_1}, \boldsymbol{\rho_2}) = \sum_n I_n E_n^*(\boldsymbol{\rho}_1) E_n(\boldsymbol{\rho}_2), \tag{1.26}$$

where $n$ represents the mode index, $E_n(\boldsymbol{\rho})$ are the eigenmodes and $I_n$ are the eigenvalues of the following integral equation

$$\int W(\boldsymbol{\rho_1}, \boldsymbol{\rho_2}) E_n(\boldsymbol{\rho}_1) d\boldsymbol{\rho}_1 = I_n E_n(\boldsymbol{\rho}_2). \tag{1.27}$$

We note that Eq. (1.26) describes a partially coherent field as an incoherent mixture of spatially completely coherent eigenmodes $E_n(\boldsymbol{\rho})$ with proportions given by their corresponding eigenvalues $I_n$. The first condition implies the sum of all eigen values $\sum_n I_n < \infty$ is finite. The second and third conditions ensure that all $I_n$ are real and non-negative, respectively. The Eq.( 1.26) can be written as a sum of cross-spectral density function of coherent eigenmodes $W_n(\boldsymbol{\rho_1}, \boldsymbol{\rho_2}) = E_n^*(\boldsymbol{\rho}_1) E_n(\boldsymbol{\rho}_2)$ in the following way

$$W(\boldsymbol{\rho_1}, \boldsymbol{\rho_2}) = \sum_n I_n W_n(\boldsymbol{\rho_1}, \boldsymbol{\rho_2}). \tag{1.28}$$

For a completely coherent field the coherent mode representation contains only one term, whereas for a completely incoherent field the coherent mode representation contains an infinite number of terms. The Eq. (1.28) implies that for a given $W(\boldsymbol{\rho}_1, \boldsymbol{\rho}_2)$, atleast one basis will exist in which the it can be represented as an incoherent mixture of coherent modes that are spatially perfectly coherent. We note that the eigenmodes are orthonormal, that is, $\iint E_n^*(\boldsymbol{\rho}_1) E_m(\boldsymbol{\rho}_2) d\boldsymbol{\rho}_1 d\boldsymbol{\rho}_2 = \delta_{mn}$. Now if the $W(\boldsymbol{\rho}_1, \boldsymbol{\rho}_2)$ has a coherent mode representation in a continuous variable basis, then the Eq.( 1.26) takes the form [15,70]

$$W(\boldsymbol{\rho_1}, \boldsymbol{\rho_2}) = \int I(\boldsymbol{k}) W_{\boldsymbol{k}}(\boldsymbol{\rho_1}, \boldsymbol{\rho_2}) d\boldsymbol{k}, \tag{1.29}$$

where $\boldsymbol{k}$ is the mode index in the continuous variable basis. In chapter 2, we propose and demonstrate a new experimental technique for generating spatially partially coherent fields by using their coherent mode representation.

## 1.5 Wigner Distribution Function

So far we have used the cross-spectral density function for characterizing spatial correlation or coherence in an optical field. Here, we introduce an alternative approach for characterizing the same through a distribution function named Wigner distribution function [71–74]. The Wigner distribution function $F(\boldsymbol{\rho},\boldsymbol{q})$ resepresnt an optical field simultaneously in transverse position $\boldsymbol{\rho}$ and transverse wave-vector $\boldsymbol{q}$ bases. The relation between Wigner distribution function and cross-spectral density function is given by [73,74]

$$F(\boldsymbol{\rho},\boldsymbol{q}) = A\int W(\boldsymbol{\rho}+\boldsymbol{\rho}'/2,\boldsymbol{\rho}-\boldsymbol{\rho}'/2)\exp(-i\boldsymbol{q}\cdot\boldsymbol{\rho}')d\boldsymbol{\rho}'. \tag{1.30}$$

The intensity distribution functions $I(\boldsymbol{\rho})$ and $I(\boldsymbol{q})$ in transverse position and wave-vector bases are given by [73,74]

$$I(\boldsymbol{\rho}) = \int F(\boldsymbol{\rho},\boldsymbol{q})d\boldsymbol{q}, \qquad I(\boldsymbol{q}) = \int F(\boldsymbol{\rho},\boldsymbol{q})d\boldsymbol{\rho}. \tag{1.31}$$

For a single-photon field the Wigner distribution function $F(\boldsymbol{\rho},\boldsymbol{p})$ represents the joint probability distribution of the photon in position $\boldsymbol{\rho}$ and momentum $\boldsymbol{p}$ bases. The position and momentum probability distribution function of a single-photon field are given by

$$P(\boldsymbol{\rho}) = \int F(\boldsymbol{\rho},\boldsymbol{p})d\boldsymbol{p}, \qquad P(\boldsymbol{p}) = \int F(\boldsymbol{\rho},\boldsymbol{p})d\boldsymbol{\rho}. \tag{1.32}$$

The Eq. (1.30) for a single-photon field is written as [75]

$$F(\boldsymbol{\rho},\boldsymbol{p}) = A/\hbar\int W(\boldsymbol{\rho}+\boldsymbol{\rho}'/2,\boldsymbol{\rho}-\boldsymbol{\rho}'/2)\exp\left[-i\boldsymbol{p}\cdot\boldsymbol{\rho}'/\hbar d\boldsymbol{\rho}'\right]. \tag{1.33}$$

We note that inverting the Eqs. (1.30) and (1.33), one can extract the spatial coherence in classical and signgle-photon optical fields through Wigner function measurements [76].

## 1.6 Spatial entanglement and Einstein-Podolsky-Rosen (EPR) correlation

Entanglement is a strange correlation witnessed in a multipartite quantum system. If the global state of a multipartite system is not equivalent to the tensor product of individual subsystem states, then it implies that the subsystems are entangled. Mathematically, it is represented by $|\Psi\rangle \neq |u\rangle_1 \otimes |v\rangle_2$, where $|\Psi\rangle$ represents the global state, $|u\rangle_1$ and $|v\rangle_2$ denote the state of subsystem 1 and 2 respectively. Entanglement displays strong measurement correlations between spatially separated subsystems in conjugate bases. We now describe spatial entanglement in position-momentum and angle-OAM bases through Einstein-Podolsky-Rosen (EPR) correlation measurement.

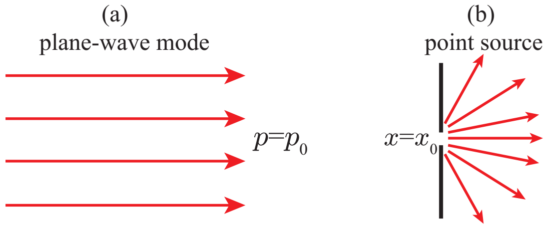

FIGURE 1.6: Illustrates (a) plane-wave mode and (b) a diffracting point source.

We first review the position-momentum Heisenberg uncertainty relation in a single-particle system. Consider an example: a single-particle state is described by a plane-wave mode and it is illustrated in Fig. 1.6(a). The corresponding position wavefunction $\psi(x)$ and momentum wavefunction $\psi(p)$ are given by

$$\psi(x) = Ae^{ip_0x/\hbar}, \qquad \psi(p) = A'\delta(p - p_0). \tag{1.34}$$

The particle has a well defined momentum $p = p_0$ and the uncertainty associated with the momentum is $\Delta p = 0$. On the other hand, the particle can be found at any position

$x$ with equal probability and the uncertainty in the position becomes $\Delta x = \infty$. Now, we consider another example: a diffracting point source and it is illustrated in Fig. 1.6(b). The wavefunction in the position and momentum bases are given by

$$\psi(x) = A\delta(x - x_0), \qquad \psi(p) = A' e^{ipx_0/\hbar}. \tag{1.35}$$

In this case, the particle has a well-defined position $x = x_0$; consequently, the uncertainty associated with the position distribution becomes $\Delta x = 0$, whereas the particle has all the possible values of momentum with equal probability and the uncertainty associated with the momentum distribution is $\Delta p = \infty$.

These two examples show that for a single-particle state, we can not have accurate knowledge of both position and momentum simultaneously. In general, this feature is captured in the Heisenberg inequality

$$\Delta x \Delta p \geq \hbar/2. \tag{1.36}$$

In 1935, A. Einstein, B. Podolsky, and N. Rosen envisioned a two-particle system in which the particles are spatially separated with no causal influence. They described the system by the following two-particle wavefunction [33]

$$\Psi(x_1, x_2) = \int \psi_k^{(1)}(x_1)\phi_k^{(2)}(x_2)dk. \tag{1.37}$$

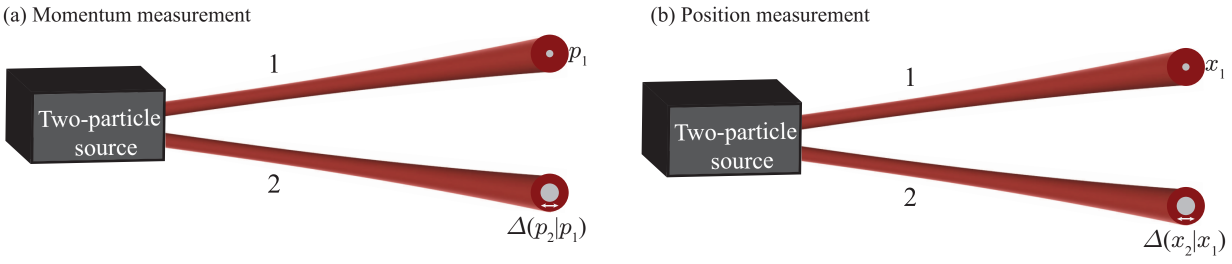
(a) Momentum measurement

(b) Position measurement

FIGURE 1.7: Illustrates the concept of (a) conditional momentum uncertainty and (b) conditional position uncertainty.

The above wavefunction is a continuous superposition of two-particle wavefunctions $\psi_k^{(1)}(x_1)\phi_k^{(2)}(x_2)$ and it can not be written as the product of the wavefunctions of the individual particles. The Eq. (1.37) implies that if we find the first particle with wavefunction $\psi_k^{(1)}(x_1)$, then the wavefunction of second particle is guaranteed to be $\phi_k^{(2)}(x_2)$. Consider a specific situation where $\psi_k^{(1)}(x_1) = e^{ikx_1}$ and $\phi_k^{(2)}(x_2) = e^{-ik(x_2-x_0)}$. This shows that if the momentum of the first particle is found to be $p_1 = k\hbar$, then the momentum of the second particle is certainly $p_2 = -k\hbar$. This measurement correlation between two particles is quantified through a physically measurable quantity called conditional momentum uncertainty $\Delta(p_2|p_1)$. It is defined as the uncertainty associated with the momentum of the second particle $p_2$, given that the first particle momentum is found to be $p_1 = k\hbar$. Figure 1.7(a) illustrates the concept of conditional momentum uncertainty. Smaller the value of $\Delta(p_2|p_1)$, stronger is the two-particle momentum correlation. In this case, $\Delta(p_2|p_1) = 0$. Now, we rewrite the Eq. (1.37) in the following form

$$\Psi(x_1, x_2) = \int u_x^{(1)}(x_1)v_x^{(2)}(x_2)dx, \tag{1.38}$$

where, $u_x^{(1)}(x_1) = \delta(x_1 - x)$ and $v_x^{(2)}(x_2) = \delta(x - x_2 + x_0)$. This implies that if the first particle is found at $x_1 = x$, then the second particle is gauranteed to be found at $x_2 = x + x_0$. The conditional position uncertainty $\Delta(x_2|x_1)$ is defined as the uncertainty associated with the position of second particle $x_2$, given that the first particle is found at $x_1 = x$. Figure 1.7(b) illustrates the concept of conditional position uncertainty. In this case, $\Delta(x_2|x_1) = 0$. This two-particle state displays a simultaneous strong measurement correlations in position and momentum bases between two spatially separated particles. Now, the product of conditional position and momentum uncertainties is

$$\Delta(x_2|x_1)\Delta(p_2|p_1) = 0. \tag{1.39}$$

For this two-particle wavefunction, we witness that the product of conditional position and momentum uncertainties violates the Heisenberg uncertainty relation, that is,

$$\Delta(x_2|x_1)\Delta(p_2|p_1) < \hbar/2. \tag{1.40}$$

This violation is the signature of position-momentum EPR correlation, and it also implies that the particles are entangled in position-momentum bases. We note that this section has presented position-momentum EPR correlation for a pure two-particle state. The EPR correlation has also been used as a certifier for mixed state entanglement [77,78]. Over the years, the position-momentum entanglement has been experimentally certified through EPR correlation for the two-photon field generated by spontaneous parametric down-conversion (SPDC) [39,53,56,78–82] and spontaneous four wave mixing (SFWM) [83,84] processes.

Like the linear position and linear transverse momentum, the angular position and z-component of orbital angular momentum (OAM) forms a conjugate pair. For a single particle state, the corresponding Heisenberg uncertainty relation is written as [85]

$$\Delta\theta\Delta l \geq \hbar/2[1 - 2\pi P(\theta = \theta_0)], \tag{1.41}$$

where $\Delta\theta$ and $\Delta l$ are angle and OAM uncertainties respectively, associated with a single-particle state. Here $P(\theta = \theta_0)$ is the probability of detecting the particle at the boundary $\theta = \theta_0$. The above uncertainty relation has been experimentally demonstrated with optical fields [86].

In the context of two-particle system, if the product of conditional angle and OAM uncertainties of one the particle (say the second particle) violates the above Heisenberg uncertainty relation in Eq. (1.41), that is,

$$\Delta(\theta_2|\theta_1)\Delta(l_2|l_1) < \hbar/2[1 - 2\pi P(\theta_2 == \theta_0|\theta_1)], \tag{1.42}$$

then it implies the signature of angle-OAM EPR correlation and the particles are entangled in angle-OAM degrees of freedom [40,87]. Here $\Delta(\theta_2|\theta_1)$ and $\Delta(l_2|l_1)$ are the conditional angle and OAM uncertianties respectively, of the second particle and $P(\theta_2|\theta_1 = \theta_0)$ is the probability of detecting the second particle at the boundaty $\theta_2 = \theta_0$ conditioned that first particle is detected at $\theta_1$. The EPR correlation has been used for certifyting angle-OAM entanglement of two-photon state generated in the SPDC process [40, 87].

The EPR correlation is a widely used experimental tool for certifying the other continuous-variable entanglement such as radial position-radial momentum [88], time-energy [41, 89], and number-phase [90] degrees of freedom. In this thesis, we study entanglement of SPDC two-photon field in position-momentum and angle-OAM bases through EPR correlation. Our results and conclusions on entanglement in position-momentum and angle-OAM bases are based on the behavior EPR correlation. In chapters 4 and 6, we present a new method for measuring position-momentum EPR-correlation and we explore entanglement propagation in position-momentum and angle-OAM bases through EPR-correlation respectively.

## 1.7 Introduction to nonlinear optics

Nonlinear optics studies the interaction of an electromagnetic field with a material, where the material optical properties depend on the strength of the external field [91]. Due to this interaction, electrons in the atoms experience a Columb force. As a result, the electrons get displaced from their equilibrium. This displacement creates a net dipole moment in the atom, which relies on the strength of the electric field. We define the dipole moment per unit volume as polarization. For the sake of simplicity, we assume both polarization $P(\boldsymbol{r}, t)$ and external electric field $V(\boldsymbol{r}, t)$ are scalar quantities. In the linear optics regime, the strength of the external field is considered to be weak and the polarization $P(\boldsymbol{r}, t)$ follows a linear relation with the external field $V(\boldsymbol{r}, t)$ and is given by (see Eq. 1.1.1 in Ref. [91])

$$P(\boldsymbol{r}, t) = \epsilon_0 \chi^{(1)} V(\boldsymbol{r}, t), \tag{1.43}$$

where $\chi^{(1)}$ and $\epsilon_0$ are the linear susceptibility and free space permitivity.

Now, we consider the external field to be strong enough such that the polarization $P(\boldsymbol{r},t)$ no longer varies linearly with $V(\boldsymbol{r},t)$. We now write $P(\boldsymbol{r},t)$ as a power series expansion of $V(\boldsymbol{r},t)$ (see Eq. 1.1.2 in Ref. [91])– which corresponds to the nonlinear optics regime.

$$P(\boldsymbol{r},t) = \epsilon_0\chi^{(1)}V(\boldsymbol{r},t) + \epsilon_0\chi^{(2)}V^2(\boldsymbol{r},t) + \epsilon_0\chi^{(3)}V^3(\boldsymbol{r},t) + ..., \tag{1.44}$$

where $\chi^{(2)}$, $\chi^{(3)}$,... are the second, third order nonlinear susceptibility of the material and so on. For crystals with no inversion symmetry i.e. non-centrosymmetric, the second order nonlinear polarization becomes $P^{(2)}(\boldsymbol{r},t) = \epsilon_0\chi^{(2)}E^2(\boldsymbol{r},t)$. For a noncentrosymmetric crystal the electric displacement $D(\boldsymbol{r},t)$ inside the crystal is given by

$$D(\boldsymbol{r},t) = \epsilon_0 V(\boldsymbol{r},t) + P(\boldsymbol{r},t). \tag{1.45}$$

We now find the energy density $W$ inside the crystal

$$W = \frac{1}{2}V(\boldsymbol{r},t)D(\boldsymbol{r},t) = \frac{1}{2}\left[\epsilon_0\chi^{(1)}V(\boldsymbol{r},t) + \epsilon_0\chi^{(2)}V^2(\boldsymbol{r},t) + \epsilon_0\chi^{(3)}V^3(\boldsymbol{r},t) + ...\right]V(\boldsymbol{r},t). \tag{1.46}$$

Here we only focus on the second order nonlinear effects and restrict the above series upto $\chi^{(2)}$ term. The above Eq. (1.46) takes the form

$$W = W_L + W_{NL}, \tag{1.47}$$

where $W_L = \epsilon_0(1+\chi^{(1)})V^2(\boldsymbol{r},t)/2$, and $W_{NL} = \epsilon_0\chi^{(2)}V^2(\boldsymbol{r},t)/2$ are linear and nonlinear energy densities respectively. The form of the Hamiltonian due to the nonlinear effect is [92]

$$H(t) = \int_{\mathcal{V}} W_{NL} d^3\boldsymbol{r} = \frac{\epsilon_0}{2}\int_{\mathcal{V}} \chi^{(2)}V^3(\boldsymbol{r},t)d^3\boldsymbol{r}, \tag{1.48}$$

where the intergration is performed over the crystal volume $\mathcal{V}$. We next present a physically realized second order nonlinear process: spontaneous parametric down-conversion (SPDC).

## 1.8 Spontaneous parametric down-conversion

Spontaneous parametric down-conversion (SPDC) is a second-order nonlinear process in which a stream of pump photons interacts with a noncentrosymmetric crystal. A fraction of pump photons gets annihilated into signal and idler photons. Figure 1.8(a) shows the schematic of the SPDC process. The word parametric implies that the process obeys energy and momentum conservations, and the word down-conversion refers that the frequencies of signal and idler photons are lower than the frequency of the pump photon. The energy conservation in down-conversion ensures that the pump photon energy equals the sum of the energies of signal and idler photons. Similarly, the momentum conservation ensures that the pump photon momentum equals the sum of the momenta of signal and idler photons. Due to these conservation laws, the down-converted photons get entangled in position-momentum, time-energy, and angle-OAM bases. The two-photon state generated in this process depends on the crystal configuration and the details of the pump photon. For example, both signal and idler photons propagate almost collinearly with the pump photon called collinear phase-matching for a specific crystal configuration. By changing the crystal orientation, the photon pair comes out in two different propagation directions is known as non-collinear phase-matching. We next derive the interaction Hamiltonian operator in SPDC process from the classical interaction Hamiltonian in Eq. (1.48) and for this process, it takes the form [92]

$$H(t) = \frac{\epsilon_0}{2} \int_{\mathcal{V}} \chi^{(2)} V_p(\boldsymbol{r},t) V_s(\boldsymbol{r},t) V_i(\boldsymbol{r},t) d^3\boldsymbol{r}, \tag{1.49}$$

where $V_j(\boldsymbol{r},t)$ represent the electric field for pump $(p)$, signal $(s)$ and idler $(i)$ photons. We have discussed in section 1.2.2, in quantum treatment the electric field amplitude $V(\boldsymbol{r},t)$ is substituted by a Hermitian operator $\hat{E}(\boldsymbol{r},t)$, which is expressed as a sum of positive and negative field operators in Eq. (1.8). We use the Eq. (1.8) for computing the Hamiltonian operator $\hat{H}(t)$ corresponding to the above classical Hamiltonian $H(t)$. Now, we write the operators $\hat{V}_j(\boldsymbol{r};t)$ for $j = p, s,$ and $i$ as a sum of their positive and negative field operators, and evalute their product. The product comprises of total eight terms

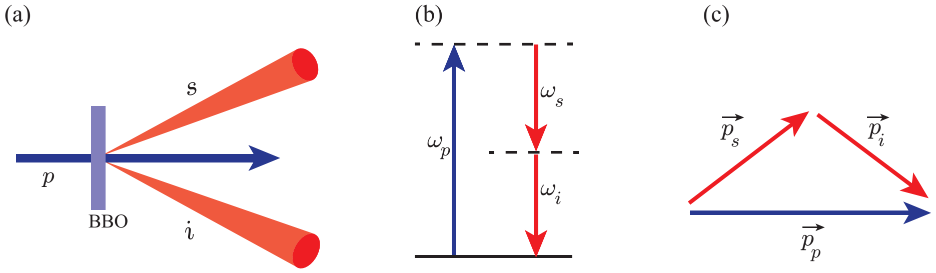

FIGURE 1.8: (a) Schematic of SPDC process– out of $10^8$ pump photons one pump photon is down-converted into signal and idler photons. (b) Energy level diagram represents that the pump frequency is equal to the sum of frequencies of signal and idler photons. (c) Linear momentum conservation diagram: pump momentum is equal to the sum of momenta of signal and idler photons.

corresponding to all the combinations of positive and negative field operators. Here $\hat{V}_p^{(+)}(\boldsymbol{r},t)\hat{V}_s^{(-)}(\boldsymbol{r},t)\hat{V}_i^{(-)}(\boldsymbol{r},t)$ and $\hat{V}_p^{(-)}(\boldsymbol{r},t)\hat{V}_s^{(+)}(\boldsymbol{r},t)\hat{V}_i^{(+)}(\boldsymbol{r},t)$ are the only energy conserving terms, contribute to the product $\hat{V}_p(\boldsymbol{r},t)\hat{V}_s(\boldsymbol{r},t)\hat{V}_i(\boldsymbol{r},t)$. The rest six non-energy conserving terms average out to zero when we integrate the Hamiltonian over time as per rotating wave approximation (see Section 2.3 of Ref. [93]). The interaction Hamiltonian operator $\hat{H}(t)$ for SPDC process takes the following form

$$\hat{H}(t) = \frac{\epsilon_0}{2}\int_{\mathcal{V}} \chi^{(2)}\hat{V}_p^{(+)}(\boldsymbol{r},t)\hat{V}_s^{(-)}(\boldsymbol{r},t)\hat{V}_i^{(-)}(\boldsymbol{r},t)d^3\boldsymbol{r} + H.c.. \tag{1.50}$$

We will use the above Hamiltonian expression for computing the two-photon wavefunction in the position and momentum bases for collinear phase-matching in Chapter 4.

## 1.9 Summary

In summary, this chapter has reviewed spatial coherence, quantum entanglement, and spontaneous parametric down-conversion concepts. The rest of this thesis will present our experimental results on generation, measurement, and applications of spatial coherence and entanglement. In chapter 2, we will present a method for generating spatially partially coherent fields based on their coherent mode representations. Using this method, we will demonstrate the generation of propagation-invariant spatially stationary and GSM fields. In chapter 3, we will present a method for measuring two-dimensional spatial coherence in a two-shot manner. In chapter 4, we will use the above measurement technique for certifying the position-momentum entanglement in a pure two-photon field by measuring the position and momentum coherence functions of one of the photons. In chapter 5, we will demonstrate the applications of spatial coherence in the context of imaging and free-space communications through random media. Finally, in chapter 6, we will explore the propagation of spatial entanglement in SPDC two-photon fields and report a novel feature that the propagation induces entanglement revival in the angle-OAM degrees of freedom.

# Chapter 2

# Generation of spatial coherence in optical field

## 2.1 Introduction

Optical fields having partial spatial coherence [70,94,95] offer numerous practical applications such as wide-field optical coherence tomography (OCT) [96], imaging through scattering [21], optical communication [97,98], particle trapping [99,100], laser scanning [101], plasma instability suppression [102], photographic noise reduction [103], and optical scattering [104]. A spatially partially coherent field can be divided into two categories: spatially stationary and spatially nonstationary. In analogy with the temporally stationary fields, when the intensity of a field is independent of the spatial position and when the two-point spatial cross-spectral function depends on the spatial positions only through their difference, the field is called spatially stationary, at least in the wide sense [105–113]. A spatially stationary field has the unique property that its cross-spectral density function is propagation-invariant [107,113]. Such fields have several unique applications such as 3D coherence holography [111] and photon correlation holography [112]. If the field is not spatially stationary, it is categorized as spatially nonstationary. For example, Gaussian Schell Model (GSM) field, sunlight, etc.

There are several different ways of producing spatially partially coherent fields. While one of the earliest experiments used a laser and an acousto-optical cell [113], later experiments utilized a laser and a rotating ground glass plate (RGGP) to produce fields with desired partial spatial coherence [105,111,114–121]. More modern methods involve using a laser, and either a spatial light modulator (SLM) [122–125] or an RGGP in combination with an SLM to achieve the purpose [112, 126, 127]. As far as propagation-invariant spatially stationary partially coherent fields are concerned, to the best of our knowledge, there have been only two experimental studies so far. In the first experiment the field was generated using a laser and an acousto-optic cell [113] and in the second experiment the generation was done using a laser and an RGGP [107]. Nevertheless, both these techniques have demonstrated generation of only those cross-spectral density functions that can be represented as Fourier transforms of circularly-symmetric functions. Thus, all these existing experimental techniques for producing both spatially stationary and spatially nonstationary partially coherent fields use a laser as the primary source, which, to begin with, is spatially a completely coherent source. One then tries to make the field emanating from such a source spatially partially coherent by introducing randomness in the field-path by using either an acousto-optic cell [113], or a rotating ground glass plate (RGGP) [105,111,114–116,118–121] or a spatial light modulator (SLM) [112,122–127].

In this chapter, we propose and demonstrate a novel generation technique based on coherent mode representation of a spatially partially coherent field, which, in contrast to the existing techniques does not require the introduction of additional randomness. We demonstrate the generation of both propagation-invariant spatially stationary partially coherent and Gaussian Schell Model (GSM) fields. By producing an incoherent mixture of plane waves using a planar primary spatially uncorrelated light-emitting diodes (LEDs) source, we generate propagation-invariant spatially stationary partially coherent fields with desired cross-spectral density functions. We next demonstrate the generation of a GSM field by incoherently mixing its coherent eigenmodes in a proportion fixed by their normalized eigenspectrum.

The chapter has been adopted veritably from Ref. [128, 129], and the contents are organized in the following manner. In section 2.2.1, we present the theoretical modelling of the propagation-invariant spatially stationary partially coherent fields and show its coherent mode decomposition. In section 2.2.2- 2.2.5, we demonstrate the generation of such spatially partially coherent fields and present the corresponding experimental results. In section 2.3.1, we present the coherent mode decomposition of GSM fields. In section 2.3.2- 2.3.4, we demonstrate the scheme for generating GSM field and present the experimental results. In section 2.4, we present the summary of this chapter.

## 2.2 Propagation-invariant spatially stationary partially coherent fields

### 2.2.1 Theory

Figure 2.1 illustrates a planar, monochromatic, spatially completely incoherent primary source is kept at the back focal plane $z=-f$ of a lens kept at $z=0$. The planar primary source along with the lens constitute our source of spatially partially coherent fields. We represent the field radiating out from spatial location $\boldsymbol{\rho}'$ at $z$ by $E_s(\boldsymbol{\rho}', z)$. Since our primary source is spatially completely incoherent, the fields $E_s(\boldsymbol{\rho}'_1, -f)$ and $E_s(\boldsymbol{\rho}'_2, -f)$ radiating out from $\boldsymbol{\rho}'_1$ and $\boldsymbol{\rho}'_2$, respectively, at $z=-f$ are completely uncorrelated, that is,

$$\langle E_s^*(\boldsymbol{\rho}'_1, -f) E_s(\boldsymbol{\rho}'_2, -f)\rangle_e = \frac{\lambda_0^2}{\pi} I_s(\boldsymbol{\rho}'_1, -f)\delta(\boldsymbol{\rho}'_1 - \boldsymbol{\rho}'_2). \tag{2.1}$$

Here $I_s(\boldsymbol{\rho}'_1, -f)$ is the intensity of the primary source at $z=-f$ and $\lambda_0$ is the central wavelength. We note that no realistic primary source can truly have a position correlation given by Eq. (2.1), which requires that the spatial coherence length be zero. The smallest spatial coherence length that can be associated with a primary source is of the order of the wavelength $\lambda_0$ of the source, and only a black body emitter can be idealized

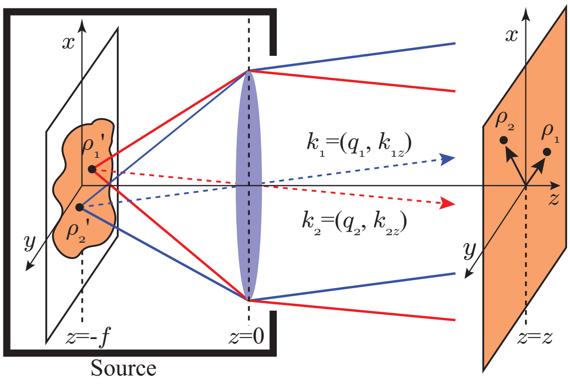

FIGURE 2.1: Schematic illustration of how a propagation-invariant spatially stationary field can be generated using a spatially completely-uncorrelated primary source.

as such a source [130]. Nevertheless, for a millimeter-size source at optical wavelengths, the position correlations of the order of $\lambda_0$ can very well be approximated by Eq. (2.1). In our experiments, we use LEDs as our primary incoherent sources, which are considered spatially completely incoherent in the sense that their position correlations are approximated by the form given in Eq. (2.1) [131].

Thus, for our primary source whose position correlation is represented by Eq. (2.1), every point on the source is radiating out as an independent point source and since each of these points is kept at the back focal plane of a converging lens, the field $E_s(\boldsymbol{\rho}_1', -f)$ radiating out from $\boldsymbol{\rho}_1'$ gets transformed into a plane wave with amplitude $V(\boldsymbol{q_1})$ by the lens, where $\boldsymbol{q_1}$ represents the transverse wave-vector associated with the plane wave [132, 133]. Here, we are assuming that the aperture-size of the lens is infinite. This turns out to be a very good approximation for our purposes in this section and the effects due to a finite aperture-size lens is discussed and demonstrated in section 2.2.5. The lens, therefore, transforms the non-correlation of the planar source in the position basis to non-correlation in the transverse wave-vector basis. The correlations between different transverse wave-vectors are quantified using the angular cross-spectral density function $\mathcal{A}(\boldsymbol{q_1}, \boldsymbol{q_2})$. It is defined as $\mathcal{A}(\boldsymbol{q_1}, \boldsymbol{q_2}) \equiv \langle \mathrm{U}^*(\boldsymbol{q_1})\mathrm{U}(\boldsymbol{q_2})\rangle_e$ where $\langle \cdots \rangle_e$ represents the ensemble average. The angular cross-sprectral density function of our partially coherent source is the angular cross-spectral density function $\mathcal{A}(\boldsymbol{q_1}, \boldsymbol{q_2})$ just after the lens plane, that is, at $z = 0$, and is thus given by

$$\mathcal{A}(\boldsymbol{q_1},\boldsymbol{q_2}) \equiv \langle \mathrm{U}^*(\boldsymbol{q_1})\mathrm{U}(\boldsymbol{q_2})\rangle_e = I_s(\boldsymbol{q_1})\delta(\boldsymbol{q_1}-\boldsymbol{q_2}). \tag{2.2}$$

Here $I_s(\boldsymbol{q_1})$ is the spectral density of the field; it has the same functional form as that of the primary source intensity. As we show below, this form of the angular cross-spectral density function is the requirement for the partially coherent field coming out of a source to be spatially stationary and propagation-invariant.

In section 1.3 of chapter 1, we have already worked out the relation between cross-spectral density function $W(\boldsymbol{\rho}_1,\boldsymbol{\rho}_2,z)$ at $z = z$ and angular cross-spectral density function $\mathcal{A}(\boldsymbol{q_1},\boldsymbol{q_2})$ and it is given by

$$W(\boldsymbol{\rho}_1,\boldsymbol{\rho}_2,z) = \iint_{-\infty}^{\infty} \mathcal{A}(\boldsymbol{q_1},\boldsymbol{q_2})e^{-i\boldsymbol{q_1}\cdot\boldsymbol{\rho}_1+i\boldsymbol{q_2}\cdot\boldsymbol{\rho}_2}e^{-i\frac{(q_1^2-q_2^2)z}{2k_0}}d\boldsymbol{q_1}d\boldsymbol{q_2}. \tag{2.3}$$

Equation (2.3) governs how spatial correlations of the field, as represented by the cross-spectral density function, change upon propagation in the region $z > 0$ after the lens. Substituting the form of the angular cross-spectral density function from Eq. (2.2) into Eq. (2.3), we obtain

$$W(\boldsymbol{\rho}_1,\boldsymbol{\rho}_2,z) = W(\boldsymbol{\Delta}\rho,z) = \int_{-\infty}^{\infty} I_s(\boldsymbol{q})e^{-i\boldsymbol{q}\cdot\boldsymbol{\Delta\rho}}d\boldsymbol{q} = \int_{-\infty}^{\infty} I_s(\boldsymbol{q})E_{\boldsymbol{q}}^*(\boldsymbol{\rho}_1)E_{\boldsymbol{q}}(\boldsymbol{\rho}_2)d\boldsymbol{q}, \tag{2.4}$$

where $\boldsymbol{\Delta}\rho = \boldsymbol{\rho_1} - \boldsymbol{\rho_2}$, $E_{\boldsymbol{q}}(\boldsymbol{\rho}) = e^{i\boldsymbol{q}\cdot\boldsymbol{\rho}}$. The intensity $I(\boldsymbol{\rho},z)$ corresponding to the above cross-spectral density function is

$$I(\boldsymbol{\rho},z) = W(\boldsymbol{\rho},\boldsymbol{\rho},z) = \int_{-\infty}^{\infty} I_s(\boldsymbol{q})d\boldsymbol{q} = K, \tag{2.5}$$

where $K$ is a constant. We find that the cross-spectral density function $W(\boldsymbol{\Delta}\rho,z)$ in Eq. (2.4) is in the coherent-mode representation, with the plane waves being the coherent modes. In other words, our source produces a field that is an incoherent mixture of plane-wave modes. As a result, the generated field has the following properties: (1) *The field is propagation-invariant*—This is because the cross-spectral density function as well as the intensity is independent of $z$. (2) *The field is spatially stationary at a given $z$, at least in the wide sense.*—The intensity $I(\boldsymbol{\rho}, z)$ does not depend on $\boldsymbol{\rho}$ and the cross-spectral density function depends on $\Delta\boldsymbol{\rho}$ only. (3) *The cross-spectral density function $W(\boldsymbol{\Delta}\rho, z)$ of the field is the Fourier transform of its spectral density $I_s(\boldsymbol{q})$*—this is the spatial analog of the Wiener-Khintchine theorem for temporally stationary fields (see Section 2.4 of [2]). Moreover, since the spectral density has the same functional form as the intensity of the primary source, the cross-spectral density function of the field is the Fourier transform of the intensity profile of the primary source. We note that in our proposed technique, there is no restriction on the form of the intensity function $I_s(\boldsymbol{\rho}')$ that the primary incoherent source can have. The primary source can be continuous or having a finite size, or even in the form of a collection of points. Therefore, using our proposed technique, one can produce on-demand custom-designed, spatially stationary and propagation-invariant cross-spectral density functions and not just the ones that are Fourier transforms of circularly-symmetric functions [107, 113].

### 2.2.2 Experimental setup

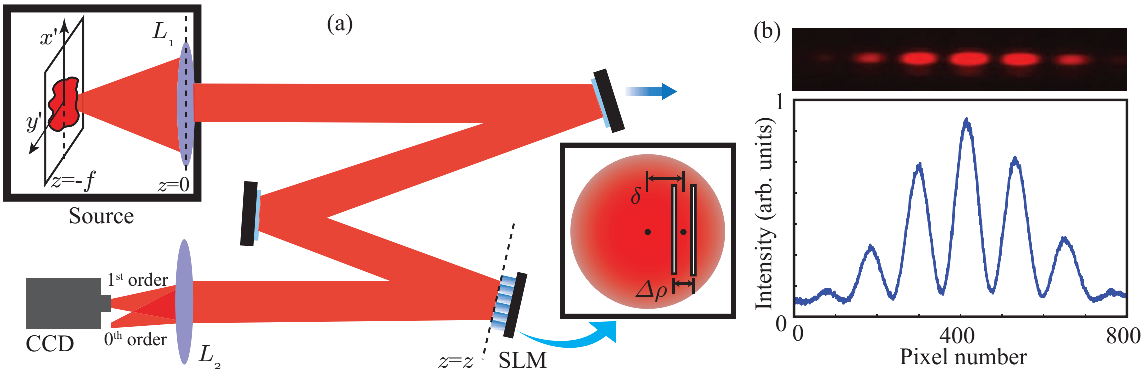

FIGURE 2.2: (a) Schematic diagram of the experimental setup. A planar, spatially incoherent primary source is placed at the back focal plane of lens $L_1$. The cross-spectral density of the field produced by the source is measured using the Spatial Light Modulator (SLM). The propagation length $z$ is the distance between the lens $L_1$ and the SLM, and the CCD-camera is placed at the focal plane of lens $L_2$. (b) A representative experimental interference pattern produced by the double-slit simulated on the SLM, and the associated one-dimensional plot.

Fig. 2.2(a) shows the schematic of our experimental setup for generating spatially partially coherent fields with propagation-invariant and spatially stationary cross-spectral density function. Our primary source is a commercially available 9 W planar LED bulb. We use an interference filter centered at 632.8 nm having a wavelength-bandwidth of 10 nm. The LED bulb consists of 9 separate LEDs arranged in a 3×3 grid. We take the individual LEDs to be spatially completely incoherent [131,134] in the sense that their spatial cross-spectral density function can be approximated by Eq. (2.1). The individual LEDs are dimensions of $0.8 \times 0.8$ mm, and the separation between the two nearest LEDs is 1.9 mm. We let the field produced by our source at $z = 0$ propagate to $z = z$ and then measure the cross-spectral density function using a Young's double-slit pattern simulated on an SLM kept at $z = z$ [135–137], with the separation between the slits being $\boldsymbol{\Delta}\rho$. The offset parameter $\delta$ is the distance between the center of the field and the center of the double-slit. We record the resulting interference fringe pattern by keeping a CCD camera at the focal plane of lens $L_2$ and then capturing only the first diffraction order due to the SLM. Figure 2.2(b) shows the interference pattern captured by the CCD camera and the associated one-dimensional section of the intensity pattern. We note that since the two simulated slits are the same and the field is uniform in intensity, the magnitude $|W(\boldsymbol{\Delta}\rho, z)|$ of the cross-spectral density function is the visibility of interference fringes. Therefore, by measuring the interference visibility as a function of the slit separation $\boldsymbol{\Delta}\rho$, we directly measure $|W(\boldsymbol{\Delta}\rho, z)|$ as a function of $\boldsymbol{\Delta}\rho$. We further note that any pattern simulated on an SLM is seen by only one polarization component of an incoming field [137], and it is only this component that contributes at the first diffraction order. The other polarization component, if present, ends up at the zeroth diffraction order. Since our measurements are made only at the first diffraction order, only one polarization component gets measured. Therefore, the scalar theory of section 2.2.1 should be sufficient to describe the present experiments.

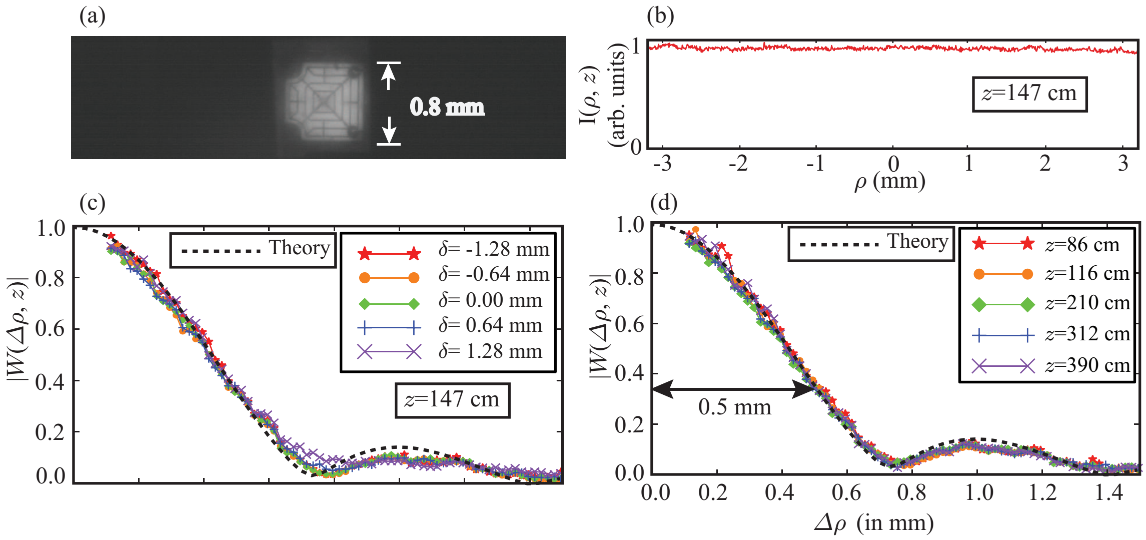

FIGURE 2.3: (a) The CCD-camera image of the LED. (b) Plot of intensity $I(\boldsymbol{\rho}, z)$ as a function of $\boldsymbol{\rho}$ at $z = 147$ cm. (c) Plots of $|W(\boldsymbol{\Delta}\rho, z)|$ as a function of $\boldsymbol{\Delta}\rho$ at $z = 147$ cm for various values of the offset parameter $\delta$. (d) Plots of $|W(\boldsymbol{\Delta}\rho, z)|$ as a function of $\boldsymbol{\Delta}\rho$ for various values of $z$. In the above figures, the black dashed curves represent the theoretical prediction based on Eq. (2.4).

### 2.2.3 Spatially stationary and propagation-invariant cross-spectral density functions

Figure 2.3(a) is the image of the central LED of our bulb, which is our primary source. The focal length $f$ of lens $L_1$ is 75 cm. From Eq. (2.3), the cross-spectral density function is the Fourier transform of the primary source intensity profile. Figure 2.3(a) shows that the primary source has almost symmetric intensity profile. As a result, we expect that the generated $W(\Delta\rho, z)$ is real. Under this assumption, the measurement of $|W(\boldsymbol{\Delta}\rho, z)|$ is suffiecient for demonstrating the spatially stationarity and propagation-invariance of the generated cross-spectral density function.

Figure 2.3(b) shows the plot of the intensity at $z = 147$ cm and Fig. 2.3(c) shows plots of $|W(\boldsymbol{\Delta}\rho, z)|$ at $z = 147$ cm as a function of $\boldsymbol{\Delta}\rho$ for several offset values $\delta$. These results verify that the generated field is spatially stationary. Figure 2.2(d) shows plots of $|W(\boldsymbol{\Delta}\rho, z)|$ as a function of $\boldsymbol{\Delta}\rho$ for various propagation distances up to 3.9 m. There is little variation between the different plots. This proves that the cross-spectral density function of the generated field is propagation-invariant at least up to a distance of 3.9

meters. We note that the spatial coherence length of the field, which we define to be the value of $\Delta\rho$ at which $|W(\Delta\rho, z)|$ drops down to $1/e$, is about 0.5 mm and remains propagation-invariant. This is in contrast to the field produced by a bare primary source of the same shape and size as that of the source in Fig. 2.3(a), in which case the spatial coherence length, following the conventional van-Cittert Zernike theorem, increases by about 5 times after propagating for 4 meters. Using Eq. (2.4) and the image of our primary sources shown in Figs. 2.3(a), we calculate the theoretical cross-spectral density function and plot them along with the experimental results in Figs. 2.2(c) and 2.3(d) as shown by the solid dashed curve. We find a very good match between experimental and theoretical results.

### 2.2.4 Engineering of spatial cross-spectral density function

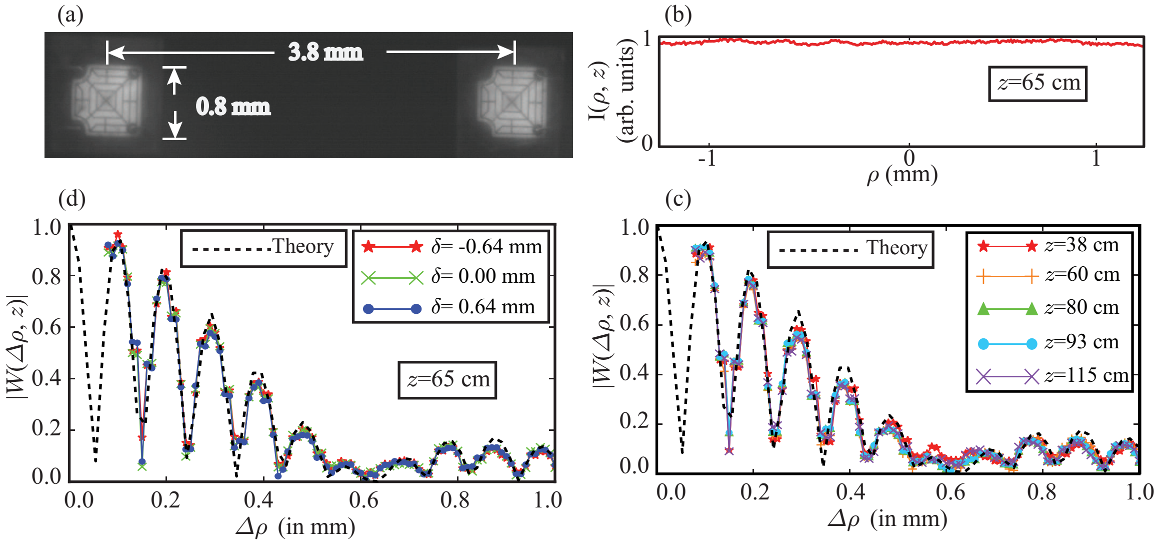

FIGURE 2.4: (a) The CCD-camera image of the LED. (b) Plot of intensity $I(\rho, z)$ as a function of $\rho$ at $z = 65$ cm. (c) Plots of $|W(\Delta\rho, z)|$ as a function of $\Delta\rho$ at $z = 65$ cm for various values of the offset parameter $\delta$. (d) Plots of $|W(\Delta\rho, z)|$ as a function of $\Delta\rho$ for various values of $z$. In the above figures, the black dashed curves represent the theoretical prediction based on Eq. (2.4).

In section 2.2.1, we have already discussed that using Eq. (2.4), one can engineer any structure in the cross-spectral density function. Now, in order to experimentally verify our claim, we use a primary source containing two spatially separated LEDs. The image of the primary source is shown in Fig. 2.4(a). Figure 2.4(b) shows the plot of the intensity at $z = 65$ cm. Figure 2.3(c) shows plots of $|W(\boldsymbol{\Delta\rho}, z)|$ as a function of $\boldsymbol{\Delta\rho}$ for various values of the offset parameter $\delta$ at $z = 65$ cm, and Fig. 2.4(d) shows plots of $|W(\boldsymbol{\Delta\rho}, z)|$ as a function of $\boldsymbol{\Delta\rho}$ at various $z$. These results again demonstrate spatial stationarity and propagation invariance. It is interesting to note that the cross-spectral density function in this case is in the form of a fringe pattern which is nothing but the Fourier transform of our source shown in Fig. 2.4(a). The theoretical prediction is shown by the dashed curve in Figs. 2.4(c) and 2.4(d). Our reported experimental results match very well with the theoretical predictions, demonstrating the accuracy and effectiveness with which custom-designed, spatially stationary propagation-invariant cross-spectral density function can be generated using our method. In order to produce a field with a given cross-spectral density function one simply needs to construct a primary source with an intensity distribution that is the inverse Fourier transform of the desired cross-spectral density function.

### 2.2.5 Effects due to a finite aperture lens

The theoretical modeling presented so far assumes that the lens that constitutes our partially coherent source has an infinite aperture size. However, in a realistic experimental situation, the aperture size of a lens is finite, and in our case, it is of the order of an inch. As discussed in Ref. [107], and as illustrated in Fig. 2.5(a), the finite aperture size of the lens restricts the propagation invariance properties to distance $z_{\rm max}$, given by $z_{\rm max} = Df/s$, where $D$ is the aperture size of the lens, $f$ is the focal length and $s$ is the size of the primary source. In order to experimentally demonstrate $z_{\rm max}$, we use the LED source shown in Fig. 2.2(a) with an $f = 30$ cm lens. Figures 2.5(b) and 2.5(c) show how the transverse spatial coherence length changes as a function of $z$ for two different values of the aperture-size $D$. As the aperture-size becomes bigger $z_{\rm max}$ gets larger. Nevertheless, even with realistic aperture sizes, one can easily achieve a $z_{\rm max}$ of up to tens of meters. Although the finite aperture size of the lens may seem to only have the restricting effect on $z_{\rm max}$, it can in fact lead to restructuring of spatial correlations in a way that can have its own set of advantages. We now report such a restructuring effect when the primary source is in the form of two spatially separated LEDs, as shown in Fig. 2.4(a). As illustrated

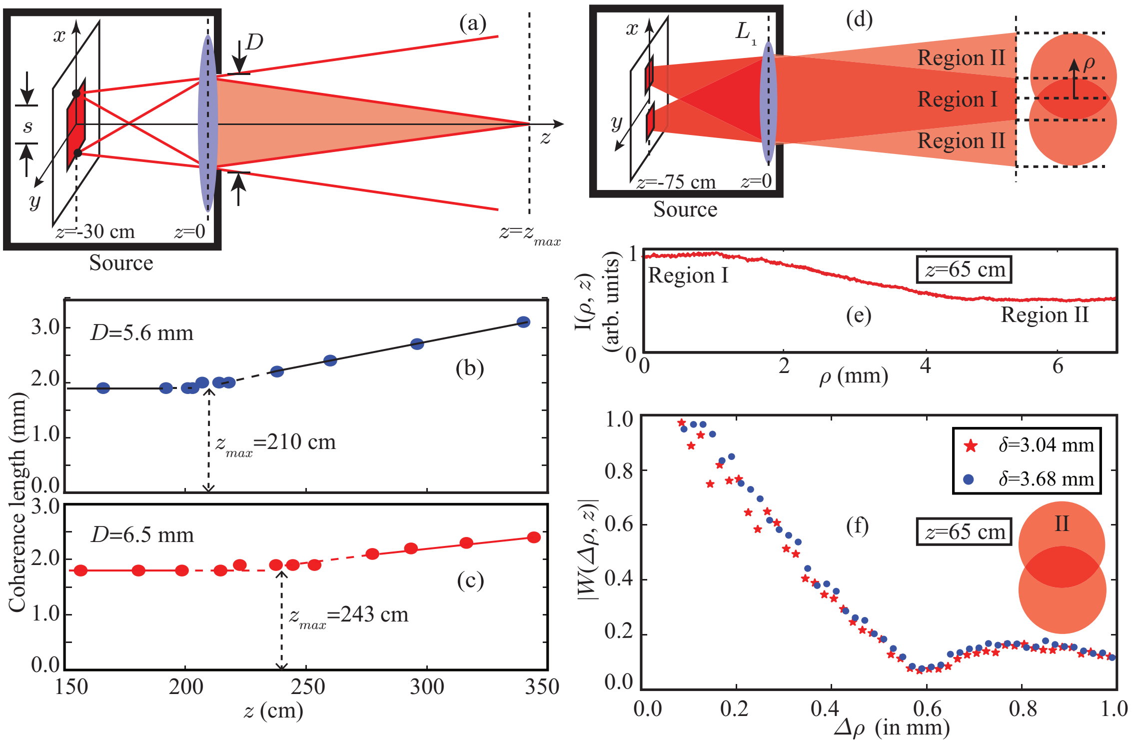

FIGURE 2.5: (a) Diagram illustrating how the aperture-size $D$ of the lens and the spatial width $s$ of the primary source fixes $z_{\mathrm{max}}$. (b) and (c) show plots of the transverse coherence length as a function of $z$ for $D = 5.6$ mm and $D = 6.5$ mm, respectively. (d) Diagram illustrating the generation of region-wise spatially stationary fields. (e) Plot of intensity $I(\boldsymbol{\rho}, z)$ as a function of $\boldsymbol{\rho}$ at $z = 65$ cm. (f) Plots of $|W(\boldsymbol{\Delta}\rho, z)|$ as a function of $\boldsymbol{\Delta}\rho$ at $z = 65$ cm for various values of the offset parameter $\delta$.

in Fig. 2.5(d), the propagation-invariant field generated due to such a primary source has two distinct regions over which spatial stationarity is observed. Region-I receives plane wave contributions from both LEDs, while Region-II only receives contributions from a single LED. This leads to the two regions having two distinct spatially stationary propagation-invariant cross-spectral density functions. We term such fields as "region-wise spatially stationary fields." Figure 2.5(f) shows the plots of $|W(\boldsymbol{\Delta}\rho, z)|$ as a function of $\boldsymbol{\Delta}\rho$ for various values of the offset parameter $\delta$ in Region-II. These results demonstrate the spatial stationarity in Region-II. The spatial stationarity of Region-I is already shown in Fig. 2.4(c). Therefore, the finite aperture size of the lens offers an advantage in creating region-wise spatially stationary fields.

## 2.3 Gaussian Schell Model fields

### 2.3.1 Theory

The cross-spectral density function of a Gaussian Schell Model (GSM) field is given by

$$W(\boldsymbol{\rho_1}, \boldsymbol{\rho_2}) = \sqrt{I(\boldsymbol{\rho_1})I(\boldsymbol{\rho_2})}\mu(\boldsymbol{\rho_1} - \boldsymbol{\rho_2}), \tag{2.6}$$

where $I(\boldsymbol{\rho}) = A^2 \exp\left[-\rho^2/(2w_0^2)\right]$ and $\mu(\boldsymbol{\rho_1} - \boldsymbol{\rho_2}) = \exp\left[-(\Delta\rho)^2/(2\sigma_c^2)\right]$ are the transverse intensity distribution and spatial coherence function of the field respectively. Here $w_0$ and $\sigma_c$ are the beam size and spatial coherence length respectively, $\boldsymbol{\rho_1} \equiv (x_1, y_1)$, $\boldsymbol{\rho_2} \equiv (x_2, y_2)$, $\Delta\rho = |\boldsymbol{\rho_1} - \boldsymbol{\rho_2}|$, and $A$ is a constant. Following Ref. [138], we represent the coherent mode decomposition of Eq. (2.6) as

$$W(\boldsymbol{\rho_1}, \boldsymbol{\rho_2}) = \sum_m \sum_n I_{mn} E^*_{mn}(x_1, y_1) E_{mn}(x_2, y_2), \tag{2.7}$$

where $E_{mn}(x, y)$ are the coherent eigenmodes and $I_{mn}$ are the distribution of corresponding eigenmodes.

$$I_{mn} = I_{00} \left[ \frac{1}{(q^2/2) + 1 + q[(q/2)^2 + 1]^{1/2}} \right]^{(m+n)}, \tag{2.8}$$

$$E_{mn}(x, y) = \left(\frac{2c}{\pi}\right)^{\frac{1}{2}} \frac{1}{\sqrt{2^{m+n} m! n!}} H_m(x\sqrt{2c}) H_n(y\sqrt{2c}) e^{-c(x^2+y^2)}. \tag{2.9}$$

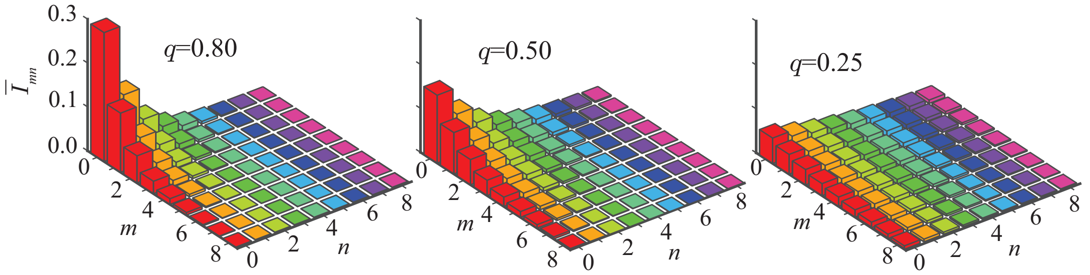

FIGURE 2.6: Theoretical plots of the normalized eigenvalues $\bar{I}_{mn}$ for three different values of the degree of global coherence, namely, for $q = 0.80$, $q = 0.50$, and $q = 0.25$.

Here $H_m(x)$ are the Hermite polynomials and the quantity $q = \sigma_c/w_0$ is called "global degree of coherence" of the field. For fixed $w_0$, higher values of $q$ imply higher values for the degree of spatial coherence. In what follows it will be very convenient to work with the normalized eigenvalues $\bar{I}_{mn}$. So, for that purpose, we first take $I_{00} = 1$ and then define $\bar{I}_{mn}$ as :$\bar{I}_{mn} = I_{mn}/\left(\sum_{mn} I_{mn}\right)$ such that $\sum_{mn} \bar{I}_{mn} = 1$. The Eq. (2.7) shows that to generate a GSM field, one needs to generate the spatially completely coherent eigenmodes $E_{mn}(x, y)$ and then mix them incoherently in $\bar{I}_{mn}$ proportion. We also find that for a normalized eigenspectrum, the coherent mode representation of Eq. (2.7) has only $q$ and $c$ as free parameters. The parameter $q$ decides the exact proportion $\bar{I}_{mn}$ of the eigenmodes $E_{mn}(x, y)$ and the parameter $c$ decides the overall transverse extent of the field. Thus by controlling $q$ and $c$ one can generate any desired GSM field. Figure 2.6 shows the theoretical plots of normalized eigenvalues $\bar{I}_{mn}$ for three different values of $q$, namely, $q = 0.8$, $q = 0.5$, and $q = 0.25$. The value of $c$ for all the fields is 1.34 $\mathrm{mm}^{-2}$. We find that to generate GSM fields with the smaller global degree of coherence $q$ one requires to mix a larger number of eigenmodes.

### 2.3.2 Experimental generation

Figures 2.7(a) and 2.7(b) show the experimental setup for generating the GSM field and measuring its cross-spectral density function using an wavefront inversion based interferometer, respectively. The details of cross-spectral density measurement is described in Chapter 3. The Gaussian field from a 5-mW He-Ne laser incident on a Holoeye Pluto spatial light modulator (SLM) and an appropriate phase pattern is displayed on the SLM to generate a given eigenmode at the detection plane of the EMCCD camera. In particular, the SLM is programmed to generate different eigenmodes $E_{mn}(x, y)$ using the Arrizon method [139]. Figure 2.7 (c) shows the experimentally measured and theoretically expected intensity profiles of eigenmodes: $E_{11}(x, y)$, $E_{44}(x, y)$, and $E_{77}(x, y)$. We find a good match between the theory and experiment. Now, to produce a GSM field with a given $q$, that is, a given eigenspectrum $\bar{I}_{mn}$, we need to produce the incoherent mixture of different eigenmodes with proportion given by $\bar{I}_{mn}$. It has been done in the following manner.

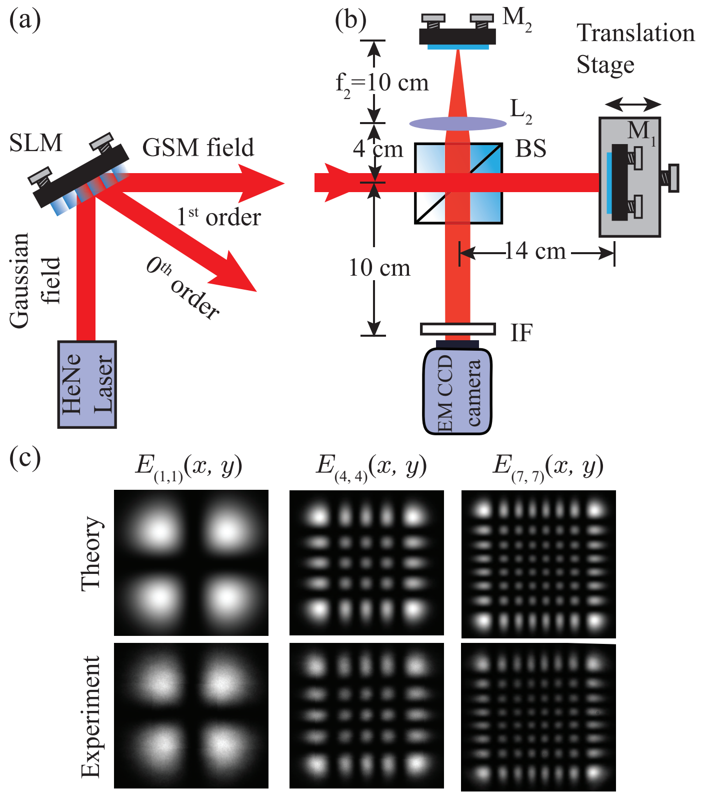

FIGURE 2.7: (a) Schematic setup for generating GSM fields. (b) Schematic setup for measuring the cross-spectral density function. Here, we have L: converging lens; SLM: Spatial Light Modulator; M: mirror; and BS: beam splitter, (c) The theoretically expected and experimentally generated intensity corresponding to the eigenmodes $E_{11}(x,y)$, $E_{44}(x,y)$, and $E_{77}(x,y)$.

First, the phase patterns corresponding to different eigenmodes are displayed on the SLM sequentially. The weights $\bar{I}_{mn}$ are fixed by making the display-time of the phase pattern corresponding to an eigenmode $E_{mn}(x,y)$ proportional to the corresponding eigenvalue $\bar{I}_{mn}$. In our experiment, the SLM works at 60 Hz. The display-time of a given phase pattern on the SLM is of the order of tens of milliseconds, while the coherence time of our He-Ne laser is in tens of picoseconds. Although the SLM introduces a deterministic phase modulation along the beam cross-section for a given eigenmode, the phase modulation for a given eigenmode is completely uncorrelated with that for any other eigenmode. In this way, the SLM produces an incoherent mixture of coherent modes, as long as the observation time is kept long enough for all the modes to get detected. Therefore, the exposure time of the EMCCD camera is made equal to the total display-time of all the phase patterns such that the camera collects all the generated eigenmodes.

Using the procedure described above, we generate GSM fields for three different values of $q$, namely, $q = 0.8$, $q = 0.5$, and $q = 0.25$. Although in principle, for any given $q$ we need an infinite number of modes to produce the corresponding GSM field precisely. However, the plots in Fig. 2.6 show that for any finite $q$, the number of eigenvalues $\bar{I}_{mn}$ with significant contributions are only finite and that the number of significant eigenvalues increases with decreasing $q$. In our experiment, we keep $0.07 \times \bar{I}_{00}$ as the cutoff for deciding the eigenmodes with a significant contribution. This means that for a given $q$ we generate only those eigenmodes for which $\bar{I}_{mn} \geq 0.07 \times \bar{I}_{00}$. With this cutoff, we generate 10, 21, and 66 eigenmodes, respectively, for the three values of $q$. The sum of these eigenvalues $\sum_{mn} \bar{I}_{mn}$ turns out to be about 0.87, 0.84, and 0.82, respectively, for the three $q$ values, which are quite close to one.

### 2.3.3 Cross-spectral density function

Each of the generated GSM fields is made incident on the interferometer in Figure 2.7(b). In our experiment, the SLM works at 60 Hz, and the EMCCD camera was kept opened for 1.40, 3.00, and 5.76 seconds, respectively, for the three $q$ values. This was for ensuring that the camera collects all the generated eigenmodes. The value of $c$ in each case was 1.34 mm$^{-2}$. Now, using the interferometer in Fig. 2.7(b) we measure the cross-spectral density function $W(\boldsymbol{\rho}, -\boldsymbol{\rho}) \equiv W(2\boldsymbol{\rho}) \equiv W(2x, 2y)$ of the generated GSM field. Figures 2.8(a), 2.8(d), and 2.8(g) show the experimentally measured cross-spectral density functions $W(2x, 2y)$ for the three values of $q$ while Figs. 2.8(b), 2.8(e), and 2.8(h) show the corresponding theoretical cross-spectral density functions plotted using Eq. (2.6). Both experimental and theoretical cross-spectral density functions are both scaled such that maximum value of $W(2x, 2y)$ is equal to one. In order to compare our experimental results with the theory, we take the one-dimensional cuts of the theoretical and experimental cross-spectral density functions and plot them together in Figs. 2.8(c), 2.8(f), and 2.8(i), for the three values of $q$.

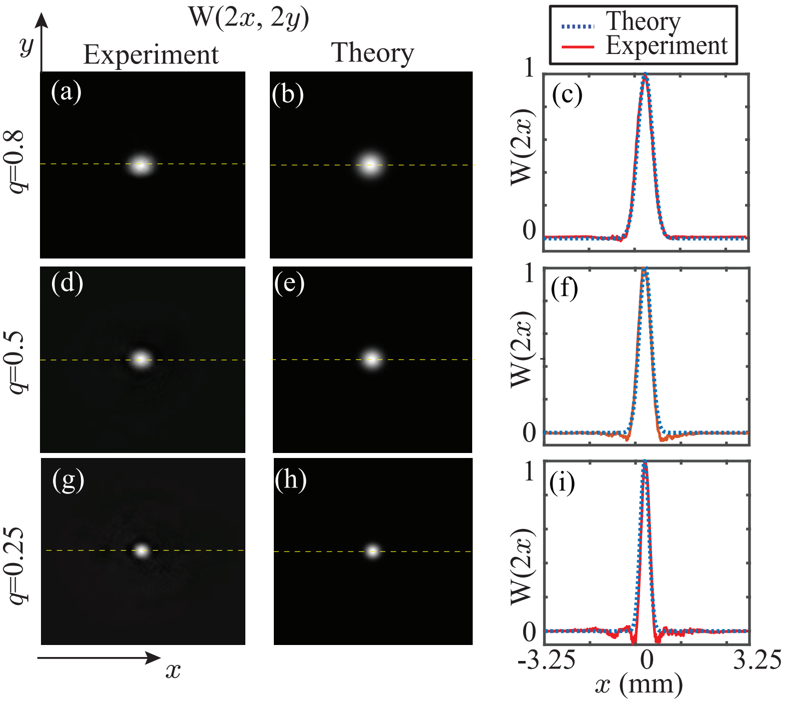

FIGURE 2.8: Plots of the the cross-spectral density function of GSM fields with $q = 0.8$, $q = 0.5$,and $q = 0.25$. For the three values of $q$, (a),(d) and (g) are the experimentally measured cross-spectral density functions $W(2x, 2y)$ while (b),(e) and (h) are the corresponding theoretical plots. (c),(f) and (i) are the plots of the one-dimensional cuts along the $x$-direction of the theoretical and experimental cross-spectral density functions.

### 2.3.4 Transverse intensity profile and spatial coherence function

Next, we measure the transverse intensity profile of the GSM field for different values of $q$. For measuring the intensity profile, we block the interferometric arm containing the lens and record the intensity at the EMCCD camera plane. Figures 5.4(a), 5.4(g) and 5.4(m) show the measured intensity profiles $I(\boldsymbol{\rho}) = I(x, y)$ for the three values of $q$. The corresponding theoretical intensities as given by Eq. (2.6) are plotted in Figures 2.9(b), 2.9(h) and 2.9(n), respectively. The experimental and theoretical plots are both scaled such that the value of the most intense pixel is equal to one. Again, for comparing our experimental results with theory, we plot the one-dimensional cuts along the $x$-direction of the theoretical and experimental intensity profiles in Figs 2.9(c), 2.9(i) and 2.9(o).

Finally, using the above measured intensity $I(\boldsymbol{\rho})$ and cross-spectral density func-

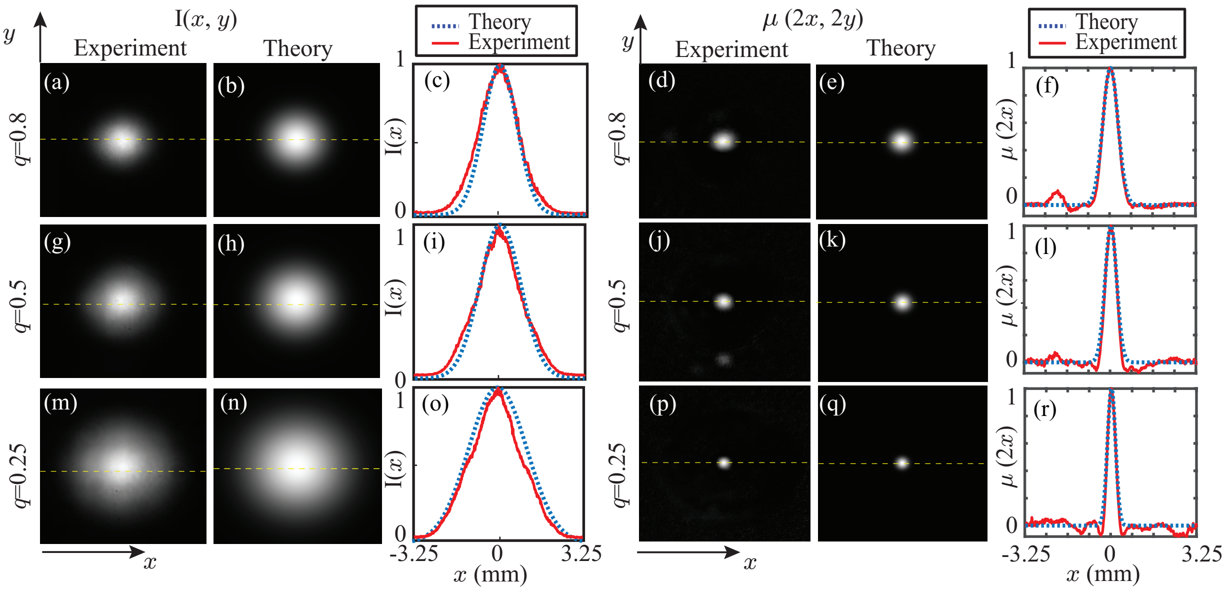

FIGURE 2.9: Plots of the intensity and the degree of coherence of GSM fields with $q = 0.8$, $q = 0.5$,and $q = 0.25$. For the three values of $q$, (a),(g) and (m) show the experimentally measured intensity profiles $I(x,y)$ while (b),(h) and (n) are the corresponding theoretical plots. (c),(i) and (o) are the plots of the one-dimensional cuts along the $x$-direction of the theoretical and experimental intensity profiles. For the three values of $q$, (d),(j) and (p) are the experimental degree of coherence $\mu(2x,2y)$ while (e),(k) and (q) are the corresponding theoretical plots. (f),(l) and (r) are the plots of the one-dimensional cuts along the $x$-direction of the theoretical and experimental degree of coherence functions.

tion $W(2\boldsymbol{\rho})$, we find the spatial coherence function $\mu(2\boldsymbol{\rho}) \equiv \mu(2x,2y)$. Figures 2.9(d), 2.9(j) and 2.9(p) show the experimental coherence function for the three $q$ values while Figs. 2.9(e), 2.9(k), and 2.9(q) show the corresponding theoretical plots. We scale the both experimental and theoretical plot such that the value of the most intense pixel is equal to one. To further compare our experimental results with the theory, we take the one-dimensional cuts along the $x$-direction of the theoretical and experimental coherence functions and plot them together in Figs. 2.9(f), 2.9(l) and 2.9(r) for three values of $q$. The results show that with decreasing $q$ the width of coehrence function decreases while the width of the transverse intensity profile increases. This is due to the fact that for generating fields with smaller $q$ values, one requires to mix together a larger number of eigenmodes, as illustrated in Fig. 2.5 and the increase in the number of eigenmodes in the incoherent mixture increases the randomness and thereby decreases the spatial coherence

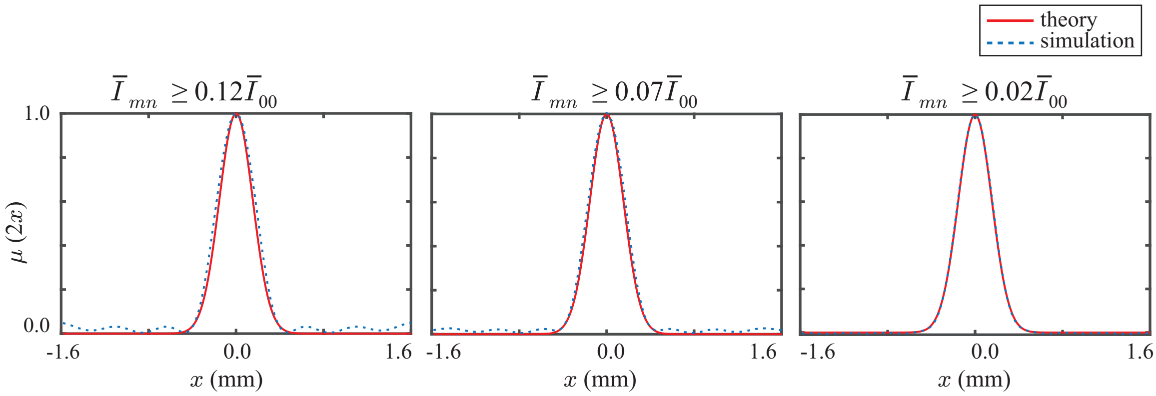

FIGURE 2.10: Plots of the numerically simulated degree of coherence function for $q = 0.25$ have been shown for the three values of the cutoff on $\bar{I}_{mn}$. For each plot, the solid line represents the theoretical degree of coherence generated using Eq.( 2.6).

length while increases the transverse width of the beam. We find a good match between the theory and experiment for each value of $q$.

The above result shows that the GSM field with $q = 0.80$ has a better match with the theory than the field with $q = 0.25$. The reasons for this are as follows. First of all, as illustrated in Fig. 2.6, the eigenvalue distribution for $q = 0.25$ is much broader than that for $q = 0.80$. As a result, for producing the GSM field with $q = 0.25$, we need to generate a larger number of modes with corresponding eigenvalues $\bar{I}_{mn}$. As mentioned earlier, the eigenvalue $\bar{I}_{mn}$ is assigned by the display time of the corresponding eigenmode $E_{m,n}(x,y)$ on the SLM. Now, since the refresh rate of the SLM is 60 Hz, and the collection time of the detection camera is in seconds, we have only a few hundred discrete time-bins for assigning the eigenvalues $\bar{I}_{mn}$. This puts a limit on the precision with which a given number of modes with eigenvalues $\bar{I}_{mn}$ could be generated and therefore results in a better match for GSM field with $q = 0.80$ since that requires a lower number of modes to be produced. Nevertheless, this limitation can be overcome by using a faster SLM, which can provide a greater number of time-bins for a given collection time and thereby can improve the precision with which $\bar{I}_{mn}$ could be generated. The other reason for a better match at $q = 0.80$ is the cutoff on $\bar{I}_{mn}$, which restricts the number of eigenmodes in the incoherent mixture. For the given cutoff of $0.07 \times \bar{I}_{00}$ on $\bar{I}_{mn}$, the sum $\sum_{mn} \bar{I}_{mn}$

becomes 0.87 and 0.82 for $q = 0.80$ and 0.25, respectively, resulting in a better match for $q = 0.80$. We now analyse the effect of the cutoff on the accuracy with which GSM field could be generated. by ploting the numerically simulated $\mu(2x, 2y)$ at $q = 0.25$ for three different cutoffs values as shown in Fig. 2.10. We find that the generation accuracy can be improved by decreasing the cutoff value. Thus, one can decide the cutoff for the eigenvalues depending on the accuracy requirement for a given application.

## 2.4 Summary

In summary, we have proposed and demonstrated a method for generating spatially partially coherent fields based on their coherent mode representation. Our method has produced an incoherent mixture of plane wave modes by using a planar spatially uncorrelated primary LED source and demonstrated the generation of propagation-invariant spatially stationary fields with very good accuracy. We have demonstrated propagation invariance of cross-spectral density functions up to almost 4 meters. We have further showcased the effectiveness of this technique by generating custom-designed structure in the cross-spectral density function. Next, we have reported the generation of GSM field by incoherently mixing its coherent eigenmodes. In order to show the flexibility of this generation scheme, we have generated GSM fields with wide range of values for the global degree of coherence, and to the best of our knowledge, such a demonstration has not been reported earlier. Compared to the existing techniques for producing spatially partially coherent fields [112, 114–116, 118–121, 126, 127], the main advantage of our technique is that it does not explicitly involve introducing any additional randomness. As a result, the errors involved in our scheme are mostly systematic and are easily controllable. Thus, our method provides much better control and accuracy. The recent experimental schemes have used coherent mode decomposition for producing different types of spatially partially coherent fields without introducing additional randomness [140, 141]. Moreover, the recent work in Ref. [142] has aslso highlighted the advantage of coherent coherent mode decomposition based generation technique in the context of GSM fields. In chapter 5, we present the applications of spatially partially coherent fields with propagation-invariant and structured spatial coherence functions in imaging and optical communication through random media, respectively.

# Chapter 3

# Measurement of spatial coherence in optical field

## 3.1 Introduction

Spatial coherence in an optical field is quantified through spatial cross-spectral density function or spatial coherence function. In the previous chapter, we have briefly discussed the implications of partial spatial coherence in various applications, including imaging through turbulence [21], free-space optical communication [97, 98], wide-field optical coherence tomography [96], sensing [27], microscopy [25], etc. For all of these applications, a fast and accurate way of measuring the cross-spectral density function is an essential requirement.

Over the years, several experimental methods have been proposed and demonstrated for measuring the spatial cross-spectral density function. The Young's double-slit interferometer [2, 3, 107, 143] and its variants [144, 145] are among the most commonly used techniques. However, the techniques based on Young's double-slit interferometry have several drawbacks. First of all, in order to measure the cross-spectral density function with increased resolution, one requires progressively narrower slits. This requirement makes such techniques very difficult for light fields with very low intensities or to generalize them for measuring two-dimensional functions. Furthermore, the measurement of cross-spectral density functions using such techniques requires multiple measurements with varying slit separations. This increases the measurement time as well as the stability requirements for the interferometers. Other schemes for measuring the cross-spectral density function include shearing interferometry [146, 147], phase-space tomography [148, 149], the schemes based on free-space propagation [150, 151] and the schemes based on scanning a small obstacle over the test plane and then measuring the resulting radiant intensity [152, 153]. However, these methods are either not suitable for low-intensity fields or require multiple measurements. Thus, existing methods are unsuitable for efficiently measuring two-dimensional cross-spectral density functions. A scheme proposed by Wessely *et al.* [154] does measure the two-dimensional cross-spectral density function in a single shot manner without requiring multiple measurements; however, due to the finite edge-width of the prisms used in the scheme, the scheme misses out some information and as a result does not measure the entire cross-spectral density function.

In this chapter, we propose and demonstrate an image-inversion based interferometric technique for measuring the two-dimensional cross-spectral density function in a two-shot manner. Our technique is the spatial analog of the recently implemented technique in Ref. [155] for measuring the angular coherence function [156]. Using this technique, we measure several lab synthesized two-dimensional cross-spectral density functions with very good accuracy.

The chapter has been adopted veritably from Ref. [157], and the contents of this chapter are organized in the following manner. In section 3.2, we present the theoretical description of our method. In section 3.3, we present experimental demonstrations and results. Section 3.4 summarizes the entire chapter.

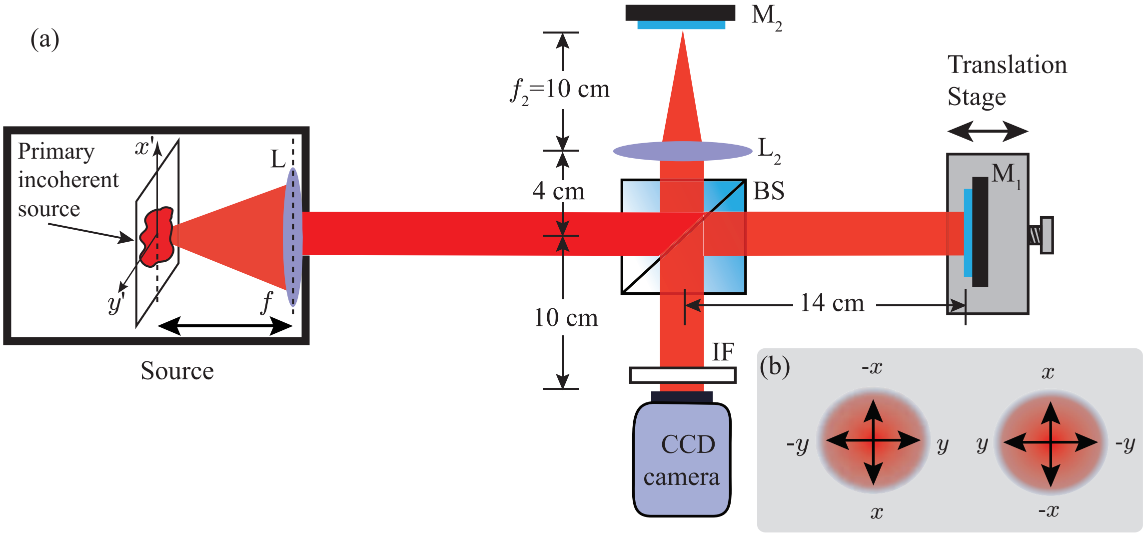

FIGURE 3.1: (a) Schematic diagram of the experimental setup. The primary incoherent source is kept at the back focal plane of a converging lens L with focal length $f = 200$ cm. The mirror $M_2$ is kept at the back focal plane of the converging lens $L_2$ of focal length $f_2 = 10$ cm. The length of each interferometric arm is about 14 cm, and the CCD camera is kept at about 10 cm from the beam splitter (BS). An interference filter (IF) centered at 632.8 nm having a wavelength-bandwidth of 10 nm is used before the CCD camera. The spatially partially coherent field exiting the lens L ends up having the cross-spectral density function that depends on the spatial coordinates only through their difference. (b) The two interfering wavefronts at the CCD camera plane. The wavefront coming through the interferometric arm having lens $L_2$ is inverted in both $x$ and $y$ directions compared to the wavefront coming through the arm having no lens. In the above figure, we have used the following abbreviations: BS stands for beam splitter, M for mirror, L for converging lens, and IF for interference filter.

## 3.2 Theory: Description of two-shot measurement scheme

Figure 3.1 illustrates our proposed method and shows the schematic diagram of our experimental setup. The source generates a spatially partially coherent field. We represent the field produced by the source in any given realization by $E_{\text{in}}(\boldsymbol{\rho})$. The corresponding cross-spectral density function of the field is given by $W(\boldsymbol{\rho}_1, \boldsymbol{\rho}_2) = \langle E^*_{\text{in}}(\boldsymbol{\rho}_1) E_{\text{in}}(\boldsymbol{\rho}_2)\rangle_e$, where $\langle \cdots \rangle_e$ denotes the ensemble average over many different realizations of the field. We aim to measure the cross-spectral density function using the interferometer shown in Fig. 3.1(a). The interferometer has two arms. One arm contains a mirror, while the other arm contains a converging lens along with a mirror kept at the back focal plane of the converging lens. For a collimated field, the lens produces an inverted wavefront at the mirror, which is reflected back onto the lens. After reflection, the wavefront is collimated back by the lens, producing a wavefront that is inverted in both $x$ and $y$ directions with respect to the incoming collimated field, that is, $\boldsymbol{\rho} \to -\boldsymbol{\rho}$. The two interfering wavefronts at the detection plane (CCD camera) have been illustrated in Fig. 3.1(b). The field at the output port of the interferometer can therefore be written as

$$E_{\text{out}}(\boldsymbol{\rho}) = \sqrt{k_1} E_{in}(\boldsymbol{\rho}) e^{i(\omega_0 t_1 + \beta_1)} + \sqrt{k_2} E_{in}(-\boldsymbol{\rho}) e^{i(\omega_0 t_2 + \beta_2)}. \tag{3.1}$$

Here, $t_1$ and $t_2$ denote the times taken by the field to travel through the two arms of the interferometer; $\omega_0$ is the frequency of the field; $\beta_1$ and $\beta_2$ are the phases other than the dynamical phases acquired in both the arms; $k_1$ and $k_2$ are the scaling constants in the two arms. The intensity $I_{\text{out}}(\boldsymbol{\rho})$ at the output port of the interferometer is given by $I_{\text{out}}(\boldsymbol{\rho}) = \langle E^*_{\text{out}}(\boldsymbol{\rho}) E_{\text{out}}(\boldsymbol{\rho}) \rangle$ and can be shown to be

$$I_{\text{out}}(\boldsymbol{\rho}) = k_1 \langle E^*_{\text{in}}(\boldsymbol{\rho}) E_{\text{in}}(\boldsymbol{\rho}) \rangle + k_2 \langle E^*_{\text{in}}(-\boldsymbol{\rho}) E_{\text{in}}(-\boldsymbol{\rho}) \rangle + \sqrt{k_1 k_2} \langle E^*_{\text{in}}(\boldsymbol{\rho}) E_{\text{in}}(-\boldsymbol{\rho}) \rangle e^{i\delta} + \text{c.c.}, \tag{3.2}$$

where $\delta = \omega_0(t_2 - t_1) + (\beta_2 - \beta_1)$. We write $\langle E^*_{\text{in}}(\boldsymbol{\rho}) E_{\text{in}}(-\boldsymbol{\rho}) \rangle = W(\boldsymbol{\rho}, -\boldsymbol{\rho})$, $\langle E^*_{\text{in}}(\boldsymbol{\rho}) E_{\text{in}}(\boldsymbol{\rho}) \rangle = I(\boldsymbol{\rho})$, and $\langle E^*_{\text{in}}(-\boldsymbol{\rho}) E_{\text{in}}(-\boldsymbol{\rho}) \rangle = I(-\boldsymbol{\rho})$. Therefore $I_{\text{out}}(\boldsymbol{\rho})$ can be written as

$$I_{\text{out}}(\boldsymbol{\rho}) = k_1 I(\boldsymbol{\rho}) + k_2 I(-\boldsymbol{\rho}) + 2\sqrt{k_1 k_2} \{\text{Re}[W(\boldsymbol{\rho}, -\boldsymbol{\rho})] \cos\delta - \text{Im}[W(\boldsymbol{\rho}, -\boldsymbol{\rho})] \sin\delta\}. \tag{3.3}$$

Here $\text{Re}[W(\boldsymbol{\rho}, -\boldsymbol{\rho})]$ and $\text{Im}[W(\boldsymbol{\rho}, -\boldsymbol{\rho})]$ denote the real and imaginary parts of the cross-spectral density function, respectively. It is clear from the above equation that the output intensity $I_{\text{out}}(\boldsymbol{\rho})$ has the cross-spectral density function $W(\boldsymbol{\rho}, -\boldsymbol{\rho})$ encoded in it. If the cross-spectral density function is real and if we know the values of $k_1$, $k_2$, $I(\boldsymbol{\rho})$ and $\delta$ then in principle a single-shot measurement of the output interferogram $I_{\text{out}}(\boldsymbol{\rho})$ will yield the cross-spectral density function $W(\boldsymbol{\rho}, -\boldsymbol{\rho})$ of the field. However, it is in general very difficult to obtain $W(\boldsymbol{\rho}, -\boldsymbol{\rho})$ using this strategy because of the requirement that $k_1$, $k_2$, $I(\boldsymbol{\rho})$ and $\delta$ should be known precisely. Any error in the knowledge of these quantities introduces error in the estimation of the cross-spectral density function. Furthermore, there are wavefront errors introduced by the interferometer which also degrade the fidelity of the estimation. Nevertheless, it has been shown in Ref. [155] that if, instead of one, two suitable output interferograms are collected then not only the estimation becomes independent of wavefront errors but also there remains no need to know $k_1$, $k_2$, $I(\boldsymbol{\rho})$ and $\delta$. This can be illustrated as follows. Suppose the experimentally measured output intensity $\bar{I}^{\delta}_{\text{out}}(\boldsymbol{\rho})$ at $\delta$ contains some background $I^{\delta}_{b}(\boldsymbol{\rho})$ in addition to the signal $I_{\text{out}}(\boldsymbol{\rho})$. Therefore, $\bar{I}^{\delta}_{\text{out}}(\boldsymbol{\rho})$ can be written as

$$\bar{I}^{\delta}_{\text{out}}(\boldsymbol{\rho}) = \; I^{\delta}_{b}(\boldsymbol{\rho}) + k_1 I(\boldsymbol{\rho}) + k_2 I(\boldsymbol{\rho}) + 2\sqrt{k_1 k_2}\{\text{Re}[W(\boldsymbol{\rho}, -\boldsymbol{\rho})]\cos\delta - \text{Im}[W(\boldsymbol{\rho}, -\boldsymbol{\rho})]\sin\delta\}. \tag{3.4}$$

Now, let us assume that we have two output interferograms with intensities $\bar{I}^{\delta_c}_{\text{out}}(\boldsymbol{\rho})$ and $\bar{I}^{\delta_d}_{\text{out}}(\boldsymbol{\rho})$ measured at $\delta = \delta_c$ and $\delta = \delta_d$, respectively. The difference $\Delta\bar{I}_{\text{out}}(\boldsymbol{\rho}) = \bar{I}^{\delta_c}_{\text{out}}(\boldsymbol{\rho}) - \bar{I}^{\delta_d}_{\text{out}}(\boldsymbol{\rho})$ in the intensities of the two interferograms is therefore given by

$$\begin{aligned}\Delta\bar{I}_{\text{out}}(\boldsymbol{\rho}) = \Delta I_b(\boldsymbol{\rho}) + 2\sqrt{k_1 k_2}\{\text{Re}[W(\boldsymbol{\rho}, -\boldsymbol{\rho})](\cos\delta_c - \cos\delta_d) - \text{Im}[W(\boldsymbol{\rho}, -\boldsymbol{\rho})] \\ \times (\sin\delta_c - \sin\delta_d)\},\end{aligned} \tag{3.5}$$

where $\Delta I_b(\boldsymbol{\rho}) = I^{\delta_c}_{b}(\boldsymbol{\rho}) - I^{\delta_d}_{b}(\boldsymbol{\rho})$ is the difference in background intensities. We assume that the background does not vary from shot to shot, that is, $\Delta I_b(\boldsymbol{\rho}) \approx 0$. Furthermore, we assume that the cross-spectral density function is either completely real or has a negligible imaginary part. Now, along with these assumptions, if we measure the two interferograms at $\delta_c \approx 0$ and $\delta_d \approx \pi$, we have $\text{Im}[W(\boldsymbol{\rho}, -\boldsymbol{\rho})](\sin\delta_c - \sin\delta_d) \ll \text{Re}[W(\boldsymbol{\rho}, -\boldsymbol{\rho})](\cos\delta_c - \cos\delta_d)$, and thus $\Delta\bar{I}_{\text{out}}(\boldsymbol{\rho})$ becomes effectively proportional to the real part of the cross-spectral density function, that is,

$$\Delta\bar{I}_{\text{out}}(\boldsymbol{\rho}) \propto \text{Re}[W(\boldsymbol{\rho}, -\boldsymbol{\rho})]. \tag{3.6}$$

Therefore, by measuring the difference intensity $\Delta\bar{I}_{\text{out}}(\boldsymbol{\rho})$, one can directly measure the real part of the cross-spectral density function $W(\boldsymbol{\rho}, -\boldsymbol{\rho})$ of the input field. We note that for a spatially stationary source, the cross-spectral density function depends on the spatial coordinates only through difference $\Delta\boldsymbol{\rho}$. As a result, for such fields we write $W(\boldsymbol{\rho}, -\boldsymbol{\rho})$ as $W(2\boldsymbol{\rho})$, which is same as the cross-spectral density function $W(\boldsymbol{\rho}_1, \boldsymbol{\rho}_2)$ for any pair of space points in the field. However, even for spatially nonstationary fields in which the intensity is not a constant but $I(\boldsymbol{\rho}) = I(-\boldsymbol{\rho})$, our method can measure the cross-spectral density function $W(\boldsymbol{\rho}, -\boldsymbol{\rho})$ around $\rho = 0$, and reconstruct the entire $W(\boldsymbol{\rho}_1, \boldsymbol{\rho}_2)$. Using this technique, we have demonstrated the measurement of cross-spectral density function of GSM field (see chapter 2, section 2.3), which is a spatially nonstationary field.

We further note that the above formalism has been worked out for a cross-spectral density function that is either completely real or has a negligible imaginary part. A cross-spectral density function can in general be complex. For such cross-spectral density functions, one can work out a two-shot formalism that is analogous to the one presented in the methods section of Ref. [155]. However, in contrast to the above formalism, the analogous formalism would require $\delta_c$ and $\delta_d$ to be known precisely.

## 3.3 Experiment and Results

We now experimentally measure spatial cross-spectral density functions using the proposed scheme. We use the experimental technique described in chapter 2 for generating spatially partially coherent fields, in which a spatially incoherent primary source is placed at the back focal plane of a converging lens (see Fig. 3.1(a)). As a consequence, the field exiting the lens ends up having the cross-spectral density function given by [128].

$$W(\boldsymbol{\rho}_1, \boldsymbol{\rho}_2) \rightarrow W(\Delta\boldsymbol{\rho}) = \int_{-\infty}^{\infty} I(\boldsymbol{q}) e^{-i\boldsymbol{q}.\Delta\boldsymbol{\rho}} d\boldsymbol{q}, \tag{3.7}$$

where $I(\boldsymbol{q})$ is the spectral density of the field exiting the lens and is proportional to the intensity $I_s(\boldsymbol{\rho}')$ of the primary incoherent source [128], where $\boldsymbol{\rho}'$ represent the spatial co-ordinates at the plane of the primary incoherent source while $\boldsymbol{\rho}$ represent the spatial co-ordinates at a plane after the converging lens. The cross-spectral density function $W(\Delta\boldsymbol{\rho})$ depends only on $\boldsymbol{\Delta}\rho = |\boldsymbol{\rho}_1 - \boldsymbol{\rho}_2|$ and is the Fourier transform of $I(\boldsymbol{q})$. Thus it

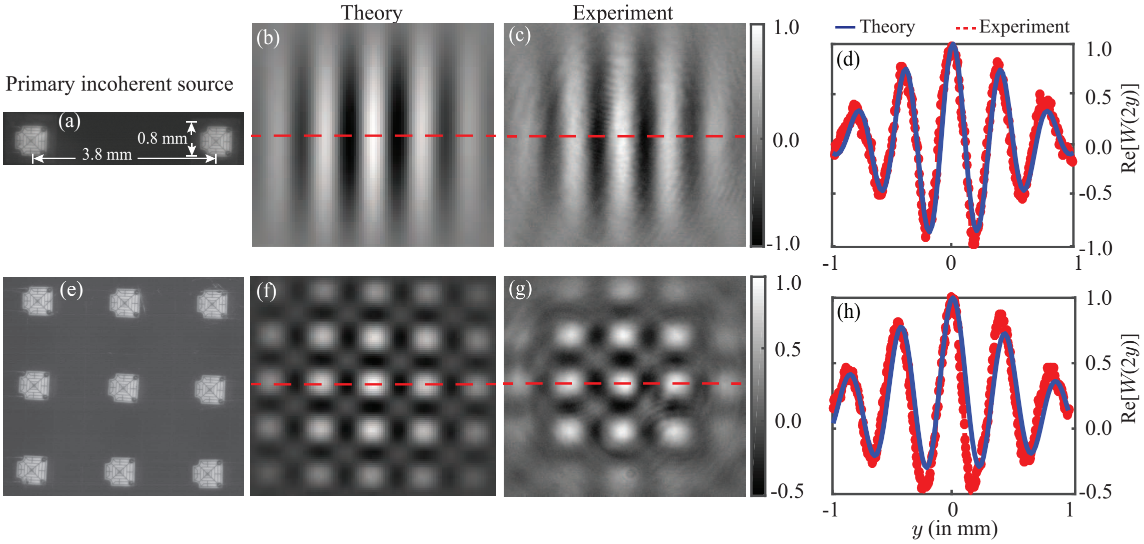

FIGURE 3.2: (a) and (e) CCD camera images of two separate primary incoherent sources. (b) and (f) The theoretical cross-spectral density function Re$[W(2\boldsymbol{\rho})]$ of the spatially partially coherent fields produced by the combination of the primary incoherent source and the converging lens. (c) and (g) The experimentally measured Re$[W(2\boldsymbol{\rho})]$. (d) and (h) Plots of the one-dimensional cuts along the $y$-direction of the theoretical and experimental cross-spectral density functions. The theoretical and experimental plots have been scaled such that the maximum of Re$[W(2\boldsymbol{\rho})]$ is one.

is proportional to the Fourier transform of the source intensity $I_s(\boldsymbol{\rho}')$. We note that the cross-spectral density function of Eq. (3.7) represents a field that is propagation-invariant invariant [128]. We further note that when $I(\boldsymbol{q})$ is a symmetric function, $W(\Delta\boldsymbol{\rho})$ is real. For any real source $I(\boldsymbol{q})$ cannot entirely be symmetric. However, we assume that the spectral density $I(\boldsymbol{q})$ of our source is almost symmetric such that $W(\Delta\boldsymbol{\rho})$ has a negligible imaginary part. Our experiments use a commercially available 9-W planar light-emitting diode (LED) bulb as the primary incoherent source. The LED bulb consists of 9 separate LEDs arranged in a 3×3 grid (see Fig. 3.2(e)). The primary source in Fig. 3.2(a) is obtained by covering the remaining 7 LEDs. The individual LEDs are of dimensions 0.8 × 0.8 mm, and the separation between the two nearest LEDs is 1.9 mm. The source is kept at the back focal plane of lens L having focal length $f = 200$ cm. The mirror $\text{M}_2$ is kept at the back focal plane of the converging lens $\text{L}_2$ of focal length $f_2 = 10$ cm. The length of each interferometric arm is about 14 cm, and the CCD camera is kept at about 10 cm from the beam splitter (BS). An interference filter (IF) centered at 632.8 nm having a wavelength-bandwidth of 10 nm is used before the CCD camera. Figure 3.2 shows our experimental results. Figures 3.2(a) and 3.2(e) are the CCD camera images of the two separate primary incoherent sources used. Figures 3.2(b) and 3.2(f) are the theoretical cross-spectral density functions of the spatially partially coherent fields generated by the combination of the primary incoherent source and the converging lens. These theoretical plots have been generated by first performing the Fourier transform of Eq. (3.7) with intensity $I_s(\boldsymbol{\rho}')$ of the images in Figs 3.2(a) and 3.2(e) and then taking the real parts. Figures 3.2(c) and 3.2(g) show the experimentally measured $\mathrm{Re}[W(2\boldsymbol{\rho})]$ through our two-shot technique, by collecting suitable interferograms at two different values of $\delta$, in each case. In our experiment, $\delta$ was varied by manually moving the translation stage, and the sets of two interferogram images were collected with $\delta_c \approx 0$ and $\delta_d \approx \pi$. In order to compare our experimental results with theory, we plot in Figs. 3.2(d) and 3.2(h) the one-dimensional cuts along $y$-direction of the theoretical and experimental cross-spectral density functions. The theoretical and experimental plots have been scaled such that the maximum of $\mathrm{Re}[W(2\boldsymbol{\rho})]$ is one. We find a good agreement between the theory and experiment. This also verifies our assumption that the spectral density $I(\boldsymbol{q})$ produced by our source is almost symmetric, and thus the imaginary part of the cross-spectral density function is negligible. The slight mismatch between the theory and experiment can be attributed to the very low but finite shot-to-shot background variations and to the negligible but finite imaginary part of the cross-spectral density function. We believe that the finite shot-to-shot background variations can be minimized even further if the phase difference $\delta$ is varied in an automated manner.

## 3.4 Summary

In summary, we have proposed and demonstrated a scheme for measuring the two-dimensional cross-spectral density function in a two-shot manner. We have reported the measurements of a few lab-synthesized cross-spectral density functions with very good agreement with theory. Our measurement technique overcomes the limitations of the conventional interferometers for measuring the cross-spectral density function in that it yields the entire cross-spectral density function using just two shots, is insensitive to background noise, and does not require precise knowledge of experimental parameters. We expect our technique to have important implications for applications such as correlation holography and wide-field OCT based on utilizing the partial spatial coherence properties of optical fields. In chapter 4, we use this interferometric technique for measuring position and momentum cross-spectral density functions of one of the SPDC photons.

## Chapter 4

# Measurement of spatial entanglement in two-photon field

## 4.1 Introduction

If a two-photon field is entangled in position and momentum variables, it is certified through position-momentum Einstein Podolsky Rosen (EPR) correlation measurements [33]. For two-dimensional variables, such as polarization, entanglement can be verified through the violations of Bell's inequalities [158] and can be quantified through measures such as concurrence [159]. However, for continuous variables, such as position-momentum, angle-OAM, time-energy, there is no entanglement quantifier and one can at best certify entanglement through various ways such as EPR correlation [33, 39, 40, 56, 82, 90, 160], partial transpose method [161–164], Rényi entropy [165, 166], etc. The EPR correlation measurements are the most widely used experimentals tool among all the entanglement certifiers. In the past, several studies have used EPR correlation measurements in the position-momentum variables in order to demonstrate entanglement [39, 53, 56, 78–82]. More recently, EPR correlation measurements have become important tools for witnessing continuous-variable entanglement even in entangled systems not consisting of photons. These include macroscopic objects [167], Bose-Einstein condensate [168], and cold atoms [169].

The demonstration of position-momentum EPR correlation is very important for many applications such as quantum key distribution [54], quantum information processing [52], quantum metrology [50], quantum imaging [43–45, 170, 171], and quantum holography [47], since the efficiency of these applications relies on how accurately the EPR correlation could be measured. Therefore, it is very important to have a more accurate technique for measuring EPR correlation. In the past few years, many schemes with increased accuracy have been demonstrated [39–41, 53, 56, 78–82, 88, 89, 172, 173]. However, all these methods involve coincidence detection, implemented either by using two scanning single-photon detectors [79], or two scanning slits [39, 78], or array of single-photon detectors [53, 80], or EMCCD cameras [56, 81, 82]. As a result, these measurement methods suffer from either too much loss of light, or strict alignment requirements, or multiple measurements, which adversely affect the accuracy of measurements.

On the other hand, for the two-dimensional two-particle state, that is, the two-qubit states (both pure and mixed), the entanglement quantifiers [159, 174] can be measured by doing measurements on only one of the qubits [175–178], without requiring coincidence detection. Furthermore, the idea has extended for the continuous variable pure two-photon states, several two-photon properties such as two-photon angular Schmidt spectrum [155, 156, 179], two-photon spatial Schmidt number [180], and momentum correlations [181] can be measured by doing intensity measurements on only one of the subsystems. These measurement schemes based on intensity detection provide much better accuracy than those based on coincidence detection.

In this chapter, utilizing the same physics, we propose a technique for measuring the position-momentum EPR correlation that does not require coincidence detection. We show that if the state of a pure two-photon field satisfies a specific set of conditions, then the position-momentum EPR correlation can be obtained by doing the intensity measurements on only one of the photons. Our technique works for a pure two-photon field, irrespective of whether it is separable or entangled. We experimentally demonstrate our method for the pure two-photon field produced by type-I collinear SPDC. We obtain the most accurate measurement of position-momentum EPR correlation reported so far.

The chapter has been adopted veritably from Ref. [182], and the contents are organized in the following manner. In section 4.2, we theoretically show that if a pure two-photon state satisfies a certain set of conditions, then the position-momentum entanglement can be certified by measuring cross-spectral density functions of one of the photons. In section 4.3, we derive the position and momentum wavefunctions of the two-photon field produced by type-I collinear SPDC and show that these wavefunctions satisfy the conditions required for our proposed scheme. In section 4.4, we present our experimental setup and results. In section 4.5, we outline the advantage of our method over the existing coincidence methods. In section 4.6, we present the numerical simulations for showcasing the suitability of our technique for mixed two-photon states. In section 4.7, we discuss the practical implications of the demonstrated technique. In section 4.8, we summarize the chapter.

## 4.2 Entanglement certification through single-photon cross-spectral density function measurement

Consider $|\Psi\rangle$ represent the state of a pure two-photon field or a pure two-photon state, and it can be written in the transverse momentum basis as

$$|\Psi\rangle = \iint d\boldsymbol{p}_1 d\boldsymbol{p}_2 \psi(\boldsymbol{p}_1, \boldsymbol{p}_2) |\boldsymbol{p}_1, \boldsymbol{p}_2\rangle . \tag{4.1}$$

Here, $\boldsymbol{p}_1 \equiv (p_{1x}, p_{1y})$ and $\boldsymbol{p}_2 \equiv (p_{2x}, p_{2y})$ are the transverse momenta of the first and the second photon, respectively, $|\boldsymbol{p}_1, \boldsymbol{p}_2\rangle$ is the two-photon state, and $\psi(\boldsymbol{p}_1, \boldsymbol{p}_2)$ represents the two-photon transverse-momentum wavefunction. Now if second photon is detected with transverse momentum $\boldsymbol{p}_2 = 0$, then the conditional momentum probability distribution $P(\boldsymbol{p}_1|\boldsymbol{p}_2 = 0)$ of the first photon is given by

$$P(\boldsymbol{p}_1|\boldsymbol{p}_2 = 0) = |\psi(\boldsymbol{p}_1, \boldsymbol{p}_2 = 0)|^2. \tag{4.2}$$

Now, the momentum cross-spectral density function of the first photon can be calculated as $W(\boldsymbol{p}_1, \boldsymbol{p}_1') = \langle\Psi| E_1^{(+)}(\boldsymbol{p}_1)E_1^{(-)}(\boldsymbol{p}_1') |\Psi\rangle$ [61], where $E_1^{(+)}(\boldsymbol{p}_1)$ and $E_1^{(-)}(\boldsymbol{p}_1')$ are the negative- and positive-frequency parts of the electric field operators respectively. For $\boldsymbol{p}_1' = -\boldsymbol{p}_1$, we have

$$W(\boldsymbol{p}_1, -\boldsymbol{p}_1) = \iint \psi^*(\boldsymbol{p}_1, \boldsymbol{p}_2)\psi(-\boldsymbol{p}_1, \boldsymbol{p}_2)d\boldsymbol{p}_2. \tag{4.3}$$

Next, we find that if the two-photon wavefunction satisfies the following condition.

$$\psi^*(\boldsymbol{p}_1, \boldsymbol{p}_2)\psi(-\boldsymbol{p}_1, \boldsymbol{p}_2) \propto |\psi(\boldsymbol{p}_1, \boldsymbol{p}_2 = 0)\psi(\boldsymbol{p}_1 = 0, \boldsymbol{p}_2)|^2, \tag{4.4}$$

then using Eqs. (4.2) and (4.3), one can show that

$$W(\boldsymbol{p}_1, -\boldsymbol{p}_1) \propto P(\boldsymbol{p}_1|\boldsymbol{p}_2 = 0). \tag{4.5}$$

We note that the condition in Eq. (4.4) can be satisfied by both separable and inseparable pure two-photon wavefunctions. Eq. (4.5) is the main theoretical result of this chapter. It states that as long as a two-photon state is pure, whether separable or entangled, and satisfies the condition in Eq. (4.4), the momentum cross-spectral density function of the first photon remains proportional to its conditional momentum probability distribution function. This implies that the standard deviations of $W(\boldsymbol{p}_1, -\boldsymbol{p}_1)$ and $P(\boldsymbol{p}_1|\boldsymbol{p}_2 = 0)$ are equal and that by measuring the standard deviation of $W(\boldsymbol{p}_1, -\boldsymbol{p}_1)$, one can obtain the standard deviation of $P(\boldsymbol{p}_1|\boldsymbol{p}_2 = 0)$. We denote the standard deviation of the conditional $x$-momentum of the first photon by $\Delta(p_{1x}|p_{2x} = 0)$.

Now, by writing the two-photon wavefunction of Eq. (4.1) in the position basis and proceeding in the similar manner, we can show that if the two-photon position wavefunction $\psi(\boldsymbol{\rho}_1, \boldsymbol{\rho}_2)$ satisfies the condition

$$\psi^*(\boldsymbol{\rho}_1, \boldsymbol{\rho}_2)\psi(-\boldsymbol{\rho}_1, \boldsymbol{\rho}_2) \propto |\psi(\boldsymbol{\rho}_1, \boldsymbol{\rho}_2 = 0)\psi(\boldsymbol{\rho}_1 = 0, \boldsymbol{\rho}_2)|^2, \tag{4.6}$$

where $\boldsymbol{\rho}_1 \equiv (x_1, y_1)$ and $\boldsymbol{\rho}_2 \equiv (x_2, y_2)$ are the transverse position vectors of the first and the second photon, then the position cross-spectral density function $W(\boldsymbol{\rho}_1, -\boldsymbol{\rho}_1)$ of the first photon is proportional to its conditional position probability distribution function $P(\boldsymbol{\rho}_1|\boldsymbol{\rho}_2 = 0)$, that is,

$$W(\boldsymbol{\rho}_1, -\boldsymbol{\rho}_1) \propto P(\boldsymbol{\rho}_1|\boldsymbol{\rho}_2 = 0). \tag{4.7}$$

Thus, by measuring the standard deviation of $W(\boldsymbol{\rho}_1, -\boldsymbol{\rho}_1)$, one can obtain the standard deviation of $P(\boldsymbol{\rho}_1|\boldsymbol{\rho}_2 = 0)$. We denote the standard deviation of the conditional $x$-position of the first photon by $\Delta(x_1|x_2 = 0)$. We note that although the above analysis has been presented with respect to making measurements on the first photon, we obtain the same result even when analyzed with the second photon. Now, it is known that if the two-photon wavefunction is separable, then the product $U$ of the conditional uncertainties satisfies the Heisenberg uncertainty relation, that is,

$$U \equiv \Delta(x_1|x_2 = 0)\Delta(p_{1x}|p_{2x} = 0) \geqslant 0.5\hbar. \tag{4.8}$$

However, a violation of this inequality implies that the two-photon wavefunction is non-separable and that the two photons are entangled having EPR correlation in position-momentum variables [33]. Thus, one can certify the position-momentum entanglement by doing cross-spectral density function measurements on one of the photons.

## 4.3 Derivation of two-photon spatial wavefunction in collinear type-I SPDC

We now derive position and momentum wavefunctions of the two-photon field produced by type-I SPDC process. We follow the calculations presented in Ref. [92, 183, 184]. We have already derived the interaction Hamiltonian $\hat{H}(t')$ in section 1.8 is given by

$$\hat{H}(t') = \frac{\epsilon_0}{2} \int_{\mathcal{V}} \chi^{(2)} \hat{V}_p^{(+)}(\boldsymbol{r}, t') \hat{V}_s^{(-)}(\boldsymbol{r}, t') \hat{V}_i^{(-)}(\boldsymbol{r}, t') d^3\boldsymbol{r} + H.c, \tag{4.9}$$

where $\chi^{(2)}$ and $\mathcal{V}$ denote the second order susceptibility and interaction volume of the nonlinear crystal, respectively. $\hat{V}_j^{(+)}(\boldsymbol{r}, t')$ and $\hat{V}_j^{(-)}(\boldsymbol{r}, t')$ are the positive and negative complex analytic field operators of the field with $j = p, s$ and $i$ corresponding to the pump, signal and idler, respectively. The field operators are represented in the plane-wave or transverse wave-vector basis in the following manner

$$\begin{aligned}
\hat{V}_p^{(+)}(\boldsymbol{r}, t') &= \int_{-\infty}^{\infty} A_p \mathrm{U}(\boldsymbol{q}_p, \omega_p) e^{i(\boldsymbol{q}_p \cdot \boldsymbol{\rho} + k_{pz} z - \omega_p t')} d^2\boldsymbol{q}_p d\omega_p, \\
\hat{V}_s^{(+)}(\boldsymbol{r}, t') &= \int_{-\infty}^{\infty} A_s^* \hat{a}_s^\dagger(\boldsymbol{q}_s, \omega_s) e^{-i(\boldsymbol{q}_s \cdot \boldsymbol{\rho} + k_{sz} z - \omega_s t')} d^2\boldsymbol{q}_s d\omega_s, \\
\hat{V}_i^{(-)}(\boldsymbol{r}, t') &= \int_{-\infty}^{\infty} A_i^* \hat{a}_i^\dagger(\boldsymbol{q}_i, \omega_i) e^{-i(\boldsymbol{q}_i \cdot \boldsymbol{\rho} + k_{iz} z - \omega_i t')} d^2\boldsymbol{q}_i d\omega_i.
\end{aligned}$$

Here $\boldsymbol{r} \equiv (\boldsymbol{\rho}, z)$, $\boldsymbol{k}_j \equiv (\boldsymbol{q}_j, k_{jz})$, and $\mathrm{U}(\boldsymbol{q}_p, \omega_p)$ represents the pump field in the transverse wave-vector basis and it is intense enough to be treated as a classical pump. Now, we substitute $\hat{V}_p^{(+)}(\boldsymbol{r}, t')$, $\hat{V}_s^{(-)}(\boldsymbol{r}, t')$ and $\hat{V}_i^{(-)}(\boldsymbol{r}, t')$ in Eq. (4.9) and it takes the form

$$\begin{aligned}
\hat{H}(t') = \frac{A_p A_s^* A_i^* \epsilon_0 \chi^{(2)}}{2} \int_{\mathcal{V}} d^2\boldsymbol{\rho} dz \iiint d^2\boldsymbol{q}_p d^2\boldsymbol{q}_s d^2\boldsymbol{q}_i \iiint d\omega_p d\omega_s d\omega_i \mathrm{U}(\boldsymbol{q}_p, \omega_p) \hat{a}_s^\dagger(\boldsymbol{q}_s, \omega_s) \\
\times \hat{a}_i^\dagger(\boldsymbol{q}_i, \omega_i) e^{[i(\boldsymbol{q}_p - \boldsymbol{q}_s - \boldsymbol{q}_i) \cdot \boldsymbol{\rho} + i(k_{pz} - k_{sz} - k_{iz}) z]} e^{-i(\omega_p - \omega_s - \omega_i) t'} + H.c.
\end{aligned} \tag{4.10}$$

Now using the interaction picture in time-dependent perturbation theory we write the two-photon state $|\psi(t'=0)\rangle$ at $t'=0$ in the following form [185,186]

$$|\psi(t'=0)\rangle = \left[1+\left(\frac{-i}{\hbar}\right)\int_{-t_{int}}^{0} dt'\hat{H}(t')+\left(\frac{-i}{\hbar}\right)^2\int_{-t_{int}}^{0} dt'\int_{-t_{int}}^{t'} dt''\hat{H}(t')\hat{H}(t'')+...\right] \times |\psi(-t_{int})\rangle, \quad (4.11)$$

where $|\psi(-t_{int})\rangle = |vac\rangle_s|vac\rangle_i$ is the two-photon state before the SPDC process, where both signal and idler photons are in the vaccum state. We assume that the parametric interaction is weak and restrict the perturbative expansion in Eq. (4.11) upto second term. The first term represents the vacuum state and it can be ignored because it does not contribute in photon detection. Now, we write the second term $|\psi\rangle$ as

$$|\psi\rangle = \frac{A_p A_s^* A_i^* \epsilon_0 \chi^{(2)}}{2i\hbar}\int_{-t_{int}}^{0} dt' \iint d^2\boldsymbol{\rho}\int_{-L/2}^{L/2} dz \iiint d^2\boldsymbol{q}_p d^2\boldsymbol{q}_s d^2\boldsymbol{q}_i \iiint d\omega_p d\omega_s d\omega_i$$
$$\times\, \mathrm{U}(\boldsymbol{q}_p,\omega_p)e^{[i(\boldsymbol{q}_p-\boldsymbol{q}_s-\boldsymbol{q}_i)\cdot\boldsymbol{\rho}]+i(k_{pz}-k_{sz}-k_{iz})z}e^{-i(\omega_p-\omega_s-\omega_i)t'}\hat{a}_s^\dagger(\boldsymbol{q}_s,\omega_s)\hat{a}_i^\dagger(\boldsymbol{q}_i,\omega_i)|vac\rangle_s|vac\rangle_i. \quad (4.12)$$

Here, $\hat{a}_s^\dagger(\boldsymbol{q}_s,\omega_s)\hat{a}_i^\dagger(\boldsymbol{q}_i,\omega_i)|vac\rangle_s|vac\rangle_i = |\boldsymbol{q}_s,\omega_s\rangle_s|\boldsymbol{q}_i,\omega_i\rangle_i$ represents the two-photon state, where $|\boldsymbol{q}_s,\omega_s\rangle_s$ is the state of the signal photon with transverse wave-vector $\boldsymbol{q}_s$ and frequency $\omega_s$, $|\boldsymbol{q}_i,\omega_i\rangle_i$ is the state of the idler photon with transverse wave-vector $\boldsymbol{q}_i$ and frequency $\omega_i$. We assume that the time scale $t_{int}$ is much larger than that of the down-conversion process and smaller than the time interval between two subsequent down-conversion events. For SPDC experiment with a nonlinear crystal of thickness few millimeters and pump power of few tens of milliwatts, $t_{int}$ is of the order of picoseconds and the separation between two successive down-conversion events varies from milliseconds to microseconds [12]. Thus, we perform the integration over $dt'$ from $-\infty$ to $\infty$ in Eq. (4.12), and obtain $\int_{-\infty}^{\infty} e^{i(\omega_p-\omega_s-\omega_i)t'}dt' = \delta(\omega_p-\omega_s-\omega_i)$. Next, we assume that the spatial extent of the pump field is much smaller than the area of the nonlinear crystal and the limit of $\boldsymbol{\rho}$ extends from $-\infty$ to $\infty$ and it yields $\int_{-\infty}^{\infty} e^{i(\boldsymbol{q}_p-\boldsymbol{q}_s-\boldsymbol{q}_i)\cdot\boldsymbol{\rho}}d^2\boldsymbol{\rho} = \delta(\boldsymbol{q}_p-\boldsymbol{q}_s-\boldsymbol{q}_i)$. We evaluate the integral with respect to $dz$ over the length of the crystal $L$ and find

$\int_{-\frac{L}{2}}^{\frac{L}{2}} e^{i(k_{pz}-k_{sz}-k_{iz})z}dz = \operatorname{sinc}(\Delta kL/2)$, where $\Delta k = k_{pz} - k_{sz} - k_{iz}$. The above Eq. (4.12) takes the form

$$|\psi\rangle = A \iiint d^2\boldsymbol{q}_p d^2\boldsymbol{q}_s d^2\boldsymbol{q}_i \iiint d\omega_p d\omega_s d\omega_i \delta(\boldsymbol{q}_p - \boldsymbol{q}_s - \boldsymbol{q}_i)\delta(\omega_p - \omega_s - \omega_i) \\ \times \mathrm{U}(\boldsymbol{q}_p, \omega_p) \operatorname{sinc}\left(\frac{\Delta kL}{2}\right) |\boldsymbol{q}_s, \omega_s\rangle_s |\boldsymbol{q}_i, \omega_i\rangle_i. \quad (4.13)$$

All the constants are absorbed in $A$. After performing integration over $\boldsymbol{q}_p$ and $\omega_p$, we assume that both signal and idler photons have a very narrow frequency bandwidth around the central frequency $\omega_p/2$. In the experiment, we achieve this by introducing narrow wavelength filters before the detectors. The two-photon state becomes

$$|\psi\rangle = A \iint d^2\boldsymbol{q}_s d^2\boldsymbol{q}_i \mathrm{U}(\boldsymbol{q}_s + \boldsymbol{q}_i) \operatorname{sinc}\left(\frac{\Delta kL}{2}\right) |\boldsymbol{q}_s\rangle_s |\boldsymbol{q}_i\rangle_i. \quad (4.14)$$

This is the general expression for a two-photon state produced by SPDC process in the transverse wave-vector basis. We now write the corresponding two-photon wavefunction

$$\psi(\boldsymbol{q}_s, \boldsymbol{q}_i) = A\mathrm{U}(\boldsymbol{q}_s + \boldsymbol{q}_i) \operatorname{sinc}\left(\frac{\Delta kL}{2}\right). \quad (4.15)$$

From now on we only work with collinear type-I phase-matching [187] within paraxial approximation, and under this condition, the function $\operatorname{sinc}(\Delta kL/2)$ is routinely approximated by a Gaussian function of form $\exp\left[-|\boldsymbol{q}_s - \boldsymbol{q}_i|^2\sigma_0^2/4\right]$ [52, 56, 57], $\sigma_0 = \sqrt{\frac{0.455L\lambda_p}{2\pi}}$, $\lambda_p = 2\pi/k_p$ is the pump wavelength.

$$\psi(\boldsymbol{p}_s, \boldsymbol{p}_i) = A \exp\left[-\frac{(\boldsymbol{p}_i+\boldsymbol{p}_s)^2 w_0^2}{4\hbar^2}\right] \exp\left[-\frac{|\boldsymbol{p}_i-\boldsymbol{p}_s|^2\sigma_0^2}{4\hbar^2}\right], \quad (4.16)$$

where $w_0$ is the pump beam waist, $\boldsymbol{p}_s \equiv \boldsymbol{q}_s\hbar \equiv (p_{sx}, p_{sy})$ and $\boldsymbol{p}_i \equiv \boldsymbol{q}_i\hbar \equiv (p_{ix}, p_{iy})$ are the transverse momenta of the signal and idler photons, respectively. By taking the Fourier transform of the wavefunction given in Eq. (4.16), we write the two-photon wavefunction in the position basis as

$$\psi(\boldsymbol{\rho_s},\boldsymbol{\rho_i}) = A' \exp\left[-\frac{(\boldsymbol{\rho_i}+\boldsymbol{\rho_s})^2}{4w_0^2}\right] \exp\left[-\frac{|\boldsymbol{\rho_i}-\boldsymbol{\rho_s}|^2}{4\sigma_0^2}\right]. \tag{4.17}$$

Here, $A'$ is a normalization constant, $\boldsymbol{\rho_s} \equiv (x_s, y_s)$ and $\boldsymbol{\rho_i} \equiv (x_i, y_i)$ are the transverse positions of the signal and idler photons at the crystal plane. We note that the above wavefunctions $\psi(\boldsymbol{p}_s, \boldsymbol{p}_i)$ and $\psi(\boldsymbol{\rho_s}, \boldsymbol{\rho_i})$ satisfy the conditions given in Eqs. (4.4) and (4.6), respectively.

## 4.4 Experiment and Results

Next, we present our experimental results demonstrating how the conditional position and momentum uncertainties can be obtained by measuring the cross-spectral density functions of just the signal photon. Figures 4.1(a)-4.1(c) show the schematics of our experimental setup. An ultraviolet (UV) Gaussian pump beam of wavelength $\lambda_p = 405$ nm and beam waist $w_0 = 388$ $\mu$m is incident on a 2 mm thick $\beta-$barium borate (BBO) crystal and produces two-photon state using SPDC with the type-I collinear phase-matching. Figure 4.1(c) shows an inversion-based interferometer that we use for measuring the cross-spectral density functions [155, 157]. Figures 4.1(a) and 4.1(b) show the lens configurations for imaging, respectively, the crystal plane and the Fourier plane of the crystal onto an EMCCD camera having 512 × 512 pixels and 60 second acquisition time. For measuring the position cross-spectral density function of the signal photon, we use the configuration of Fig. 4.1(a) with $f_1 = 10$ cm and $f_2 = 40$ cm and image the crystal onto the EMCCD plane, kept at 40 cm from $f_2$, with a magnification $M = 4$. We take $(x_s, y_s)$ and $(\tilde{x}_s, \tilde{y}_s)$ to be the position coordinates at the crystal plane and at the EMCCD plane, respectively. The two sets of coordinates are related as $\tilde{x}_s = Mx_s$ and $\tilde{y}_s = My_s$. The intensity $I^{\delta}_{\rm out}(\tilde{x}_s, \tilde{y}_s)$ of the output interferogram at the EMCCD plane is given by $I^{\delta}_{\rm out}(\tilde{x}_s, \tilde{y}_s) = k_1 I(\tilde{x}_s, \tilde{y}_s) + k_2 I(-\tilde{x}_s, \tilde{y}_s) + 2\sqrt{k_1 k_2} W(\tilde{x}_s, \tilde{y}_s, -\tilde{x}_s, \tilde{y}_s) \cos\delta$ [155]. Here, $k_1$ and $k_2$ are the scaling constants, while $k_1 I(\tilde{x}_s, \tilde{y}_s)$ and $k_2 I(-\tilde{x}_s, \tilde{y}_s)$ are the intensities at the EMCCD plane coming through the two arms of the interferometer. The

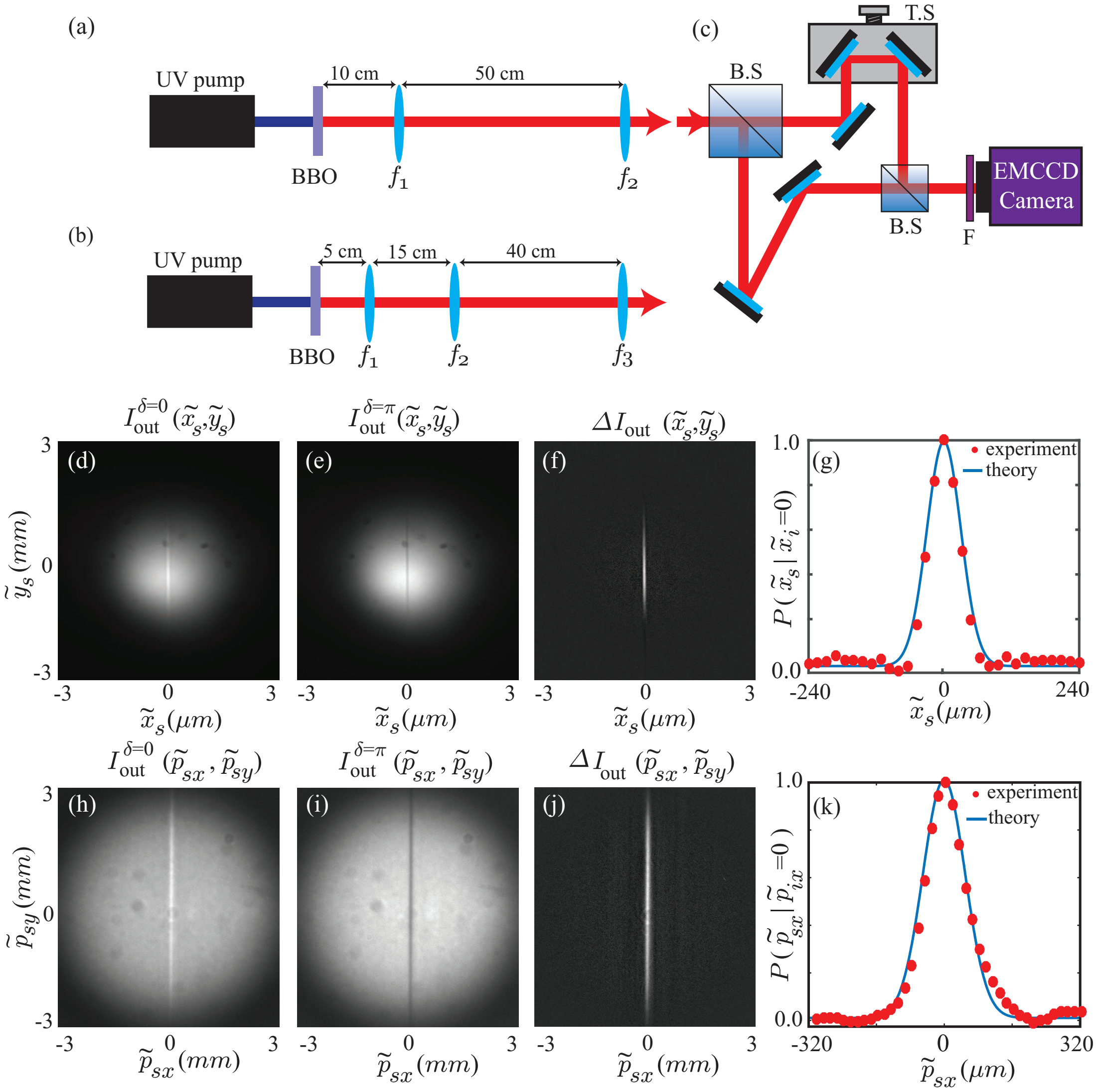

FIGURE 4.1: (a) Lens configuration for measuring position correlation. (b) Lens configuration for measuring momentum correlation. (c) Inversion-based interferometer for measuring position and momentum cross-spectral density functions. B.S: Beam Splitter, T.S: Translational Stage, F: an interference filter of 10 nm spectral width centered at 810 nm. (d) and (e) The two interferograms recorded at $\delta_c = 0$ and $\delta_d = \pi$ with the configuration in Fig. 1(a). (f) The difference intensity image $\Delta I(\tilde{x}_s, \tilde{y}_s)$. (g) Experimental and theoretical conditional probability distribution $P(\tilde{x}_s|\tilde{x}_i = 0)$. (h) and (i) The two interferograms recoded at $\delta_c = 0$ and $\delta_d = \pi$ with the configuration in Fig. 1(b). (j) The difference intensity image $\Delta I(\tilde{p}_{sx}, \tilde{p}_{sy})$. (k) Experimental and theoretical conditional probability distribution $P(\tilde{p}_{sx}|\tilde{p}_{ix} = 0)$.

quantity $\delta$ is the phase difference between the two interferometric arms. If we take two interferograms $I^{\delta_c}_{\text{out}}(\tilde{x}_s, \tilde{y}_s)$ and $I^{\delta_d}_{\text{out}}(\tilde{x}_s, \tilde{y}_s)$ at $\delta = \delta_c$ and $\delta = \delta_d$, respectively, then it can be shown that the difference intensity $\Delta I_{\text{out}}(\tilde{x}_s, \tilde{y}_s) = I^{\delta_c}_{\text{out}}(\tilde{x}_s, \tilde{y}_s) - I^{\delta_d}_{\text{out}}(\tilde{x}_s, \tilde{y}_s)$ is proportional to the position cross-spectral density function, that is, $\Delta I_{\text{out}}(\tilde{x}_s, \tilde{y}_s) \propto W(\tilde{x}_s, \tilde{y}_s, -\tilde{x}_s, \tilde{y}_s)$ [155, 157]. Figures 4.1(d) and 4.1(e) show the two experimentally measured interferograms at $\delta = \delta_c \approx 0$ and $\delta = \delta_d \approx \pi$, respectively, and Fig. 4.1(f) shows the difference intensity $\Delta I_{\text{out}}(\tilde{x}_s, \tilde{y}_s)$. From Eq. (4.7), we have that $W(\tilde{x}_s, \tilde{y}_s, -\tilde{x}_s, -\tilde{y}_s)$, is proportional to the conditional position probability distribution function of the signal photon, that is, $P(\tilde{x}_s, \tilde{y}_s|\tilde{x}_i = 0, \tilde{y}_i = 0) \propto W(\tilde{x}_s, \tilde{y}_s, -\tilde{x}_s, -\tilde{y}_s)$. Therefore, we obtain the one-dimensional conditional position probability distribution function $P(\tilde{x}_s|\tilde{x}_i = 0)$ by averaging $\Delta I_{\text{out}}(\tilde{x}_s, \tilde{y}_s)$ over the $\tilde{y}_s$-direction and plotting it in Fig. 4.1(g). Using Eq. (4.17) and the relevant experimental parameters, we calculate the theoretical $P(\tilde{x}_s|\tilde{x}_i = 0)$ and plot it in Fig. 4.1(g) (solid curve). We scale the $P(\tilde{x}_s|\tilde{x}_i = 0)$ plots in Fig. 1(g) such that the maximum value is one. We fit the experimental $P(\tilde{x}_s|\tilde{x}_i = 0)$ with a Gaussian function and find the standard deviation to be 26.25 $\mu$m. The standard deviation of the theoretical plot is 30.6 $\mu$m. Now, we use $\tilde{x}_s = Mx_s$ and obtain the experimental and theoretical values of $\Delta(x_s|x_i = 0)$ to be 6.56 $\mu$m and 7.65 $\mu$m, respectively.

For measuring the momentum cross-spectral density function of the signal photon, we use the configuration of Fig. 4.1(b) with $f_1 = 5$ cm, $f_2 = 10$ cm, and $f_3 = 30$ cm. The effective focal length of this combination is $f_e = 15$ cm. The EMCCD is kept at 30 cm from $f_3$, which is the Fourier plane of this configuration. We take $(p_{sx}, p_{sy})$ to be the transverse momentum at the crystal plane and $(\tilde{p}_{sx}, \tilde{p}_{sy})$ is the position coordinate at the EMCCD plane. These coordinates can be shown to be related as $p_{sx} = \frac{k_0\hbar}{f_e}\tilde{p}_{sx}$ and $p_{sy} = \frac{k_0\hbar}{f_e}\tilde{p}_{sy}$ [56], where $k_0 = \frac{2\pi}{\lambda_0}$. The intensity $I^{\delta}_{\text{out}}(\tilde{p}_{sx}, \tilde{p}_{sy})$ of the output interferogram at the EMCCD plane in this case can be written as $I^{\delta}_{\text{out}}(\tilde{p}_{sx}, \tilde{p}_{sy}) = k_1 I(\tilde{p}_{sx}, \tilde{p}_{sy}) + k_2 I(-\tilde{p}_{sx}, \tilde{p}_{sy}) + 2\sqrt{k_1 k_2} W(\tilde{p}_{sx}, \tilde{p}_{sy}, -\tilde{p}_{sx}, \tilde{p}_{sy}) \cos\delta$ [155]. Here, $k_1 I(\tilde{p}_{sx}, \tilde{p}_{sy})$, and $k_2 I(-\tilde{p}_{sx}, \tilde{p}_{sy})$ are the intensities at the EMCCD plane coming through the two interferometric arms. Just as discussed above, the difference intensity $\Delta I_{\text{out}}(\tilde{p}_{sx}, \tilde{p}_{sy}) = I^{\delta_c}_{\text{out}}(\tilde{p}_{sx}, \tilde{p}_{sy}) - I^{\delta_d}_{\text{out}}(\tilde{p}_{sx}, \tilde{p}_{sy})$ is proportional to the cross-spectral density function $W(\tilde{p}_{sx}, \tilde{p}_{sy}, -\tilde{p}_{sx}, \tilde{p}_{sy})$ [155, 157]. Figures 4.1(h) and 4.1(i) show the two experimentally measured interferograms at $\delta = \delta_c \approx 0$ and $\delta = \delta_d \approx \pi$, respectively, and Fig. 4.1(j) shows the difference intensity $\Delta I_{\text{out}}(\tilde{p}_{sx}, \tilde{p}_{sy})$. From Eq. (4.5), we have that $P(\tilde{p}_{sx}, \tilde{p}_{sy}|\tilde{p}_{ix} = 0, \tilde{p}_{iy} = 0) \propto W(\tilde{p}_{sx}, \tilde{p}_{sy}, -\tilde{p}_{sx}, -\tilde{p}_{sy})$. Therefore, we obtain the one-dimensional conditional probability distribution function $P(\tilde{p}_{sx}|\tilde{p}_{ix} = 0)$ by averaging $\Delta I_{\mathrm{out}}(\tilde{p}_{sx}, \tilde{p}_{sy})$, over $\tilde{p}_{sy}$-direction and plotting it in Fig. 4.1(k). Using Eq. (4.16) and the relevant experimental parameters, we calculate the theoretical $P(\tilde{p}_{sx}|\tilde{p}_{ix} = 0)$ at the EMCCD plane and plot it in Fig. 4.1(k) (solid curve). We scale the $P(\tilde{p}_{sx}|\tilde{p}_{ix} = 0)$ plots in Fig. 4.1(k) such that the maximum value is one. We fit the experimental $P(\tilde{p}_{sx}|\tilde{p}_{ix} = 0)$ with a Gaussian function and find the standard deviation to be 49.5 $\mu$m. The standard deviation of the theoretical plot is 49.8 $\mu$m. Using $p_{sx} = \frac{k_0\hbar}{f_e}\tilde{p}_{sx}$, we obtain the experimental and theoretical values of $\Delta(p_{sx}|p_{ix} = 0)$ to be $2.55 \times 10^{-3}\hbar\ \mu\mathrm{m}^{-1}$ and $2.57 \times 10^{-3}\hbar\ \mu\mathrm{m}^{-1}$, respectively.

As defined in Eq. (4.8), the experimentally measured value of the conditional uncertainty product $U_{\mathrm{ex}}$ is $1.67 \times 10^{-2}\hbar$. This is much smaller than $0.5\hbar$ and thus implies a strong EPR correlation between the two entangled photons. We find the theoretical conditional uncertainty product $U_{\mathrm{th}}$ to be $1.96 \times 10^{-2}\hbar$, and we thus find a good match between the theory and experiments.

We note that our experiment uses collinear phase-matching and the interferogram recorded by the camera is the sum of the interferograms generated by both signal and idler fields. However, since signal and idler photons are identical in their spatial degree of freedom, the functional form of individual interferograms generated by signal and idler fields is identical to that of the recorded interferogram.

## 4.5 Advantages over existing measurement schemes

Now, in order to quantify the accuracy of our measurement scheme, we use the quantity $\mathcal{F} \equiv \frac{|U_{\mathrm{th}} - U_{\mathrm{ex}}|}{U_{\mathrm{th}}}$. We note that a smaller value of $\mathcal{F}$ implies better accuracy of EPR correlation measurements. For our experimental results, we obtain $\mathcal{F} = 0.14$. This value of $\mathcal{F}$ obtained through our measurement scheme is much smaller than the previously reported values of 0.27 in Ref. [82], 0.43 in Ref. [56], 0.66 in Ref. [39], 1.9 in Ref. [52], and 3.76 in Ref. [53]. For a fair comparison we ensure that the above-monetioned coincidence detection schemes in Refs. [39,52,53,56,82] have used collinear SPDC and double gaussian wavefunction for the two-photon state that are similar to our experimental configuration and theoretical modeling. Another quantity is quite often used for quantifying the EPR correlation measurements. It is called the degree of violation and is defined as $\mathcal{D} = \left(0.5\hbar/U_{exp}\right)^2$. The degree of violation $\mathcal{D}$ does not quantify the measurement accuracy but gives an estimate of the degree with which the Heisenberg bound of $0.5\hbar$ is violated. For our experimental measurements, $\mathcal{D} = 896$, whereas the degree of violations reported earlier include 576 in Ref. [82], 380 in Ref. [56], 42 in Ref. [52], 25 in Ref. [39], and 4 in Ref. [53]. Thus we report not only the most accurate EPR correlation measurements but also the highest degree of violation.

## 4.6 Suitability of the technique for mixed two-photon states

So far we have demonstrated that our technique measures EPR correlations with very good accuracy for pure two-photon states that satisfy the conditions given in Eqs. (5.12) and (4.6). Next, we numerically analyse the suitability of our technique for mixed two-photon states. In the case of mixed two-photon states, the widths $W(x_s, -x_s)$ and $W(p_{xs}, -p_{xs})$ are not necessarily equal to $\Delta(x_s|x_i = 0)$ and $\Delta(p_{xs}|p_{xi} = 0)$ respectively. Suppose the widths of $W(x_s, -x_s)$ and $W(p_{xs}, -p_{xs})$ are $\mu_x$ and $\mu_{p_x}$, respectively. Then the error $\mathcal{E}$ inherent in the scheme can be quantified as

$$\mathcal{E} \equiv \frac{|U_{\rm th} - \mu_x \mu_{p_x}|}{U_{\rm th}} \times 100\%, \tag{4.18}$$

where $U_{\rm th} = \Delta(x_s|x_i = 0)\Delta(p_{xs}|p_{xi} = 0)$. The quantity $\mathcal{E}$ varies from 0 to 100%, and the higher values of $\mathcal{E}$ implies higher inaccuracies of the scheme for the mixed two-photon states.

There are two broad schemes by which one can generate mixed two-photon states. One is by introducing turbulence in the path of the generated pure two-photon state and the other one is by generating the two-photon states using a spatially partially coherent

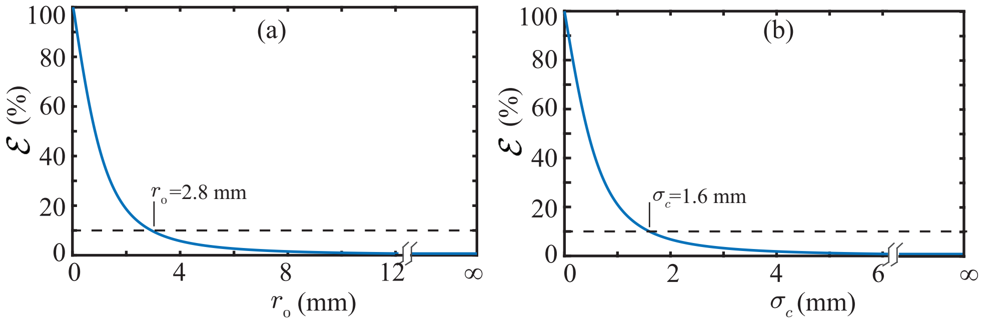

FIGURE 4.2: (a) Plot of error $\mathcal{E}$ as a function of the Fried parameter $r_0$ and (b) Plot of error $\mathcal{E}$ as a function of the transverse coherence length $\sigma_c$ of the pump field.

pump field. Next, for these two schemes of generating the mixed two-photon states, we numerically analyse how the inherent error $\mathcal{E}$ of our scheme changes as a function of the mixedness of the two-photon state.

### 4.6.1 Introducing mixedness through turbulence

We consider the situation in which both signal and idler photons pass through a planar turbulence medium right after the crystal plane. The turbulence introduces statistical randomness in both signal and idler photon fields. As a result, the two-photon state produced by SPDC does not remain pure and thus does not satisfy the conditions in Eqs. (4.4) and (4.6). We write the mixed two-photon state thus produced using the two-photon cross-spectral density function in the position basis as

$$W_{\text{tp}}(\boldsymbol{\rho}_{s_1}, \boldsymbol{\rho}_{i_1}, \boldsymbol{\rho}_{s_2}, \boldsymbol{\rho}_{i2}) = \psi^*(\boldsymbol{\rho}_{s_1}, \boldsymbol{\rho}_{i_1})\psi(\boldsymbol{\rho}_{s_2}, \boldsymbol{\rho}_{i_2})W_{\text{turb}}(\boldsymbol{\rho}_{s_1}, \boldsymbol{\rho}_{s_2}, \boldsymbol{\rho}_{i_1}, \boldsymbol{\rho}_{i_2}), \tag{4.19}$$

where $\psi^*(\boldsymbol{\rho}_{s_1}, \boldsymbol{\rho}_{i_1})\psi(\boldsymbol{\rho}_{s_2}, \boldsymbol{\rho}_{i_2})$ is the two-photon cross-spectral density function just before the turbulence, and the influence of turbulence is captured by the cross-spectral density function $W_{\text{turb}}(\boldsymbol{\rho}_{s_1}, \boldsymbol{\rho}_{s_2}, \boldsymbol{\rho}_{i_1}, \boldsymbol{\rho}_{i_2}) = \exp\left[-6.88[|\boldsymbol{\rho}_{s_2} - \boldsymbol{\rho}_{s_1}|^2 + |\boldsymbol{\rho}_{i_2} - \boldsymbol{\rho}_{i_1}|^2]/(2r_0^2)\right]$ [188, 189], where $r_0$ is the so-called Fried parameter. Smaller values of $r_0$ implies higher turbulence strength, with $r_0 = 0$ implying infinite turbulence and a completely mixed state and $r_0 = \infty$ implying no turbulence and thus a pure two-photon state.

From the above two-photon cross-spectral density function $W_{\rm tp}(\boldsymbol{\rho}_{s_1}, \boldsymbol{\rho}_{s_2}, \boldsymbol{\rho}_{i_1}, \boldsymbol{\rho}_{i_2})$, we numerically calculate the one-dimensional conditional probability $P(x_s|x_i = 0)$ and the cross-spectral density function $W(x_s, -x_s)$ and evaluate their respective widths $\Delta(x_s|x_i = 0)$ and $\mu_x$ as a function of $r_0$ (see Appendix A section A.0.1.). We next find the corresponding two-photon momentum cross-spectral density function $W_{\rm tp}(\boldsymbol{p}_{s_1}, \boldsymbol{p}_{i_1}, \boldsymbol{p}_{s_2}, \boldsymbol{p}_{i_2})$ using the following equation

$$W_{\rm tp}(\boldsymbol{p}_{s_1}, \boldsymbol{p}_{i_1}, \boldsymbol{p}_{s_2}, \boldsymbol{p}_{i_2}) = \int W_{\rm tp}(\boldsymbol{\rho}_{s_1}, \boldsymbol{\rho}_{i_1}, \boldsymbol{\rho}_{s_2}, \boldsymbol{\rho}_{i_2}) e^{-i(\boldsymbol{\rho}_{s_1}\cdot\boldsymbol{p}_{s_1} + \boldsymbol{\rho}_{i_1}\cdot\boldsymbol{p}_{i_1} - \boldsymbol{\rho}_{s_2}\cdot\boldsymbol{p}_{s_2} - \boldsymbol{\rho}_{s_2}\cdot\boldsymbol{p}_{s_2})/\hbar} d\boldsymbol{\rho}_{s_1} d\boldsymbol{\rho}_{s_2} d\boldsymbol{\rho}_{i_1} d\boldsymbol{\rho}_{i_2}. \tag{4.20}$$

We then calculate the one-dimensional momentum probability distribution function $P(p_{xs}|p_{xi} = 0)$ and the cross-spectral density function $W(p_{xs}, -p_{xs})$ of the signal photon and thereby the widths $\Delta(p_{xs}|p_{xi} = 0)$ and $\mu_{p_x}$ at different $r_0$ (see Appendix A section A.0.1). Finally, we evaluate $\mathcal{E}$ as a function of $r_0$ and plot it in Fig. 4.2(a). We find that $\mathcal{E}$ decreases with increasing $r_0$. In other words, $\mathcal{E}$ decreases with decreasing turbulence strength. We note that the realistic turbulences are distributed and the Fried parameter typically varies from $r_0 = 4$ mm to 30 mm [190, 191]. We expect our results to remain valid even for a distributed turbulence, and from Fig. 4.2(a), we note that in the range from $r_0 = 4$ mm to 30 mm, the error $\mathcal{E}$ is less than 10%. We thus expect our technique to be practically useful even for measuring the EPR correlations of mixed two-photon state and thus be useful for experimental scenarios related to propagation of entangled photons through random media [189].

### 4.6.2 Introducing mixedness by using a spatially partially coherent pump field

Next, we consider the situation in which the two-photon states is produced by SPDC using a spatially partially coherent pump field. To keep the analysis simple, we consider a Gaussian Schell Model (GSM) field [70] as the spatially partially coherent pump field. The generated mixed two-photon state can be described in terms of the following two-photon cross-spectral density function [192]:

$$W_{\mathrm{tp}}(\boldsymbol{\rho}_{s_1}, \boldsymbol{\rho}_{i_1}, \boldsymbol{\rho}_{s_2}, \boldsymbol{\rho}_{i_2}) = A \exp\left[-\frac{|\boldsymbol{\rho}_{s_1} + \boldsymbol{\rho}_{i_1}|^2 + |\boldsymbol{\rho}_{s_2} + \boldsymbol{\rho}_{i_2}|^2}{4w_0^2}\right]$$
$$\times \exp\left[-\frac{|\boldsymbol{\rho}_{s_2} + \boldsymbol{\rho}_{i_2} - \boldsymbol{\rho}_{s_1} - \boldsymbol{\rho}_{i_1}|^2}{2\sigma_c^2}\right] \exp\left[-\frac{|\boldsymbol{\rho}_{s_1} - \boldsymbol{\rho}_{i_1}|^2 + |\boldsymbol{\rho}_{s_2} - \boldsymbol{\rho}_{i_2}|^2}{4\sigma_0^2}\right], \quad (4.21)$$

where $w_0$ and $\sigma_c$ are the beam-waist of the pump at the crystal plane and the transverse spatial coherence length of the pump at the crystal plane, respectively. The transverse spatial coherence length of the pump $\sigma_c$ ranges from 0 to $\infty$, with $\sigma_c = 0$ implying a completely mixed state and $\sigma_c = \infty$ implying a pure state. Using Eq. (4.21) we numerically calculate the one-dimensional conditional probability $P(x_s|x_i = 0)$ and the cross-spectral density function $W(x_s, -x_s)$ as a function of $\sigma_c$ (see Appendix A section A.0.2 for details). Next, using Eq. (4.21), we calculate two-photon momentum cross-spectral density function $W_{\mathrm{tp}}(\boldsymbol{p}_{s_1}, \boldsymbol{p}_{i_1}, \boldsymbol{p}_{s_2}, \boldsymbol{p}_{i_2})$ and thereby evaluate $P(p_{xs}|p_{xi} = 0)$ and $W(p_{xs}, -p_{xs})$ as a function of $\sigma_c$ (see Appendix A section A.0.2 for details). Finally, using Eq. (4.18), we evaluate $\mathcal{E}$ and plot it as a function of $\sigma_c$ in Fig. 4.2(b). We find that the error $\mathcal{E}$ decreases with increasing $\sigma_c$, that is, the error decreases as the purity of the two-photon state increases. From Fig. 4.2(b), we find that even with $\sigma_c = 1.6$ mm, which indicates substantial partial coherence, the error $\mathcal{E}$ is less than 10%. This implies that our scheme could be useful even for mixed two-photon states and thus be relevant for experimental scenarios involving spatially entangled mixed two-photon states [78].

## 4.7 Practical implications

We note that several quantum information applications require either the knowledge or measurement of position and momentum conditional probability distribution functions. For example, the resolution of a coincidence imaging scheme relies on conditional position and momentum uncertainties [43] and the communication protocols based on position-momentum entanglement require the measurement of conditional position and momentum probability distribution functions [52,54]. Thus from the application perspective, it is important to have a technique that measures the EPR correlations accurately. So far many coincidence imaging and communication protocols [43, 45, 47, 51, 52, 171] have utilized the position-momentum entanglement in the two-photon state described by position and momentum wavefunctions given in Eqs. (4.16) and (4.17) respectively. Hence our measurement technique has direct applications in the above imaging and communication protocols. Moreover, we note that two-photon wavefunctions produced by non-collinear SPDC [193, 194], type-II SPDC [195], and spontaneous four-wave mixing (SFWM) [83, 196] processes satisfy the set of conditions given in Eqs. (4.4) and (4.6). Thus our technique is applicable for certifying position-momentum entanglement in such processes and these processes cover most of the existing optical platforms for generating position-momentum entangled states. In this article, although we have demonstrated our scheme for the position-momentum EPR correlations, it can be extended for measuring EPR-correlations in other continuous variables such as time-energy [41, 89, 172] and angle-OAM [40].

## 4.8 Summary

In summary, we have demonstrated a scheme for measuring two-photon position−momentum EPR correlations that does not require coincidence detection. Our method works for any pure two-photon state, irrespective of whether the state is separable or entangled. We have experimentally demonstrated this technique with the pure two-photon state produced with collinear phase-matching and have obtained the most accurate measurement of position-momentum EPR correlations reported so far. We have also presented a numerical analysis to study the suitability of this technique for a broad range of mixed two-photon states that do not satisfy the requisite conditions. Therefore, we expect our work to have practical implications for a wide range of experimental configurations and processes employed in continuous-variable quantum information applications.

# Chapter 5

# Applications of spatial coherence in optical field

## 5.1 Introduction

Propagation of optical fields through random media is an important subject of research [197–200] due to its implications for a wide range of applications. For example, performing imaging, free-space optical communication, navigation in foggy environments are inevitable in many realistic scenarios, including railways, defence, medical, and road transports. The difficulties in performing any task through random media arise due to the inhomogeneities in the media, introducing random phase variations at different spatial locations in the light field passing through it. If the light field is spatially coherent, these random phase variations result in a random interference pattern known as the speckle pattern [201]. As a consequence, the information carried by the field is superimposed with the speckle pattern, and it gets corrupted. This severely affects the performance of many real-world applications. We now only focus on the difficulties involved in imaging and free-space optical communication through scattering or turbulent media.

Over the years, several imaging techniques have been proposed and demonstrated for addressing the above-mentioned speckle issue in the presence of scattering media. These techniques can be categorized into two sets. The first set of techniques use spatially completely coherent light sources such as lasers for illumination. In this set of techniques, one tries to minimize the speckle effects either by imaging with ballistic photons [26, 200, 202, 203], or by descrambling the phase of the scattered light field using a hologram or a spatial light modulator (SLM) [204–207]. Such techniques either require prior knowledge of the scattering media or find difficulties in real-time imaging. The other set of techniques for imaging through scattering media is based on using spatially partially coherent light sources. In this set of techniques, the speckle pattern gets reduced as the spatial coherence length of the illuminating field becomes smaller. Moreover, such techniques provide real-time imaging and do not require prior knowledge of the scattering medium. In chapter 2, we have discussed different approaches for generating spatially partially coherent light fields. The most common technique involves introducing randomness in a spatially coherent laser field by using either an acousto-optical cell [113], a rotating ground glass plate [114, 116], or an SLM [122, 123]. A more recent approach involves using random lasers [21, 23] with small spatial coherence lengths. The other approach is to use light-emitting diodes (LEDs) or thermal sources [130, 134], which are spatially completely incoherent primary light sources. Although the techniques based on spatially completely coherent sources such as lasers are useful for some applications requiring intense illumination, they still have limited applicability in full-field imaging due to speckle effects. As a result, the techniques based on using spatially partially coherent sources are being preferred for imaging two-dimensional objects in scattering media [21–23, 208–210]. However, the spatial coherence length of most partially coherent sources increases upon propagation, causing speckle effects to become progressively pronounced. Therefore, such sources become unsuitable for imaging spatially separated transverse planes along the propagation direction.

Recently, structured fields that are spatially completely coherent, such as Laguerre Gaussian (LG) and Hermite Gaussian (HG) modes have gained attention due to their implications in optical communication protocols [211–220]. The structure in the intensity profile of such fields is used for encoding information in the long-distance free-space optical communication [190, 191, 221]. However, the presence of turbulence introduces random phase fluctuations at different spatial locations in the field, which results in the degradation of the intensity structures of such coherent fields. As a consequence, the retrieval of information encoded in the intensity structures becomes difficult. For this reason, the structures in a spatially perfectly coherent field become unsuitable for optical communication in turbulent environments. On the other hand, it is now known that a spatially partially coherent field is less affected by turbulence [97, 222–225]. Furthermore, theoretical studies have now shown that in the presence of turbulent environments, the structures in the intensity profiles and in the cross-spectral density functions of a spatially partially coherent field degrade less in comparison to the intensity structures of a spatially perfectly coherent field [226–230]. This implies that the structural robustness of the intensity profiles and the cross-spectral density functions of a spatially partially coherent field could be utilized towards optical communication even in the presence of a turbulent environment. To the best of our knowledge, no experimental demonstration of structural robustness of the cross-spectral density function of such fields in turbulence has been reported so far.

In this chapter, we overcome the above issues in imaging and optical communication through random media by adequately controlling the spatial coherence of the field. First, we address the imaging of spatially separated transverse planes through scattering environments by engineering the propagation of spatial coherence of the illuminating source. We report a proof-of-principle experimental demonstration of imaging different transverse planes with equal contrast over a distance of 40 cm along the propagation direction. This is achieved using an earlier demonstrated source (in the previous chapter 2) in which the spatial coherence is controlled in a manner that the spatial coherence function remains propagation-invariant [128]. Next, we demonstrate a source in which the propagation of spatial coherence is controlled to yield the minimum-possible spatial coherence length at the plane of the object to be imaged. Using such a partially coherent source, we demonstrate imaging different transverse planes along the propagation direction with the maximum possible contrast.

We then generate spatially partially coherent fields with custom-designed structure in cross-spectral density function and demonstrate its structural robustness in turbulence to overcome the difficulties in performing optical communication through turbulence. Simulating a planar turbulence with the help of an SLM, we show that for a given turbulence strength, the structural robustness of a spatially partially coherent field increases as the spatial coherence length of the field decreases.

The chapter has been adopted veritably from Ref. [231, 232], and the contents are organized in the following manner. Section 5.2 presents how to achieve enhanced imaging in scattering environments by controlling the propagation of spatial coherence of the illuminating field. In section 5.2.1, we work out a formalism for controlling the propagation of spatial coherence for a generic spatially partially coherent source. In section 5.2.2, we model our earlier demonstrated spatially partially coherent source with propagation-invariant spatial coherence using the above worked out formalism of propagation of coherence. In section 5.2.3, we model a spatially partially coherent source, whose spatial coherence can be controlled in a manner to yield the minimum possible coherence length at a given transverse plane. Section 5.2.4 presents the details of our experiment. In section. 5.2.5- 5.2.6, we demonstrate enhanced imaging of different transverse plane by using two sources mentioned in sections 5.2.2 and 5.2.3. Section 5.3 demonstrates the robustness of structured fields having partial spatial coherence and outline its implications in free-space communication through turbulence. In section 5.3.1, we describe the propagation of our structured spatially partially coherent field. Section 5.3.2 describes our experimental setup. In section 5.3.3- 5.3.4, we present the experimental results and section 5.3.5 discusses the implication of structured spatially partially coherent fields in optical communication. In section 5.4, we summarize the chapter.

## 5.2 Enhanced imaging through controlling propagation of spatial coherence

### 5.2.1 Theory: controlling the propagation of spatial coherence

(a) Partially Coherent Source

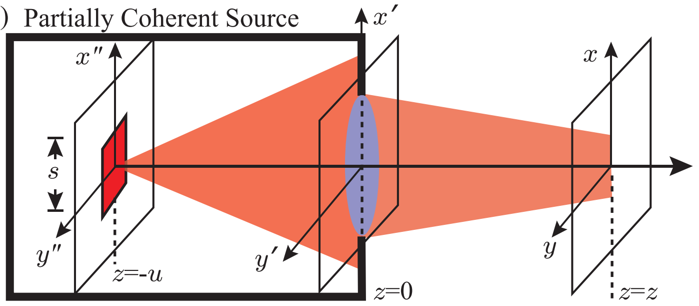

(b) PIC Source

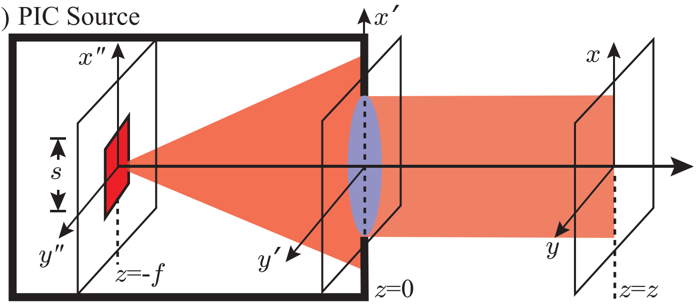

(c) MPC Source

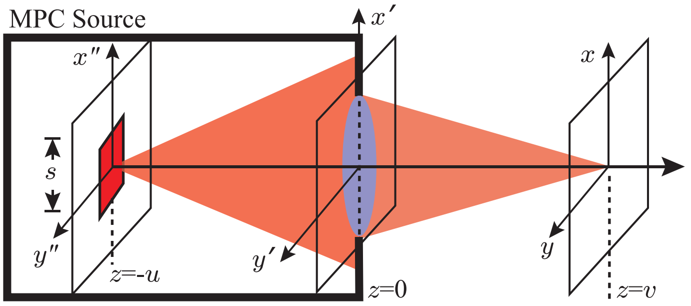

FIGURE 5.1: Schematic illustration of (a) a sptially partially coherent source, (b) a propagation-invariant coherence (PIC) source, and (c) a minimum-possible coherence (MPC) source.

Figure 5.1(a) shows a generic spatially partially coherence source, in which a planar monochromatic spatially completely incoherent source is kept at a distance $u$ behind a lens located at $z = 0$. We represent the transverse spatial location at $z = -u$ by $\boldsymbol{\rho}'' \equiv (x'', y'')$ and that at $z = 0$ and $z = z$ by $\boldsymbol{\rho}' \equiv (x', y')$ and $\boldsymbol{\rho} \equiv (x, y)$, respectively. The primary incoherent source along with the lens constitutes our spatially partially coherent source. Since our primary source is spatially completely incoherent, the cross-spectral density of the field at $z = -u$ is given by

$$W(\boldsymbol{\rho}_1'', \boldsymbol{\rho}_2''; z = -u) = N I_s(\boldsymbol{\rho}_1''; z = -u)\delta(\boldsymbol{\rho}_1'' - \boldsymbol{\rho}_2''), \tag{5.1}$$

where $I_s(\boldsymbol{\rho}_1'', z = -u)$ is the intensity of the primary source at $z = -u$ and is given by $I_s(\boldsymbol{\rho}''; z = -u) = A$, if $-s/2 < x'' < s/2$ and $-s/2 < y'' < s/2$, else 0 with $A$ being a constant. $N = \frac{\lambda_0^2}{\pi}$ (see Ref [20], section 5.5.4), where $\lambda_0$ is the central wavelength. Following section 1.3 of chapter 1, we write the cross-spectral density function $W(\boldsymbol{\rho}_1, \boldsymbol{\rho}_2; z)$ of the field at $z$ in terms of the cross-spectral density function $W(\boldsymbol{\rho_1'}, \boldsymbol{\rho_2'}; z = 0)$ of the field at $z = 0$ right after the converging lens as

$$W(\boldsymbol{\rho}_1, \boldsymbol{\rho}_2; z) = \frac{1}{(\lambda_0 z)^2} e^{\frac{ik_0}{2z}(\rho_2^2 - \rho_1^2)} \iint W(\boldsymbol{\rho_1'}, \boldsymbol{\rho_2'}; z = 0) e^{\frac{ik_0}{2z}(\rho_2'^2 - \rho_1'^2)} e^{-\frac{ik_0}{z}(\boldsymbol{\rho_2} \cdot \boldsymbol{\rho_2'} - \boldsymbol{\rho_1} \cdot \boldsymbol{\rho_1'})} d\boldsymbol{\rho_1'} d\boldsymbol{\rho_2'}. \tag{5.2}$$

Here $k_0 = 2\pi/\lambda_0$ with $\lambda_0$ being the central wavelength and $\rho_1 = |\boldsymbol{\rho}_1|$, $\rho_2 = |\boldsymbol{\rho}_2|$, etc. The cross spectral density $W(\boldsymbol{\rho_1'}, \boldsymbol{\rho_2'}; z = 0)$ after the lens can be calculated by propagating the cross-spectral density at $z = -u$ until $z = 0$ before the lens and then propagating it through the lens. This way we obtain

$$\begin{aligned} W(\boldsymbol{\rho_1'}, \boldsymbol{\rho_2'}; z = 0) = \frac{1}{(\lambda_0 u)^2} e^{\frac{ik_0}{2u}(\rho_2'^2 - \rho_1'^2)} T^*(\boldsymbol{\rho_1'}) T(\boldsymbol{\rho_2'}) \iint W(\boldsymbol{\rho_1''}, \boldsymbol{\rho_2''}; z = -u) e^{\frac{ik_0}{2u}(\rho_2''^2 - \rho_1''^2)} \\ \times e^{-\frac{ik_0}{u}(\boldsymbol{\rho_2'} \cdot \boldsymbol{\rho_2''} - \boldsymbol{\rho_1'} \cdot \boldsymbol{\rho_1''})} d\boldsymbol{\rho_1''} d\boldsymbol{\rho_2''}. \end{aligned} \tag{5.3}$$

Here $T(\boldsymbol{\rho})$ is the amplitude transmittance function of the lens and is given by $T(\boldsymbol{\rho}) = \exp(-ik_0\rho^2/2f)$, where $f$ is the focal length of the lens. Substituting the expressions for the amplitude transmission function and also that of the cross-spectral density function $W(\boldsymbol{\rho_1''}, \boldsymbol{\rho_2''}; z = -u)$ of Eq. (5.1) into Eq. (5.3), evaluating the $\boldsymbol{\rho}_2''$ integral, and replacing $\boldsymbol{\rho}_1''$ by $\boldsymbol{\rho}''$, we can write Eq. (5.3) as

$$W(\boldsymbol{\rho_1'}, \boldsymbol{\rho_2'}; z = 0) = \frac{AN}{\lambda_0^2 u^2} e^{\frac{ik_0}{2}(\rho_2'^2 - \rho_1'^2)(\frac{1}{u} - \frac{1}{f})} \int e^{-\frac{ik_0}{u}(\boldsymbol{\rho_2'} - \boldsymbol{\rho_1'}) \cdot \boldsymbol{\rho}''} d\boldsymbol{\rho}''. \tag{5.4}$$

Now, substituting Eq. (5.4) into Eq. (5.2), we obtain the cross-spectral density function $W(\boldsymbol{\rho}_1, \boldsymbol{\rho}_2; z)$ at $z$:

$$W(\boldsymbol{\rho}_1, \boldsymbol{\rho}_2; z) = \frac{AN}{\lambda_0^2 u^2 z^2} e^{\frac{ik_0}{2z}(\rho_2^2 - \rho_1^2)} \iiint e^{-\frac{ik_0}{u}(\boldsymbol{\rho}_2' - \boldsymbol{\rho}_1')\cdot\boldsymbol{\rho}''} e^{-\frac{ik_0}{2\Delta(z)}(\rho_2'^2 - \rho_1'^2)} e^{-\frac{ik_0}{z}(\boldsymbol{\rho}_2\cdot\boldsymbol{\rho}_2' - \boldsymbol{\rho}_1\cdot\boldsymbol{\rho}_1')} \times d\boldsymbol{\rho}'' d\boldsymbol{\rho}_1' d\boldsymbol{\rho}_2', \quad (5.5)$$

where $\frac{1}{\Delta(z)} = \frac{1}{f} - \frac{1}{u} - \frac{1}{z}$. This is the general expression for $W(\boldsymbol{\rho}_1, \boldsymbol{\rho}_2; z)$. We note that the lens is symmetric with respect to $x''$ and $y''$. Thus, $W(\boldsymbol{\rho}_1, \boldsymbol{\rho}_2; z)$ can be written as $W(\boldsymbol{\rho}_1, \boldsymbol{\rho}_2; z) = W(x_1, x_2; z)W(y_1, y_2; z)$. For conceptual clarity, we numerically solve only the $x$-integral which is given by

$$W(x_1, x_2; z) = \frac{\sqrt{AN}}{\lambda_0 u z} e^{\frac{ik_0}{2z}(x_2^2 - x_1^2)} \iint_{-D/2}^{D/2} \int_{-s/2}^{s/2} e^{-\frac{ik_0}{u}(x_2' - x_1')x''} e^{-\frac{ik_0}{2\Delta(z)}(x_2'^2 - x_1'^2)} e^{-\frac{ik_0}{z}(x_2 x_2' - x_1 x_1')} \times dx'' dx_1' dx_2'. \quad (5.6)$$

The integral over $x''$ needs to be evaluated over the source size, that is, from $-s/2$ to $s/2$ while the integrals over $x_1'$ and $x_2'$ need to be evaluated over the size of the lens, which we take to be $D$. We are interested in the cross-spectral density function that is symmetric about the $z$-axis. Thus, by substituting $x_1 = x$ and $x_2 = -x$ and then evaluating the $x''$ integral, we obtain the following expression for the symmetric cross-spectral density function $W(x, -x; z)$ and the corresponding intensity $I(x) = W(x, x; z)$:

$$W(x, -x; z) = \frac{\sqrt{ANs}}{\lambda_0 u z} \iint_{-D/2}^{D/2} \text{sinc}\left\{\frac{k_0 s}{2u}(x_2' - x_1')\right\} e^{-\frac{ik_0}{2\Delta(z)}(x_2'^2 - x_1'^2)} e^{\frac{ik_0}{z}(x_2' + x_1')x} dx_1' dx_2'. \quad (5.7)$$

$$I(x; z) = \frac{\sqrt{ANs}}{\lambda_0 u z} \iint_{-D/2}^{D/2} \text{sinc}\left\{\frac{k_0 s}{2u}(x_2' - x_1')\right\} e^{-\frac{ik_0}{2\Delta(z)}(x_2'^2 - x_1'^2)} e^{-\frac{ik_0}{z}(x_2' - x_1')x} dx_1' dx_2'. \quad (5.8)$$

The degree of coherence function $|\mu(x, -x, z)|$ is given by

$$|\mu(x, -x, z)| = |\mu(2x, z)| = W(x, -x, z)/I(x, z). \quad (5.9)$$

We take the half-width $\sigma_c$ of this function as the transverse spatial coherence length. We

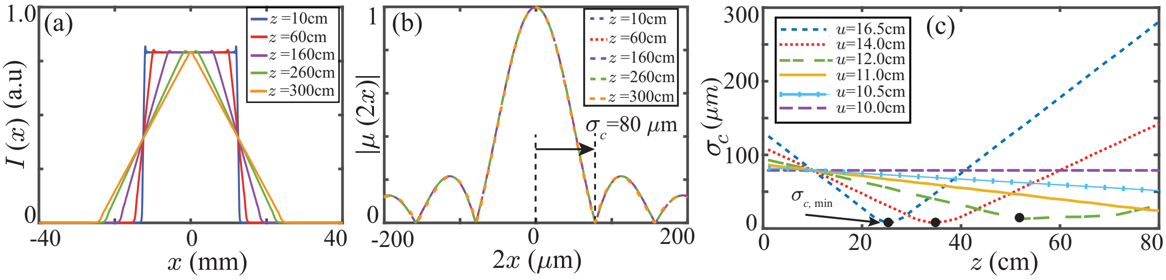

FIGURE 5.2: Plots of (a) intensity $I(x)$ and (b) the degree of coherence $|\mu(2x)|$ of the PIC source for various $z$ values. (c)Plots of transverse spatial coherence length $\sigma_c$ of the MPC source as a function of $z$ for various values of $u$. The minimum $\sigma_{c,\text{min}}$ appears near $z = v$, where $v$ is the image plane of the primary incoherent source.

next evaluate $\mu(2x; z)$ and $I(x; z)$ for two special cases.

### 5.2.2 Propagation-Invariant Coherence (PIC) source $(u = f)$

We consider the situation in which $u = f$, that is, when the primary incoherent source is kept at the back focal plane of the lens. Figure 5.1(b) shows the configuration of the source in this case. We have already shown in chapter 2 that when the aperture size of the lens is infinite, the degree of coherence function $|\mu(2x; z)|$ and the intensity $I(x; z)$ become independent of $z$. Even when the aperture size is finite, the degree of coherence function remains $z$-independent up to the distance given by $z_{\text{max}} = Df/s$. Therefore, such sources are referred to as the propagation-invariant coherence (PIC) source. We numerically evaluate Eqs. (5.8) and (5.9) for $D = 2.5$ cm, $f = 10$ cm $s = 0.8$ mm, and plot $I(x; z)$ and $|\mu(2x, z)|$ in Fig. 5.2(a) and Fig. 5.2(b), respectively, for various values of $z$. We find that while the intensity profile of the source starts to broaden as a function of $z$, the degree of coherence function remains independent of $z$, that is, it remains propagation invariant up to 300 cm. Taking the distance to the first zero of $|\mu(2x; z)|$ function as $\sigma_c$, we find it to be about 80 $\mu$m.

### 5.2.3 Minimum-Possible Coherence (MPC) source $(u > f)$

Next, we consider the situation in which $u > f$ (see Figure 5.1(c)). Using Eq. (5.9), we numerically evaluate $|\mu(2x; z)|$ as a function of $x$, and taking the distance to its first zero to be $\sigma_c$, we calculate and plot $\sigma_c$ as a function of $z$ for various values of $u$ (see Fig. 5.2). For a given $u$, $\sigma_c$ decreases with $z$ and reaches its minimum possible value $\sigma_{c,\mathrm{min}}$ near $z = v$, where $v$ is the image distance of our primary source. As $u$ is decreased, $v$ increases and therefore the $z$ value at which $\sigma_{c,\mathrm{min}}$ appears shifts to the right with $\sigma_{c,\mathrm{min}}$ remaining almost constant. Thus, we refer to this source as minimum-possible coherence (MPC) source. It can be used for imaging two-dimensional objects kept at $z = v$ with maximum possible imaging contrast. Furthermore, within the $z$-range over which $\sigma_{c,\mathrm{min}}$ remains almost constant, a two-dimensional object could be placed at any $z$ and be imaged with maximum possible contrast by adjusting $u$ in a way that $\sigma_{c,\mathrm{min}}$ appears at the given $z$. For $D = 2.5$ cm, $f = 10$ cm $s = 0.8$ mm, $\sigma_{c,\mathrm{min}}$ changes from 6.5 $\mu$m to about 8.5 $\mu$m from $z = 25$ cm to $z = 35$ cm. We note that when $u$ approaches $f$, the MPC source becomes the PIC source.

### 5.2.4 Experimental setup

We next present our experimental results demonstrating how PIC and MPC sources can be used for imaging different transverse planes with enhanced imaging contrast through scattering media. In our experiments, we use lab-synthesized ground glass plates and stack together varying number of them in order to get scattering media of different scattering strengths. We characterize the strength of thus-constructed scattering media in the following manner. We make a laser beam pass through the scattering medium whose strength we need to measure. We record the intensity of a small central portion of the laser beam on a $50 \times 50$-pixel area of the CCD camera, kept at a distance of 30 cm from the scattering medium. The measured intensity in the presence and in the absence of the scattering medium is called $I$ and $I_0$, respectively. For our scattering media, the material absorption is negligible; so any drop in the recorded laser intensity in the presence of a scattering medium is solely due to scattering. Therefore, we take the ratio $I_0/I$ of the two intensities as the scattering strength of the medium and write it as $\alpha = \frac{I_0}{I}$. The quantity can be shown to be related to the scattering coefficient $\mu_s$ as $\alpha = e^{\mu_s d}$, where $d$ is the thickness of the scattering medium [233]. We note that in our experiments, we use scattering media of varying scattering coefficient $\mu_s$ and thickness $d$. Therefore, for characterizing the strength of our scattering media, $\alpha = e^{\mu_s d}$ is a more pertinent quantity instead of $\mu_s$. The larger values represent increased scattering strength, with $\alpha = 1$ representing no scattering.

### 5.2.5 Imaging with Propagation-Invariant Coherence (PIC) source

First, we present our experimental results of imaging through scattering medium in transmitting configuration with a PIC source and compare its performance with that of a spatially perfectly coherent source and a conventional partially coherent source wherein the transverse spatial coherence length increases with propagation. Figure 5.3(a) shows the schematic diagram of the experimental setup. A source kept at $z = 0$ illuminates a transmission object kept at $z = z$. We use a 632-nm, 5-mW HeNe laser with a Gaussian beam profile as a spatially coherent source, while we use an LED for the conventional source. We consider the same LED as the primary source in the configuration of the PIC source, as shown in Figs. 5.1(a). In the experiment, we use $D = 2.5$ cm, $s = 0.8$ mm and $f = 10$ cm, and $\lambda_0 = 632$ nm. As a result, while the transverse spatial coherence length $\sigma_c = 80$ $\mu$m of the PIC source stays $z$-invariant for over 300 cm, the transverse spatial coherence length of the conventional source increases with $z$ as $\sigma_c = \frac{\lambda_0 z}{s}$. After transmitting through the object, the light from the source first encounters a scattering medium before getting imaged at the CCD camera. The CCD camera has 1024 × 1280 pixels with the size of each pixel being 5 $\mu$m, the distance $d$ between the scatterer and the object is 3.5 cm, and the focal length $f$ of the imaging lens is 5 cm, which images the object with a magnification of about 3. In order to avoid the saturation of the camera, we use a neutral density (ND) filter of optical density (OD) equal to 1, placed immediately before the camera. In order to mimic objects at different transverse planes along the direction of propagation, we keep

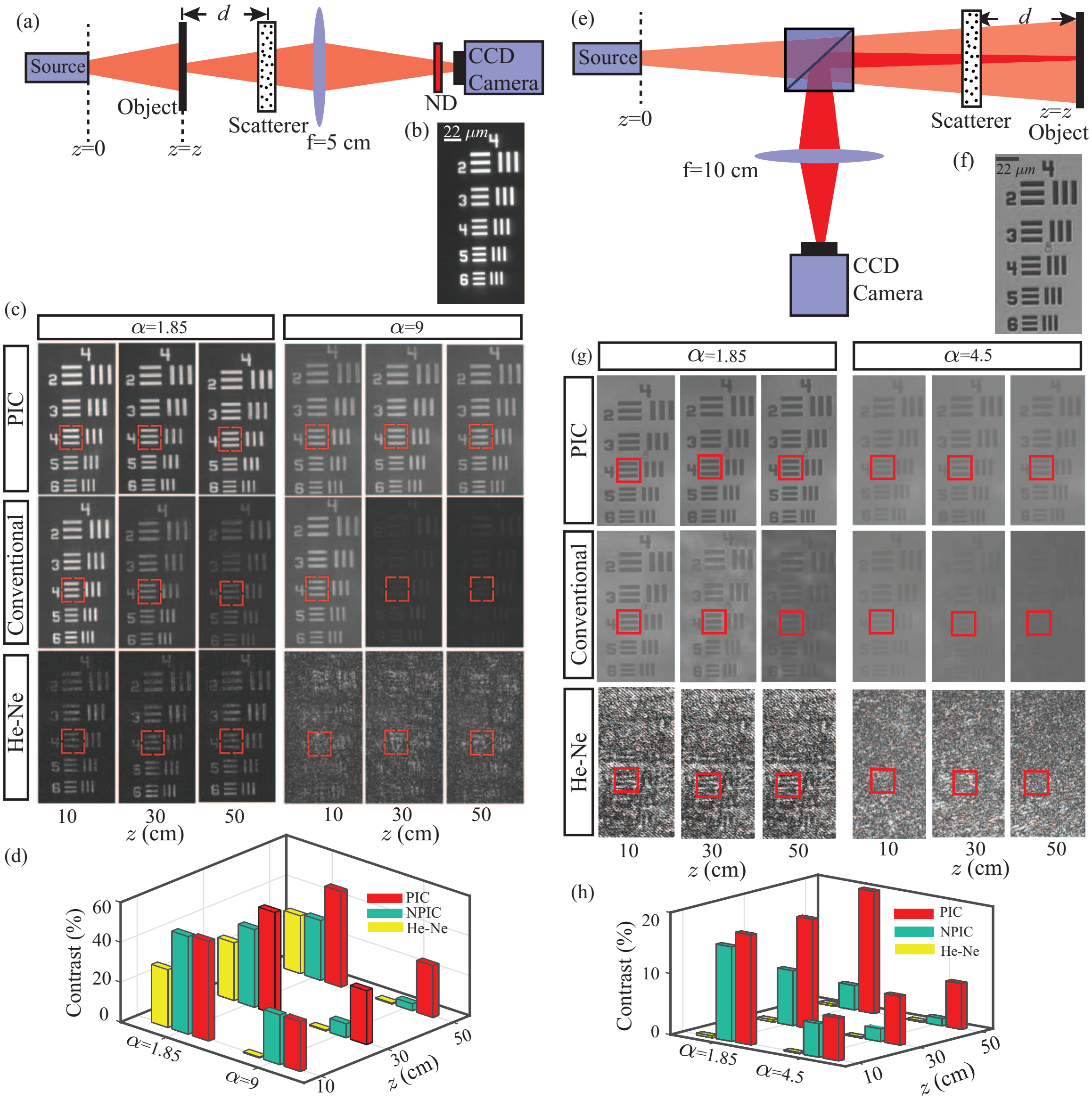

FIGURE 5.3: (a) Schematic of the setup for imaging in transmitting configuration. (b) Image of the object in the absence of scattering. (c) Images of the object and (d) imaging contrast obtained with the three different sources at different $z$ and $\alpha$ values. (e) Schematic of the setup for imaging in reflecting configuration. (f) Image of the object in the absence of scattering. (g) Images of the object in reflecting configuration and (h) Imaging contrast obtained with the three different sources at different $z$ and $\alpha$ values.

our source at various longitudinal distances from the object. This way, the imaging condition and the distance between the object and the scattering medium remain constant when imaging various transverse planes with different sources. Figure 5.3(b) shows the image of the object in the absence of any scattering. Figure 5.3(c) shows images of the object obtained with the three sources at three different $z$ values and with two different scattering strengths. In order to get a quantitative estimate of the image quality, we use image contrast defined as $C = (I_{\max} - I_{\min})/(I_{\max} + I_{\min})$, where $I_{\max}$ and $I_{\min}$ are the maximum and minimum intensity respectively. For calculating the contrast, we first select an area in the image, as shown by the dotted square, and then define $I_{\max}$ and $I_{\min}$ as the average pixel-intensities in the bright and dark regions within the square, respectively. We calculate the contrast of each image shown in Fig. 5.3(c) and plot it as a function of $z$ and for the three sources in Fig. 5.3(d).

The results in Fig. 5.3(c) and Fig. 5.3(d) demonstrate how a PIC source performs imaging of different transverse planes with almost equal contrast in the presence of scattering. We find that the measured image contrast at $z = 10$ cm is the same with both PIC and conventional sources, and for the two $\alpha$ values, the contrast is about 50% and 25%, respectively. As $z$ is increased to 50 cm, the contrast with the PIC source remains invariant at 50% and 25% while the contrast with the conventional source drops down to about 30% and 4%, respectively, for the two $\alpha$ values. This is because $\sigma_c$ of both the sources are very similar at $z = 10$ cm. However, for $z > 10$ cm, $\sigma_c$ of the PIC source remains invariant while that of the conventional source increases, causing the imaging contrast to decrease. As expected, the speckle effect is more prominent for the spatially coherent source and increases with increasing scattering strengths. We note that although PIC-like sources have been earlier used in microscopy [24], here we demonstrated their usefulness in enhancing the imaging contrast at various transverse planes through a scattering medium.

Although imaging in transmitting configuration is important, many real-life scenarios require imaging in reflecting configuration, where both the source and the detector are on the same side of the object. So, next, we demonstrate the imaging capabilities of our PIC source in a reflecting configuration. Figure 5.3(e) shows the schematic diagram of the experimental setup. A source kept at $z = 0$ illuminates the object at $z = z$. The light from the source first passes through a beam splitter and then after transmitting through the scatterer illuminates the object. The reflected light from the object passes through the scatterer, gets reflected by the beam splitter, and is then imaged at the CCD camera. The CCD camera has 1024 × 1280 pixels with the size of each pixel being 5 $\mu$m, the distance $d$ between the scatterer and the object is 4 cm, the imaging lens of focal length $f = 10$ cm images the object with a magnification of about 3. As earlier, in order to mimic the object at different transverse planes, we keep our source at various longitudinal distances from the object. Figure 5.3(f) shows the image of the object in the absence of any scattering. We use the same object as in the transmitting configuration. However, since it is a binary object with only transparent and opaque regions, the image of the object in 5.3(f) has reversed bright and dark regions as compared to the image in 5.2(b). Figure 5.3(g) shows the images of the object obtained with the three sources at three different $z$ values and with two different scattering strengths. We calculate the contrast of each image shown in 5.3(g) and plot it in 5.3(h). We find that in general, the results of Figs. 5.3(g-h) obtained in the reflecting configuration are qualitatively similar to those obtained in the transmitting imaging configuration. However, the contrast of the images in the reflecting configuration is lower than that in the transmitting configuration. This is simply because the light has to go through the scatterer medium twice in the reflecting configuration.

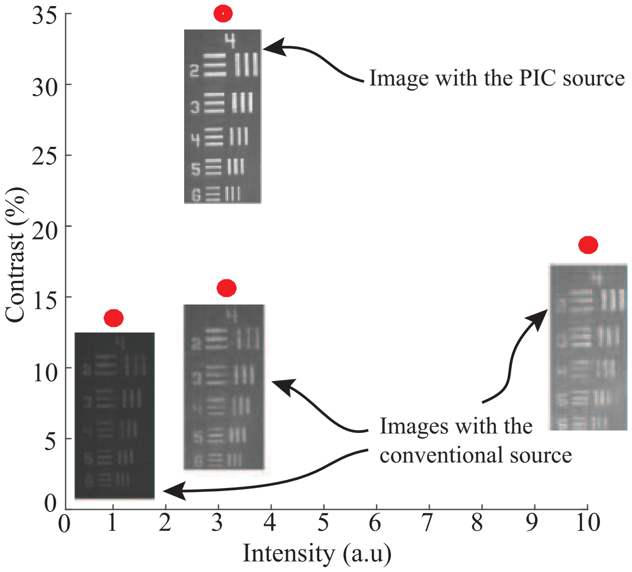

FIGURE 5.4: The image and image contrast obtained with the PIC source and those with the conventional source at varying intensities. All the images were obtained at $z = 30$ cm and with the scattering strength $\alpha = 4.5$.

In both the reflecting and transmitting imaging configurations, we find that, as $z$ increases for a given scattering strength, the image contrast and the illumination intensity of the images obtained with the conventional source decreases. So, a question that can arise is whether the decrease in the image contrast with increasing $z$ is due to the increase in the spatial coherence length of the source or due to the decrease in the illumination intensity. We address this question in the transmitting configuration at $z = 30$ cm and $\alpha = 4.5$. We record images at increased intensities of the conventional source and compare them with the image obtained with the PIC source under same experimental conditions. Figure 5.4 shows one image obtained with the PIC source and the three images obtained with the conventional source at various illumination intensities. Along with the images, Fig. 5.4 also shows the corresponding image contrasts. The image obtained with the PIC source has an image contrast equal to 35%. The other three images of Fig. 5.4 are obtained with the conventional source at various intensities. The first of these images is obtained under the same experimental conditions as those in the PIC source case, with an ND filter of OD equal to 1. The illumination intensity in this case is about three times lower compared to that in the case of the PIC source. The second image is obtained with an ND filter of OD equal to 0.5 such that the illumination intensity is very close to that in the case of the PIC source. The third image is obtained with no ND filter such that the illumination intensity is increased by a factor of more than three compared to that in the case of the PIC source. We find that the image contrast with the conventional source is less than 15%, compared to the 35% contrast obtained with the PIC source under the same experimental conditions. When the intensity of the conventional source is increased such that the illumination becomes comparable to that of the PIC source, the image contrast increases to only 15.6%. A subsequent increase in the intensity does not improve the image contrast much further. This confirms that the decrease in the image contrast with the conventional source is indeed due to the increase in the spatial coherence length of the source and that it cannot be compensated by simply increasing the illumination intensity. Furthermore, we note that the incremental increase in the contrast as a function of the illumination intensity is due to the increased signal-to-noise ratio and that it saturates very quickly.

### 5.2.6 Imaging with Minimum-Possible Coherence (MPC) source

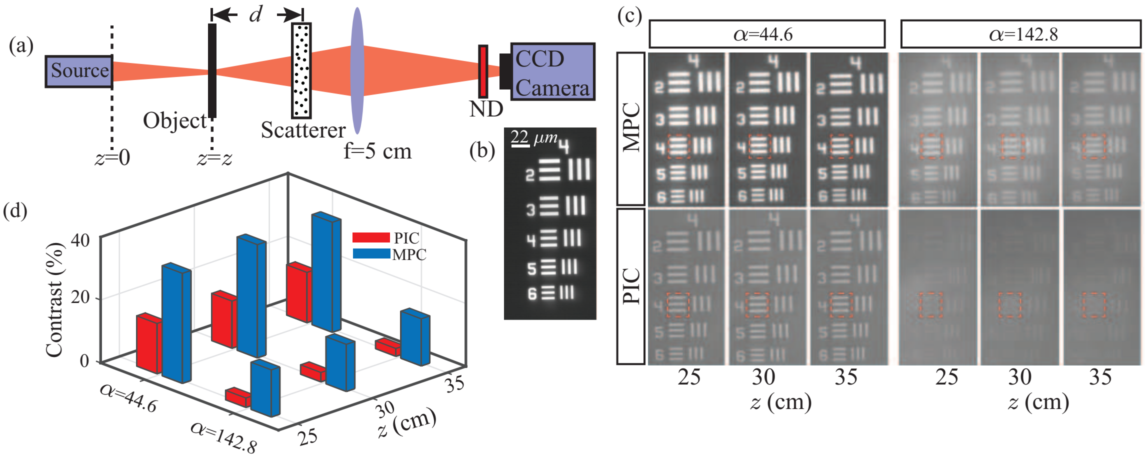

FIGURE 5.5: (a) Schematic of the setup for imaging in transmitting configuration with an MPC source. (b) Image of the object in the absence of scattering. (c) Images of the object and (d) Imaging contrast obtained with MPC and PIC sources at different $z$ and $\alpha$ values.

Figure 5.5 (a) shows the schematic experimental setup for imaging with an MPC source. We image the object kept at three different values of $z$, namely, $z = 25$ cm, $z = 30$ cm and $z = 35$ cm. For each $z$, we choose $u$ such that the primary incoherent source gets imaged onto a plane at $z$ and the field achieves its $\sigma_{c,\text{min}}$ at $z$. The rest of our experimental setup is the same as that in the case of the transmission configuration of Fig.5.3(a). Next, in order to demonstrate enhanced imaging capabilities of our MPC source, we compare its performance with that of at PIC source under the same experimental conditions. Figure 5.5(b) shows the image of the object in the absence of any scattering. Figure 5.5(c) shows images obtained with the two sources for three different values of $z$ and two different values of $\alpha$ . Figure 5.5(d) shows the imaging contrast as a function of $z$ and $\alpha$. These results demonstrate that the MPC source images different transverse planes with maximum possible imaging contrast. Furthermore, in the presence of a scattering medium, the MPC source provides much better imaging contrast compared not only to the conventional or coherent sources but also to the PIC source. Nevertheless, for smaller scattering strengths, a PIC source would still be preferable over an MPC source, since as opposed to the MPC source, which requires choosing a suitable $u$ for every $z$, a PIC source works with the same configuration at every $z$.

## 5.3 Robustness of structured spatially partially coherent fields in turbulence

### 5.3.1 Theory: propagation and detection of structured spatially partially coherent fields through turbulence

Figure 5.6 illustrates how our structured partially coherent field propagates through a planar simulated turbulence and gets detected. We use the technique described in chapter 2 for generating spatially partially coherent fields with structures in their cross-spectral density functions. A planar, monochromatic, spatially completely incoherent primary source is kept at the back focal plane $z = -F$ of a lens located at $z = 0$. The central wavelength of the source is $\lambda_0 = 2\pi/k_0$, where $k_0$ is the magnitude of the wavevector. The combination of the primary incoherent source along with the lens constitutes our structured spatially partially coherent source. The structured partially coherent field propagates through a planar simulated turbulence kept at $z = z'$ and then gets observed by the detection system consisting of a converging lens of focal length $f$ kept at $z = z_d$ and a camera kept at $z = z_f = z_d + f$. The detection system essentially measures the cross-spectral density function of the field at $z = z_d$. We represent the transverse position coordinates at $z = -F$, $z = z'$, $z = z_d$, and $z = z_f$ by $\boldsymbol{\rho}'' \equiv (x'', y'')$, $\boldsymbol{\rho}' \equiv (x', y')$,

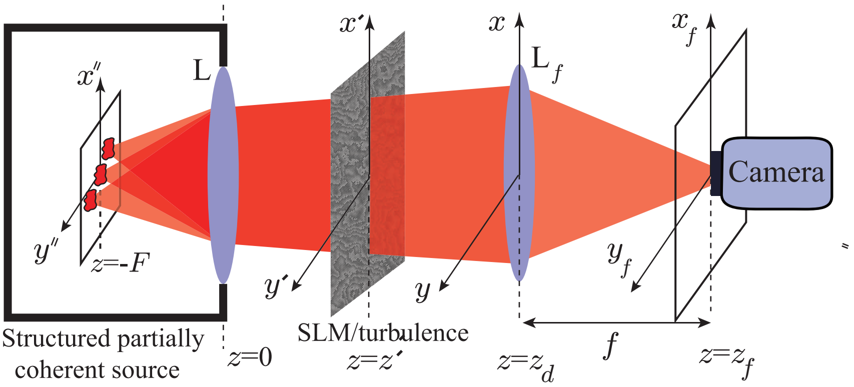

FIGURE 5.6: Schematic of the experimental setup illustrating propagation of our structured partially coherent source through a turbulent medium. (b) Simulated intensity of the primary source. (c) Simulated cross-spectral density $W_s(\Delta\rho; z = z_d)$ of the source at $z = z_d$

$\boldsymbol{\rho} \equiv (x, y)$, and $\boldsymbol{\rho}_f \equiv (x_f, y_f)$, respectively. The intensity of the primary source at $z = -F$ is given by $I(\boldsymbol{\rho}'', z = -F)$. Therefore, the cross-spectral density function $W_s(\rho'_1, \rho'_2; z = z')$ of our partially coherent field at $z = z'$ can be shown to be [128, 231]

$$W_s(\boldsymbol{\rho}'_1, \boldsymbol{\rho}'_2; z = z') \rightarrow W_s(\Delta\rho'; z = z') = \tfrac{A}{F^2} \iint I(\boldsymbol{\rho}''; z = -F) e^{-i\frac{k_0}{F}\boldsymbol{\rho}''\cdot\Delta\boldsymbol{\rho}'} d\boldsymbol{\rho}'', \tag{5.10}$$

where $\Delta\rho' = |\boldsymbol{\rho}'_2 - \boldsymbol{\rho}'_1|$. We note that the cross-spectral density function $W_s(\boldsymbol{\rho}'_1, \boldsymbol{\rho}'_2; z = z')$ of our source depends on the transverse coordinates only through their difference $\Delta\rho'$. Therefore, we write it as $W_s(\Delta\rho'; z = z')$. Such sources are referred to as statistical homogeneous source [2] or even spatially stationary source [128]. The cross-spectral density $W(\boldsymbol{\rho}'_1, \boldsymbol{\rho}'_2; z = z')$ at $z = z'$ right after the turbulence plane is given by $W(\boldsymbol{\rho}'_1, \boldsymbol{\rho}'_2; z = z') = W_s(\Delta\rho'; z = z') W_t(\boldsymbol{\rho}'_1, \boldsymbol{\rho}'_2)$, where $W_t(\boldsymbol{\rho}'_1, \boldsymbol{\rho}'_2)$ is the cross-spectral density induced due to the turbulence. According to the Kolmogorov model,

$$W_t(\boldsymbol{\rho}'_1, \boldsymbol{\rho}'_2) = e^{-3.44\left(\frac{\Delta\rho'}{r_0}\right)^{\frac{5}{3}}}. \tag{5.11}$$

The quantity $r_0$ is called Fried's coherence diameter [234], and it quantifies the strength of turbulence. The value of $r_0$ ranges from 0 to $\infty$, with limit $r_0 \rightarrow 0$ implying infinite turbulence strength and limit $r_0 \rightarrow \infty$ implying no turbulence. In order to show the structural robustness of our partially coherent field in turbulence, we obtain the cross-spectral density function of the field after it has propagated up to $z = z_d$. Using Eqs. (5.10) and (5.11) and the propagation Eq. (1.21) (section 1.3 of chapter 1), we find the cross spectral density function $W(\boldsymbol{\rho}_1, \boldsymbol{\rho}_2; z = z_d) \rightarrow W(\Delta\rho; z = z_d)$ of the field at $z = z_d$ to be

$$W(\Delta\rho; z = z_d) = e^{-3.44\left(\frac{\Delta\rho}{r_0}\right)^{\frac{5}{3}}} W_s(\Delta\rho; z = z_d), \tag{5.12}$$

where

$$W_s(\Delta\rho; z = z_d) = \frac{A}{F^2} \iint I(\boldsymbol{\rho}''; z = -F) e^{-i\frac{k_0}{F}\boldsymbol{\rho}''\cdot\Delta\boldsymbol{\rho}} d\boldsymbol{\rho}'' \tag{5.13}$$

is the cross-spectral density function of the field at $z = z_d$ in the absence of turbulence, and $\Delta\rho = |\boldsymbol{\rho}_2 - \boldsymbol{\rho}_1|$. We note that the cross-spectral density functions $W(\Delta\rho; z = z_d)$ and $W_s(\Delta\rho; z = z_d)$ depend on the transverse position coordinates only through their difference $\Delta\rho$ and thus that the field at $z = z_d$ remains spatially-stationary with or without the turbulence. Furthermore, we note that $W_s(\Delta\rho; z = z_d)$ remains propagation-invariant [128] and therefore it has the same functional form as that of the cross-spectral density function $W_s(\Delta\rho; z = z')$ at $z = z'$, as given in Eq. (5.10).

We note that since $W(\Delta\rho; z = z_d)$ is spatially stationary, it can be expressed in terms of the intensity $I(\rho_f; z = z_f)$ at $z = z_f$. In order to show this we first write the cross-spectral density $W_l(\boldsymbol{\rho_1}, \boldsymbol{\rho_2}; z_d)$ at $z = z_d$ right after the lens $L_f$ as $W_l(\boldsymbol{\rho_1}, \boldsymbol{\rho_2}; z = z_d) = W(\Delta\rho; z = z_d) T^*(\boldsymbol{\rho_1}) T(\boldsymbol{\rho_2})$, where $T(\boldsymbol{\rho}) = e^{i\frac{k_0}{2f}\rho^2}$ is the transmission function of lens $L_f$ [235]. Next, using the propagation Eq. (1.21), we propagate the field from $z = z_d$ to $z = z_f$ and find the intensity $I(\boldsymbol{\rho_f}; z = z_f)$ at $z = z_f$ plane to be

$$I(\boldsymbol{\rho_f}; z = z_f) = W(\boldsymbol{\rho_f}, \boldsymbol{\rho_f}; z = z_f) = \iint W(\Delta\rho; z = z_d) e^{i\frac{k_0}{f}\boldsymbol{\rho_f}\cdot\Delta\boldsymbol{\rho}} d\Delta\boldsymbol{\rho}. \tag{5.14}$$

We Fourier-invert the above equation and write it as

$$W(\Delta\rho; z = z_d) = \iint I(\boldsymbol{\rho_f}; z = z_f) e^{-i\frac{k_0}{f}\boldsymbol{\rho_f}\cdot\Delta\boldsymbol{\rho}} d\boldsymbol{\rho_f}. \tag{5.15}$$

Thus we see that by measuring the intensity $I(\rho_f; z = z_f)$ at the focal plane $z = z_f$, one obtains the cross-spectral density function $W(\Delta\rho, z = z_d)$ at $z = z_d$.

### 5.3.2 Experimental Setup

We next present our experimental demonstration of structural robustness of spatially partially coherent fields in the presence of turbulent media. Figure 5.6 shows the schematic of the experimental setup, where the structured partially coherent source is kept at $z = 0$. We use an SLM for simulating planar turbulence at $z = z'$ [236] and an electron multiplied charged coupled device (EMCCD) camera for measuring the intensity at $z = z_f$ plane. From Eq. (5.13), we have that the cross-spectral density function $W_s(\Delta\rho; z = z_d)$ at

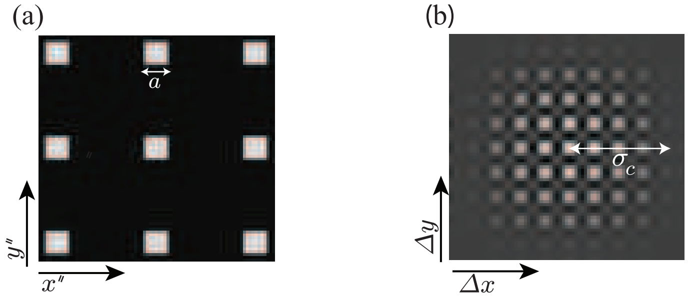

FIGURE 5.7: (a) Simulated intensity of the primary source. (b) Simulated cross-spectral density $W_s(\Delta\rho; z = z_d)$ of the source at $z = z_d$

$z = z_d$ is the Fourier transform of the intensity $I(\boldsymbol{\rho}''; z = -F)$ of the primary incoherent source. Therefore, in order to generate spatially partially coherent field with structured cross-spectral density function, we use a light emitting diode (LED) array as our primary source. The array consists of 9 LEDs arranged in a 3 × 3 grid. The size of the individual LED is $a = 0.58$ mm. Figure 5.7(a) shows the simulated intensity $I(\boldsymbol{\rho}''; z = -F)$ of our primary incoherent source at $z = -F$ while Fig. 5.7(b) shows the corresponding cross spectral density function $W_s(\Delta\rho; z = z_d)$ at $z = z_d$. As the Fig. 5.7(a) shows that $I(\boldsymbol{\rho}''; z = -F)$ is a symmetric function, so we expect that the cross spectral density function $W_s(\Delta\rho; z = z_d)$ of is a real function. We note that the oscillatory features of the cross-spectral density function in Fig. 5.7(b) decays over a length scale $\sigma_c$ in the transverse direction. Using Eq. (5.13), it can be shown that $\sigma_c$ is decided by the transverse size $a$ of the individual LEDs at $z = -F$ and that it can be written as $\sigma_c = \lambda_0 F/a$ (see Ref. [2], section 4.4.4). We take $\sigma_c$ as the spatial coherence length of the field. This definition of the spatial coherence length is consistent with the definition of temporal coherence length for a multi-mode continuous wave (CW) laser with structured temporal cross-spectral density function [237]. By using lenses of focal lengths $F = 30$ cm, 50 cm, and 75 cm in the source configuration, we generate structured spatially partially coherent fields with $\sigma_c = 0.33$ mm, 0.55 mm, and 0.82 mm, respectively. In order to simulate turbulence using an SLM kept at $z = z'$, we display around 200 random phase patterns on the SLM with Kolmogorov statistics in a sequential manner at a frame rate of 30 Hz. We set an exposure

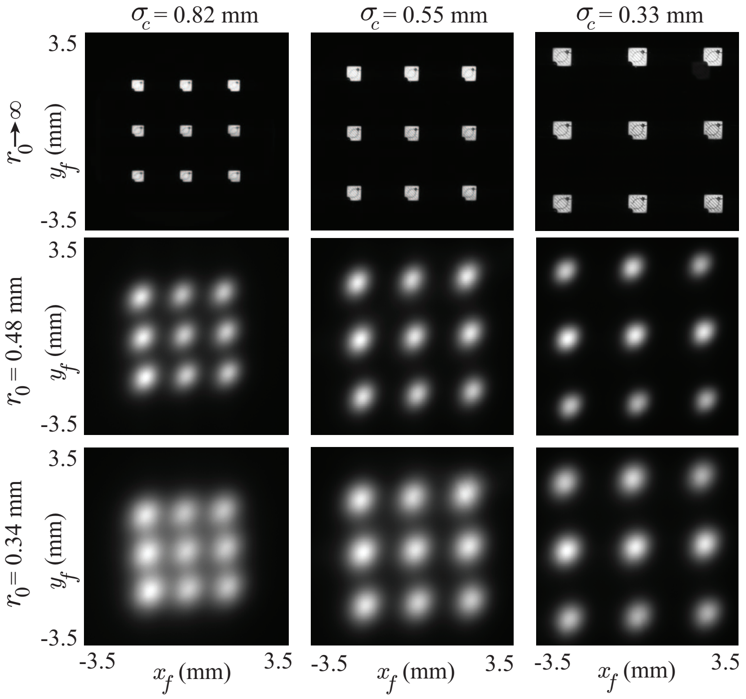

FIGURE 5.8: Experimentally measured $I(\boldsymbol{\rho_f}; z = z_f)$ with different transverse spatial coherence lengths at various turbulence strengths.

time of 7 seconds such that the EMCCD camera records the entire ensemble of fields corresponding to the 200 phase patterns. In this way, we generate Kolmogorov turbulence. We perform experiments at three different turbulence strengths $r_0 \rightarrow \infty$, $r_0 = 0.48$ mm, and $r_0 = 0.34$ mm. In our experiments, we use $f = 30$ cm, $z' = 20$ cm, $z_d = 50$ cm, and $z_f = z_d + f = 80$ cm.

### 5.3.3 Transverse intensity measurements

Figure 5.8 shows the experimentally measured intensity $I(\boldsymbol{\rho_f}; z = z_f)$ at $z = z_f$ for different spatial coherence lengths $\sigma_c$ at various turbulence strengths $r_0$. With no turbulence, that is, at $r_0 \rightarrow \infty$, the intensity $I(\boldsymbol{\rho}_f; z = z_f)$ at different $\sigma_c$ is the same as the intensity $I(\boldsymbol{\rho}''; z = -F)$ of the primary source shown in Fig. 5.7(a), apart from a change in scale. In the presence of turbulence, we find that as the spatial coherence length $\sigma_c$ of the field decreases from 0.82 mm to 0.33 mm, the degradation in the structural features of the intensity $I(\boldsymbol{\rho}_f; z = z_f)$ reduces. The small tilt in the measured intensity of Fig. 5.8 is attributed to the imperfections in the alignment of the experimental setup.

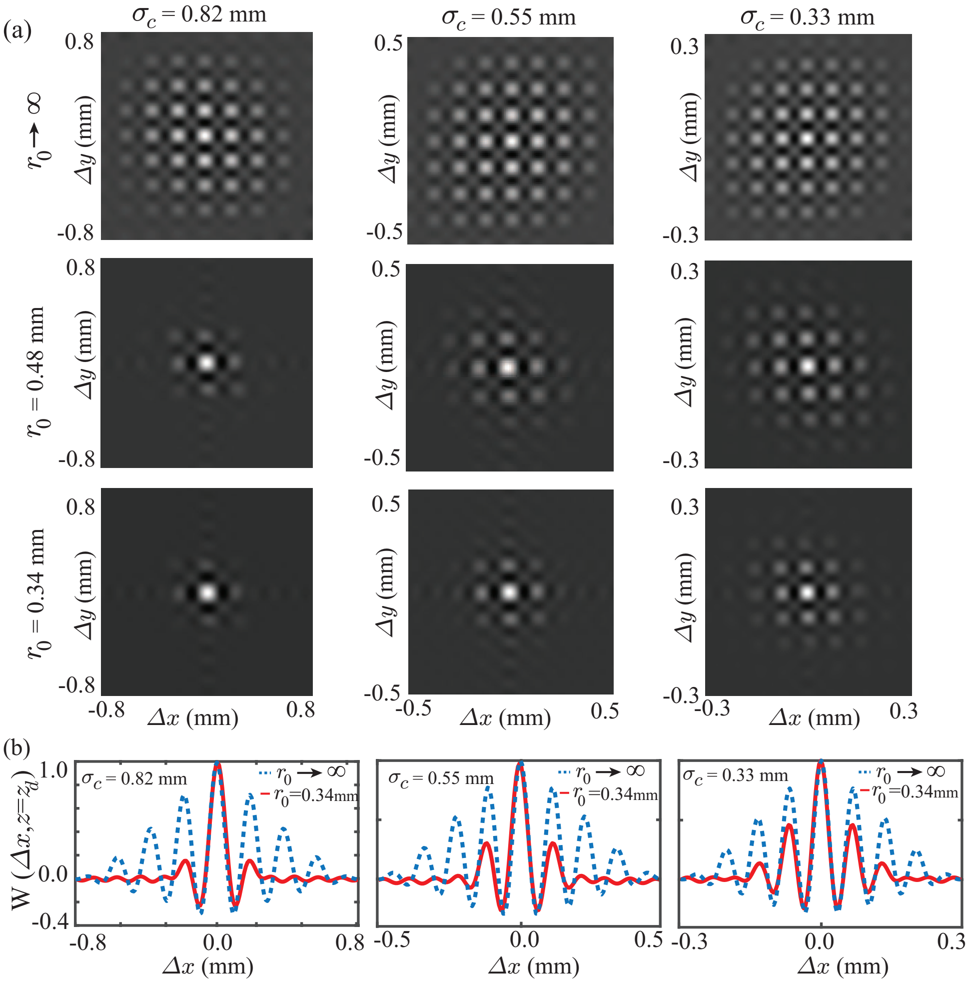

FIGURE 5.9: (a) Reconstructed cross-spectral density function $W(\Delta\rho; z = z_d)$ for different transverse spatial coherence lengths at various turbulence strengths. (b) The plots of one-dimensional cuts along the $x-$direction of $W(\Delta\rho; z = z_d)$ at $r_0 \to \infty$ and $r_0 = 0.34$ mm for different $\sigma_c$.

### 5.3.4 Reconstruction of cross-spectral density function and its structural robustness

Next, using Eq. (5.15), we reconstruct the cross-spectral density function $W(\Delta\rho; z = z_d)$ at $z = z_d$ from the above measured intensity $I(\boldsymbol{\rho_f}; z = z_f)$. Figure 5.9(a) shows the reconstructed cross-spectral density function $W(\Delta\rho; z = z_d)$ at $z = z_d$ for different $\sigma_c$ at various $r_0$. We see that in the absence of turbulence, that is at $r_0 \to \infty$, the two-dimensional structure profile of $W(\Delta\rho; z = z_d)$ is same for all three $\sigma_c$ values, apart from a change in scale. In the presence of turbulence, we find that the two-dimensional structures suffer degradation for all three $\sigma_c$ values. However, at a given turbulence strength, the structural degradation becomes less as the spatial coherence length is decreased. We note that in Fig. 5.9(b), we have plotted $W(\Delta\rho; z = z_d)$ over different range of $\Delta\rho = (\Delta x, \Delta y)$ at different $\sigma_c$. This is so that we can better compare the structural degradation at different $\sigma_c$ values. Finally, in order to highlight the main claim of this chapter, which is that the structural robustness increases as $\sigma_c$ is decreased, we plot in Fig. 5.9(b) the one-dimensional cross-spectral density function $W(\Delta x; z = z_d)$ by taking one-dimensional cuts of $W(\Delta\rho; z = z_d)$ plots in Fig. 5.9(a). For each $\sigma_c$, we plot $W(\Delta x; z = z_d)$ at $r_0 \to \infty$, and $r_0 = 0.34$ together. These plots clearly show that the structural robustness of the cross-spectral density function of a spatially partially coherent field increases as we decrease the spatial coherence length of the field.

In order to demonstrate the structural robustness cross-spectral density function, one can also use the wavefront inversion-based interferometric technique described in chapter 3. In this chapter, we use a different technique that reconstructs $W(\Delta\rho; z = z_d)$ just by recording intensity $I(\boldsymbol{\rho}_f; z = z_f)$ instead of using the technique in chapter 3 because the reconstruction algorithm provides more experimental ease than that of the method in chapter 3. Although the presented reconstruction algorithm is only suitable for demonstrating the structural robustness for our experimental situation, for a general experimental situation, one requires the technique in chapter 3 for demonstrating the same.

### 5.3.5 Implication in free-space communication

The above results ensure that a structured field with partial spatial coherence is more robust than that with complete spatial coherence in the presence of turbulence. By utilizing this fact, one can propose a free-space communication protocol analogous to the protocols in Ref. [190, 191]. The proposed protocol encodes information in different structures in cross-spectral density functions of spatially partially coherent fields, and the structural robustness of cross-spectral density functions can make this protocol more insensitive to turbulence than that of the existing protocols based on structured spatially completely coherent fields [190, 191]. A recent article [238] has already adopted a similar free-space communication protocol based on structured spatially partially coherent fields.

## 5.4 Summary

In summary, we have demonstrated the advantages of spatial coherence engineering in the context of imaging and optical communication. We have begun with the demonstration of enhanced imaging of different transverse planes along the propagation direction through scattering media by controlling the propagation of spatial coherence of the illuminating field. Using a PIC source, we have demonstrated imaging spatially separated transverse planes without losing contrast. Next, by making a source that has minimum-possible coherence (MPC), we have shown improved imaging with maximum possible contrast. We note that in our experiments, we have used scattering media of thickness ranging from 1 mm to 6 mm. In addition, in the reflecting configuration, we have essentially imaged an object kept between a set of two scattering media, which to some extent mimics the experimental situation in which an object is kept in a distributed scatterer. Therefore, our results suggest that controlling the propagation of spatial coherence would offer similar qualitative imaging benefits even in the presence of a distributed scatterer.

We have then demonstrated the structural robustness of spatially partially coherent fields in turbulence to address the issue involved in free-space optical communication with structured light. We have shown that at a given turbulence strength, the structural robustness of a partially coherent field increases with the decrease in the spatial coherence length of the field. We note that in the experiments, we have worked with simulated planar turbulence of strength $r_0$ ranging from $\infty$ to 0.34 mm. On the other hand, the real atmospheric turbulence is distributed and can even cause amplitude fluctuations in addition to random phase fluctuations. The typical values of $r_0$ for atmospheric turbulence range from 4 mm to 30 mm [190, 191, 213]. So, although there are some basic differences between the real atmospheric turbulence and the planar turbulence used in our experiments, we expect that our results on structural robustness remain qualitatively valid even for the real atmospheric turbulence.

# Chapter 6

# Revival of spatial entanglement in two-photon field

## 6.1 Introduction

Quantum Entanglement [33–35,239] is the key resource behind the advancement of many applications such as quantum imaging [240], quantum communication [241], quantum information processing [242], and quantum computing [243]. Spontaneous parametric down-conversion (SPDC) is one of the most widely used methods for generating entangled two-photon fields. The entanglement in down-converted two-photon field has been extensively studied in the discrete finite-dimensional bases such as polarization [38], time-bin [244, 245], and orbital angular momentum (OAM) [246, 247] as well as in the continuous-variable bases such as position-momentum [39, 56, 82], angle-OAM [40], radial position-radial momentum [88], time-energy [89,172,248]. The feasibility of utilizing entanglement in the finite-dimensional bases for long-distance quantum-information applications has been demonstrated in several experimental works [249–253]. However, the suitability of entanglement in the continuous-variable bases for long-distance applications has not been established so far. Among the continuous-variable bases, position-momentum bases have been extensively investigated for its applicability in several applications such as quantum imaging [42–46], quantum holography [47,48], quantum metrology [50], and quantum secure communication [51, 54]. Although position-momentum entanglement has found uses in many of these applications, it has not been found suitable for applications involving long-distance propagation. This is because as the photons propagate away from the down-conversion crystal, the entanglement in position-momentum decays very rapidly [57,58] and this effect becomes worse in the presence of turbulent environments.

In this chapter, we explore propagation of entanglement in the angle-OAM bases and demonstrate that the entanglement of down-converted photons in the angle-OAM bases exhibits a remarkably different behaviour than in the position-momentum bases. Just as in the case of position-momentum bases, initially, the entanglement in angle-OAM bases decays with propagation, but as the photons continue to travel further from the source, the entanglement gets revived. We refer to this behaviour as the propagation-induced entanglement revival. We theoretically and experimentally demonstrate this behaviour and show that the propagation-induced entanglement revival takes place even in the presence of strong turbulence. This feature of angle-OAM entanglement can therefore have important implications for long-distance quantum information applications. Figures 6.1(a) and 6.1(b) illustrate how entanglement in the position-momentum and angle-OAM bases propagate as a function of the propagation distance $z$ based on the propagation dynamics of EPR correlation. The entanglement in the position-momentum bases gets lost after the photons propagate a short distance away from the crystal, and once lost, the entanglement does not revive upon further propagation. On the other hand, the angle-OAM entanglement also gets lost just like position-momentum as the photons start to propagate away from the crystal; however, a further propagation by some distance revives the entanglement. Once revived, the entanglement remains intact upto an arbitrary propagation distance.

The chapter has been adopted veritably from Ref. [254], and the contents are organized in the following manner. In section 6.2, we present the theory of entanglement

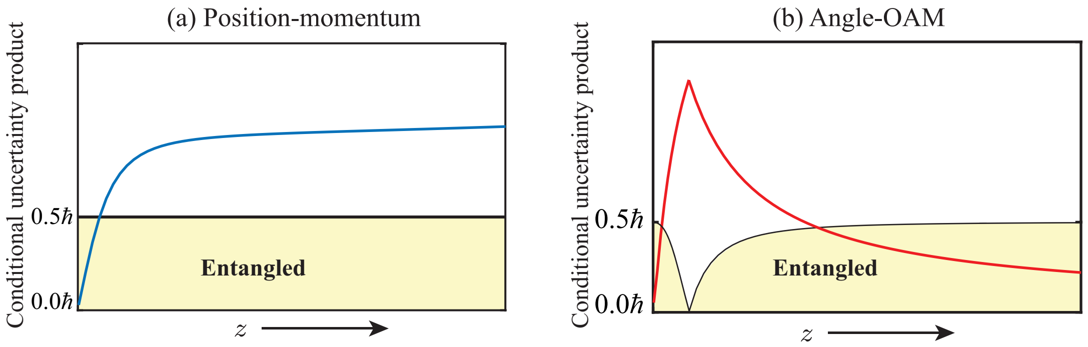

FIGURE 6.1: (a) and (b) illustrate how entanglement in the position-momentum and angle-OAM bases change as the two photons propagate away from the down-conversion crystal. The plots present a qualitative depiction of how entanglement in the position-momentum and the angle-OAM bases changes as a function of the propagation distance $z$.

propagation in position-momentum and angle-OAM bases, and verify entanglement revival in angle-OAM bases. In section 6.3, we experimentally demonstrate the revival of angle-OAM entanglement by measuring EPR correlation upto a propagation distance of 60 cm. Section 6.4 demonstrates the entanglement revival behaviour in the presence of turbulence. Section 6.5 summarizes the chapter.

## 6.2 Theory

### 6.2.1 Propagation of position and angle conditional uncertainties

Figures 6.2(a) and (b) illustrate the concept of conditional position and angle uncertainties respectively, in SPDC collinear type-I process. Figures 6.2(a) shows that a pump beam gets down-converted into co-propagating signal-idler photon field and at a given transverse plane signal and idler fields are on the top of each other, $w_s$ represents the position uncertainty of the individual signal or idler photon fields. If the idler photon gets detected at $y_i$ then the corresponding signal photon certainty gets detected in the shaded region and its width is referred as the conditional position uncertainty of the signal photon $\Delta(y_s|y_i)$. Similarly, Fig. 6.2(b) depicts that if the idler photon gets detected at the angular location $\theta_i$ then the signal photon gets detected in the shaded angular region and its width is referred as the conditional angle uncertainty of the signal photon $\Delta(\theta_s|\theta_i)$. We next present an quantitative analysis of the propagation of conditional position and angle uncertainties of the signal photon in SPDC.

For a Gaussian pump with beam waist at the crystal plane $z = 0$, the two-photon wavefunction in the position basis at the crystal plane $z = 0$ is given by [56–58]:

$$\psi(\boldsymbol{\rho}_s'', \boldsymbol{\rho}_i''; 0) = A \exp\left[-\frac{(\boldsymbol{\rho}_s'' + \boldsymbol{\rho}_i'')^2}{4w_0^2}\right] \exp\left[-\frac{|\boldsymbol{\rho}_s'' - \boldsymbol{\rho}_i''|^2}{4\sigma_0^2}\right], \tag{6.1}$$

where $\boldsymbol{\rho}_s'' \equiv (x_s'', y_s'')$ and $\boldsymbol{\rho}_i'' \equiv (x_i'', y_i'')$ are the transverse positions of the signal and idler photons, respectively at $z = 0$, and $k = \pi/\lambda_p$. Also, $w_0$ is the pump beam waist at $z = 0$, $\sigma_0 = \sqrt{0.455L\lambda_p/2\pi}$, $L$ is the length of the crystal, and $\lambda_p$ is the wavelength of the pump field. Using the two-photon wave-function $\psi(\boldsymbol{\rho}_s'', \boldsymbol{\rho}_i''; 0)$ at $z = 0$, we calculate the two-photon wave-function at $\psi(\boldsymbol{\rho}_s, \boldsymbol{\rho}_i; z)$ (see appendix B for derivation) at $z$ and thereby the two-photon position probability distribution function $P(\boldsymbol{\rho}_s, \boldsymbol{\rho}_i; z) = \psi(\boldsymbol{\rho}_s, \boldsymbol{\rho}_i; z)^* \psi(\boldsymbol{\rho}_s, \boldsymbol{\rho}_i; z)$ at $z$, which can be shown to be

$$P(\boldsymbol{\rho}_s, \boldsymbol{\rho}_i; z) = |A'|^2 \exp\left[-\frac{(\boldsymbol{\rho}_s + \boldsymbol{\rho}_i)^2}{2w(z)^2}\right] \exp\left[-\frac{|\boldsymbol{\rho}_s - \boldsymbol{\rho}_i|^2}{2\sigma(z)^2}\right], \tag{6.2}$$

where $w(z) = w_0\sqrt{1 + z^2/(k^2 w_0^4)}$ and $\sigma(z) = \sigma_0\sqrt{1 + z^2/(k^2\sigma_0^4)}$.

We now obtain the two-photon angle probability distribution by first writing $P(\boldsymbol{\rho}_s, \boldsymbol{\rho}_i; z)$ of Eq. (6.2) in the polar coordinates using the transformations $\boldsymbol{\rho}_s = (r_s \cos\theta_s, r_s \sin\theta_s)$ and $\boldsymbol{\rho}_i = (r_i \cos\theta_i, r_i \sin\theta_i)$, where $(r_s, \theta_s)$ and $(r_i, \theta_i)$ are the polar coordinates of the signal and idler photons at $z$, etc. We therefore get:

$$\begin{aligned}
|\boldsymbol{\rho}_s + \boldsymbol{\rho}_i|^2 &= r_s^2 + r_i^2 + 2r_s r_i \cos(\theta_s - \theta_i) \\
|\boldsymbol{\rho}_s - \boldsymbol{\rho}_i|^2 &= r_s^2 + r_i^2 - 2r_s r_i \cos(\theta_s - \theta_i) \\
P(r_s, \theta_s, r_i, \theta_i; z) &= |A|^2 \exp\left[-\frac{r_s^2 + r_i^2 + 2r_s r_i \cos(\theta_s - \theta_i)}{2w(z)^2}\right] \\
&\quad \times \exp\left[-\frac{r_s^2 + r_i^2 - 2r_s r_i \cos(\theta_s - \theta_i)}{2\sigma(z)^2}\right]
\end{aligned} \tag{6.3}$$

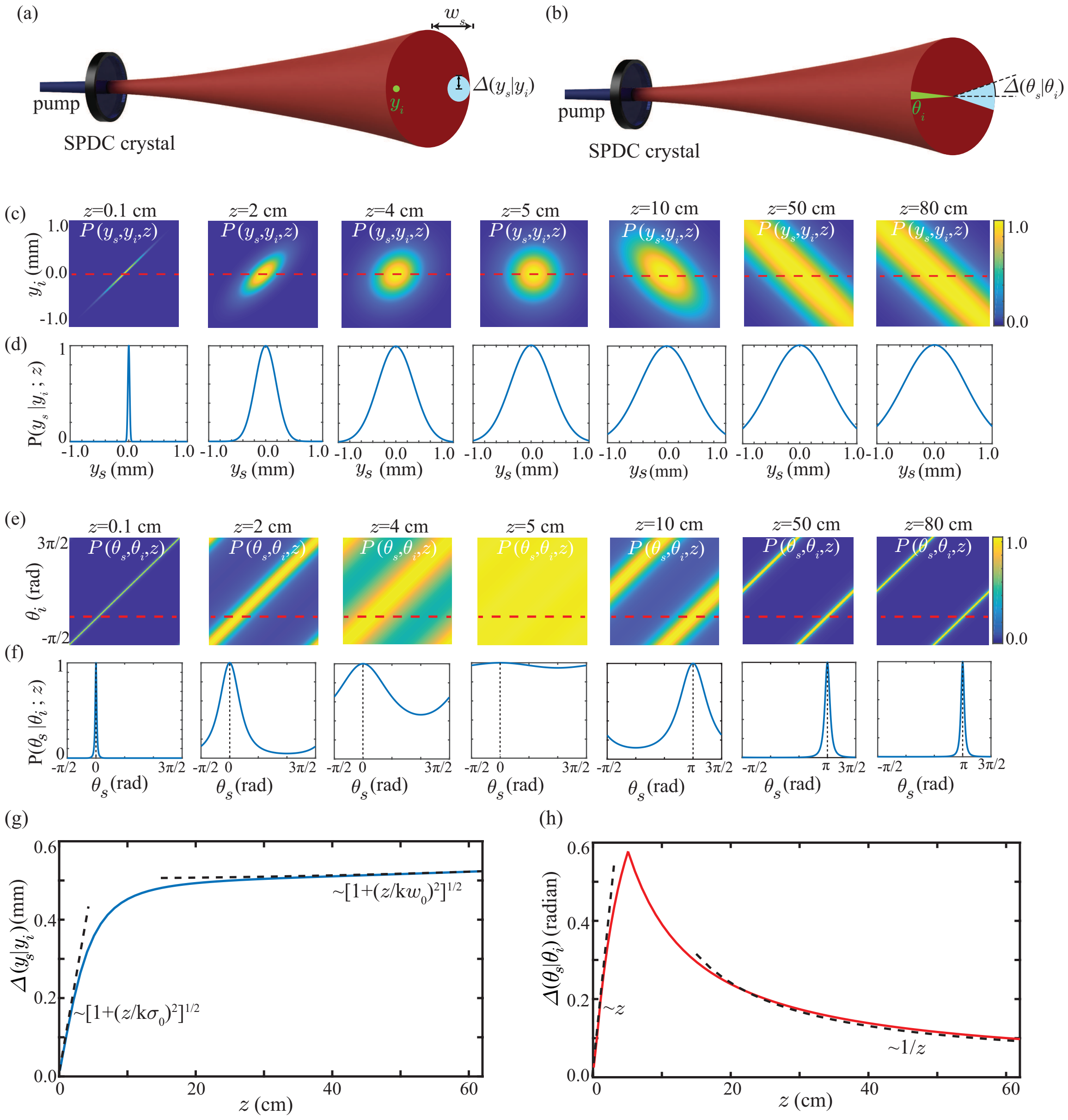

FIGURE 6.2: (a) and (b) illustrate the concept of conditional position and angle uncertainty respectively.(c) and (d) show the two-photon position probability distribution function $P(y_s, y_i; z)$ and the angle probability distribution function $P(\theta_s, \theta_i; z)$ respectively at various $z$ values. (e) and (f) show the conditional position probability distribution function $P(y_s|y_i; z)$ and the conditional angle probability distribution function $P(\theta_s|\theta_i; z)$ of the signal photon at various $z$ values. (g) Numerically calculated conditional position uncertainty $\Delta(y_s|y_i; z)$ as a function of $z$. The two dotted lines show the $z$-scaling of the uncertainty in the near- and far-field regions. (h) Numerically calculated conditional angle uncertainty $\Delta(\theta_s|\theta_i; z)$ as a function of $z$. The two dotted lines show the $z$-scaling of the uncertainty in the near- and far-field regions.

We then integrate $P(r_s, \theta_s, r_i, \theta_i; z)$ over the radial coordinates in order to obtain the two-photon angle probability distribution function $P(\theta_s, \theta_i; z)$ as:

$$P(\theta_s, \theta_i; z) = \iint r_s r_i P(r_s, \theta_s, r_i, \theta_i; z) dr_s dr_i, \tag{6.4}$$

Now, using the relevant experimental parameters $w_0 = 507$ $\mu$m, $L = 5$ mm, and $\lambda_p = 355$ nm in Eqs. (6.2), and (6.4), we calculate the two-photon position probability distribution $P(y_s, y_i; z)$ and the two-photon angle probability distribution $P(\theta_s, \theta_i; z)$ at different propagation distances $z$ as shown in Figs. 6.2(c) and 6.2(e) respectively. In plotting $P(y_s, y_i; z)$ and $P(\theta_s, \theta_i; z)$ in Figs. 6.2(c) and 6.2(e), we scale them in order to make their maximum value equals to one. We next calculate the corresponding conditional position probability distribution function $P(y_s|y_i; z)$ and the angle probability distribution function $P(\theta_s|\theta_i; z)$ by fixing $y_i = 0$ in $P(y_s, y_i; z)$ and $\theta_i = 0$ in $P(\theta_s, \theta_i; z)$ respectively. Figures 6.2(d) and 6.2(f) show $P(y_s|y_i; z)$ and $P(\theta_s|\theta_i; z)$ respectively. Figures 6.2(c) and 6.2(d) show that in the near-field region the two down-converted photons have the maximum probability of arriving at the same transverse position. This is referred to as the position-correlation in the near-field region [39]. As the photon pair propagates away from the crystal plane, they become anti-correlated in position. Figures 6.2(e) and 6.2(f) show how the correlations in the angle basis change as a function of $z$. We find that in the near field, the signal and idler photons have the maximum probability of arriving at the same angular positions. However, in the far field, the two photons are most likely to arrive at antipodal location, that is, at an angle difference of $\pi$ radians. The standard deviations of $P(y_s|y_i; z)$, and $P(\theta_s|\theta_i; z)$ are referred to as the conditional position uncertainty $\Delta(y_s|y_i; z)$ and the conditional angle uncertainty $\Delta(\theta_s|\theta_i; z)$, respectively. Figures 6.2(g) and 6.2(h) show the plot of the numerically calculated $\Delta(y_s|y_i; z)$ and $\Delta(\theta_s|\theta_i; z)$ respectively, as a function of $z$. we find that as the down-converted photons propagate away from the crystal, the conditional position uncertainty increases monotonically. However, the conditional angle uncertainty increases initially but later begins to decrease monotonically.

Although it is very difficult to derive the general analytical expressions for the conditional position and angle uncertainties as a function of $z$, we derive expressions for how

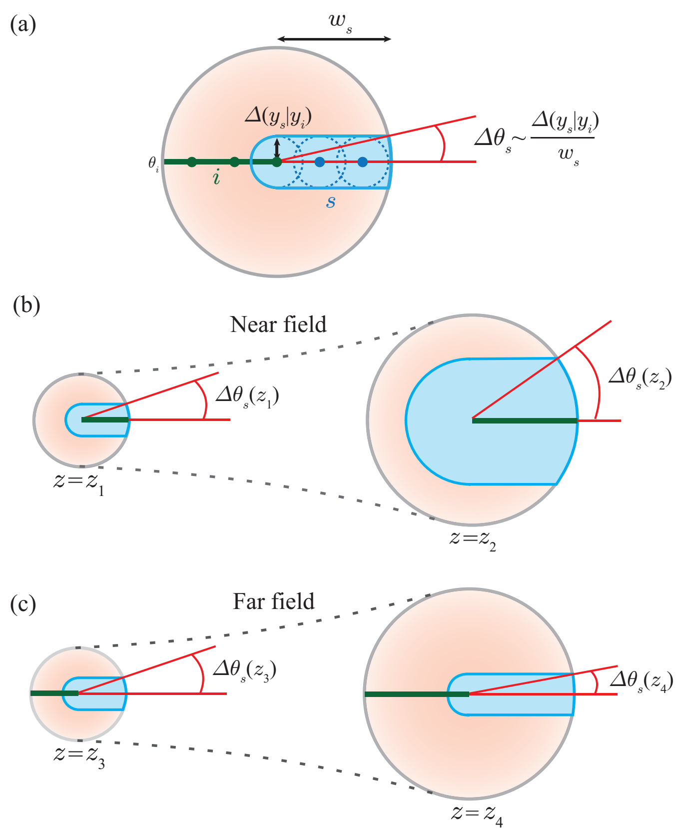

FIGURE 6.3: (a) Illustrates that if a idler photon gets detected at a point depicted by any one of the dots, the corrsponding signal photon certainty gets detected within the diameterically opposite dashed circle. Similarly, if a idler photon gets detected at a angular position depicted by the line, the corrsponding signal photon certainty gets detected in the shaded area. The angular width of that shaded area scales with the angular sector $\Delta\theta_s \sim \Delta(y_s|y_i)/w_s$. (b) Illustrates the propagation of signal-idler field in the near-fields and depicts the increasing trend of $\Delta\theta_s(z)$. (c) Illustrates the propagation of signal-idler field in the far-field and depicts the decreasing trend of $\Delta\theta_s(z)$.

the conditional uncertainties scale with $z$ in the near- and far-field regions. The two dotted lines in Figs. 6.2(g) show how the conditional position uncertainty $\Delta(y_s|y_i;z)$ scales with $z$ in the near and far fields. We find that $\Delta(y_s|y_i;z)$ increases monotonically as a function of $z$ in both the near- and far-field regions. While the uncertainty increases as $\sigma(z)$ in the near-field, it increases as $w(z)$ in the far-field. The two dotted lines in Figs. 6.2(h) show how the conditional angle uncertainty $\Delta(\theta_s|\theta_i;z)$ scales with $z$ in the near and far field. We find that while $\Delta(\theta_s|\theta_i;z)$ increases as $z$ in the near field regions, it decreases as $1/z$ in the far-field regions. (For detailed theoretical calculation see Appendix C).

We now present an illustration in Fig. 6.3 to intuitively explain the propagation of

$\Delta(\theta_s|\theta_i;z)$in the near- and far-field. Figure 6.3(a) illustrates that if the idler photon gets detected at the angular position $\theta_i$ depicted by the solid line, the corresponding signal photon gets detected in the shaded region. The conditional angle uncertainty $\Delta(\theta_s|\theta_i)$ of the signal photon is obtained by radially integrating the shaded region, which scales with the angular sector $\Delta\theta_s$. It is given by $\Delta\theta_s \sim \Delta(y_s|y_i)/w_s$. The propagation of $\Delta(y_s|y_i)$ and $w_s$ decides how $\Delta\theta_s$ changes with $z$. Figures 6.2(e) and B.2 in Appendix B show $\Delta(y_s|y_i;z)$ and $w_s(z)$ respectively, as a function of $z$. Based on these two plots, we find that $\Delta(y_s|y_i;z)$ increases faster than $w_s(z)$ in the near-field and $w_s(z)$ increases faster than $\Delta(y_s|y_i;z)$ in the far-field. Figure 6.3(b) illustrates the propagation of collinear signal-idler photon field in the near-field, where idler and signal photons are detected in the same region illustrated by a solid line and a shaded area respectively. The spatial extent of the signal photon (shaded area) increases much faster than that of the signal or idler field. As a result, the angular sector $\Delta\theta_s(z_2)$ at $z = z_2$ becomes significantly larger than the angular sector $\Delta\theta_s(z_1)$ at $z = z_1$. This explains the increasing trend of $\Delta(\theta_s|\theta_i;z)$ in the near-field. Figure 6.3(c) illustrates the propagation of the signal-idler photon in the far-field. If the idler gets detected at an angular position depicted by the solid line, the signal gets detected in the shaded region and the spatial extent of the signal photon (shaded area) changes much slower than that of the signal or idler photon field as a function of the propagation distance. As a result, the angular secotor $\Delta\theta_s(z_3)$ at $z = z_3$ becomes smaller than the angular sector $\Delta\theta_s(z_4)$ at $z = z_4$, which also explains the decreasing trend of $\Delta(\theta_s|\theta_i;z)$ in the far-field.

### 6.2.2 Propagation of two-photon momentum and OAM probability distributions

Using the two-photon wave-function in the position basis $\psi(\boldsymbol{\rho}_s, \boldsymbol{\rho}_i; z)$ calculated in the previous section, we calculate the two-photon wave-function $\psi(\boldsymbol{p}_s, \boldsymbol{p}_i; z)$ in the transverse momentum basis, which is given by [57]

$$\psi(\boldsymbol{p}_s, \boldsymbol{p}_i; z) = B \exp\left[-\frac{(\boldsymbol{p}_s + \boldsymbol{p}_i)^2 w_0^2}{4\hbar^2}\right] \exp\left[-\frac{|\boldsymbol{p}_s - \boldsymbol{p}_i|^2 \sigma_0^2}{4\hbar^2}\right] \exp\left[-\frac{iz}{k\hbar^2}(\boldsymbol{p}_s^2 + \boldsymbol{p}_i^2)\right], \quad (6.5)$$

where $\boldsymbol{p}_s \equiv (p_{sx}, p_{sy})$ and $\boldsymbol{p}_i \equiv (p_{ix}, p_{iy})$ are the transverse momenta of the signal and idler photons, respectively. Now by fixing $\boldsymbol{p}_i = 0$ in the above equation we find the conditional momentum probability distribution function $P(\boldsymbol{p}_s|\boldsymbol{p}_i; z)$ of the signal photon is given by

$$P(\boldsymbol{p}_s|\boldsymbol{p}_i; z) = A \exp\left[-\frac{\boldsymbol{p}_s^2(w_0^2 + \sigma_0^2)}{2\hbar^2}\right]. \quad (6.6)$$

The standard deviation of $P(\boldsymbol{p}_s|\boldsymbol{p}_i; z)$ along the $y$-direction $\Delta(p_{sy}|p_{iy}; z)$ is the conditional momentum uncertainty of the signal photon. The above equation shows that $P(\boldsymbol{p}_s|\boldsymbol{p}_i; z)$ is independent of $z$ and that $\Delta(p_{sy}|p_{iy}; z)$ does not change upon propagation. For the experimental parameter as given above, the calculated value of $\Delta(p_{sy}|p_{iy}; z)$ is $1.97\hbar$ mm$^{-1}$.

For a Gaussian pump, the two-photon state produced by SPDC in the OAM basis can be written as [40, 155]

$$|\Psi\rangle = \sum_{l_s=-\infty}^{\infty} \sqrt{S_{l_s}} |l_s\rangle_s | -l_s\rangle_i, \quad (6.7)$$

where $l_s\hbar$ and $-l_s\hbar$ are the OAMs of signal and idler photons, respectively. The form of the two-photon state above implies that if the signal photon is detected with OAM $l_s\hbar$, then the idler photon is guaranteed to be detected with OAM $-l_s\hbar$. For the above equation, the conditional two-photon OAM probability distribution function takes the following form: $P(l_s|l_i; z) = S_{l_s}\delta_{l_s,0}$. This implies that the corresponding conditional OAM uncertainty $\Delta(l_s|l_i; z)$ is equal to zero. However, in an experimental situation, one always measures $\Delta(l_s|l_i; z)$ to be non-zero [40]. There are several reasons for this, which includes the pump not being an ideal Gaussian beam, the experimental imperfections such as misalignment and background noise, and the mode dependent detection efficiencies of OAM detectors. These cause an additional contribution in $P(l_s|l_i; z)$ measurement. Therefore, in our experiments, we model the conditional OAM probability distribution function as:

$$P(l_s|l_i;z) = S_{l_s}\delta_{l_s,0} + N\exp\left[-\frac{l_s^2}{2\sigma_f^2}\right], \tag{6.8}$$

where $S_0$, $\sigma_f$ and $N$ are the fitting parameters. We take the width of $P(l_s|l_i;z)$ as the conditional OAM uncertainty $\Delta(l_s|l_i;z)$. We fit the above $P(l_s|l_i;z)$ with the experimental OAM conditional distribution in Fig. 6.8 and find its width $\Delta(l_s|l_i;z)$ to be $0.72\hbar$ radian$^{-1}$.

### 6.2.3 Propagation of position-momentum and angle-OAM entanglement

We now use EPR correlation for certifying entanglement, and if the product $\Delta(y_s|y_i;z)$ $\Delta(p_{sy}|p_{iy}.z) < 0.5\hbar$, the two photons are said to be entangled in the position-momentum bases at $z$ [33,39]. Similarly, we write the EPR correlation for entanglement in the angle-OAM bases as: $\Delta(\theta_s|\theta_i;z)\Delta(l_s|l_i;z) < 0.5\hbar[1 - 2\pi P(\theta_s|\theta_i = \theta_0;z)]$. We find that the probability $P(\theta_s|\theta_i = \theta_0;z)$ does not remain constant with propagation distance $z$. As a result, the Heiseberg uncertainty bound changes with propagation distance $z$ and it is shown in Fig. 6.9(b). We note that the conditional momentum and OAM uncertainties $\Delta(p_{sy}|p_{iy};z)$ and $\Delta(l_s|l_i;z)$ remain constant as a function of $z$. As a result, the functional dependence of $\Delta(y_s|y_i;z)\Delta(p_{sy}|y_{iy};z)$ and $\Delta(\theta_s|\theta_i;z)\Delta(l_s|l_i;z)$ on $z$ is same as that of $\Delta(y_s|y_i;z)$ and $\Delta(\theta_s|\theta_i;z)$, respectively. This implies that both position-momentum and angle-OAM entanglements are lost within a short propagation distance from the down-conversion crystal; however, the angle-OAM entanglement only revives through further propagation. We plot the theoretically calculated uncertainty products in Figs. 6.9, and compare them with the experimental data.

## 6.3 Experimental demonstration

### 6.3.1 Measurement of two-photon position and angle probability distribution functions

Figures 6.4 shows the schematic of the experimental setup for measuring the two-photon probability distribution functions $P(y_s, y_i; z)$, and $P(\theta_s, \theta_i; z)$ through coincidence measurements of the two photons. An ultraviolet (UV) continuous wave (CW) Gaussian pump (Coherent Genesis STM UV laser) of wavelength $\lambda_p = 355$ nm, beam waist $w_0 = 507\ \mu$m is incident on a 5 mm × 5 mm × 5 mm $\beta$-barium borate (BBO) crystal. The crystal is cut in a manner that it produces signal and idler photons with collinear type-I phase-matching condition. A long-pass filter (LPF) is placed after the crystal to block the UV pump. We use an EMCCD camera having 512 × 512 pixel grid with 16 × 16 $\mu$m$^2$ pixel-size for measuring $P(y_s, y_i; z)$ and $P(\theta_s, \theta_i; z)$. For this, we record $10^6$-$10^7$ images of the SPDC field with an average flux of 0.5 - 2.0 photons per pixel. Appendix B describes how to measure coincidence counts using an EMCD camera. A 10 nm bandpass filter centered at 710 nm is used in order to detect the down-converted photons. The blower heater (BH) produces turbulence by blowing hot air, and it is switched on during our experiments involving turbulence. In order to measure $P(y_s, y_i; z)$ and $P(\theta_s, \theta_i; z)$ as a function of propagation distance $z$, we image different $z$ planes onto the EMCCD camera plane using $4f$ imaging systems. For imaging the transverse planes between $z = 0.35$ cm and $z = 1.5$ cm, we keep the magnification of the imaging system to be 1 while for imaging the transverse planes between $z = 10$ and $z = 60$ cm, we keep the magnification to be 0.25. For measuring the two-photon position probability distribution function $P(y_s, y_i; z)$, we take millions of images using the EMCCD camera. For each image, we group the pixels into horizontal strips, $y_s$ and $y_i$, as shown in Fig. 6.5(a). The coincidence count between $y_s$ and $y_i$ can be written as (see appendix C Eq. (D.3))

$$C_{y_s y_i} = \frac{1}{N} \sum_{k=1}^{N} n_{y_s}^{(k)} n_{y_i}^{(k)} - \frac{1}{N} \sum_{k=1}^{N} n_{y_s}^{(k)} n_{y_i}^{(k+1)}, \tag{6.9}$$

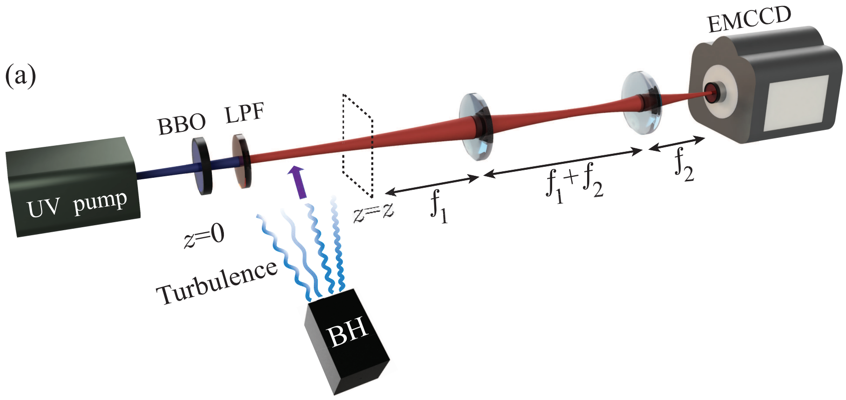

FIGURE 6.4: Schematic of the experimental setup for measuring position and angle coincidences. LPF: long pass filter.

where $n_{y_s}^{(k)}$ and $n_{y_i}^{(k)}$ are the photon counts of $y_s$ and $y_i$ respectively. The top image in Fig. 6.5(b) represents total coincidence as a function of $y_s$ and $y_i$, and it is evaluated by using the first term of Eq. (6.9). The bottom image in Fig. 6.5(b) represents the accidental coincidence as a function of $y_s$ and $y_i$, and it is evaluated using the second term of Eq. (6.9). The difference of these two images is proportional to the true coincidence $C_{y_s y_i}$ and thus to the two-photon position probability distribution function $P(y_s, y_i; z)$, as shown in Fig. 6.5(c). At $y_s = y_i$, the correlation becomes artificially perfect because we correlate a pixel with itself. We manually discard the value of $P(y_s, y_i; z)$ at all $y_s = y_i$ pixels by substituting it with a constant value and we exclude all $y_s = y_i$ pixels while extracting $\Delta(y_s|y_i; z)$ from the measured $P(y_s, y_i; z)$.

For measuring the two-photon angle probability distribution $P(\theta_s, \theta_i; z)$, we group the pixels for each image into angular sectors as shown in Fig. 6.5(d). The coincidence count between the angular sectors at $\theta_s$ and $\theta_i$ is given by (see appendix C Eq. (D.3))

$$C_{\theta_s \theta_i} = \frac{1}{N} \sum_{k=1}^{N} n_{\theta_s}^{(k)} n_{\theta_i}^{(k)} - \frac{1}{N} \sum_{k=1}^{N} n_{\theta_s}^{(k)} n_{\theta_i}^{(k+1)}, \tag{6.10}$$

where $n_{\theta_s}^{(k)}$ and $n_{\theta_i}^{(k)}$ are the photon counts of angular sectors $\theta_s$ and $\theta_i$ respectively. The top image in Fig. 6.5(e) represents the total coincidence as a function of $\theta_s$ and $\theta_i$, and it is evaluated using the first term of Eq. (6.10). The bottom image in Fig. 6.5(e) represents the accidental coincidence as a function of $\theta_s$ and $\theta_i$, and it evaluated using the second

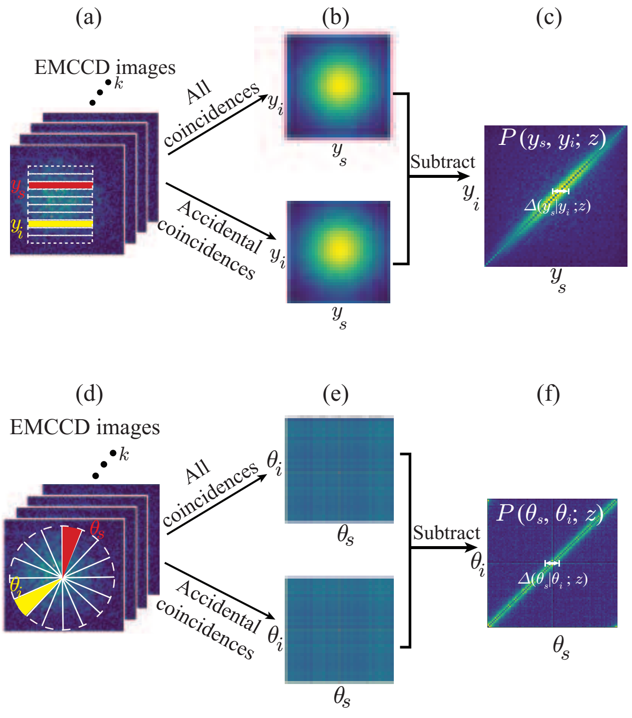

FIGURE 6.5: (a) Acquired images of SPDC field and binning the pixels into signal $y_s$ and idler $y_i$ bars. (b) The top and the bottom images represent the total coincidence and the accidental coincidence calculated using the first and the second terms of Eq. (6.9), respectively. Subtraction of these two terms gives (c) the measured two-photon position probability distribution function $P(y_s, y_i; z)$. (d) Acquired images of SPDC field and binning the pixels into signal angular sector $\theta_s$ and idler angular sector $\theta_i$. (e) The top and the bottom images represent the total coincidence and the accidental coincidence calculated using the first and the second terms of Eq. (6.10), respectively. Subtraction of these two terms gives (f) the measured two-photon angle probability distribution function $P(\theta_s, \theta_i)$.

term of Eq. (6.10). The difference of these two images is proportional to the two-photon angle probability distribution $P(\theta_s, \theta_i; z)$, as shown in Fig. 6.5(f). At $\theta_s = \theta_i$, the correlation becomes artificially perfect because we are correlating a pixel with itself. In order to avoid this we substitute the value of $P(\theta_s, \theta_i; z)$ at all $\theta_s = \theta_i$ pixels with a constant value. We exclude all $\theta_s = \theta_i$ pixels while extracting $\Delta(\theta_s|\theta_i; z)$ from the measured $P(\theta_s, \theta_i; z)$.

Figure 6.6(a) shows the experimentally measured two-photon position probability distribution function $P(y_s, y_i; z)$ at different $z$. We scale the measured $P(y_s, y_i; z)$ such that its maximum value is equal to one. We find that the photons are correlated in position in the near field whereas they get position anti-correlated in the far-field. In order to extract $\Delta(y_s|y_i = 0; z)$ from the measured $P(y_s, y_i; z)$, we fit $P(y_s, y_i; z)$ with the function: $P_f(y_s, y_i; z) = bP_r(y_s, y_i; z) + aP_n(y_s, y_i; z)$, where $P_r(y_s, y_i; z) = \exp[-(y_s + y_i - d)^2/(2\sigma_1^2(z))] \times \exp[-(y_s - y_i - f)^2/(2\sigma_2^2(z))]$ is considered as the probability distribution due to the down-converted photons, while $P_n(y_s, y_i) = \exp[-(y_s + y_i - d)^2/(2n^2)] \times \exp[-(y_s - y_i - f)^2/(2m^2)]$ is considered as the noise contribution. Here $b$, $a$, $\sigma_1(z)$, $\sigma_2(z)$, $d$, $f$, $m$ and $n$ are the fitting parameters. We consider $n \gg \sigma_1(z)$, $m \gg \sigma_2(z)$ such that the noise contribution remains much broader than the two-photon position probability distribution. The width $\Delta(y_s|y_i; z)$ can now be expressed as $\Delta(y_s|y_i; z) = \sigma_1(z)\sigma_2(z)/\sqrt{\sigma_1^2(z) + \sigma_2^2(z)}$. Figure 6.6(c) shows $\Delta(y_s|y_i; z)$ as a function of $z$. The theory plot has been calculated using the expression given in Eq. (6.2).

Figure 6.6(b) shows the experimentally measured $P(\theta_s, \theta_i; z)$ at different $z$. We scale $P(\theta_s, \theta_i; z)$ such its maximum value is equal to one. The $P(\theta_s, \theta_i; z)$ plots show that near the crystal plane the signal and idler photons have the highest probability of arriving at the same angular positions. However in the far-field the two photons are most likely to arrive at angular positions separated by $\pi$ radians. We fit the measured $P(\theta_s, \theta_i; z)$ with the analytic function: $P_f(\theta_s, \theta_i; z) = bP_r(\theta_s, \theta_i; z) + a$, where $P_r(\theta_s, \theta_i; z) = 1/(1 + q\cos(\theta_s - \theta_i - c))^{3/2}$. Here, $b$, $a$, $q$, and $c$, are the fitting parameters. We derive the fitting function by putting $r_s = r_i$ in Eq. (6.4). Next, we evaluate $\Delta(\theta_s|\theta_i; z)$ by finding the standard deviation of $P_r(\theta_s|\theta_i; z)$ at various $z$ values. Figure 6.6(d) shows the experimental $\Delta(\theta_s|\theta_i; z)$ as a function of $z$. We find that near the crystal $\Delta(\theta_s|\theta_i; z)$ increases as a function of $z$. However, beyond $z = 10$ cm $\Delta(\theta_s|\theta_i; z)$ starts to monotonically decreas as a function of $z$. The theory plot has been calculated using the expression given in Eq. (6.4). We see that our experimental results qualitatively follow the corresponding theoretical results. We further use fitting parameters for ploting the error bars in Fig. 6.6(c) and 6.6(c). We find still that the experimental points are above the theory line. This is can be attributed to the fact that the background noise model is not an accurate one. As a result, we over estimate the measured conditional uncertainties. Furthermore, We note that using an EMCCD camera it is relatively easy to measure $\Delta(y_s|y_i; z)$ and $\Delta(\theta_s|\theta_i; z)$ close to the crystal ($z < 3$ cm) or in the far field ($z > 10$ cm). However, due to the signal-to-noise limitations, it is not

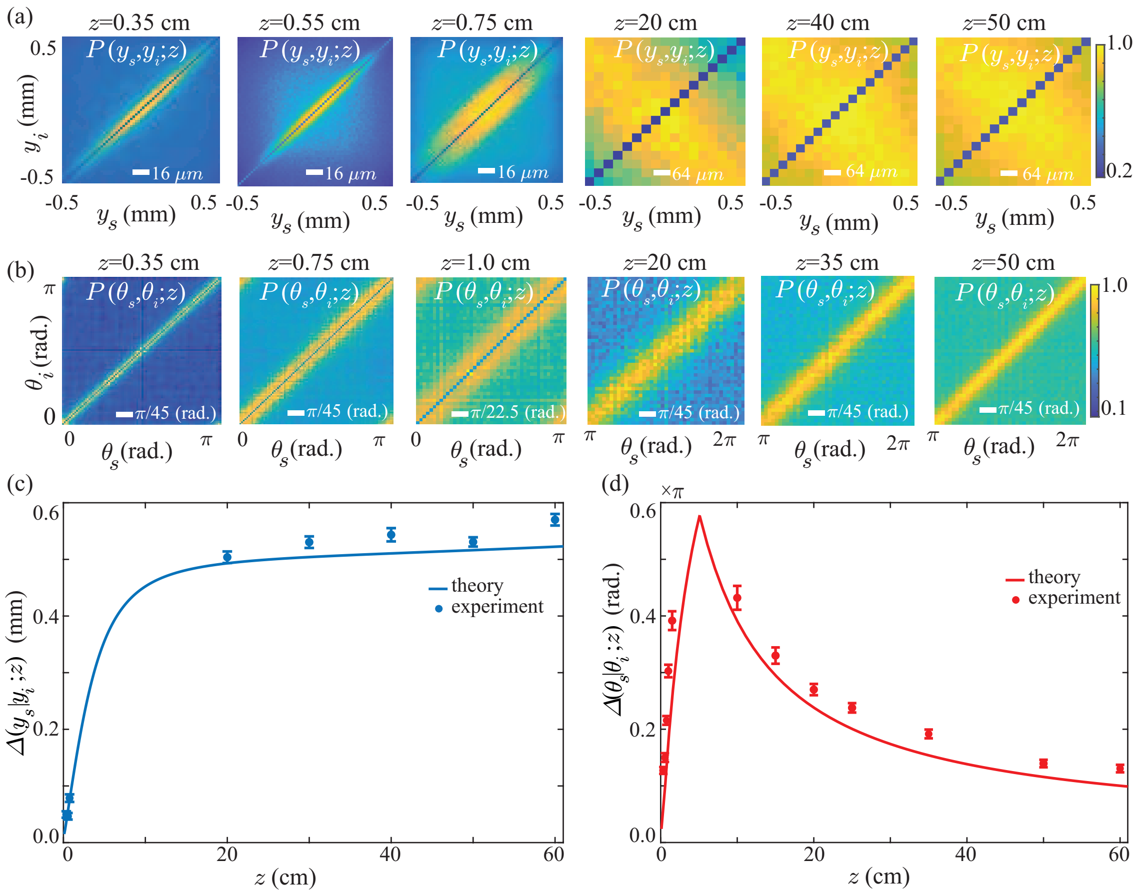

FIGURE 6.6: (a) and (b) show the experimentally measured two-photon position and angle probability distribution $P(y_s, y_i; z)$ and $P(\theta_s, \theta_i; z)$ as a function of the propagation distance $z$. (c) and (d) show the plots of conditional position and angle uncertainties $\Delta(y_s|y_i; z)$ and $\Delta(\theta_s|\theta_i; z)$ as a function of $z$. The experimental points are shown with solid dots while the solid curve represents the theoretical predictions.

possible to make measurements in the intermediate regions.

### 6.3.2 Measurement of two-photon momentum and OAM probability distributions

For measuring $P(p_{sy}, p_{iy}; z)$ at $z$, we use a $2f$ imaging system and keep the EMCCD camera at the Fourier plane of the transverse plane at $z$, as depicted in Fig. 6.7(a). We then measure the two-photon position probability distribution function at the EMCCD camera plane, which is proportional to the two-photon momentum probability distribution function $P(p_{sy}, p_{iy}; z)$ at $z$. The conditional momentum uncertainty $\Delta(p_{sy}|p_{iy}; z)$ is obtained by

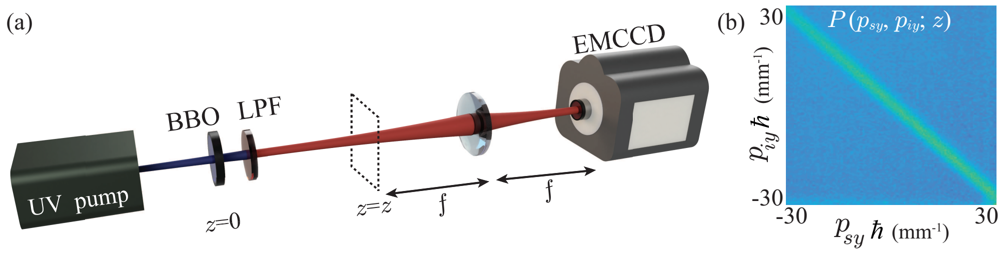

FIGURE 6.7: (a) Schematic of the experimental setup for measuring momentum coincidence. (b) Experimentally measured two-photon momentum probability distribution. LPF: long pass filter.

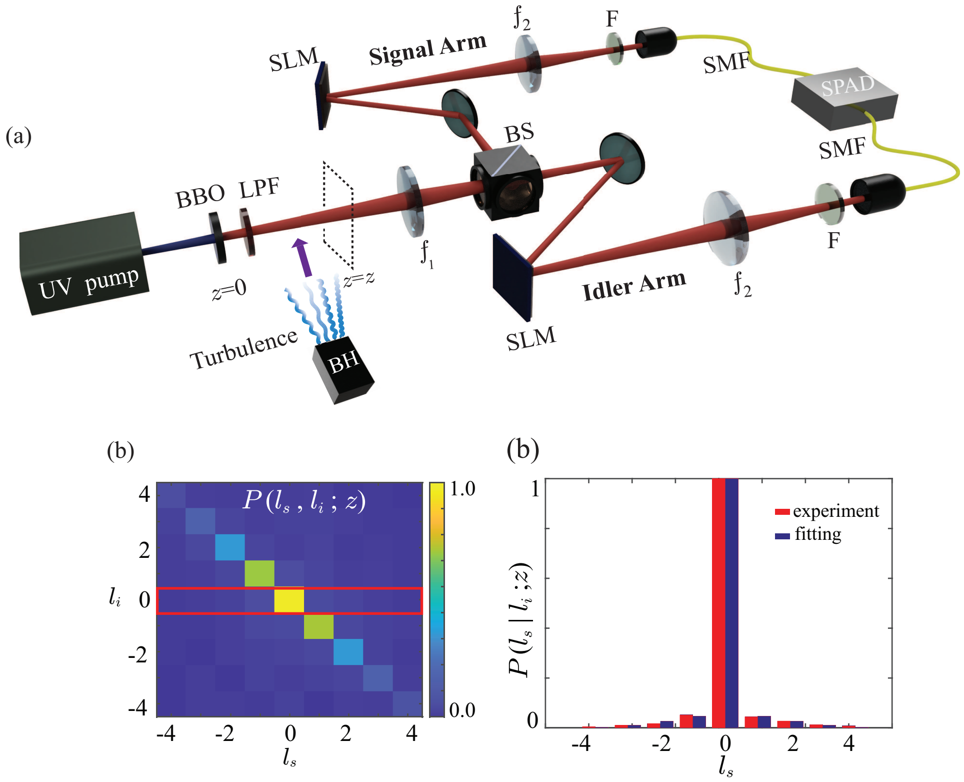

FIGURE 6.8: (a) Schematic of the experimental setup for measuring OAM coincidence and the OAM correlation. LPF: long-pass filter, BS: beam splitter, SLM: spatial light modulator, SMF: single-mode fiber, F: interference filter. The blower heater (BH) is used for generating turbulence, and it is switched on in the path of the SPDC field when studying the effect of turbulence on entanglement propagation. (b) and (c) are the experimentally measured $P(l_s, l_i; z)$ and $P(l_s|l_i; z)$ at $z = 50$ cm. The fitting is the based on the noise model depicted in Eq. (6.8).

multiplying the conditional position uncertainty at the EMCCD plane by $k\hbar/f$, where $f$ is the focal length of the lens. Figure 6.7(b) shows the measured $P(p_{ys}, p_{yi}; z)$ and the experimental value of $\Delta(p_{sy}|p_{iy})$ is $2.13\hbar \pm 0.1\hbar$ mm$^{-1}$ and it matches quite well with the theoretical value $1.97\hbar$ mm$^{-1}$.

For measuring the two-photon OAM probability distribution, we use single-photon avalanche diode (SPAD) detectors [40, 53]. Figure 6.8(a) shows the schematic of the experimental setup. As illustrated in the figure, we image the transverse plane at $z$ onto the SLMs kept in the signal and idler arms. Specific holograms are displayed on both the SLMs, and then the signal and idler SLM planes are imaged onto the input facets of single-mode fibers (SMFs) kept in the signal and idler arms. The combination of the hologram and SMF in each arm projects the input field into a particular OAM mode which then gets detected by the SPAD detector through the SMF. An electronic coincidence circuit then yields the coincidence counts. By displaying different holograms on the SLMs, we measure the two-photon OAM probability distribution.

In section 6.2.2, we have already discussed that $\Delta(l_s|l_i;z)$ is independent of $z$ due to the conservation of OAM in SPDC process. We verify this by making several measurements of $P(l_s, l_i; z)$ as a function of $z$. We plot the experimentally measured two-photon OAM probability distribution function $P(l_s, l_i; z)$ and the conditional OAM probability distribution function $P(l_s|l_i;z)$ at $z = 50$ cm in Figs. 6.8(b) and 6.8(c), respectively. As described in section 6.2.2, we fit the conditional distribution with the analytical function $P(l_s|l_i;z) = S_{l_s}\delta_{l_s,0} + N \exp\left[-l_s^2/(2\sigma_f^2)\right]$, where $S_0$, $N$, and $\sigma_f$ are the fitting parameters. We find the standard deviation of $P(l_s|l_i;z)$ and thus $\Delta(l_s|l_i;z)$ to be $0.72\hbar \pm 0.04\hbar$ in our experiments.

### 6.3.3 Revival of angle-OAM entanglement

We now plot the measured conditional uncertainty products $\Delta(y_s|y_i;z)\Delta(p_{sy}|p_{iy};z)$ and $\Delta(\theta_s|\theta_i;z)\Delta(l_s|l_i;z)$ as a function of $z$ in Figs. 6.9(a) and 6.9(b), respectively. Figures 6.9(a) and 6.9(b) also show the theory plots. We see good agreement bewteen the theory and experiments. We find that entanglements in both position-momentum and angle-OAM bases are lost within a few centimeters from the down-conversion crystal. However, while the position-momentum entanglement never revives, the angle-OAM entanglement revives after the photons have propagated 24 cm away from the crystal; experi-

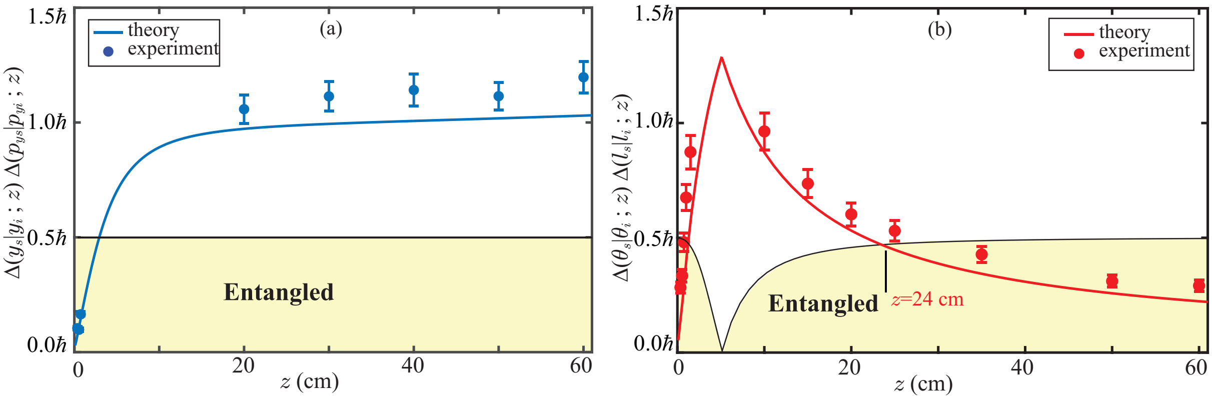

FIGURE 6.9: (a) Conditional position-momentum uncertainty product $\Delta(y_s|y_i;z)\Delta(p_{sy}|p_{iy};z)$ as a function of the propagation distance $z$. The solid dots are the experimental results and the solid line is the best theoretical fit. (b) Conditional angle-OAM uncertainty product $\Delta(\theta_s|\theta_i;z)\Delta(l_s|l_i;z)$ as a function of the propagation distance $z$. The solid dots are the experimental results and the solid line is the best theoretical fit. The solid dots are the experimental results and the solid line is the best theoretical fit. As indicated on the plot, the theoretical prediction for entanglement revival is at $z = 24$ cm while we observe it at about $z = 28$ cm.

mentally, we find this distance to be about 28 cm. After the revival, the angle-OAM entanglement does not decay again, as demonstrated in our experiments up to 60 cm.

## 6.4 Angle-OAM entanglement revival in turbulence

We next investigate whether or not the propagation-induced entanglement revival feature survives in the presence of turbulence, which is often the limiting factor in any realistic long-distance application.

### 6.4.1 Propagation of two-photon angle probability distribution in turbulence

Figure 6.10(a) illustrates the propagation of SPDC photons through a planar turbulence kept at a distance $z = d$ from the crystal plane located at $z = 0$. We are interested in finding the two-photon angle probability distribution function at a propagation distance $z$. The presence of turbulence introduces statistical randomness in the two-photon field, and so we need to describe the field propagation in terms of the two-photon cross-spectral

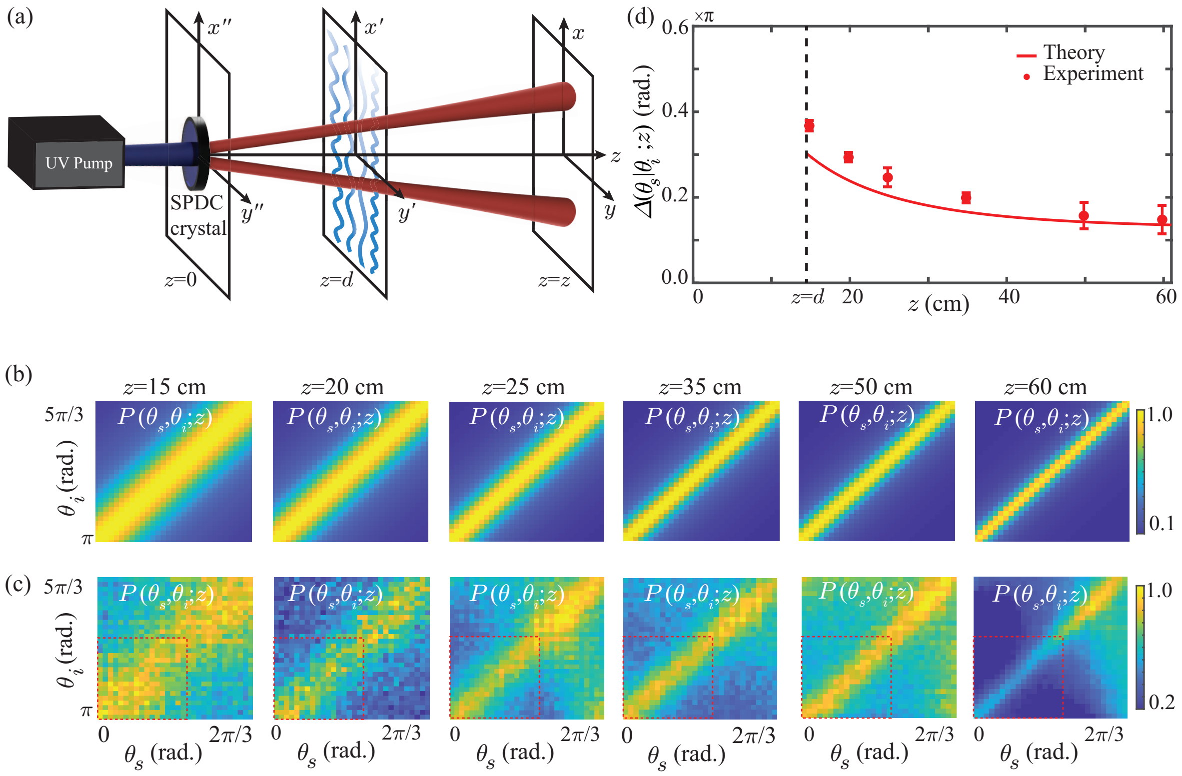

FIGURE 6.10: (a) Illustrating the propagation of the down-converted field in the presence of turbulence. (b) Theoretically calculated and (c) experimentally measured two-photon angle probability distribution function $P(\theta_s, \theta_i; z)$ at various $z$ in the presence of turbulence. (d) The theoretical and experimental plots of $\Delta(\theta_s|\theta_i; z)$ as a function of $z$.

density function. From $z = 0$ up to $z = d$, the two-photon field remains pure and can be described by the two-photon wavefunction $\psi(\boldsymbol{\rho}'_s, \boldsymbol{\rho}'_i; d)$. Therefore, the two-photon cross-spectral density function $W(\boldsymbol{\rho}'_{s1}, \boldsymbol{\rho}'_{i1}, \boldsymbol{\rho}'_{s2}, \boldsymbol{\rho}'_{i2}; d)$ right after the turbulence plane $z = d$ can be written as

$$W(\boldsymbol{\rho}'_{s1}, \boldsymbol{\rho}'_{i1}, \boldsymbol{\rho}'_{s2}, \boldsymbol{\rho}'_{i2}; d) = \psi^*(\boldsymbol{\rho}'_{s1}, \boldsymbol{\rho}'_{i1}; d)\psi(\boldsymbol{\rho}'_{s2}, \boldsymbol{\rho}'_{i2}; d)W_{\text{turb}}(\boldsymbol{\rho}'_{s1}, \boldsymbol{\rho}'_{s2}, \boldsymbol{\rho}'_{i1}, \boldsymbol{\rho}'_{i2}), \tag{6.11}$$

where, $\boldsymbol{\rho}'_s \equiv (x'_s, y'_s)$, and $\boldsymbol{\rho}'_i \equiv (x'_i, y'_i)$ are the transverse co-ordinates of signal and idler photons respectively, at $z = d$. The term $\psi^*(\boldsymbol{\rho}'_{s1}, \boldsymbol{\rho}'_{i1}; d)\psi(\boldsymbol{\rho}'_{s2}, \boldsymbol{\rho}'_{i2}; d)$ is the two-photon cross-spectral density function right before the turbulence plane. The effect due to the turbulence is captured through the cross-spectral density function, which we approximate by modelling the turbulence in terms of a Gaussian function: $W_{\text{turb}}(\boldsymbol{\rho}'_{s1}, \boldsymbol{\rho}'_{s2}, \boldsymbol{\rho}'_{i1}, \boldsymbol{\rho}'_{i2}) = \exp\left[-[(\boldsymbol{\rho}'_{s2} - \boldsymbol{\rho}'_{s1})^2 + (\boldsymbol{\rho}'_{i2} - \boldsymbol{\rho}'_{i1})^2]/(2r^2)\right]$, where $r$ is the turbulence strength [188, 234].

We write the above equation as

$$W(\boldsymbol{\rho}'_{s1},\boldsymbol{\rho}'_{i1},\boldsymbol{\rho}'_{s2},\boldsymbol{\rho}'_{i2};d) = \frac{1}{(\lambda d)^4} W_{\text{turb}}(\boldsymbol{\rho}'_{s1},\boldsymbol{\rho}'_{s2},\boldsymbol{\rho}'_{i1},\boldsymbol{\rho}'_{i2}) e^{\frac{ik}{2d}(\boldsymbol{\rho}'^2_{s2}+\boldsymbol{\rho}'^2_{i2}-\boldsymbol{\rho}'^2_{s1}-\boldsymbol{\rho}'^2_{i1})} \int \psi^*(\boldsymbol{\rho}''_{s1},\boldsymbol{\rho}''_{i1};0)$$
$$\psi(\boldsymbol{\rho}''_{s2},\boldsymbol{\rho}''_{i2};0) e^{\frac{ik}{2d}(\boldsymbol{\rho}''^2_{s2}+\boldsymbol{\rho}''^2_{i2}-\boldsymbol{\rho}''^2_{s1}-\boldsymbol{\rho}''^2_{i1})} e^{-\frac{ik}{d}(\boldsymbol{\rho}'_{s2}\cdot\boldsymbol{\rho}''_{s2}-\boldsymbol{\rho}'_{s1}\cdot\boldsymbol{\rho}''_{s1})} e^{-\frac{ik}{d}(\boldsymbol{\rho}'_{i2}\cdot\boldsymbol{\rho}''_{i2}-\boldsymbol{\rho}'_{i1}\cdot\boldsymbol{\rho}''_{i1})} d\boldsymbol{\rho}''_{s2} d\boldsymbol{\rho}''_{s1} d\boldsymbol{\rho}''_{i2} d\boldsymbol{\rho}''_{i1}, \tag{6.12}$$

where $\psi(\boldsymbol{\rho}''_s,\boldsymbol{\rho}''_i;0)$ is the two-photon wave-function at the crystal plane $z=0$ and is given by [56–58]:

$$\psi(\boldsymbol{\rho}''_s,\boldsymbol{\rho}''_i;0) = A\exp\left[-\frac{(\boldsymbol{\rho}''_s+\boldsymbol{\rho}''_i)^2}{4w_0^2}\right]\exp\left[-\frac{|\boldsymbol{\rho}''_s-\boldsymbol{\rho}''_i|^2}{4\sigma_0^2}\right].$$

Now, by propagating $W(\boldsymbol{\rho}'_{s1},\boldsymbol{\rho}'_{i1},\boldsymbol{\rho}'_{s2},\boldsymbol{\rho}'_{i2};d)$ from $z=d$ up to $z=z$, we find the two-photon cross-spectral density function at $z$ and thereby the two-photon position probability distribution function $P(\boldsymbol{\rho}_s,\boldsymbol{\rho}_i;z)$:

$$P(\boldsymbol{\rho}_s,\boldsymbol{\rho}_i;z) = \frac{1}{\lambda^4(z-d)^4}\int W(\boldsymbol{\rho}'_{s1},\boldsymbol{\rho}'_{i1},\boldsymbol{\rho}'_{s2},\boldsymbol{\rho}'_{i2};d) e^{\frac{ik}{2(z-d)}(\boldsymbol{\rho}'^2_{s2}+\boldsymbol{\rho}'^2_{i2})} e^{-(\boldsymbol{\rho}'^2_{s1}+\boldsymbol{\rho}'^2_{i1})} e^{-\frac{ik}{(z-d)}\boldsymbol{\rho}_s\cdot(\boldsymbol{\rho}'_{s2}-\boldsymbol{\rho}'_{s1})}$$
$$\times\, e^{-\frac{ik}{(z-d)}\boldsymbol{\rho}_i\cdot(\boldsymbol{\rho}'_{i2}-\boldsymbol{\rho}'_{i1})} d\boldsymbol{\rho}'_{s2} d\boldsymbol{\rho}'_{s1} d\boldsymbol{\rho}'_{i2} d\boldsymbol{\rho}'_{i1}. \tag{6.13}$$

By substituting Eq. (6.12) into Eq. (6.13), we compute $P(\boldsymbol{\rho}_s,\boldsymbol{\rho}_i;z)$ as a function of $z$. We use the transformations $\boldsymbol{\rho}_s=(r_s\cos\theta_s, r_s\sin\theta_s)$ and $\boldsymbol{\rho}_i=(r_i\cos\theta_i, r_i\sin\theta_i)$ to get $P(r_s,\theta_s,r_i,\theta_i)$ and write it as

$$P(\theta_s,\theta_i;z) = \iint r_s r_i P(r_s,\theta_s,r_i,\theta_i;z)\, dr_s dr_i. \tag{6.14}$$

Figure 6.10(b) shows the theoretical $P(\theta_s,\theta_i;z)$ at different $z$ for the relevant experimental parameters of $d=15$ cm, $L=5$ mm, $w_0=507$ $\mu$m. For the theoretical plots, we use the turbulence strength $r$ as a fitting parameter and find its value to be 0.125 mm.

We now experimentally measure $P(\theta_s,\theta_i;z)$ at different $z$ using the experimental setup depicted in Figs. 6.4 with the blower heater (BH) switched on and kept at $z=15$ cm to introduce turbulence in the path of the down-converted photons. Figure 6.10(c) shows the experimentally measured $P(\theta_s,\theta_i;z)$ at different $z$. We note that the experimentally measured $P(\theta_s,\theta_i;z)$ contains some noise distribution, which gets prominent at large $z$.

This can be attributed to the fact that in the experiment, we insert a distributed turbulence in the path of the two-photon field, whereas in the theory, we approximate that as a planar turbulence. Nevertheless, the diagonal correlation in the experimentally observed $P(\theta_s, \theta_i; z)$ matches with the theoretical predictions. Using the procedure described in section 6.3.1, we extract the conditional angle uncertainty $\Delta(\theta_s|\theta_i; z)$ from Figure 6.10(c) and plot them in Figure 6.10(d). In order to minimize the effect of noise distribution on the estimation of $\Delta(\theta_s|\theta_i; z)$, we select a region of $P(\theta_s, \theta_i; z)$ as shown by the dotted red box in Fig. 6.10(c). Figure 6.10(d) shows our experimentally measured $\Delta(\theta_s|\theta_i; z)$ as a function of $z$ along with the theory prediction.

### 6.4.2 Two-photon OAM probability distribution in turbulence

First, we present a theoretical model to evaluate the influence of turbulence on the conditional OAM distribution $P(l_s|l_i; z)$. Within paraxial approximation and the Gaussian pump beam assumption [40, 155], the OAM remains conserved in SPDC. This means that if the idler photon is detected with OAM $l_i\hbar = 0$, the signal photon is guaranteed to be detected with OAM $l_s\hbar = 0$. Such a signal mode can be represented as: $\psi_s(\boldsymbol{\rho}'_s) = \exp\left[-\boldsymbol{\rho}'_s/4\sigma_r^2\right]$. For evaluating the influence of turbulence on the conditional OAM distribution $P(l_s|l_i; z)$ of the signal photon, we simply need to evaluate how the Gaussian mode $\psi_s(\boldsymbol{\rho}'_s) = \exp\left[-\boldsymbol{\rho}'_s/4\sigma_r^2\right]$ gets affected by turbulence. For this purpose, we calculate the cross-spectral density function of the signal photon right after the turbulence plane $z = d$ [see Fig. 6.10(a)]. From $z = 0$ up to $z = d$, the signal field $\psi_s(\boldsymbol{\rho}'_s)$ remains pure. Therefore, the cross-spectral density function $W(\boldsymbol{\rho}'_{s1}, \boldsymbol{\rho}'_{s2}; d)$ right after the turbulence plane $z = d$ can be written as $W(\boldsymbol{\rho}'_{s1}, \boldsymbol{\rho}'_{s2}; d) = \psi^*(\boldsymbol{\rho}'_{s1}; d)\psi(\boldsymbol{\rho}'_{s2}; d)W_{\text{turb}}(\boldsymbol{\rho}'_{s1}, \boldsymbol{\rho}'_{s2})$. where, $\boldsymbol{\rho}'_s \equiv (x'_s, y'_s)$, is the transverse co-ordinates of signal photon at $z = d$ plane. The term $\psi^*(\boldsymbol{\rho}'_{s2}; d)\psi(\boldsymbol{\rho}'_{s1}; d)$ is the cross-spectral density function of the signal photon at $z = d$ right before the turbulence plane. $W_{\text{turb}}(\boldsymbol{\rho}'_{s2}, \boldsymbol{\rho}'_{s1})$ is the cross-spectral density introduced by the turbulence. We approximate it as $W_{\text{turb}}(\boldsymbol{\rho}'_{s2}, \boldsymbol{\rho}'_{s1}) = \exp\left[-(\boldsymbol{\rho}'_{s2} - \boldsymbol{\rho}'_{s1})^2/(2r^2)\right]$, where $r$ is the turbulence strength. Therefore, the cross-spectral density of the signal

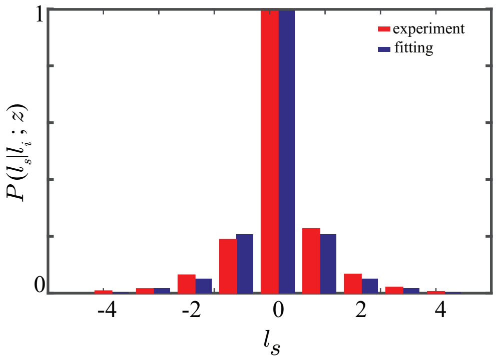

FIGURE 6.11: The experimentally measured $P(l_s|l_i;z)$ at $z = 50$ cm in turbulence. The fitting is the based on the noise model depicted in Eq. (6.18).

photon right after the turbulence becomes

$$W(\boldsymbol{\rho}'_{s1}, \boldsymbol{\rho}'_{s2}; d) = \exp\left[-\frac{\boldsymbol{\rho}'^2_{s1} + \boldsymbol{\rho}'^2_{s2}}{4\sigma_r^2}\right] \exp\left[-\frac{(\boldsymbol{\rho}'_{s2} - \boldsymbol{\rho}'_{s1})^2}{2r^2}\right]. \tag{6.15}$$

Now, by propagating the above cross-spectral density function from $z = d$ to $z = z$, we obtain the cross-spectral density function $W(\boldsymbol{\rho}_{s1}, \boldsymbol{\rho}_{s2}; z)$ at $z = z$

$$W(\boldsymbol{\rho}_{s1}, \boldsymbol{\rho}_{s2}; z) = K \exp\left[-\frac{ik}{2R(z)}(\boldsymbol{\rho}^2_{s2} - \boldsymbol{\rho}^2_{s1})\right] \exp\left[-\frac{\boldsymbol{\rho}^2_{s1} + \boldsymbol{\rho}^2_{s2}}{4\sigma_r(z)^2}\right] \exp\left[-\frac{\Delta\rho_s^2}{2r(z)^2}\right], \tag{6.16}$$

where $K$ is a $z-$dependent constant, $\Delta\rho_s = |\boldsymbol{\rho}_2 - \boldsymbol{\rho}_1|$, $r(z) = r\sqrt{1 + \left(\frac{z-d}{k_s \sigma_r \delta}\right)^2}$, $\sigma_r(z) = \sigma_r\sqrt{1 + \left(\frac{z-d}{k_s \sigma_r \delta}\right)^2}$, $\frac{1}{\delta^2} = \frac{1}{r^2} + \frac{1}{4\sigma_r^2}$, and $k_s = \pi/\lambda_p$. We use the transformation $\boldsymbol{\rho}_{s1} \equiv (r_{s1}\cos\theta_{s1}, r_{s1}\sin\theta_{s1})$ and $\boldsymbol{\rho}_{s2} \equiv (r_{s2}\cos\theta_{s2}, r_{s2}\sin\theta_{s2})$ in order to write $W(\boldsymbol{\rho}_{s1}, \boldsymbol{\rho}_{s2}; z)$ as $W_s(r_s, \theta_{s1}, \theta_{s2}; z)$. The OAM distribution of the signal photon is same as the conditional distribution $P(l_s|l_i;z)$, which we write as

$$P(l_s|l_i;z) = \iiint r_s W_s(r_s, \theta_{s1}, \theta_{s2}; z) e^{il_s(\theta_{s2} - \theta_{s1})} dr_s d\theta_{s1} d\theta_{s2}. \tag{6.17}$$

We compute the above integral numerically and find that it fits very closely to the function of type $a\exp[-b|l_s|]$, where $a$ and $b$ are constant. We also find that $P(l_s|l_i;z)$ does not depend on $z$ after propagating through turbulence. We thus write the conditional OAM distribution as

$$P(l_s|l_i;z) = a\exp\left[-b|l_s|\right] + N\exp\left[-\frac{l_s^2}{2\sigma_f^2}\right]. \tag{6.18}$$

Here, we have added the noise term for reasons described in section 6.2.2.

We repeat the experiment depicted in Fig. 6.8(b) in the OAM basis with the blower heater (BH) switched on. Figure 6.11 shows the experimentally measured $P(l_s|l_i;z)$ at $z = 50$ cm. We fit $P(l_s|l_i;z=50)$ with Eq. (6.18) and obtain the experimental uncertainty $\Delta(l_s|l_i;z)$ to be $0.94\hbar \pm 0.02\hbar$ radian$^{-1}$.

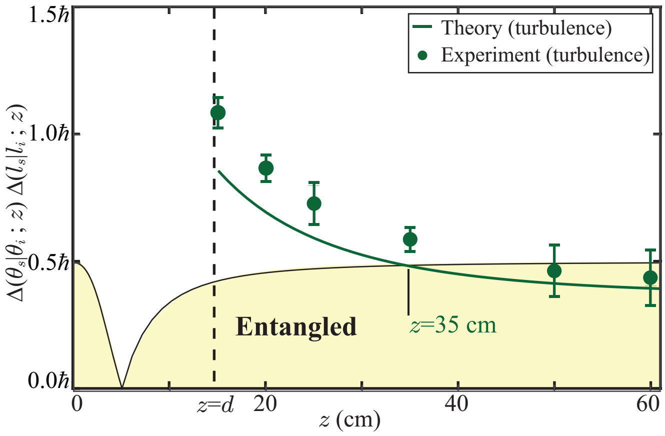

FIGURE 6.12: Conditional angle-OAM uncertainty product $\Delta(\theta_s|\theta_i;z)\Delta(l_s|l_i;z)$ as a function of the propagation distance $z$ in the presence of a turbulent medium. As indicated on the plot, in the presence of turbulence, the theoretical prediction for entanglement revival is at $z = 35$ cm while we observe it experimentally at about 45 cm.

### 6.4.3 Entanglement revival

We now plot the product $\Delta(\theta_s|\theta_i;z)\Delta(l_s|l_i;z)$ in Fig. 6.12. The solid line represents the theoretically calculated value of the uncertainty product in the presence of turbulence. Our theoretical results show that in the presence of turbulence, the angle-OAM entanglement revives at $z = 35$ cm; experimentally, we find this distance to be about 45 cm. Therefore, we find that although turbulence does adversely affect angle-OAM entanglement, its effect can be completely bypassed by just propagating the photons further ahead by some distance.

## 6.5 Summary

In summary, using the two-photon field produced by SPDC, we have reported experimental observations of propagation-induced entanglement revival in the angle-OAM bases. We have demonstrated entanglement revival even in the presence of turbulence, the only effect of which is to increase the propagation distance for revival. Once revived, the two photons remain entangled upto an arbitrary propagation distance. We note that the entanglement revival strategies in turbulence or random media are usually based on adaptive optics techniques [251, 255, 256], which are usually based on the feedback mechanism and as a result quite difficult to implement. On the other hand, in our work, we have shown that the entanglement can be revived simply by further propagating the two-photon field by some distance, without having to use any adaptive optics techniques. Thus, unlike the position-momentum bases, the angle-OAM bases bring in an independent parameter—the propagation distance—for entanglement revival in turbulent environments and can therefore have important implications for long-distance quantum information applications.

# Chapter 7

# Conclusions and Discussions

This thesis focuses on spatial coherence in spatially partially coherent fields and spatial entanglement in the two-photon SPDC field. It presents new experimental results in the context of their generation, measurement, and application.

We have begun by studying spatial coherence in spatially partially coherent fields. We have proposed and demonstrated an experimental technique for generating spatially partially coherent fields with versatile spatial coherence functions in a controllable and accurate manner. The existing techniques for generating spatially partially coherent fields are based on introducing randomness in a spatially completely coherent field and are limited in terms of control and accuracy with which these fields can be generated. In contrast, our technique does not introduce additional randomness, and it uses the coherent mode representation of a spatially partially coherent field. We have demonstrated the generation of high-quality propagation-invariant spatially stationary partially coherent fields by producing incoherent mixtures of plane waves using the combination of primary planar spatially incoherent LED source and a converging lens. To showcase the effectiveness of our generation scheme, we have generated such fields with fringe-like structures in the cross-spectral density function with good accuracy. We have used the same approach for generating the GSM fields by producing their coherent eigenmodes using an SLM and incoherently mixing them in a proportion decided by their eigenspectrum.

Next, we have focused on the measurement of spatial coherence in an optical field. We have proposed a technique for measuring two-dimensional spatial cross-spectral density function in a two-shot manner. Our technique has demonstrated that a Michelson interferometer with an additional converging lens in one of the interferometer arms results in encoding the cross-spectral density function of the input field in the output interferogram. Using this technique, we have measured several structured cross-spectral density functions with very good accuracy. In contrast, to the existing methods, our presented method does not involve any loss or require multiple measurements.

Next, we have focused on certifying the position-momentum entanglement in a two-photon field through EPR-correlation measurement. All existing schemes for measuring EPR-correlation require coincidence detection and thus suffer from several experimental difficulties that adversely affect the measurement accuracy. We have proposed that if a pure two-photon state satisfies a specific set of conditions, then the position-momentum EPR-correlations can be obtained by measuring position and momentum cross-spectral density functions of one of the photons. Our measurement scheme does not require coincidence detection. We have experimentally demonstrated this proposed scheme for pure two-photon states produced by collinear type-I SPDC. We have reported the most accurate measurement of position-momentum EPR-correlations in the literature.

Next, we have focused on applications of spatial coherence in the context of imaging and optical communication through random media. First, we have demonstrated that enhanced imaging in scattering environments can be achieved by controlling the propagation of spatial coherence of the illuminating field. Spatially partially coherent light fields have been routinely used for imaging a particular transverse plane through scattering media. However, the increasing spatial coherence length of such fields upon propagation results in degradation in image quality as the object moves away from the illuminating source. We have demonstrated imaging spatially separated transverse planes with the same image contrast using the above-mentioned partially coherent source with propagation-invariant spatial coherence. Furthermore, we have tailored the propagation of coherence of the illuminating field to access the minimum-possible spatial coherence length at the plane of the object to be imaged. Using this source, we have demonstrated imaging of different transverse planes with maximum possible image contrast. We have then demonstrated the implication of structured spatial coherence function in optical communication through turbulence. Many free-space communication protocols have used the transverse intensity profile of a structured spatially perfectly coherent field for encoding information. However, the structures in the intensity profiles of such coherent fields start to degrade in turbulent environments, and the structural degradation increases with the increase in turbulence strength. As a result, free-space communication becomes difficult with structured coherent light in turbulent environments. We have addressed this issue by demonstrating the structural robustness of both transverse intensity and spatial coherence functions of a partially coherent field in the presence of turbulence. We have shown that for a given turbulence strength, the structural degradation can be mitigated by reducing the spatial coherence length of the field.

Lastly, we have reported the revival of entanglement in angle-OAM bases through propagation. The position-momentum entanglement starts decaying as the SPDC photons propagate away from the down-conversion crystal, and the entanglement is completely lost within a few centimeters of propagation distance. As a result, the position-momentum entanglement does not remain a suitable resource for long-distance quantum information applications. To address this issue, we have explored the propagation of angle-OAM entanglement and reported that the angle-OAM entanglement displays a remarkable propagation behaviour. We have found that the angle-OAM entanglement in SPDC photons also decays within a few centimeters from the source; however, a further propagation induces the revival behaviour in entanglement. We have experimentally demonstrated the propagation-induced entanglement revival in angle-OAM bases by measuring EPR correlation upto a propagation distance of 60 cm. We have further demonstrated the entanglement revival behaviour of SPDC photons even in the turbulent environment, and its influence is to increases the propagation distance for revival.

The results of this thesis can offer new avenues in the direction of spatial correlations in optical fields. Our presented generation scheme can produce on-demand custom-designed spatial coherence functions and their structural robustness in the turbulent environment can enable a new research direction in long-distance optical communication. Our imaging scheme based on controlling the propagation of spatial coherence can be implemented in many realistic situations, including long-distance imaging, LiDAR technology, biomedical imaging, etc.

The presented measurement scheme of two-photon position-momentum EPR correlation contributes to the research theme of entanglement certification or quantification of a two-photon state by performing measurements on one of the photons. We expect that our measurement scheme can be extended for certifying other continuous variable entanglements such as time-energy and angle-OAM by developing the cross-spectral density function measurement tools in the corresponding degrees of freedom. Next, the spatial entanglement revival through propagation opens up a few interesting questions in the context of spatial entanglement propagation: how the entanglement revival feature gets affected if we change the transverse profile, propagation property, and spatial coherence of the pump, and can we engineer the propagation of entanglement using the above-mentioned pump parameters. These questions are relevant to the existing research program of quantum state engineering that attempts to enhance the performance of many applications. Moreover, strengthing of two-photon angle-correlation upon propagation has no known reported classical counterpart. Hence, such correlations can be used in quantum imaging protocols to achieve enhanced imaging of spatially separated angular objects.

We note that a significant part of this thesis has outlined the advantages of spatial partial coherence and spatial entanglement in optical fields. So far both spatial partial coherence and spatial entanglement have been used as independent tools for improving the capability and performance of many practical applications. Therefore, it can be an interesting question to explore whether combining partial coherence with spatial entanglement can offer any new advantage, which is impossible to achieve through either partial spatial coherence or spatial entanglement. This question might shed some new light on applications related to spatially entangled mixed states, a relatively less explored research theme so far.

# Appendix A

# Calculation of conditional probability distribution and cross-spectral density functions

We theoretically compute the conditional probability distribution and cross-spectral density functions of the signal photon in the position and momentum bases for the following mixed two-photon states:

### A.0.1 Introducing mixedness through turbulence

Consider a situation where the down-converted photons interact with a planar turbulence right after the crystal plane and the turbulence introduces statistical randomness in both signal and idler photon fields. As a result, the two-photon field does not remain pure after the turbulence. We describe the two-photon field through cross-spectral density function and it is written in the position basis as

$$W_{\rm tp}(\boldsymbol{\rho}_{s_1}, \boldsymbol{\rho}_{i_1}, \boldsymbol{\rho}_{s_2}, \boldsymbol{\rho}_{i_2}) = \psi^*(\boldsymbol{\rho}_{s_1}, \boldsymbol{\rho}_{i_1})\psi(\boldsymbol{\rho}_{s_2}, \boldsymbol{\rho}_{i_2})W_{\rm turb}(\boldsymbol{\rho}_{s_1}, \boldsymbol{\rho}_{s_2}, \boldsymbol{\rho}_{i_1}, \boldsymbol{\rho}_{i_2}), \tag{A.1}$$

where $\boldsymbol{\rho}_s \equiv (x_s, y_s)$ and $\boldsymbol{\rho}_i \equiv (x_i, y_i)$ are the transverse positions of the signal and idler photons respectively. $\psi^*(\boldsymbol{\rho}_{s_1}, \boldsymbol{\rho}_{i_1})\psi(\boldsymbol{\rho}_{s_2}, \boldsymbol{\rho}_{i_2})$ is the two-photon cross-spectral density function just before the turbulence, and the influence of turbulence is captured by the cross-spectral density function $W_{\rm turb}(\boldsymbol{\rho}_{s_1}, \boldsymbol{\rho}_{s_2}, \boldsymbol{\rho}_{i_1}, \boldsymbol{\rho}_{i_2}) = \exp[-6.88[|\boldsymbol{\rho}_{s_2} - \boldsymbol{\rho}_{s_1}|^2 + |\boldsymbol{\rho}_{i_2} - \boldsymbol{\rho}_{i_1}|^2]/(2r_0^2)]$ [188, 189], where $r_0$ is the Fried parameter. Smaller values of $r_0$ implies higher turbulence strength, with $r_0 = 0$ implying infinite turbulence and a completely mixed state and $r_0 = \infty$ implying no turbulence and thus a pure two-photon state. The above cross-spectral density function can be rewritten in the following product form

$$W_{\rm tp}(\boldsymbol{\rho}_{s_1}, \boldsymbol{\rho}_{i_1}, \boldsymbol{\rho}_{s_2}, \boldsymbol{\rho}_{i_2}) = W_{\rm tp}(x_{s_1}, x_{i_1}, x_{s_2}, x_{i_2}) W_{\rm tp}(y_{s_1}, y_{s_2}, y_{i_1}, y_{i_2}), \tag{A.2}$$

where

$$W_{\rm tp}(x_{s_1}, x_{i_1}, x_{s_2}, x_{i_2}) = \exp\left[-\frac{(x_{s_1} + x_{i_1})^2 + (x_{s_2} + x_{i_2})^2}{4w_0^2}\right] \exp\left[-\frac{(x_{s_1} - x_{i_1})^2 + (x_{s_2} - x_{i_2})^2}{4\sigma_0^2}\right] \\ \times \exp\left[-6.88\frac{(x_{s_2} - x_{s_1})^2 + (x_{i_2} - x_{i_1})^2}{2r_0^2}\right], \tag{A.3}$$

$$W_{\rm tp}(y_{s_1}, y_{i_1}, y_{s_2}, y_{i_2}) = \exp\left[-\frac{(y_{s_1} + y_{i_1})^2 + (y_{s_2} + y_{i_2})^2}{4w_0^2}\right] \exp\left[-\frac{(y_{s_1} - x_{i_1})^2 + (y_{s_2} - y_{i_2})^2}{4\sigma_0^2}\right] \\ \times \exp\left[-6.88\frac{(y_{s_2} - y_{s_1})^2 + (y_{i_2} - y_{i_1})^2}{2r_0^2}\right]. \tag{A.4}$$

The one dimensional conditional position probability distribution function $P(x_s|x_i = 0)$ and cross-spectral density function $W(x_s, -x_s)$ of the signal photon are given by

$$P(x_s|x_i = 0) = W_{\rm tp}(x_s, x_i = 0, x_s, x_i = 0) \tag{A.5}$$

$$W(x_s, -x_s) = \int W_{\rm tp}(x_s, x_i, -x_s, x_i) dx_i. \tag{A.6}$$

From the above equations, we calculate $P(x_s|x_i = 0)$ and $W(x_s, -x_s)$ as a function of $r_0$ and we plot them together in Fig. A.1(a). Both $P(x_s|x_i = 0)$ and $W(x_s, -x_s)$ plots have been scaled such that their maximum value is one. We find that $W(x_s, -x_s)$ shows a good match with $P(x_s|x_i = 0)$ at different $r_0$.

We next find the two-photon momentum cross-spectral density function $W_{\text{tp}}(\boldsymbol{p}_{s_1}, \boldsymbol{p}_{i_1}, \boldsymbol{p}_{s_2}, \boldsymbol{p}_{i_2})$ right after the turbulence plane using the following equation

$$W_{\text{tp}}(\boldsymbol{p}_{s_1}, \boldsymbol{p}_{i_1}, \boldsymbol{p}_{s_2}, \boldsymbol{p}_{i_2}) = \int W_{\text{tp}}(\boldsymbol{\rho}_{s_1}, \boldsymbol{\rho}_{i_1}, \boldsymbol{\rho}_{s_2}, \boldsymbol{\rho}_{i_2}) e^{-i(\boldsymbol{\rho}_{s_1}\cdot\boldsymbol{p}_{s_1} + \boldsymbol{\rho}_{i_1}\cdot\boldsymbol{p}_{i_1} - \boldsymbol{\rho}_{s_2}\cdot\boldsymbol{p}_{s_2} - \boldsymbol{\rho}_{s_2}\cdot\boldsymbol{p}_{s_2})/\hbar} d\boldsymbol{\rho}_{s_1} d\boldsymbol{\rho}_{s_2} d\boldsymbol{\rho}_{i_1} d\boldsymbol{\rho}_{i_2} \tag{A.7}$$

where $\boldsymbol{p}_s \equiv (p_{xs}, p_{ys})$ and $\boldsymbol{p}_i \equiv (p_{xi}, p_{yi})$ are transverse momenta of the signal and idler photons respectively. The one dimensional conditional momentum probability distribution function $P(p_{xs}|p_{xi} = 0)$ and cross-spectral density function $W(p_{xs}, -p_{xs})$ of the signal photon are given by

$$P(p_{xs}|p_{xi} = 0) = W_{\text{tp}}(p_{xs}, p_{xi} = 0, p_{xs}, p_{xi} = 0), \tag{A.8}$$

$$W(p_{xs}, -p_{xs}) = \int W_{\text{tp}}(p_{xs}, p_{xi}, -p_{xs}, p_{xi}) dp_{xi}, \tag{A.9}$$

where

$$W_{\text{tp}}(p_{xs_1}, p_{xi_1}, p_{xs_2}, p_{xi_2}) = \int W_{\text{tp}}(x_{s_1}, x_{i_1}, x_{s_2}, x_{i_2}) e^{-i(x_{s_1}p_{xs_1} + x_{i_1}p_{xi_1} - x_{s_2}p_{xs_2} - x_{i_2}p_{xi_2})/\hbar} dx_{s_1} dx_{s_2} dx_{i_1} dx_{i_2}. \tag{A.10}$$

Figure A.1(b) shows $P(p_{xs}|p_{xi} = 0)$ (solid curve) and $W(p_{xs}, -p_{xs})$ (dashed curve) at different $r_0$. Both $P(p_{xs}|p_{xi} = 0)$ and $W(p_{xs}, -p_{xs})$ plots have been scaled such that their maximum value is one. We find that with the decrease in turbulence strength the mismatch between $W(p_{sx}, -p_{sx})$ and $P(p_{sx}|p_{ix} = 0)$ decreases. Now from the above conditional probability distribution and cross-spectral density functions we evaluate $\mathcal{E}$ as a function of $r_0$ and it is shown in Fig.2(a) in chapter 4.

### A.0.2 Introducing mixedness by using a spatially partially coherent pump

we consider the situation in which the two-photon states is produced by SPDC using a spatially partially coherent pump field. To keep the analysis simple, we consider a

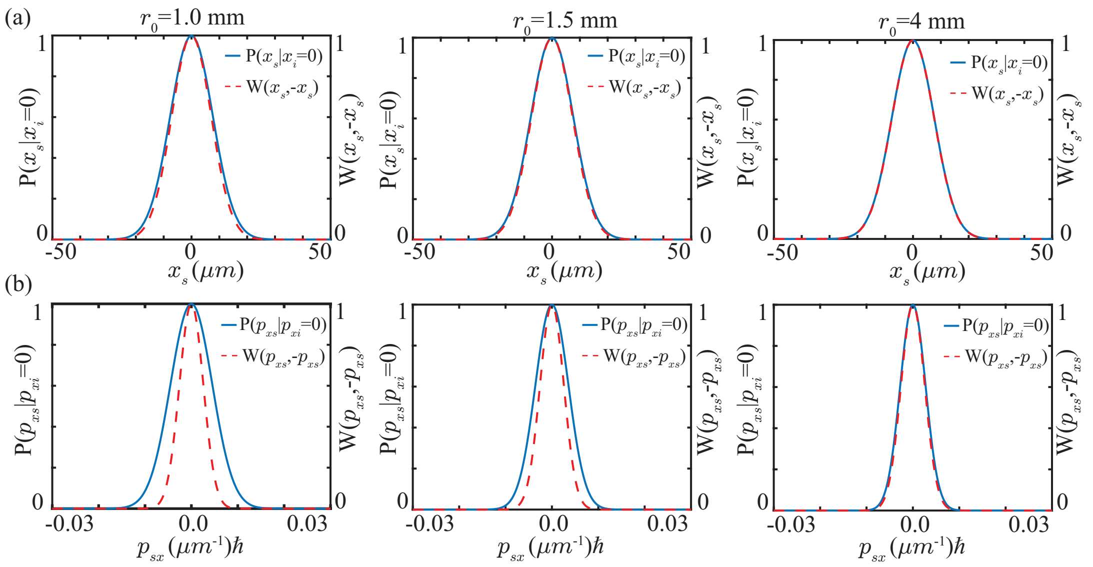

FIGURE A.1: (a) Conditional position probability distribution function $P(x_s|x_i = 0)$ (solid curve) and position cross-spectral density function $W(x_s, -x_s)$ (dashed curve) of the signal photon at different $r_0$. (b) Conditional momentum probability distribution function $P(p_{xs}|p_{xi} = 0)$ (solid curve) and momentum cross-spectral density function $W(p_{xs}, -p_{xs})$ (dashed curve) of the signal photon at different $r_0$.

Gaussian Schell Model (GSM) field [70] as the spatially partially coherent pump field. The two-photon position cross-spectral density function is given by [192]

$$W(\boldsymbol{\rho}_{s_1}, \boldsymbol{\rho}_{i_1}, \boldsymbol{\rho}_{s_2}, \boldsymbol{\rho}_{i_2}) = A \exp\left[-\frac{|\boldsymbol{\rho}_{s_1} + \boldsymbol{\rho}_{i_1}|^2 + |\boldsymbol{\rho}_{s_2} + \boldsymbol{\rho}_{i_2}|^2}{4w_0^2}\right]$$
$$\times \exp\left[-\frac{|\boldsymbol{\rho}_{s_2} + \boldsymbol{\rho}_{i_2} - \boldsymbol{\rho}_{s_1} - \boldsymbol{\rho}_{i_1}|^2}{2\sigma_c^2}\right] \exp\left[-\frac{|\boldsymbol{\rho}_{s_1} - \boldsymbol{\rho}_{i_1}|^2 + |\boldsymbol{\rho}_{s_2} - \boldsymbol{\rho}_{i_2}|^2}{4\sigma_0^2}\right], \quad \text{(A.11)}$$

where $w_0$ and $\sigma_c$ are the pump beam waist and pump transverse spatial coherence length respectively, at the crystal plane. The transverse spatial coherence length of the pump $\sigma_c$ ranges from 0 to $\infty$, with $\sigma_c = 0$ implying a completely mixed state and $\sigma_c = \infty$ implying a pure state. The above cross-spectral density function in Eq. (A.11) can be rewritten as

$$W_{\text{tp}}(\boldsymbol{\rho}_{s_1}, \boldsymbol{\rho}_{i_1}, \boldsymbol{\rho}_{s_2}, \boldsymbol{\rho}_{i_2}) = W_{\text{tp}}(x_{s_1}, x_{i_1}, x_{s_2}, x_{i_2}) W_{\text{tp}}(y_{s_1}, y_{s_2}, y_{i_1}, y_{i_2}), \quad \text{(A.12)}$$

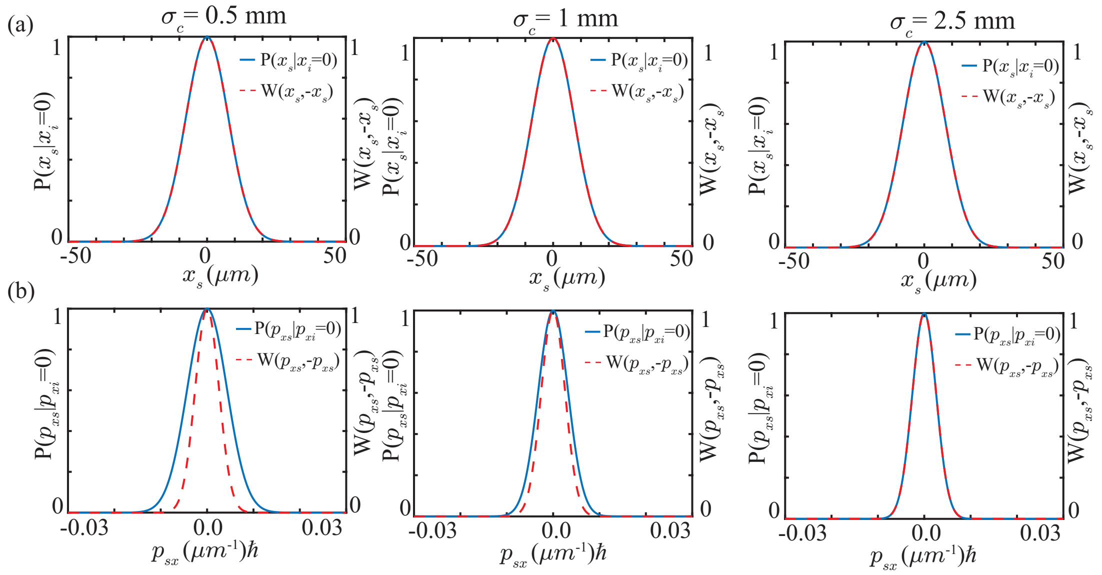

FIGURE A.2: (a) Conditional position probability distribution function $P(x_s|x_i = 0)$ (solid curve) and position cross-spectral density function $W(x_s, -x_s)$ (dashed curve) of the signal photon at different $\sigma_c$. (b) Conditional momentum probability distribution function $P(p_{xs}|p_{xi} = 0)$ (solid curve) and momentum cross-spectral density function $W(p_{xs}, -p_{xs})$ (dashed curve) of the signal photon at different $\sigma_c$.

where

$$\begin{aligned} W_{\text{tp}}(x_{s_1}, x_{i_1}, x_{s_2}, x_{i_2}) = A' \exp\left[-\frac{(x_{s_1} + x_{i_1})^2 + (x_{s_2} + x_{i_2})^2}{4w_0^2}\right] \\ \times \exp\left[-\frac{(x_{s_2} + x_{i_2} - x_{s_1} - x_{i_1})^2}{2\sigma_c^2}\right] \exp\left[-\frac{(x_{s_1} - x_{i_1})^2 + (x_{s_2} - x_{i_2})^2}{4\sigma_0^2}\right], \end{aligned} \tag{A.13}$$

$$\begin{aligned} W_{\text{tp}}(y_{s_1}, y_{i_1}, y_{s_2}, y_{i_2}) = A' \exp\left[-\frac{(y_{s_1} + y_{i_1})^2 + (y_{s_2} + y_{i_2})^2}{4w_0^2}\right] \\ \times \exp\left[-\frac{(y_{s_2} + y_{i_2} - y_{s_1} - y_{i_1})^2}{2\sigma_c^2}\right] \exp\left[-\frac{(y_{s_1} - y_{i_1})^2 + (y_{s_2} - y_{i_2})^2}{4\sigma_0^2}\right], \end{aligned} \tag{A.14}$$

From the above equations we evaluate the one dimensional conditional position probability distribution $P(x_s|x_i = 0)$ and cross-spectral density function $W(x_s, -x_s)$ respectively, of the signal photon and plot them together in Fig. A.2(b) as a function of $\sigma_c$. We scale both $P(x_s|x_i = 0)$ and $W(x_s, -x_s)$ such that their maximum value is one. We find that $W(x_s, -x_s)$ almost matches with $P(x_s|x_i = 0)$ at different $\sigma_c$. We next use

Eq. (A.13) along with Eq. (A.10) to evaluate two-photon momentum cross-spectral density function $W_{\rm tp}(p_{xs_1}, p_{xi_1}, p_{xs_2}, p_{xi_2})$ and from that we plot $P(p_{xs}|p_{xi} = 0)$ (solid curve) and $W(p_{xs}, -p_{xs})$ (dashed curve) in Fig. A.2(b) as a function of $\sigma_c$. We scale both $P(p_{xs}|p_{xi}=0)$ and $W(p_{xs}, -p_{xs})$ such that their maximum value is one. We find that the mismatch between $W(p_{xs}, -p_{xs})$ and $P(p_{xs}|p_{xi} = 0)$ decreases with the increase in $\sigma_c$. From the above conditional probability distribution functions and cross-spectral density functions, we evaluate $\mathcal{E}$ as a function of $\sigma_c$ and it is shown in Fig.2(b) in chapter 4.

# Appendix B

# Derivation of two-photon and single-photon position probability distribution

## B.1 Two-photon position probability distribution as a function of propagation distance $z$

Figure B.1 illustrates the propagation of two-photon SPDC field from the crystal plane at $z = 0$ to a propagation distance $z$. For a Gaussian pump with beam waist at the crystal plane $z = 0$, the two-photon wavefunction in the position basis at the crystal plane $z = 0$ is given by [56–58]:

$$\psi(\boldsymbol{\rho}_s'', \boldsymbol{\rho}_i''; 0) = A \exp\left[-\frac{(\boldsymbol{\rho}_s'' + \boldsymbol{\rho}_i'')^2}{4w_0^2}\right] \exp\left[-\frac{|\boldsymbol{\rho}_s'' - \boldsymbol{\rho}_i''|^2}{4\sigma_0^2}\right], \tag{B.1}$$

where $\boldsymbol{\rho}_s'' \equiv (x_s'', y_s'')$ and $\boldsymbol{\rho}_i'' \equiv (x_i'', y_i'')$ are the transverse positions of the signal and idler photons, respectively at $z = 0$, and $k = \pi/\lambda_p$. Also, $w_0$ is the pump beam waist at $z = 0$, $\sigma_0 = \sqrt{0.455L\lambda_p/2\pi}$, $L$ is the length of the crystal, and $\lambda_p$ is the wavelength of the pump field. Now we use the propagation equation in Ref [57,58] for propagating the two-

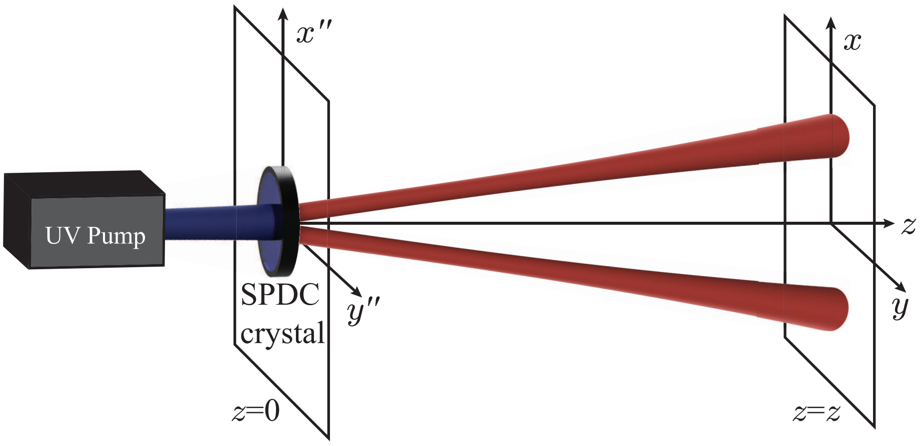

FIGURE B.1: Illustrating the propagation of the two-photon down-converted field.

photon wavefuntion $\psi(\boldsymbol{\rho}''_s, \boldsymbol{\rho}''_i; 0)$ from $z = 0$ to $z = z$ plane and write the wavefunction $\psi(\boldsymbol{\rho}_s, \boldsymbol{\rho}_i; z)$ at $z = z$ as

$$\psi(\boldsymbol{\rho}_s, \boldsymbol{\rho}_i; z) = \left(1/z^2\right) e^{\frac{ik}{2z}(\boldsymbol{\rho}_s^2+\boldsymbol{\rho}_i^2)} \int \psi(\boldsymbol{\rho}''_s, \boldsymbol{\rho}''_i; 0) e^{\frac{ik}{2z}(\boldsymbol{\rho}''^2_s+\boldsymbol{\rho}''^2_i)} e^{-\frac{ik}{z}(\boldsymbol{\rho}_s\cdot\boldsymbol{\rho}''_s+\boldsymbol{\rho}_i\cdot\boldsymbol{\rho}''_i)} d\boldsymbol{\rho}''_s d\boldsymbol{\rho}''_i, \tag{B.2}$$

where $\boldsymbol{\rho}_s \equiv (x_s, y_s)$ and $\boldsymbol{\rho}_i \equiv (x_i, y_i)$ are the transverse positions of the signal and idler photons, respectively, at $z = z$. We use the transformation

$$\boldsymbol{\rho}''_+ = (\boldsymbol{\rho}''_s + \boldsymbol{\rho}''_i)/\sqrt{2} \qquad \boldsymbol{\rho}''_- = (\boldsymbol{\rho}''_s - \boldsymbol{\rho}''_i)/\sqrt{2}, \tag{B.3}$$

$$\boldsymbol{\rho}_+ = (\boldsymbol{\rho}_s + \boldsymbol{\rho}_i)/\sqrt{2} \qquad \boldsymbol{\rho}_- = (\boldsymbol{\rho}_s - \boldsymbol{\rho}_i)/\sqrt{2}, \tag{B.4}$$

in Eq. (B.2) and it takes the following form

$$\psi(\boldsymbol{\rho}_+, \boldsymbol{\rho}_-; z) = \left(1/z^2\right) e^{\frac{ik}{2z}(\boldsymbol{\rho}_+^2+\boldsymbol{\rho}_-^2)} \int \psi(\boldsymbol{\rho}''_+, \boldsymbol{\rho}''_-; 0) e^{\frac{ik}{2z}(\boldsymbol{\rho}''^2_++\boldsymbol{\rho}''^2_-)} e^{-\frac{ik}{z}(\boldsymbol{\rho}_+\cdot\boldsymbol{\rho}''_++\boldsymbol{\rho}_-\cdot\boldsymbol{\rho}''_-)} d\boldsymbol{\rho}''_+ d\boldsymbol{\rho}''_-. \tag{B.5}$$

Here $\psi(\boldsymbol{\rho}''_+, \boldsymbol{\rho}''_-; 0) = A \exp\left[-\boldsymbol{\rho}''^2_+/2w_0^2\right] \exp\left[-\boldsymbol{\rho}''^2_-/2\sigma_0^2\right]$ and we write the above Eq. (B.5) in the following product form

$$\psi(\boldsymbol{\rho}_+, \boldsymbol{\rho}_-; z) = \left(A/z^2\right) \psi(\boldsymbol{\rho}_+; z) \times \psi(\boldsymbol{\rho}_-; z), \tag{B.6}$$

where

$$\psi(\boldsymbol{\rho}_+;z) = e^{\frac{ik}{2z}\boldsymbol{\rho}_+^2}\int \exp\left[-\boldsymbol{\rho}_+''^2/2w_0^2\right] e^{\frac{ik}{2z}\boldsymbol{\rho}_+''^2} e^{-\frac{ik}{z}\boldsymbol{\rho}_+\cdot\boldsymbol{\rho}_+''} d\boldsymbol{\rho}_+'',$$
$$\psi(\boldsymbol{\rho}_-;z) = e^{\frac{ik}{2z}\boldsymbol{\rho}_-^2}\int \exp\left[-\boldsymbol{\rho}_-''^2/2\sigma_0^2\right] e^{\frac{ik}{2z}\boldsymbol{\rho}_-''^2} e^{-\frac{ik}{z}\boldsymbol{\rho}_-\cdot\boldsymbol{\rho}_-''} d\boldsymbol{\rho}_-''$$

We now evaluate the above intergrals analytically and obtain the expression for two-photon wavefunction $\psi(\boldsymbol{\rho}_s,\boldsymbol{\rho}_i;z)$ in the following form

$$\psi(\boldsymbol{\rho}_s,\boldsymbol{\rho}_i;z) = A'\exp\left[-\frac{(\boldsymbol{\rho}_s+\boldsymbol{\rho}_i)^2}{4w(z)^2}\right]\exp\left[-\frac{|\boldsymbol{\rho}_s-\boldsymbol{\rho}_i|^2}{4\sigma(z)^2}\right]\exp\left[-\frac{ik}{4z}c(z)(\boldsymbol{\rho}_s+\boldsymbol{\rho}_i)^2\right] \times\exp\left[-\frac{ik}{4z}d(z)(\boldsymbol{\rho}_s-\boldsymbol{\rho}_i)^2\right], \quad \text{(B.7)}$$

where $c(z) = 1/\left(1+k^2w_0^4/z^2\right)$, $d(z) = 1/\left(1+k^2\sigma_0^4/z^2\right)$, $w(z) = w_0\sqrt{1+z^2/(k^2w_0^4)}$, and $\sigma(z) = \sigma_0\sqrt{1+z^2/(k^2\sigma_0^4)}$. $A'$ is a $z$-dependent constant. The corresponding two-photon proabaility distribution function is given by

$$P(\boldsymbol{\rho}_s,\boldsymbol{\rho}_i;z) = |\psi^*(\boldsymbol{\rho}_s,\boldsymbol{\rho}_i;z)\psi(\boldsymbol{\rho}_s,\boldsymbol{\rho}_i;z)|^2 = |A'|^2\exp\left[-\frac{(\boldsymbol{\rho}_s+\boldsymbol{\rho}_i)^2}{2w(z)^2}\right]\exp\left[-\frac{|\boldsymbol{\rho}_s-\boldsymbol{\rho}_i|^2}{2\sigma(z)^2}\right]. \quad \text{(B.8)}$$

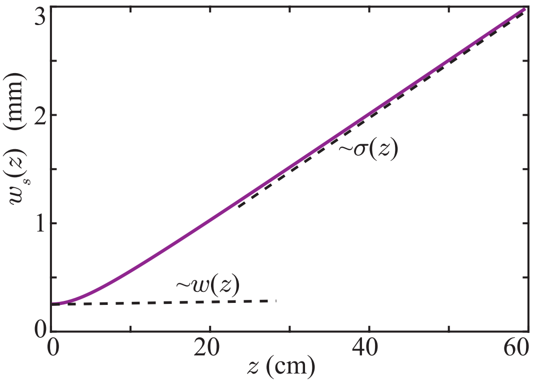

FIGURE B.2: Numerically calculated position uncertainty $w_s(z)$ of the signal photon as a function of $z$. The two dotted lines show the $z$-scaling of the uncertainty in the near- and far-field regions.

## B.2 Calculation of signal photon position uncertainty

From the two-photon probability distribution in Eq. (6.2), we find the position probability distribution $P(\boldsymbol{\rho}_s; z)$ of the signal photon in the following manner

$$P(\boldsymbol{\rho}_s; z) = \int P(\boldsymbol{\rho}_s, \boldsymbol{\rho}_i; z) d\boldsymbol{\rho}_i = N \exp\left[-\rho_s^2/2w_s(z)^2\right], \tag{B.9}$$

where $w_s(z) = \Delta(y_s|y_i; z)/\sqrt{1-(D/C)^2}$ is the position uncertainty of the signal photon. We now plot $w_s(z)$ as a function of $z$ in Fig. (B.2). We find that $w_s(z)$ monotonically increases upon propagation. The two dotted lines in Fig. (B.2) show the near- and far-field $z$ scaling of $w_s(z)$. We find that in the near- and far-field behaves as $w_s(z) \approx w(z)/2$ and $w_s(z) \approx \sigma(z)/2$ respectively.

# Appendix C

# Near-field and far-field behaviours of the conditional position and angle uncertainties

## C.1 Conditional position uncertainty

The two-photon position probability distribution function is given by Eq. (6.2). By setting $\boldsymbol{\rho}_i = 0$, we write the conditional positional probability distribution function $P(\boldsymbol{\rho}_s|\boldsymbol{\rho}_i; z)$ as

$$\begin{aligned} P(\boldsymbol{\rho}_s|\boldsymbol{\rho}_i; z) &= |A|^2 \exp\left[-\frac{\rho_s^2}{2}\left(\frac{1}{w(z)^2} + \frac{1}{\sigma(z)^2}\right)\right], \\ \text{where} \qquad w(z)^2 &= w_0^2\left[1 + \frac{z^2}{k^2 w_0^4}\right], \\ \sigma(z)^2 &= \sigma_0^2\left[1 + \frac{z^2}{k^2 \sigma_0^4}\right], \end{aligned} \tag{C.1}$$

and $|\boldsymbol{\rho}_s|^2 = \rho_s^2$. From Eq. (C.1), we obtain the conditional position uncertainty in the $y$-direction as

$$\Delta(y_s|y_i; z) = \sqrt{\frac{1}{\frac{1}{w(z)^2} + \frac{1}{\sigma(z)^2}}}. \tag{C.2}$$

For the experimental parameters of interest, we have $w_0 = 507$ $\mu$m and $\sigma_0 = 11.3$ $\mu$m. Therefore, in the near-field region, we have $w(z) \gg \sigma(z)$ and thus the conditional uncertainty in the $y$-direction becomes

$$\Delta(y_s|y_i;z) \approx \sigma(z) = \sigma_0\sqrt{1+\frac{z^2}{k^2\sigma_0^4}}. \tag{C.3}$$

In the far-field, we have $w(z) \ll \sigma(z)$ and thus the conditional uncertainty in the $y$-direction becomes

$$\Delta(y_s|y_i;z) \approx w(z) = w_0\sqrt{1+\frac{z^2}{k^2 w_0^4}}. \tag{C.4}$$

From Eqs. (C.3) and (C.4), we find that the conditional position uncertainty $\Delta(y_s|y_i;z)$ increases monotonically as a function of $z$ in both the near- and far-field regions. While the uncertainty increases as $\sigma(z)$ in the near-field, it increases as $w(z)$ in the far-field. Figure C.1(a) shows the plot of the numerically calculated conditional position uncertainty $\Delta(y_s|y_i;z)$ as a function of $z$. The two dotted lines in Fig. C.1(a) show the $z$-scaling of the uncertainty in the near- and far-field regions.

### C.1.1 Conditional angle uncertainty

The two-photon angle probability distribution function is given by Eq. (6.4). The conditional angle probability distribution function $P(\theta_s|\theta_i;z)$ is obtained by setting $\theta_i = 0$ in Eq. (6.4). As we are interested only in obtaining the near- and far-field scaling of the conditional angle uncertainty, we take $P(r_s,\theta_s,r_i,\theta_i;z) = P(r_s,\theta_s,\theta_i;z)\delta(r_s - r_i)$. Thus we write Eq. (6.4) as

$$P(\theta_s,\theta_i;z) = \int P(r,\theta_s,\theta_i;z)r^2dr. \tag{C.5}$$

Using Eq. (6.3) and the Mathematica software, we evaluate the above integral and obtain

$$P(\theta_s,\theta_i;z) = \frac{P_0}{[C + D\cos(\theta_s - \theta_i)]^{3/2}}, \tag{C.6}$$

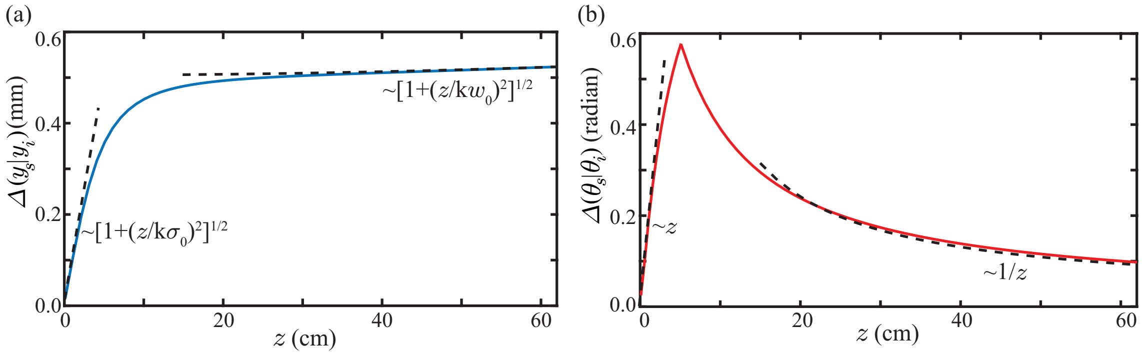

FIGURE C.1: (a) Numerically calculated conditional position uncertainty $\Delta(y_s|y_i;z)$ as a function of $z$. The two dotted lines show the $z$-scaling of the uncertainty in the near- and far-field regions. (b) Numerically calculated conditional angle uncertainty $\Delta(\theta_s|\theta_i;z)$ as a function of $z$. The two dotted lines show the $z$-scaling of the uncertainty in the near- and far-field regions.

where

$$\begin{aligned} P_0 &= \frac{|A|^2\sqrt{\pi/2}}{8}, \\ C &= \frac{1}{2}\left[\frac{1}{w(z)^2}+\frac{1}{\sigma(z)^2}\right], \\ D &= \frac{1}{2}\left[\frac{1}{w(z)^2}-\frac{1}{\sigma(z)^2}\right]. \end{aligned} \tag{C.7}$$

The ratio of $C$ and $D$ can be written as

$$\begin{aligned} \frac{C}{D} &= \frac{w(z)^2+\sigma(z)^2}{-w(z)^2+\sigma(z)^2} \\ &= \frac{(w_0^2+\sigma_0^2)+\frac{z^2}{k^2}\left[\frac{1}{w_0^2}+\frac{1}{\sigma_0^2}\right]}{(-w_0^2+\sigma_0^2)+\frac{z^2}{k^2}\left[-\frac{1}{w_0^2}+\frac{1}{\sigma_0^2}\right]}. \end{aligned} \tag{C.8}$$

In our experiments, we have $w_0 = 507\ \mu$m and $\sigma_0 = 11\ \mu$m. Thus we have $w_0 \gg \sigma_0$, and under this approximation we write the above ratio as

$$\frac{C}{D} = \frac{w_0^2+z^2/(k^2\sigma_0^2)}{-w_0^2+z^2/(k^2\sigma_0^2)} = \frac{z^2+k^2\sigma_0^2w_0^2}{z^2-k^2\sigma_0^2w_0^2}. \tag{C.9}$$

Next, we study the behaviour of $P(\theta_s, \theta_i; z)$ in the near field regions. We make use of the fact that for $\theta_i = 0$, $P(\theta_s, \theta_i; z)$ is maximum at $\theta_s = 0$. Therefore, we have

$$P^{\mathrm{max}}(\theta_s, \theta_i = 0; z) = \frac{P_0}{[C+D]^{3/2}}. \tag{C.10}$$

We next find the value of $\theta_s$ at which $P(\theta_s, \theta_i; z) = P^{\mathrm{max}}(\theta_s, \theta_i = 0; z)/2$, in which case $\theta_s$ can be taken as the half-width of the conditional angle probability distribution function. We thus equate

$$\begin{aligned} & P(\theta_s, \theta_i; z) = P^{\mathrm{max}}(\theta_s, \theta_i = 0; z)/2 \\ \text{or,} \quad & \frac{P_0}{[C + D\cos\theta_s]^{3/2}} = \frac{P_0}{2[C+D]^{3/2}} \\ \text{or,} \quad & C + D\cos\theta_s = 2^{2/3}(C+D) \end{aligned} \tag{C.11}$$

Solving the above equation, we get two solutions for $\theta_s$:

$$\begin{aligned} & \theta_s^{(+)} = \cos^{-1}\left[(2^{2/3}-1)\frac{C}{D} + 2^{2/3}\right] \\ \text{and} \qquad & \theta_s^{(-)} = -\cos^{-1}\left[(2^{2/3}-1)\frac{C}{D} + 2^{2/3}\right]. \end{aligned} \tag{C.12}$$

The angle uncertainty $\Delta(\theta_s|\theta_i; z)$ can therefore be written as

$$\begin{aligned} \Delta(\theta_s|\theta_i; z) &= \theta_s^{(+)} - \theta_s^{(-)} \\ &= 2\cos^{-1}\left[(2^{2/3}-1)\frac{C}{D} + 2^{2/3}\right]. \end{aligned} \tag{C.13}$$

Using the approximation $\cos^{-1} x = \sqrt{2(1-x)}$ for $x \in [0, 1]$, we write the above uncertainty as:

$$\Delta(\theta_s|\theta_i; z) = 2\sqrt{2(2^{2/3}-1)\left[-\frac{C}{D} - 1\right]}. \tag{C.14}$$

Substituting for $C/D$ from Eq. (C.8), we obtain

$$\Delta(\theta_s|\theta_i;z) = 4\sqrt{2^{2/3}-1} \times \sqrt{\frac{z^2}{k^2\sigma_0^2 w_0^2 - z^2}}. \tag{C.15}$$

In the near-field regions, we have $k^2\sigma_0^2 w_0^2 \gg z^2$. Therefore, we can write the angle uncertainty in the near-field regions as

$$\Delta(\theta_s|\theta_i;z) \approx \frac{4\sqrt{2^{2/3}-1}}{k\sigma_0 w_0} z. \tag{C.16}$$

Thus in the near-field regions the angle uncertainty increases linearly with $z$. In the far-field, we use the fact that for $\theta_i = 0$, $P(\theta_s, \theta_i; z)$ is maximum at $\theta_s = \pi$. Therefore, in the far-filed we have $P^{\max}(\theta_s, \theta_i = 0; z) = P_0/[C-D]^{3/2}$. Now, proceeding in the similar manner as above, and using the far-field approximation $z^2 \gg k^2\sigma_0^2 w_0^2$, we find the angle uncertainty in the far-field regions to be

$$\Delta(\theta_s|\theta_i;z) \approx 4\sqrt{2^{2/3}-1} k\sigma_0 w_0 \frac{1}{z} \tag{C.17}$$

We thus find that in the far-field region the angle uncertainty $\Delta(\theta_s|\theta_i;z)$ becomes inversely proportional to $z$ and as a consequence decreases upon propagation. Figure C.1(b) shows the numerically calculated conditional angle uncertainty $\Delta(\theta_s|\theta_i;z)$ as a function of $z$. The two dotted lines in Fig. C.1(b) show the $z$-scaling of the uncertainty in the near- and far-field regions.

# Appendix D

# Coincidence measurement with EMCCD camera

Here we outline how we use an EMCCD camera with a 512 × 512 pixel grid with each pixel $16 \times 16\ \mu\text{m}^2$ for measuring coincidence counting. For this, we record $10^6$-$10^7$ images of the SPDC field with an exposure time of 1 ms - 5 ms over a few hours with average flux of 0.5 - 2.0 photons per pixel. We operate the camera at -60°C with the electron-multiplication gain of 1000, the horizontal pixel readout rate of 5-17 MHz, the vertical pixel shift speed of 0.3 $\mu$s, and the vertical clock amplitude of +4V. As detailed in Ref. [81, 257], the coincidence count between two pixels or two group of pixels, $p$ and $q$, of the EMCCD camera is given by

$$c_{pq} = \frac{1}{N}\sum_{k=1}^{N} n_p^{(k)} n_q^{(k)} - \frac{1}{N^2}\sum_{k=1}^{N} n_p^{(k)} \sum_{j=1}^{N} n_q^{(j)}, \tag{D.1}$$

where $n_p^{(k)}$ and $n_q^{(k)}$ are the number of photons detected at pixel (or pixel group) $p$ and $q$, respectively, in the $k^{th}$ image. In SPDC, a signal and idler photon pair gets generated within a very short time interval, usually of the order of 100 fs, which is much smaller than the exposure time $(1-5$ ms) of the EMCCD camera. Therefore, in all likelihood, the signal and idler photons belonging to a pair arrive within the same image. However, within the same image, we can also have pairs of photons that are not the same down-converted pair. These cause background noise and are called the accidental coincidences. This accidental coincidence count between the pixels (or pixel groups) $p$ and $q$ can be estimated by computing the coincidence counts between $k^{th}$ and $(k+1)^{th}$ images and it is given by (as described in appendix G of Ref. [257])

$$c'_{pq} = \frac{1}{N}\sum_{k=1}^{N} n_p^{(k)} n_q^{(k+1)} - \frac{1}{N^2}\sum_{k=1}^{N} n_p^{(k)} \sum_{j=1}^{N} n_q^{(j)}. \tag{D.2}$$

Here $n_p^{(k)}$ is the photon count at pixel (or pixel group) $p$ of $k^{th}$ image and $n_q^{(k+1)}$ is the photon count at pixel (or pixel group) $q$ of $(k+1)^{th}$ image. We take $n_q^{(i+1)} = n_q^{(1)}$ for the last image $(k = N)$. We subtract Eq. (D.2) from Eq. (D.1), and obtain the genuine coincidences between two pixels (or pixel groups) $p$ and $q$ as:

$$C_{pq} = \frac{1}{N}\sum_{k=1}^{N} n_p^{(k)} n_q^{(k)} - \frac{1}{N}\sum_{k=1}^{N} n_p^{(k)} n_q^{(k+1)}. \tag{D.3}$$

In Eq. (D.3), above, the first term is the coincidences due to down-converted pairs along with accidental coincidences while the second term is the accidental coincidences.

# References

[1] M. Born and E. Wolf, Principles of optics: electromagnetic theory of propagation, interference and diffraction of light. Elsevier, 2013. 1

[2] L. Mandel and E. Wolf, Optical Coherence and Quantum Optics. Cambridge university press, New York, 1995. 1, 11, 13, 14, 32, 47, 91, 93

[3] F. Zernike, "The concept of degree of coherence and its application to optical problems," Physica **5** No. 8, (1938) 785–795. 1, 47

[4] P. A. M. Dirac, The principles of quantum mechanics. No. 27. Oxford university press, 1981. 1

[5] L. Mandel, "Quantum effects in one-photon and two-photon interference," Review of Modern Physics (1999) 460–473. 1

[6] T. Herzog, J. Rarity, H. Weinfurter, and A. Zeilinger, "Frustrated two-photon creation via interference," Physical review letters **72** No. 5, (1994) 629. 1

[7] D. Strekalov, T. Pittman, and Y. Shih, "What we can learn about single photons in a two-photon interference experiment," Physical Review A **57** No. 1, (1998) 567. 1

[8] C.-K. Hong, Z.-Y. Ou, and L. Mandel, "Measurement of subpicosecond time intervals between two photons by interference," Physical review letters **59** No. 18, (1987) 2044. 1, 10

[9] J. D. Franson, "Bell inequality for position and time," Physical review letters **62** No. 19, (1989) 2205. 1, 2, 10

[10] X. Zou, L. J. Wang, and L. Mandel, "Induced coherence and indistinguishability in optical interference," Physical review letters **67** No. 3, (1991) 318. 1

[11] M. O. Scully, B.-G. Englert, and H. Walther, "Quantum optical tests of complementarity," Nature **351** No. 6322, (1991) 111–116. 1

[12] A. K. Jha, M. N. O'Sullivan, K. W. C. Chan, and R. W. Boyd, "Temporal coherence and indistinguishability in two-photon interference effects," Physical Review A **77** No. 2, (2008) 021801. 1, 63

[13] L. Mandel, "Coherence and indistinguishability," Optics letters **16** No. 23, (1991) 1882–1883. 1

[14] E. Wolf, “A macroscopic theory of interference and diffraction of light from finite sources ii. fields with a spectral range of arbitrary width,” Proceedings of the Royal Society of London. Series A. Mathematical and Physical Sciences **230** No. 1181, (1955) 246–265. 1

[15] E. Wolf, “New theory of partial coherence in the space–frequency domain. part i: spectra and cross spectra of steady-state sources,” JOSA **72** No. 3, (1982) 343–351. 1, 3, 4, 14, 15

[16] E. Wolf, “New theory of partial coherence in the space-frequency domain. part ii: Steady-state fields and higher-order correlations,” JOSA A **3** No. 1, (1986) 76–85. 1

[17] R. J. Glauber, “The quantum theory of optical coherence,” Physical Review **130** No. 6, (1963) 2529. 1, 7, 9

[18] R. J. Glauber, Quantum theory of optical coherence: selected papers and lectures. John Wiley & Sons, 2007. 1

[19] E. Sudarshan, “Equivalence of semiclassical and quantum mechanical descriptions of statistical light beams,” Physical Review Letters **10** No. 7, (1963) 277. 1, 10

[20] J. W. Goodman, Statistical optics. John Wiley & Sons, 2015. 1, 12, 80

[21] B. Redding, M. A. Choma, and H. Cao, “Speckle-free laser imaging using random laser illumination,” Nature photonics **6** No. 6, (2012) 355–359. 1, 27, 47, 76

[22] B. Redding, P. Ahmadi, V. Mokan, M. Seifert, M. A. Choma, and H. Cao, “Low-spatial-coherence high-radiance broadband fiber source for speckle free imaging,” Optics letters **40** No. 20, (2015) 4607–4610. 1, 76

[23] B. Redding, A. Cerjan, X. Huang, M. L. Lee, A. D. Stone, M. A. Choma, and H. Cao, “Low spatial coherence electrically pumped semiconductor laser for speckle-free full-field imaging,” Proceedings of the National Academy of Sciences **112** No. 5, (2015) 1304–1309. 1, 76

[24] J. Mertz, Introduction to optical microscopy. Cambridge University Press, 2019. 1, 86

[25] X. Chen, M. E. Kandel, and G. Popescu, “Spatial light interference microscopy: principle and applications to biomedicine,” Advances in Optics and Photonics **13** No. 2, (2021) 353–425. 1, 47

[26] D. Huang, E. A. Swanson, C. P. Lin, J. S. Schuman, W. G. Stinson, W. Chang, M. R. Hee, T. Flotte, K. Gregory, C. A. Puliafito, *et al.*, “Optical coherence tomography,” Science **254** No. 5035, (1991) 1178–1181. 2, 76

[27] M. Batarseh, S. Sukhov, Z. Shen, H. Gemar, R. Rezvani, and A. Dogariu, “Passive sensing around the corner using spatial coherence,” Nature communications **9** No. 1, (2018) 1–6. 2, 47

[28] J. M. Auñón and M. Nieto-Vesperinas, “Optical forces on small particles from partially coherent light,” JOSA A **29** No. 7, (2012) 1389–1398. 2

[29] F. Devaux, A. Mosset, P.-A. Moreau, and E. Lantz, “Imaging spatiotemporal hong-ou-mandel interference of biphoton states of extremely high schmidt number,” Physical Review X **10** No. 3, (2020) 031031. 2

[30] J. Brendel, E. Mohler, and W. Martienssen, “Time-resolved dual-beam two-photon interferences with high visibility,” Physical review letters **66** No. 9, (1991) 1142. 2, 10

[31] P. G. Kwiat, A. M. Steinberg, and R. Y. Chiao, “High-visibility interference in a bell-inequality experiment for energy and time,” Physical Review A **47** No. 4, (1993) R2472. 2

[32] A. K. Jha, M. Malik, and R. W. Boyd, “Exploring energy-time entanglement using geometric phase,” Physical review letters **101** No. 18, (2008) 180405. 2

[33] A. Einstein, B. Podolsky, and N. Rosen, “Can quantum-mechanical description of physical reality be considered complete?,” Physical review **47** No. 10, (1935) 777. 2, 18, 57, 61, 99, 108

[34] N. Friis, G. Vitagliano, M. Malik, and M. Huber, “Entanglement certification from theory to experiment,” Nature Reviews Physics **1** No. 1, (2019) 72–87. 2, 99

[35] R. Horodecki, P. Horodecki, M. Horodecki, and K. Horodecki, “Quantum entanglement,” Reviews of modern physics **81** No. 2, (2009) 865. 2, 99

[36] C. H. Bennett, G. Brassard, C. Crépeau, R. Jozsa, A. Peres, and W. K. Wootters, “Teleporting an unknown quantum state via dual classical and einstein-podolsky-rosen channels,” Physical review letters **70** No. 13, (1993) 1895. 2

[37] M. A. Nielsen and I. L. Chuang, “Quantum computation and quantum information,” Phys. Today **54** No. 2, (2001) 60. 2

[38] M. Giustina, M. A. Versteegh, S. Wengerowsky, J. Handsteiner, A. Hochrainer, K. Phelan, F. Steinlechner, J. Kofler, J.-Å. Larsson, C. Abellán, *et al.*, “Significant-loophole-free test of bell’s theorem with entangled photons,” Physical review letters **115** No. 25, (2015) 250401. 2, 99

[39] J. C. Howell, R. S. Bennink, S. J. Bentley, and R. Boyd, “Realization of the einstein-podolsky-rosen paradox using momentum-and position-entangled photons from spontaneous parametric down conversion,” Physical Review Letters **92** No. 21, (2004) 210403. 2, 20, 57, 58, 68, 69, 99, 104, 108

[40] J. Leach, B. Jack, J. Romero, A. K. Jha, A. M. Yao, S. Franke-Arnold, D. G. Ireland, R. W. Boyd, S. M. Barnett, and M. J. Padgett, “Quantum correlations in optical angle–orbital angular momentum variables,” Science **329** No. 5992, (2010) 662–665. 2, 20, 21, 57, 58, 73, 99, 107, 115, 119

[41] I. A. Khan and J. C. Howell, “Experimental demonstration of high two-photon time-energy entanglement,” Physical Review A **73** No. 3, (2006) 031801. 2, 21, 58, 73

[42] P.-A. Moreau, E. Toninelli, P. A. Morris, R. S. Aspden, T. Gregory, G. Spalding, R. W. Boyd, and M. J. Padgett, "Resolution limits of quantum ghost imaging," Optics express **26** No. 6, (2018) 7528–7536. 2, 100

[43] R. S. Aspden, D. S. Tasca, R. W. Boyd, and M. J. Padgett, "Epr-based ghost imaging using a single-photon-sensitive camera," New Journal of Physics **15** No. 7, (2013) 073032. 2, 58, 72, 73, 100

[44] H. Defienne, P. Cameron, B. Ndagano, A. Lyons, M. Reichert, J. Zhao, E. Charbon, J. W. Fleischer, and D. Faccio, "Pixel super-resolution using spatially-entangled photon pairs," arXiv preprint arXiv:2105.10351 (2021) . 2, 58, 100

[45] E. Toninelli, P.-A. Moreau, T. Gregory, A. Mihalyi, M. Edgar, N. Radwell, and M. Padgett, "Resolution-enhanced quantum imaging by centroid estimation of biphotons," Optica **6** No. 3, (2019) 347–353. 2, 8, 58, 73, 100

[46] N. Bornman, M. Agnew, F. Zhu, A. Vallés, A. Forbes, and J. Leach, "Ghost imaging using entanglement-swapped photons," npj Quantum Information **5** No. 1, (2019) 1–6. 2, 100

[47] H. Defienne, B. Ndagano, A. Lyons, and D. Faccio, "Polarization entanglement-enabled quantum holography," Nature Physics (2021) 1–7. 2, 58, 73, 100

[48] F. Devaux, A. Mosset, F. Bassignot, and E. Lantz, "Quantum holography with biphotons of high schmidt number," Physical Review A **99** No. 3, (2019) 033854. 2, 100

[49] S. Töpfer, M. G. Basset, J. Fuenzalida, F. Steinlechner, J. P. Torres, and M. Gräfe, "Quantum holography with undetected light," arXiv preprint arXiv:2106.04904 (2021) . 2

[50] G. Brida, M. Genovese, and I. R. Berchera, "Experimental realization of sub-shot-noise quantum imaging," Nature Photonics **4** No. 4, (2010) 227. 2, 58, 100

[51] L. Zhang, C. Silberhorn, and I. A. Walmsley, "Secure quantum key distribution using continuous variables of single photons," Physical review letters **100** No. 11, (2008) 110504. 2, 73, 100

[52] P. B. Dixon, G. A. Howland, J. Schneeloch, and J. C. Howell, "Quantum mutual information capacity for high-dimensional entangled states," Physical review letters **108** No. 14, (2012) 143603. 2, 58, 64, 68, 69, 72, 73

[53] J. Leach, E. Bolduc, D. J. Gauthier, and R. W. Boyd, "Secure information capacity of photons entangled in many dimensions," Physical Review A **85** No. 6, (2012) 060304. 2, 20, 57, 58, 68, 69, 115

[54] M. Almeida, S. Walborn, and P. S. Ribeiro, "Experimental investigation of quantum key distribution with position and momentum of photon pairs," Physical Review A **72** No. 2, (2005) 022313. 2, 58, 72, 100

[55] K. Chan, C. Law, and J. Eberly, "Localized single-photon wave functions in free space," Physical review letters **88** No. 10, (2002) 100402. 8

[56] M. P. Edgar, D. S. Tasca, F. Izdebski, R. E. Warburton, J. Leach, M. Agnew, G. S. Buller, R. W. Boyd, and M. J. Padgett, "Imaging high-dimensional spatial entanglement with a camera," Nature communications **3** No. 1, (2012) 1–6. 8, 20, 57, 58, 64, 67, 68, 69, 99, 102, 118, 135

[57] J. Schneeloch and J. C. Howell, "Introduction to the transverse spatial correlations in spontaneous parametric down-conversion through the biphoton birth zone," Journal of Optics **18** No. 5, (2016) 053501. 8, 64, 100, 102, 107, 118, 135

[58] S. P. Walborn, C. Monken, S. Pádua, and P. S. Ribeiro, "Spatial correlations in parametric down-conversion," Physics Reports **495** No. 4-5, (2010) 87–139. 8, 100, 102, 118, 135

[59] C. Mehta and E. Wolf, "Coherence properties of blackbody radiation. i. correlation tensors of the classical field," Physical Review **134** No. 5A, (1964) A1143. 10

[60] C. Mehta and E. Wolf, "Coherence properties of blackbody radiation. ii. correlation tensors of the quantized field," Physical Review **134** No. 5A, (1964) A1149. 10

[61] P. B. Dixon, G. Howland, M. Malik, D. J. Starling, R. Boyd, and J. C. Howell, "Heralded single-photon partial coherence," Physical Review A **82** No. 2, (2010) 023801. 10, 60

[62] P. Walther, J.-W. Pan, M. Aspelmeyer, R. Ursin, S. Gasparoni, and A. Zeilinger, "De broglie wavelength of a non-local four-photon state," Nature **429** No. 6988, (2004) 158–161. 10

[63] S. Agne, T. Kauten, J. Jin, E. Meyer-Scott, J. Z. Salvail, D. R. Hamel, K. J. Resch, G. Weihs, and T. Jennewein, "Observation of genuine three-photon interference," Physical review letters **118** No. 15, (2017) 153602. 10

[64] P. Milonni and J. Eberly, Laser Physics. John Wiley & Sons, 2010. 11

[65] A. R. Thompson, J. M. Moran, and G. W. Swenson, "Van cittert–zernike theorem, spatial coherence, and scattering," in Interferometry and Synthesis in Radio Astronomy, p. 767–786. Springer, 2017. 13

[66] E. Collett and E. Wolf, "Is complete spatial coherence necessary for the generation of highly directional light beams?," Optics letters **2** No. 2, (1978) 27–29. 13

[67] A. T. Friberg and R. J. Sudol, "Propagation parameters of gaussian schell-model beams," Optics Communications **41** No. 6, (1982) 383–387. 13

[68] Q. He, J. Turunen, and A. T. Friberg, "Propagation and imaging experiments with gaussian schell-model beams," Optics communications **67** No. 4, (1988) 245–250. 13

[69] G. Gbur and T. Visser, "The structure of partially coherent fields," Progress in optics **55** (2010) 285–341. 13

[70] L. Mandel and E. Wolf, Optical coherence and quantum optics. Cambridge university press, 1995. 14, 15, 27, 71, 132

[71] E. P. Wigner, "On the quantum correction for thermodynamic equilibrium," in Part I: Physical Chemistry. Part II: Solid State Physics, p. 110–120. Springer, 1997. 16

[72] A. Walther, "Radiometry and coherence," JOSA **58** No. 9, (1968) 1256–1259. 16

[73] M. J. Bastiaans, “The wigner distribution function applied to optical signals and systems,” Optics communications **25** No. 1, (1978) 26–30. 16

[74] M. J. Bastiaans, “Application of the wigner distribution function to partially coherent light,” JOSA A **3** No. 8, (1986) 1227–1238. 16

[75] M. Hillery, R. F. O’Connell, M. O. Scully, and E. P. Wigner, “Distribution functions in physics: Fundamentals,” Physics reports **106** No. 3, (1984) 121–167. 16

[76] L. Waller, G. Situ, and J. W. Fleischer, “Phase-space measurement and coherence synthesis of optical beams,” Nature Photonics **6** No. 7, (2012) 474–479. 17

[77] E. Giese, R. Fickler, W. Zhang, L. Chen, and R. W. Boyd, “Influence of pump coherence on the quantum properties of spontaneous parametric down-conversion,” Physica Scripta **93** No. 8, (2018) 084001. 20

[78] W. Zhang, R. Fickler, E. Giese, L. Chen, and R. W. Boyd, “Influence of pump coherence on the generation of position-momentum entanglement in optical parametric down-conversion,” Optics express **27** No. 15, (2019) 20745–20753. 20, 57, 58, 72

[79] M. Dâ€™Angelo, Y.-H. Kim, S. P. Kulik, and Y. Shih, “Identifying entanglement using quantum ghost interference and imaging,” Physical review letters **92** No. 23, (2004) 233601. 20, 57, 58

[80] M. N. Oâ€™Sullivan-Hale, I. A. Khan, R. W. Boyd, and J. C. Howell, “Pixel entanglement: experimental realization of optically entangled d= 3 and d= 6 qudits,” Physical review letters **94** No. 22, (2005) 220501. 20, 57, 58

[81] M. Reichert, H. Defienne, and J. W. Fleischer, “Massively parallel coincidence counting of high-dimensional entangled states,” Scientific reports **8** No. 1, (2018) 1–7. 20, 57, 58, 145

[82] P.-A. Moreau, F. Devaux, and E. Lantz, “Einstein-podolsky-rosen paradox in twin images,” Physical review letters **113** No. 16, (2014) 160401. 20, 57, 58, 68, 69, 99

[83] J.-C. Lee, K.-K. Park, T.-M. Zhao, and Y.-H. Kim, “Einstein-podolsky-rosen entanglement of narrow-band photons from cold atoms,” Physical review letters **117** No. 25, (2016) 250501. 20, 73

[84] C. Wang, C.-H. Lee, and Y.-H. Kim, “Generation and characterization of position-momentum entangled photon pairs in a hot atomic gas cell,” Optics Express **27** No. 24, (2019) 34611–34617. 20

[85] S. M. Barnett and D. Pegg, “Quantum theory of rotation angles,” Physical Review A **41** No. 7, (1990) 3427. 20

[86] S. Franke-Arnold, S. M. Barnett, E. Yao, J. Leach, J. Courtial, and M. Padgett, “Uncertainty principle for angular position and angular momentum,” New Journal of Physics **6** No. 1, (2004) 103. 20

[87] Y. Zeng, D. Zhang, F. Tang, S. Fang, W. Zhang, and L. Chen, “Controlling quantum correlations in optical-angle–orbital-angular-momentum variables,” Physical Review A **104** No. 5, (2021) 053719. 20, 21

[88] L. Chen, T. Ma, X. Qiu, D. Zhang, W. Zhang, and R. W. Boyd, “Realization of the einstein-podolsky-rosen paradox using radial position and radial momentum variables,” Physical Review Letters **123** No. 6, (2019) 060403. 21, 58, 99

[89] Y. Mei, Y. Zhou, S. Zhang, J. Li, K. Liao, H. Yan, S.-L. Zhu, and S. Du, “Einstein-podolsky-rosen energy-time entanglement of narrow-band biphotons,” Physical Review Letters **124** No. 1, (2020) 010509. 21, 58, 73, 99

[90] M. Fadel, L. Ares, A. Luis, and Q. He, “Number-phase entanglement and einstein-podolsky-rosen steering,” Physical Review A **101** No. 5, (2020) 052117. 21, 57

[91] R. W. Boyd, Nonlinear optics. Academic press, 2020. 21, 22

[92] C. Hong and L. Mandel, “Theory of parametric frequency down conversion of light,” Physical Review A **31** No. 4, (1985) 2409. 22, 23, 62

[93] R. Loudon, The quantum theory of light. OUP Oxford, 2000. 24

[94] Y. Cai, Y. Chen, and F. Wang, “Generation and propagation of partially coherent beams with nonconventional correlation functions: a review,” JOSA A **31** No. 9, (2014) 2083–2096. 27

[95] M. W. Hyde IV, S. Basu, D. G. Voelz, and X. Xiao, “Experimentally generating any desired partially coherent schell-model source using phase-only control,” Journal of Applied Physics **118** No. 9, (2015) 093102. 27

[96] B. Karamata, P. Lambelet, M. Laubscher, R. Salathé, and T. Lasser, “Spatially incoherent illumination as a mechanism for cross-talk suppression in wide-field optical coherence tomography,” Optics letters **29** No. 7, (2004) 736–738. 27, 47

[97] J. C. Ricklin and F. M. Davidson, “Atmospheric turbulence effects on a partially coherent gaussian beam: implications for free-space laser communication,” JOSA A **19** No. 9, (2002) 1794–1802. 27, 47, 77

[98] Y. Gu and G. Gbur, “Scintillation of pseudo-bessel correlated beams in atmospheric turbulence,” JOSA A **27** No. 12, (2010) 2621–2629. 27, 47

[99] C. Zhao, Y. Cai, X. Lu, and H. T. Eyyuboğlu, “Radiation force of coherent and partially coherent flat-topped beams on a rayleigh particle,” Optics express **17** No. 3, (2009) 1753–1765. 27

[100] Y. Dong, F. Wang, C. Zhao, and Y. Cai, “Effect of spatial coherence on propagation, tight focusing, and radiation forces of an azimuthally polarized beam,” Physical Review A **86** No. 1, (2012) 013840. 27

[101] D. Kermisch, “Partially coherent image processing by laser scanning,” JOSA **65** No. 8, (1975) 887–891. 27

[102] Y. Kato, K. Mima, N. Miyanaga, S. Arinaga, Y. Kitagawa, M. Nakatsuka, Yamanaka, and C, "Random phasing of high-power lasers for uniform target acceleration and plasma-instability suppression," Physical Review Letters **53** No. 11, (1984) 1057. 27

[103] A. Beléndez, L. Carretero, and A. Fimia, "The use of partially coherent light to reduce the efficiency of silver halide noise gratings," Optics communications **98** No. 4-6, (1993) 236–240. 27

[104] T. van Dijk, D. G. Fischer, T. D. Visser, and E. Wolf, "Effects of spatial coherence on the angular distribution of radiant intensity generated by scattering on a sphere," Physical review letters **104** No. 17, (2010) 173902. 27

[105] M. Takeda, W. Wang, Z. Duan, and Y. Miyamoto, "Coherence holography," Optics express **13** No. 23, (2005) 9629–9635. 27, 28

[106] M. Takeda, "Spatial stationarity of statistical optical fields for coherence holography and photon correlation holography," Optics letters **38** No. 17, (2013) 3452–3455. 27

[107] J. Turunen, A. Vasara, and A. T. Friberg, "Propagation invariance and self-imaging in variable-coherence optics," JOSA A **8** No. 2, (1991) 282–289. 27, 28, 32, 36, 47

[108] A. T. Friberg, A. Vasara, and J. Turunen, "Partially coherent propagation-invariant beams: passage through paraxial optical systems," Physical Review A **43** No. 12, (1991) 7079. 27

[109] M. W. Kowarz and G. S. Agarwal, "Bessel-beam representation for partially coherent fields," JOSA A **12** No. 6, (1995) 1324–1330. 27

[110] F. Gori, G. Guattari, and C. Padovani, "Modal expansion for j0-correlated schell-model sources," Optics communications **64** No. 4, (1987) 311–316. 27

[111] D. N. Naik, T. Ezawa, Y. Miyamoto, and M. Takeda, "3-d coherence holography using a modified sagnac radial shearing interferometer with geometric phase shift," Optics express **17** No. 13, (2009) 10633–10641. 27, 28

[112] D. N. Naik, R. K. Singh, T. Ezawa, Y. Miyamoto, and M. Takeda, "Photon correlation holography," Optics express **19** No. 2, (2011) 1408–1421. 27, 28, 45

[113] Y. Ohtsuka, Y. Nozoe, and Y. Imai, "Acoustically modified spatial coherence in optical fresnel diffraction region," Optics Communications **35** No. 2, (1980) 157–160. 27, 28, 32, 76

[114] Y. Chen, F. Wang, L. Liu, C. Zhao, Y. Cai, and O. Korotkova, "Generation and propagation of a partially coherent vector beam with special correlation functions," Physical Review A **89** No. 1, (2014) 013801. 28, 45, 76

[115] Y. Chen, L. Liu, F. Wang, C. Zhao, and Y. Cai, "Elliptical laguerre-gaussian correlated schell-model beam," Optics express **22** No. 11, (2014) 13975–13987. 28, 45

[116] F. Wang, C. Liang, Y. Yuan, and Y. Cai, "Generalized multi-gaussian correlated schell-model beam: from theory to experiment," Optics express **22** No. 19, (2014) 23456–23464. 28, 45, 76

[117] G. Piquero, F. Gori, P. Romanini, M. Santarsiero, R. Borghi, and A. Mondello, "Synthesis of partially polarized gaussian schell-model sources," Optics communications **208** No. 1-3, (2002) 9–16. 28

[118] A. S. Ostrovsky, G. Rodríguez-Zurita, C. Meneses-Fabián, M. Á. Olvera-Santamaría, and C. Rickenstorff-Parrao, "Experimental generating the partially coherent and partially polarized electromagnetic source," Optics express **18** No. 12, (2010) 12864–12871. 28, 45

[119] F. Wang, X. Liu, Y. Yuan, and Y. Cai, "Experimental generation of partially coherent beams with different complex degrees of coherence," Optics letters **38** No. 11, (2013) 1814–1816. 28, 45

[120] F. Wang, Y. Cai, Y. Dong, and O. Korotkova, "Experimental generation of a radially polarized beam with controllable spatial coherence," Applied Physics Letters **100** No. 5, (2012) 051108. 28, 45

[121] F. Wang and Y. Cai, "Experimental generation of a partially coherent flat-topped beam," Optics letters **33** No. 16, (2008) 1795–1797. 28, 45

[122] S. Basu, M. W. Hyde, X. Xiao, D. G. Voelz, and O. Korotkova, "Computational approaches for generating electromagnetic gaussian schell-model sources," Optics express **22** No. 26, (2014) 31691–31707. 28, 76

[123] A. S. Ostrovsky, G. Martínez-Niconoff, V. Arrizón, P. Martínez-Vara, M. A. Olvera-Santamaría, and C. Rickenstorff-Parrao, "Modulation of coherence and polarization using liquid crystal spatial light modulators," Optics express **17** No. 7, (2009) 5257–5264. 28, 76

[124] A. Ostrovsky, M. Olvera, C. Rickenstorff, G. Martínez-Niconoff, and V. Arrizón, "Generation of a secondary electromagnetic source with desired statistical properties," Optics communications **283** No. 22, (2010) 4490–4493. 28

[125] T. Shirai and E. Wolf, "Coherence and polarization of electromagnetic beams modulated by random phase screens and their changes on propagation in free space," JOSA A **21** No. 10, (2004) 1907–1916. 28

[126] C. Liang, F. Wang, X. Liu, Y. Cai, and O. Korotkova, "Experimental generation of cosine-gaussian-correlated schell-model beams with rectangular symmetry," Optics letters **39** No. 4, (2014) 769–772. 28, 45

[127] Y. Chen, F. Wang, C. Zhao, and Y. Cai, "Experimental demonstration of a laguerre-gaussian correlated schell-model vortex beam," Optics express **22** No. 5, (2014) 5826–5838. 28, 45

[128] S. Aarav, A. Bhattacharjee, H. Wanare, and A. K. Jha, "Efficient generation of propagation-invariant spatially stationary partially coherent fields," Physical Review A **96** No. 3, (2017) 033815. 29, 52, 53, 77, 91, 92

[129] A. Bhattacharjee, R. Sahu, and A. K. Jha, "Generation of a gaussian schell-model field as a mixture of its coherent modes," Journal of Optics **21** No. 10, (2019) 105601. 29

[130] W. Carter and E. Wolf, “Coherence and radiometry with quasihomogeneous planar sources,” JOSA **67** No. 6, (1977) 785–796. 30, 76

[131] H. D. L. Pires, J. Woudenberg, and M. Van Exter, “Measurement of the orbital angular momentum spectrum of partially coherent beams,” Optics letters **35** No. 6, (2010) 889–891. 30, 33

[132] M. Born and E. Wolf, Principles of optics: electromagnetic theory of propagation, interference and diffraction of light. Elsevier, 2013. 30

[133] J. W. Goodman, Introduction to Fourier optics. Roberts and Company Publishers, 2005. 30

[134] M. Tziraki, R. Jones, P. French, M. Melloch, and D. Nolte, “Photorefractive holography for imaging through turbid media using low coherence light,” Applied Physics B: Lasers and Optics **70** No. 1, (2000) 151–154. 33, 76

[135] N. Savage, “Digital spatial light modulators,” Nature Photonics **3** No. 3, (2009) 170–172. 33

[136] M. T. Gruneisen, W. A. Miller, R. C. Dymale, and A. M. Sweiti, “Holographic generation of complex fields with spatial light modulators: application to quantum key distribution,” Applied Optics **47** No. 4, (2008) A32–A42. 33

[137] K. M. Johnson, D. J. McKnight, and I. Underwood, “Smart spatial light modulators using liquid crystals on silicon,” IEEE Journal of Quantum Electronics **29** No. 2, (1993) 699–714. 33

[138] A. Starikov and E. Wolf, “Coherent-mode representation of gaussian schell-model sources and of their radiation fields,” JOSA **72** No. 7, (1982) 923–928. 38

[139] V. Arrizón, U. Ruiz, R. Carrada, and L. A. González, “Pixelated phase computer holograms for the accurate encoding of scalar complex fields,” JOSA A **24** No. 11, (2007) 3500–3507. 39

[140] X. Chen, J. Li, S. M. H. Rafsanjani, and O. Korotkova, “Synthesis of im-bessel correlated beams via coherent modes,” Optics letters **43** No. 15, (2018) 3590–3593. 45

[141] M. W. Hyde, “Partially coherent sources generated from the incoherent sum of fields containing random-width bessel functions,” Optics letters **44** No. 7, (2019) 1603–1606. 45

[142] F. Wang, H. Lv, Y. Chen, Y. Cai, and O. Korotkova, “Three modal decompositions of gaussian schell-model sources: comparative analysis,” Optics Express **29** No. 19, (2021) 29676–29689. 45

[143] B. Kanseri and H. C. Kandpal, “Experimental determination of two-point stokes parameters for a partially coherent broadband light beam,” Optics Communications **283** No. 23, (2010) 4558–4562. 47

[144] M. Santarsiero and R. Borghi, “Measuring spatial coherence by using a reversed-wavefront young interferometer,” Optics letters **31** No. 7, (2006) 861–863. 47

[145] B. Kanseri and H. C. Kandpal, "Experimental determination of electric cross-spectral density matrix and generalized stokes parameters for a laser beam," Optics letters **33** No. 20, (2008) 2410–2412. 47

[146] A. Efimov, "Lateral-shearing, delay-dithering mach–zehnder interferometer for spatial coherence measurement," Optics letters **38** No. 22, (2013) 4522–4525. 48

[147] C. Iaconis and I. A. Walmsley, "Direct measurement of the two-point field correlation function," Optics letters **21** No. 21, (1996) 1783–1785. 48

[148] K. Nugent, "Wave field determination using three-dimensional intensity information," Physical review letters **68** No. 15, (1992) 2261. 48

[149] D. Smithey, M. Beck, M. G. Raymer, and A. Faridani, "Measurement of the wigner distribution and the density matrix of a light mode using optical homodyne tomography: Application to squeezed states and the vacuum," Physical review letters **70** No. 9, (1993) 1244. 48

[150] C. Rydberg and J. Bengtsson, "Numerical algorithm for the retrieval of spatial coherence properties of partially coherent beams from transverse intensity measurements," Optics express **15** No. 21, (2007) 13613–13623. 48

[151] J. C. Petruccelli, L. Tian, and G. Barbastathis, "The transport of intensity equation for optical path length recovery using partially coherent illumination," Optics express **21** No. 12, (2013) 14430–14441. 48

[152] J. K. Wood, K. A. Sharma, S. Cho, T. G. Brown, and M. A. Alonso, "Using shadows to measure spatial coherence," Optics letters **39** No. 16, (2014) 4927–4930. 48

[153] K. A. Sharma, T. G. Brown, and M. A. Alonso, "Phase-space approach to lensless measurements of optical field correlations," Optics express **24** No. 14, (2016) 16099–16110. 48

[154] H. W. Wessely and J. O. Bolstad, "Interferometric technique for measuring the spatial-correlation function of optical radiation fields," JOSA **60** No. 5, (1970) 678–682. 48

[155] G. Kulkarni, R. Sahu, O. S. Magaña-Loaiza, R. W. Boyd, and A. K. Jha, "Single-shot measurement of the orbital-angular-momentum spectrum of light," Nature communications **8** (2017) 1054. 48, 51, 52, 58, 65, 67, 107, 119

[156] A. K. Jha, G. S. Agarwal, and R. W. Boyd, "Partial angular coherence and the angular schmidt spectrum of entangled two-photon fields," Physical Review A **84** No. 6, (2011) 063847. 48, 58

[157] A. Bhattacharjee, S. Aarav, and A. K. Jha, "Two-shot measurement of spatial coherence," Applied Physics Letters **113** No. 5, (2018) 051102. 48, 65, 67

[158] J. S. Bell, "On the Einstein Podolsky Rosen paradox," Physics **1** (1964) 195. 57

[159] W. K. Wootters, "Entanglement of formation of an arbitrary state of two qubits," Physical Review Letters **80** No. 10, (1998) 2245. 57, 58

[160] W. P. Bowen, R. Schnabel, P. K. Lam, and T. C. Ralph, "Experimental investigation of criteria for continuous variable entanglement," Physical Review Letters **90** No. 4, (2003) 043601. 57

[161] R. Simon, "Peres-horodecki separability criterion for continuous variable systems," Physical Review Letters **84** No. 12, (2000) 2726. 57

[162] G. Giedke, B. Kraus, M. Lewenstein, and J. Cirac, "Entanglement criteria for all bipartite gaussian states," Physical review letters **87** No. 16, (2001) 167904. 57

[163] G. Adesso and F. Illuminati, "Entanglement in continuous-variable systems: recent advances and current perspectives," Journal of Physics A: Mathematical and Theoretical **40** No. 28, (2007) 7821. 57

[164] L. Hutter, G. Lima, and S. P. Walborn, "Boosting entanglement generation in down-conversion with incoherent illumination," Physical Review Letters **125** No. 19, (2020) 193602. 57

[165] A. Saboia, F. Toscano, and S. Walborn, "Family of continuous-variable entanglement criteria using general entropy functions," Physical Review A **83** No. 3, (2011) 032307. 57

[166] A. E. Rastegin, "Rényi formulation of entanglement criteria for continuous variables," Physical Review A **95** No. 4, (2017) 042334. 57

[167] C. Ockeloen-Korppi, E. Damskägg, J.-M. Pirkkalainen, M. Asjad, A. Clerk, F. Massel, M. Woolley, and M. Sillanpää, "Stabilized entanglement of massive mechanical oscillators," Nature **556** No. 7702, (2018) 478–482. 58

[168] M. Fadel, T. Zibold, B. Décamps, and P. Treutlein, "Spatial entanglement patterns and einstein-podolsky-rosen steering in bose-einstein condensates," Science **360** No. 6387, (2018) 409–413. 58

[169] V. Josse, A. Dantan, A. Bramati, M. Pinard, and E. Giacobino, "Continuous variable entanglement using cold atoms," Physical review letters **92** No. 12, (2004) 123601. 58

[170] R. S. Bennink, S. J. Bentley, R. W. Boyd, and J. C. Howell, "Quantum and classical coincidence imaging," Physical review letters **92** No. 3, (2004) 033601. 58

[171] S. Asban, K. E. Dorfman, and S. Mukamel, "Quantum phase-sensitive diffraction and imaging using entangled photons," Proceedings of the National Academy of Sciences **116** No. 24, (2019) 11673–11678. 58, 73

[172] J.-P. W. MacLean, J. M. Donohue, and K. J. Resch, "Direct characterization of ultrafast energy-time entangled photon pairs," Physical review letters **120** No. 5, (2018) 053601. 58, 73, 99

[173] Z. Ou, S. F. Pereira, H. Kimble, and K. Peng, "Realization of the einstein-podolsky-rosen paradox for continuous variables," Physical Review Letters **68** No. 25, (1992) 3663. 58

[174] S. Hill and W. K. Wootters, "Entanglement of a pair of quantum bits," Physical review letters **78** No. 26, (1997) 5022. 58

[175] S. Walborn, P. S. Ribeiro, L. Davidovich, F. Mintert, and A. Buchleitner, “Experimental determination of entanglement with a single measurement,” Nature **440** No. 7087, (2006) 1022–1024. 58

[176] L.-Y. Cheng, G.-H. Yang, Q. Guo, H.-F. Wang, and S. Zhang, “Direct measurement of nonlocal entanglement of two-qubit spin quantum states,” Scientific reports **6** (2016) 19482. 58

[177] M. Lahiri, R. Lapkiewicz, A. Hochrainer, G. B. Lemos, and A. Zeilinger, “Characterizing mixed-state entanglement through single-photon interference,” Physical Review A **104** No. 1, (2021) 013704. 58

[178] G. B. Lemos, R. Lapkiewicz, A. Hochrainer, M. Lahiri, and A. Zeilinger, “Measuring mixed state entanglement through single-photon interference,” arXiv preprint arXiv:2009.02851 (2020) . 58

[179] G. Kulkarni, L. Taneja, S. Aarav, and A. K. Jha, “Angular schmidt spectrum of entangled photons: Derivation of an exact formula and experimental characterization for noncollinear phase matching,” Physical Review A **97** No. 6, (2018) 063846. 58

[180] H. D. L. Pires, C. Monken, and M. Van Exter, “Direct measurement of transverse-mode entanglement in two-photon states,” Physical Review A **80** No. 2, (2009) 022307. 58

[181] A. Hochrainer, M. Lahiri, R. Lapkiewicz, G. B. Lemos, and A. Zeilinger, “Quantifying the momentum correlation between two light beams by detecting one,” Proceedings of the National Academy of Sciences **114** No. 7, (2017) 1508–1511. 58

[182] A. Bhattacharjee, N. Meher, and A. K. Jha, “Measurement of two-photon position-momentum epr correlations through single-photon intensity measurements,” arXiv preprint arXiv:2102.04356 (2021) . 59

[183] A. K. Jha, Coherence properties of the entangled two-photon field produced by parametric down conversion. University of Rochester, 2009. 62

[184] G. Kulkarni, Novel tools for characterizing photon correlations in parametric down-conversion. PhD thesis, INDIAN INSTITUTE OF TECHNOLOGY KANPUR, 2019. 62

[185] C. Cohen-Tannoudji, B. Diu, and F. Laloe, Quantum Mechanics, Volume 1, vol. 1. 1986. 63

[186] M. Lahiri, A. Hochrainer, R. Lapkiewicz, G. B. Lemos, and A. Zeilinger, “Nonclassicality of induced coherence without induced emission,” Physical Review A **100** No. 5, (2019) 053839. 63

[187] S. Karan, S. Aarav, H. Bharadhwaj, L. Taneja, A. De, G. Kulkarni, N. Meher, and A. K. Jha, “Phase matching in $\beta$-barium borate crystals for spontaneous parametric down-conversion,” Journal of Optics **22** No. 8, (2020) 083501. 64

[188] H. Avetisyan and C. Monken, “Higher order correlation beams in atmosphere under strong turbulence conditions,” Optics express **24** No. 3, (2016) 2318–2335. 70, 117, 130

[189] S. P. Phehlukwayo, M. L. Umuhire, Y. Ismail, S. Joshi, and F. Petruccione, “Influence of coincidence detection of a biphoton state through free-space atmospheric turbulence using a partially spatially coherent pump,” Physical Review A **102** No. 3, (2020) 033732. 70, 71, 130

[190] M. Krenn, J. Handsteiner, M. Fink, R. Fickler, R. Ursin, M. Malik, and A. Zeilinger, “Twisted light transmission over 143 km,” Proceedings of the National Academy of Sciences **113** No. 48, (2016) 13648–13653. 71, 77, 96, 97, 98

[191] M. Krenn, R. Fickler, M. Fink, J. Handsteiner, M. Malik, T. Scheidl, R. Ursin, and A. Zeilinger, “Communication with spatially modulated light through turbulent air across vienna,” New Journal of Physics **16** No. 11, (2014) 113028. 71, 77, 96, 97, 98

[192] A. K. Jha and R. W. Boyd, “Spatial two-photon coherence of the entangled field produced by down-conversion using a partially spatially coherent pump beam,” Physical Review A **81** No. 1, (2010) 013828. 71, 132

[193] C. Law and J. Eberly, “Analysis and interpretation of high transverse entanglement in optical parametric down conversion,” Physical review letters **92** No. 12, (2004) 127903. 73

[194] M. Van Exter, A. Aiello, S. Oemrawsingh, G. Nienhuis, and J. Woerdman, “Effect of spatial filtering on the schmidt decomposition of entangled photons,” Physical Review A **74** No. 1, (2006) 012309. 73

[195] V. Srivastav, N. H. Valencia, S. Leedumrongwatthanakun, W. McCutcheon, and M. Malik, “Characterising and tailoring spatial correlations in multi-mode parametric downconversion,” arXiv preprint arXiv:2110.03462 (2021) . 73

[196] W. Zhang, M.-X. Dong, D.-S. Ding, S. Shi, K. Wang, S.-L. Liu, Z.-Y. Zhou, G.-C. Guo, and B.-S. Shi, “Einstein-podolsky-rosen entanglement between separated atomic ensembles,” Physical Review A **100** No. 1, (2019) 012347. 73

[197] S. Kang, S. Jeong, W. Choi, H. Ko, T. D. Yang, J. H. Joo, J.-S. Lee, Y.-S. Lim, Q.-H. Park, and W. Choi, “Imaging deep within a scattering medium using collective accumulation of single-scattered waves,” Nature Photonics **9** No. 4, (2015) 253. 75

[198] O. Katz, P. Heidmann, M. Fink, and S. Gigan, “Non-invasive single-shot imaging through scattering layers and around corners via speckle correlations,” Nature photonics **8** No. 10, (2014) 784. 75

[199] J. Bertolotti, E. G. van Putten, C. Blum, A. Lagendijk, W. L. Vos, and A. P. Mosk, “Non-invasive imaging through opaque scattering layers,” Nature **491** No. 7423, (2012) 232. 75

[200] O. Liba, M. D. Lew, E. D. SoRelle, R. Dutta, D. Sen, D. M. Moshfeghi, S. Chu, and A. de La Zerda, “Speckle-modulating optical coherence tomography in living mice and humans,” Nature communications **8** (2017) 15845. 75, 76

[201] J. W. Goodman, Speckle phenomena in optics: theory and applications. Roberts and Company Publishers, 2007. 75

[202] A. Velten, T. Willwacher, O. Gupta, A. Veeraraghavan, M. G. Bawendi, and R. Raskar, “Recovering three-dimensional shape around a corner using ultrafast time-of-flight imaging,” Nature communications **3** (2012) 745. 76

[203] E. Leith, C. Chen, H. Chen, Y. Chen, D. Dilworth, J. Lopez, J. Rudd, P.-C. Sun, J. Valdmanis, and G. Vossler, “Imaging through scattering media with holography,” JOSA A **9** No. 7, (1992) 1148–1153. 76

[204] H. Kogelnik and K. Pennington, “Holographic imaging through a random medium,” JOSA **58** No. 2, (1968) 273–274. 76

[205] W. Harm, C. Roider, A. Jesacher, S. Bernet, and M. Ritsch-Marte, “Lensless imaging through thin diffusive media,” Optics express **22** No. 18, (2014) 22146–22156. 76

[206] I. M. Vellekoop and A. Mosk, “Focusing coherent light through opaque strongly scattering media,” Optics letters **32** No. 16, (2007) 2309–2311. 76

[207] A. P. Mosk, A. Lagendijk, G. Lerosey, and M. Fink, “Controlling waves in space and time for imaging and focusing in complex media,” Nature photonics **6** No. 5, (2012) 283. 76

[208] S. Knitter, C. Liu, B. Redding, M. K. Khokha, M. A. Choma, and H. Cao, “Coherence switching of a degenerate vecsel for multimodality imaging,” Optica **3** No. 4, (2016) 403–406. 76

[209] Y. Zheng, J. Si, W. Tan, Y. H. Ren, J. Tong, and X. Hou, “Speckle-suppressed full-field imaging through a scattering medium using a supercontinuum,” Optics express **24** No. 23, (2016) 26338–26343. 76

[210] H. Farrokhi, T. M. Rohith, J. Boonruangkan, S. Han, H. Kim, S.-W. Kim, and Y.-J. Kim, “High-brightness laser imaging with tunable speckle reduction enabled by electroactive micro-optic diffusers,” Scientific Reports **7** No. 1, (2017) 15318. 76

[211] L. C. Andrews and R. L. Phillips, Laser beam propagation through random media, vol. 152. SPIE press Bellingham, WA, 2005. 76

[212] A. K. Majumdar and J. C. Ricklin, Free-space laser communications: principles and advances, vol. 2. Springer Science & Business Media, New York, 2010. 76

[213] M. P. Lavery, C. Peuntinger, K. Günthner, P. Banzer, D. Elser, R. W. Boyd, M. J. Padgett, C. Marquardt, and G. Leuchs, “Free-space propagation of high-dimensional structured optical fields in an urban environment,” Science advances **3** No. 10, (2017) e1700552. 76, 98

[214] Y. Ren, L. Li, Z. Wang, S. M. Kamali, E. Arbabi, A. Arbabi, Z. Zhao, G. Xie, Y. Cao, N. Ahmed, *et al.*, “Orbital angular momentum-based space division multiplexing for high-capacity underwater optical communications,” Scientific reports **6** (2016) 33306. 76

[215] A. Trichili, A. B. Salem, A. Dudley, M. Zghal, and A. Forbes, “Encoding information using laguerre gaussian modes over free space turbulence media,” Optics letters **41** No. 13, (2016) 3086–3089. 76

[216] V. Aksenov, V. Kolosov, and C. Pogutsa, “The influence of the vortex phase on the random wandering of a laguerre–gaussian beam propagating in a turbulent atmosphere: a numerical experiment,” Journal of Optics **15** No. 4, (2013) 044007. 76

[217] Y. Yuan, Y. Cai, J. Qu, H. T. Eyyuboğlu, and Y. Baykal, “Propagation factors of hermite–gaussian beams in turbulent atmosphere,” Optics & Laser Technology **42** No. 8, (2010) 1344–1348. 76

[218] B. Ndagano, N. Mphuthi, G. Milione, and A. Forbes, “Comparing mode-crosstalk and mode-dependent loss of laterally displaced orbital angular momentum and hermite–gaussian modes for free-space optical communication,” Optics letters **42** No. 20, (2017) 4175–4178. 76

[219] M. A. Cox, L. Cheng, C. Rosales-Guzmán, and A. Forbes, “Modal diversity for robust free-space optical communications,” Physical Review Applied **10** No. 2, (2018) 024020. 76

[220] K. Pang, H. Song, Z. Zhao, R. Zhang, H. Song, G. Xie, L. Li, C. Liu, J. Du, A. F. Molisch, *et al.*, “400-gbit/s qpsk free-space optical communication link based on four-fold multiplexing of hermite–gaussian or laguerre–gaussian modes by varying both modal indices,” Optics letters **43** No. 16, (2018) 3889–3892. 76

[221] M. Erhard, R. Fickler, M. Krenn, and A. Zeilinger, “Twisted photons: new quantum perspectives in high dimensions,” Light: Science & Applications **7** No. 3, (2018) 17146. 77

[222] H. Roychowdhury and E. Wolf, “Invariance of spectrum of light generated by a class of quasi-homogenous sources on propagation through turbulence,” Optics communications **241** No. 1-3, (2004) 11–15. 77

[223] S. Avramov-Zamurovic, C. Nelson, S. Guth, O. Korotkova, and R. Malek-Madani, “Experimental study of electromagnetic bessel-gaussian schell model beams propagating in a turbulent channel,” Optics Communications **359** (2016) 207–215. 77

[224] M. Salem, T. Shirai, A. Dogariu, and E. Wolf, “Long-distance propagation of partially coherent beams through atmospheric turbulence,” Optics Communications **216** No. 4-6, (2003) 261–265. 77

[225] M. Wang, X. Yuan, and D. Ma, “Potentials of radial partially coherent beams in free-space optical communication: a numerical investigation,” Applied optics **56** No. 10, (2017) 2851–2857. 77

[226] Z. Mei, E. Shchepakina, and O. Korotkova, “Propagation of cosine-gaussian-correlated schell-model beams in atmospheric turbulence,” Optics express **21** No. 15, (2013) 17512–17519. 77

[227] J. Yu, F. Wang, L. Liu, Y. Cai, and G. Gbur, “Propagation properties of hermite non-uniformly correlated beams in turbulence,” Optics express **26** No. 13, (2018) 16333–16343. 77

[228] J. Zhu, X. Li, H. Tang, and K. Zhu, "Propagation of multi-cosine-laguerre-gaussian correlated schell-model beams in free space and atmospheric turbulence," Optics express **25** No. 17, (2017) 20071–20086. 77

[229] X. Liu, J. Yu, Y. Cai, and S. A. Ponomarenko, "Propagation of optical coherence lattices in the turbulent atmosphere," Optics letters **41** No. 18, (2016) 4182–4185. 77

[230] R. Lin, H. Yu, X. Zhu, L. Liu, G. Gbur, Y. Cai, and J. Yu, "The evolution of spectral intensity and orbital angular momentum of twisted hermite gaussian schell model beams in turbulence," Optics Express **28** No. 5, (2020) 7152–7164. 77

[231] A. Bhattacharjee, S. Aarav, H. Wanare, and A. K. Jha, "Controlling propagation of spatial coherence for enhanced imaging through scattering media," Physical Review A **101** No. 4, (2020) 043839. 78, 91

[232] A. Bhattacharjee and A. K. Jha, "Experimental demonstration of structural robustness of spatially partially coherent fields in turbulence," Optics Letters **45** No. 14, (2020) 4068–4071. 78

[233] L. V. Wang and H.-i. Wu, Biomedical optics: principles and imaging. John Wiley & Sons, 2012. 84

[234] R. W. Boyd, B. Rodenburg, M. Mirhosseini, and S. M. Barnett, "Influence of atmospheric turbulence on the propagation of quantum states of light using plane-wave encoding," Optics express **19** No. 19, (2011) 18310–18317. 91, 117

[235] J. W. Goodman, Introduction to Fourier optics. Roberts and Company Publishers, Englewood, Colorado, 2005. 92

[236] B. Rodenburg, M. P. Lavery, M. Malik, M. N. O'Sullivan, M. Mirhosseini, D. J. Robertson, M. Padgett, and R. W. Boyd, "Influence of atmospheric turbulence on states of light carrying orbital angular momentum," Optics letters **37** No. 17, (2012) 3735–3737. 92

[237] L. Mandel and E. Wolf, "The measures of bandwidth and coherence time in optics," Proceedings of the Physical Society **80** No. 4, (1962) 894. 93

[238] D. Peng, Z. Huang, Y. Liu, Y. Chen, F. Wang, S. A. Ponomarenko, and Y. Cai, "Optical coherence encryption with structured random light," PhotoniX **2** No. 1, (2021) 1–15. 97

[239] M. Reid, P. Drummond, W. Bowen, E. G. Cavalcanti, P. K. Lam, H. Bachor, U. L. Andersen, and G. Leuchs, "Colloquium: the einstein-podolsky-rosen paradox: from concepts to applications," Reviews of Modern Physics **81** No. 4, (2009) 1727. 99

[240] P.-A. Moreau, E. Toninelli, T. Gregory, and M. J. Padgett, "Imaging with quantum states of light," Nature Reviews Physics **1** No. 6, (2019) 367–380. 99

[241] N. Gisin and R. Thew, "Quantum communication," Nature photonics **1** No. 3, (2007) 165–171. 99

[242] S. Slussarenko and G. J. Pryde, "Photonic quantum information processing: A concise review," Applied Physics Reviews **6** No. 4, (2019) 041303. 99

[243] A. Steane, "Quantum computing," Reports on Progress in Physics **61** No. 2, (1998) 117. 99

[244] R. T. Thew, A. Acin, H. Zbinden, and N. Gisin, "Bell-type test of energy-time entangled qutrits," Physical review letters **93** No. 1, (2004) 010503. 99

[245] F. Vedovato, C. Agnesi, M. Tomasin, M. Avesani, J.-Å. Larsson, G. Vallone, and P. Villoresi, "Postselection-loophole-free bell violation with genuine time-bin entanglement," Physical review letters **121** No. 19, (2018) 190401. 99

[246] A. C. Dada, J. Leach, G. S. Buller, M. J. Padgett, and E. Andersson, "Experimental high-dimensional two-photon entanglement and violations of generalized bell inequalities," Nature Physics **7** No. 9, (2011) 677–680. 99

[247] R. Fickler, R. Lapkiewicz, W. N. Plick, M. Krenn, C. Schaeff, S. Ramelow, and A. Zeilinger, "Quantum entanglement of high angular momenta," Science **338** No. 6107, (2012) 640–643. 99

[248] I. A. Khan and J. C. Howell, "Experimental demonstration of high two-photon time-energy entanglement," Physical Review A **73** No. 3, (2006) 031801. 99

[249] M. Aspelmeyer, H. R. Böhm, T. Gyatso, T. Jennewein, R. Kaltenbaek, M. Lindenthal, G. Molina-Terriza, A. Poppe, K. Resch, M. Taraba, *et al.*, "Long-distance free-space distribution of quantum entanglement," science **301** No. 5633, (2003) 621–623. 99

[250] F. Steinlechner, S. Ecker, M. Fink, B. Liu, J. Bavaresco, M. Huber, T. Scheidl, and R. Ursin, "Distribution of high-dimensional entanglement via an intra-city free-space link," Nature communications **8** No. 1, (2017) 1–7. 99

[251] N. H. Valencia, S. Goel, W. McCutcheon, H. Defienne, and M. Malik, "Unscrambling entanglement through a complex medium," Nature Physics **16** No. 11, (2020) 1112–1116. 99, 122

[252] J. Jin, J.-P. Bourgoin, R. Tannous, S. Agne, C. J. Pugh, K. B. Kuntz, B. L. Higgins, and T. Jennewein, "Genuine time-bin-encoded quantum key distribution over a turbulent depolarizing free-space channel," Optics express **27** No. 26, (2019) 37214–37223. 99

[253] S. Ecker, F. Bouchard, L. Bulla, F. Brandt, O. Kohout, F. Steinlechner, R. Fickler, M. Malik, Y. Guryanova, R. Ursin, *et al.*, "Overcoming noise in entanglement distribution," Physical Review X **9** No. 4, (2019) 041042. 99

[254] A. Bhattacharjee, M. K. Joshi, S. Karan, J. Leach, and A. K. Jha, "Propagation-induced entanglement revival," arXiv preprint arXiv:2111.04420 (2021) . 100

[255] H. Defienne, M. Reichert, and J. W. Fleischer, "Adaptive quantum optics with spatially entangled photon pairs," Physical review letters **121** No. 23, (2018) 233601. 122

[256] O. Lib, G. Hasson, and Y. Bromberg, "Real-time shaping of entangled photons by classical control and feedback," Science Advances **6** No. 37, (2020) eabb6298. 122

[257] H. Defienne, M. Reichert, and J. W. Fleischer, "General model of photon-pair detection with an image sensor," Physical review letters **120** No. 20, (2018) 203604. 145, 146